

Journal of Electrochemical Science and Engineering

J. Electrochem. Sci. Eng. 14(3) 2024, 275-416





Open Access : : ISSN 1847-9286

www.jESE-online.org

Original scientific paper

Inhibition performance of a novel quinoxaline derivative for carbon steel corrosion in 1 M HCl

Latifa Chahir¹, Fouad Benhiba¹,², Nadeem Abad³, Hassan Zarrok⁴, Ismail Warad⁵, Mousa Al-Noaimi⁶, Driss Benmessaoud Left³, Mustapha Zertoubi³, Mustapha Allali³, Abdelkebir Bellaouchou¹, Youssef Ramli³,9 and Abdelkader Zarrouk¹,⊠

¹Laboratory of Materials, Nanotechnology and Environment, Faculty of Sciences, Mohammed V University in Rabat, Av. Ibn Battouta, P.O. Box. 1014 Agdal-Rabat, Morocco

²Higher Institute of Nursing Professions and Health Techniques of Agadir Annex Guelmim, Guelmim, Morocco

³Laboratory of Medicinal Chemistry, Drug Sciences Research Center, Faculty of Medicine and Pharmacy, Mohammed V University, Rabat, Morocco

⁴Laboratory of Advanced Materials and Process Engineering, Faculty of Sciences, Ibn Tofail University, P.O. Box. 133, 14000, Kenitra, Morocco

⁵Department of Chemistry, AN-Najah National University, P.O. Box 7, Nablus, Palestine

⁶Chemistry Department, Faculty of Science, Kuwait University, P.O. Box 5969, Safat 13060, Kuwait ⁷Laboratoire Interface Matériaux Environnement (LIME), Faculty of Sciences Ain Chock University Hassan II, Casablanca, B.P 5366, Morocco

⁸Institute of Nursing Professions and Health Techniques Fez, EL Ghassani Hospital, Fez 30000, Morocco

⁹Mohammed VI Center for Research and Innovation (CM6), Rabat 10000, Morocco Corresponding author: [™]azarrouk@gmail.com

Received: November 13, 2023; Accepted: March 14, 2024; Published: May 14, 2024

Abstract

In this work, the effect of a new quinoxaline derivative, 2-phenyl-3-(prop-2-yn-1-yloxy) quinoxaline (PYQX), was evaluated as a corrosion inhibitor for carbon steel (CS) in 1 M HCl electrolyte. Weight loss measurement, atomic absorption spectroscopy, potentiodynamic polarization, electrochemical impedance spectroscopy, scanning electron microscopy with energy dispersive spectroscopy, and UV-vis spectroscopy were employed to assess the inhibitory activity. The electronic properties of the interaction between the inhibitor molecule and the CS substrate were studied using molecular dynamics (MD) simulation, density functional theory (DFT), and Fukui functions. According to AC impedance experiments, the inhibitor under consideration showed a maximum level of 98.1 % inhibition efficiency at 1 mM and 30 °C. The Langmuir adsorption isotherm model explains the adsorption of PYQX on the CS surface. A slope of 1 denotes a strong molecule-substrate interaction, suggesting that the binding occurs at specific surface locations. To understand

the functioning of the adsorption mechanism, various thermodynamic and activation parameters were evaluated. PDP tests demonstrated that PYQX functions as a mixed-type inhibitor. Computational correlations (DFT, MD, and Fukui indices) supported the experimental findings.

Keywords

Carbon-iron alloy; organic corrosion inhibitor; weight loss; electrochemical testing; quantum chemical calculations

Introduction

Carbon steel (CS) is often used for structural supports and components in railway systems, bridges, and other public works because of its high tensile strength, abrasion resistance, and superior surface properties [1]. However, exposure of steel to aggressive environments, such as acid-cleaning processes, can cause the metal to deteriorate and reduce its durability [2]. Corrosion inhibitors are a cost-efficient and highly effective way to mitigate the corrosive effects of steel in acidic environments [3,4].

Quinoxaline compounds have been extensively studied as corrosion inhibitors, which are environmentally safe and applicable to multiple fields such as chemistry, mechanics, and materials. It is suggested that the functional groups, conjugated multiple bonds, and aromatic rings present in quinoxaline-based molecules contribute to their excellent inhibitory performance.

Numerous corrosive conditions have been used to thoroughly assess the inhibitory abilities of these derivatives. Zarrouk *et al.* used gravimetric and electrochemical techniques to explore the impact of several quinoxaline analogs on the deterioration of copper in HNO₃ acid [5]. Recently, several authors have worked on the inhibition of corrosion of mild steel in 1 M HCl corrosive media by certain quinoxaline compounds using weight loss (WL) and electrochemical techniques, showing the high potential of quinoxaline molecules to prevent corrosion of metals [6-9]. The literature survey also showed that calculations using density functional theory (DFT) and molecular dynamic simulations (MDS) frequently provide good theoretical justifications for experimental findings in corrosion inhibition investigations [10].

In this study, the inhibitory effect of 2-phenyl-3-(prop-2-yn-1-yloxy) quinoxaline (PYQX) on CS corrosion in 1 M acidic electrolyte has been investigated. The adsorption mechanism of this quinoxaline derivative on the CS surface is further explained using quantum chemical calculations supported by DFT, Fukui functions, and molecular dynamics (MD) simulations.

Experimental

Materials and solution

In this study, CS plates with dimensions $1.5\times1.5\times0.3$ cm were employed for testing samples. Its composition (in weight percent) is the following: C-0.3700 %, Si-0.2300 %, Mn-0.6800 %, S-0.0160 %, Cr-0.0770 %, Ti-0.0110 %, Ni-0.0590 %, Co-0.0090 %, Cu-0.1600 %, and iron (Fe) as the remaining content. The working electrode (WE) area exposed for the electrochemical corrosion test was 1 cm² in size. Before each use, the samples were meticulously polished with abrasive paper of increasing grain size, dried, washed with distilled water and degreased with acetone.

The electrolyte medium, 1 M HCl, was obtained by diluting concentrated 37 % analytical-grade HCl with distilled water. The synthesized compound PYQX, with the structure shown in Figure 1,

dissolves readily in 1 M HCl solution, allowing the preparation of four inhibitor assays that ranged from 10^{-3} to 1 mM.

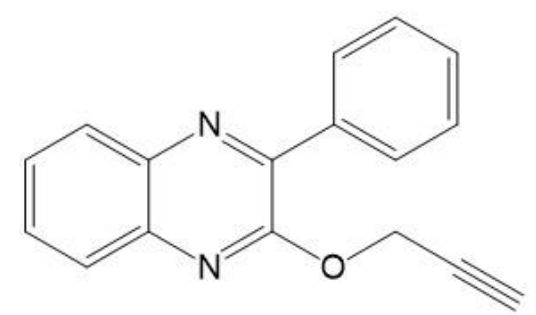


Figure 1. Molecular structure of PYQX

Weight loss measurements

Polished CS plates were weighed and in triplicate, placed into 50 mL glass beakers using plastic forceps. These beakers contained 1 M HCl solutions with and without various inhibitor dosages. After six hours, the samples were removed, rinsed with distilled water, dried, and re-weighed. The initial and final weights of the plates were used to determine the weight loss (WL) as $\Delta m/mg$ (before and after soaking). By applying the following calculations to the weight loss data, the inhibitory effectiveness η_{WL} /% and corrosion rate (CR) (mg cm⁻² h⁻¹) were determined by equations (1) and (2) [11]:

$$CR = \frac{\Delta m}{St} \tag{1}$$

$$\eta_{\text{WL}} = \left(1 - \frac{CR^{i}}{CR^{u}}\right) 100 \tag{2}$$

where and CR^u and CRⁱ are corrosion rates in the uninhibited and inhibited electrolyte.

Electrochemical testing

All electrochemical tests were carried out using a PGZ 100 potentiostat under computer control with the Voltamaster 4 program. The test model was a standard three-electrode system composed of a saturated calomel reference electrode (SCE), a platinum counter electrode, and a CS plate with an exposed surface area of 1 cm² working electrode. After observing the evolution of the open circuit potential (OCP), which usually takes approximately half an hour to stabilize, electrochemical experiments were conducted. Tafel curves were scanned by sweeping the potential with a velocity of 0.5 mV/s around the OCP in the potential range of -800 to -100 mV. The amplitude of the 10 mV peak-to-peak AC signal at OCP was used to measure the EIS at frequencies ranging from 100 kHz to 10 mHz. Impedance data were collected and presented using Nyquist and Bode plots.

The equations (3) and (4) were employed to determine the inhibition efficiency (η / %) [12]:

$$\eta_{R} = \left(\frac{R_{p} - R_{p}^{0}}{R_{p}}\right) 100 = 100 \theta \tag{3}$$

where R_p and R_p^0 stand for the polarization resistance with and without inhibitor solution, respectively, while θ represents the extent of surface coverage.

$$\eta_{p} = \left(\frac{i_{\text{corr}}^{0} - i_{\text{corr}}}{i_{\text{corr}}^{0}}\right) 100 \tag{4}$$

where i_{corr}^{0} and i_{corr} are corrosion current densities without and with inhibitor solution, respectively.

The results for the blank obtained by two electrochemical techniques (stationary and transient) in analysing the effects of concentration and temperature were taken from the previous article [12] since the experiments were carried out under the same conditions.

Atomic absorption spectroscopy

AAS was used to quantify the metallic elements in solutions. After electrochemical tests, this method was employed to determine the iron concentration in 1 M acidic media with and without varying amounts (10^{-3} to 1 mM) of PYQX at 30 °C.

Using the atomic absorption data, the equation (5) was applied to determine the inhibition efficiency [13]:

$$\eta_{A} = \frac{C_{Fe}^{0} - C_{Fe}}{C_{Fe}^{0}} 100 \tag{5}$$

where C_{Fe}^{0} and C_{Fe} represent Fe concentration in solutions without and with various PYQX amounts, respectively.

Surface characterization and electrolyte analysis

Using scanning electron microscopy with a magnification of 10000×, the surface morphologies of the CS samples were examined following their submersion in acidic media for 24 hours at 30 °C, both without and with the optimum concentration of 1 mM PYQX. At the accelerating voltage of 20 kV, energy dispersive X-ray spectroscopy (EDS) coupled with SEM was utilized to get information about the chemical composition of the material. SEM-EDS results in the absence of the inhibitor were taken from a work already published by our research team [12]. The electrolytes were carefully examined using a Jenway (series 730) UV-vis spectrophotometer before and after immersion of the CS for 72 hours at 30 °C in 1 M HCl solutions, including 1 mM of PYQX, to check for the potential formation of ferric ion-inhibitor complexes.

Computer-based research

Density functional theory (DFT) study

DFT has been utilized for a long time to assess the reactivity of organic inhibitors and correlate it to the efficiency of corrosion prevention. The program Gaussian 09 was employed to determine the DFT-based quantum physics parameters. The geometric optimization of the quinoxaline derivative PYQX in its neutral and protonated forms in the aqueous phase was produced by DFT calculations using the function B3LYP and the 6-311++G(d,p) basis set [14].

The energy gap (ΔE) energies of the lowest unoccupied molecular orbital (E_{LUMO}), highest occupied molecular orbital (E_{HOMO}), as well as the other quantum descriptors were calculated with the equations (6) to (9):

$$\Delta E = E_{\text{LUMO}} - E_{\text{HOMO}}$$
 (6)

Global hardness (η):

$$\eta = -0.5 \Delta E \tag{7}$$

Global electronegativity (χ):

$$\chi = 0.5 \left(E_{\text{LUMO}} + E_{\text{HOMO}} \right) \tag{8}$$

The fraction of electrons transferred:

$$\Delta N_{110} = \frac{\chi_{\text{Fe}_{110}} - \chi_{\text{inh}}}{2(\eta_{\text{Fe}_{110}} + \eta_{\text{inh}})} = \frac{\Phi - \chi_{\text{inh}}}{2\eta_{\text{inh}}}$$
(9)

where Φ is the work function explains the theoretical value of χ in Fe₁₁₀ with $\Phi = \chi(\text{Fe}_{110}) = 4.82 \text{ eV}$.

Fukui indice calculations

The analysis of Fukui indices was applied to the inhibitor molecule PYQX to uncover the functional groups that enable it to interact with the iron site. This comprehensive analysis revealed that the local reactivity of PYQX was mainly attributed to the interactions between certain local reactive canters and the iron region. The dual numerical polarization basis set, consisting of the d and p orbitals, was employed in the calculations. The Fukui function is determined as the primary derivative of the electron density $(\rho(\vec{r}))$ in relation to the electron number (N) in a constant external potential $(\nu(\vec{r}))$ as in equation (10) [15,16]:

$$f_{k} = \left(\frac{\partial \rho(\vec{r})}{\partial N}\right)_{\nu(\vec{r})} \tag{10}$$

The Fukui function displays the available position in the inhibitor where nucleophilic or electrophilic assaults are most likely [15,16]. The following finite difference approximation approaches can be used to express Fukui indices for nucleophilic attack (f_k^+) and electrophilic assault (f_k^-) , equations (11) and (12):

$$f_{k}^{+} = q_{k}(N+1) - q_{k}(N) \tag{11}$$

$$f_{k}^{-} = q_{k}(N) - q_{k}(N-1)$$
 (12)

where, $q_k(N)$, $q_k(N+1)$ and $q_k(N-1)$) represent the neutral, cationic and anionic species, respectively.

Molecular dynamics simulations

MD was used in order to explore the interaction of the substances under study with Fe (110). Like in our previous work [16], this simulation was carried out at a similar level using the Forcite module found in the Materials Studio/8 using simulation box " $2.730\times2.730\times3.713$ nm³" ($27.30\times27.30\times37.13$ ų). This vacuum of this box is filled by 491 H₂O, 9 H₃O⁺, 9 Cl⁻, and quinoxaline derivative. The Andersen thermostat was used to calibrate the system temperature to 303 K at 1000 ps simulation time and 1.0 fs utilizing the NVT ensemble, all while operating within the COMPASS force field.

Results and discussion

Weight loss and atomic absorption spectroscopy analysis

WL measurements were carried out to assess the corrosion inhibition ability of PYQX, as well as the impact of inhibitor concentration on the corrosion rate. Table 1 shows that after 6 hours of submersion, the corrosion speed of CS in the acid media was higher than that of the inhibitor solution. Simultaneously, raising the PYQX concentration from 10^{-3} to 1 mM lowered the corrosion rate from 0.321 to 0.072 mg cm⁻² h⁻¹ of CS, corresponding to an increase in inhibition effectiveness from 83.1 to 96.5 %. This demonstrates that the adsorption of inhibitor molecules protects the CS surface by blocking mass and charge transfer processes. Interestingly, the same outcomes were obtained using the atomic absorption technique (Table 1), where it was found that the addition of PYQX reduced the concentration of iron in the HCl medium. Hence, it seems that the inhibitor included in the mixture reduces steel degradation by improving the surface covering and retarding corrosion.

Weight loss Atomic absorption C/mMCR, mg cm⁻² h⁻¹ η_{W} L / % C_{Fe} / ppm $\eta_{\rm A}$ / % 0.000 1.946 19.286 0.001 0.321 3.253 83.5 83.1 0.010 0.187 90.4 2.064 89.3 0.100 0.142 92.7 1.311 93.2 1.000 0.072 96.3 0.675 96.5

Table 1. Weight loss and AAS data for CS in 1 M HCl without and with different concentrations of PYQX

Electrochemical analysis

Open circuit potential plots

Figure 2 illustrates how the open circuit potential (OCP) value changes depending on the duration of immersion of CS in 1 M HCl electrolyte medium, both with and without PYQX. It is obvious that 1800 s is long enough for the system to stabilize. It was also observed that the $E_{\rm OCP}$ is displaced in a positive direction following the addition of PYQX. This can result from PYQX sticking to the steel electrode surface [17]. It is noteworthy to say that there is no specific relationship between the potential shift of $E_{\rm OCP}$ and PYQX concentration.

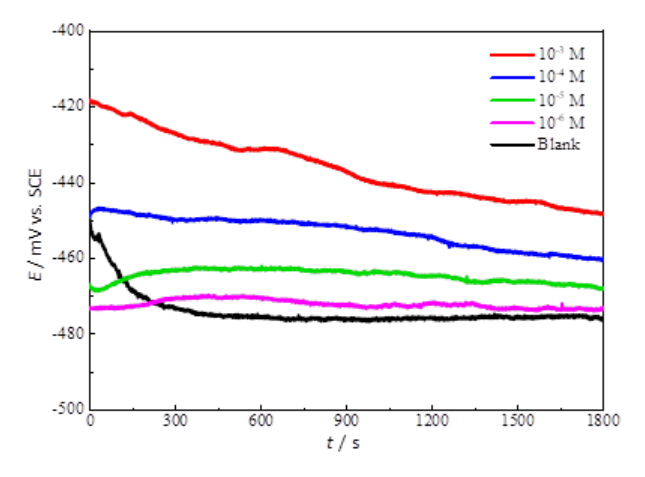


Figure 2. Time variation in E_{OCP} for CS in uninhibited 1 M HCl electrolyte, and with a variety of PYQX doses

Potentiodynamic polarization analysis

Figure 3 illustrates the PDP curves for CS performed at 30 °C in the electrolyte without and with various doses of PYQX. It is evident that including PYQX in the corrosive medium induces an overall reduction in cathodic and anodic current densities, which becomes more pronounced with increasing amounts of PYQX. This result suggests that PYQX reduces anodic oxidation and retards the reduction of H⁺ protons [17]. The reduction trend of the cathodic segment was greater than that of the anodic segment, suggesting that PYQX has a greater protective influence on the cathodic reaction than on the anodic reaction. On the downside, the cathodic portions are linear, indicating that PYQX has little influence on the H⁺ ion reduction mechanism and that the H⁺ reduction reaction at the CS interface occurs mainly by a pure activation [17].

Table 2 presents the outcomes of inhibition effectiveness (η_P / %), as well as electrochemical corrosion factors such as corrosion current density ($i_{corr.}$), corrosion potential ($E_{corr.}$), and Tafel slopes (cathodic (β_c) and anodic (β_a)) for different concentrations of PYQX, obtained by extrapolation of the linear cross-sections of the anodic and cathodic polarization plots at $E_{corr.}$ [18]. Analysing the corrosion potential allows the inspection of the inhibition mechanism of inhibitor molecules. The shift in $E_{corr.}$ with PYQX injection was significantly less than 85 mV from baseline, a value considered a threshold

for identifying the type of inhibitor. The slight shift in E_{corr} following the addition of the inhibitor demonstrated that investigated molecules function as a mixed-type inhibitor by limiting CS oxidation and H⁺ ion reduction. It follows that surface adsorption, leading to the formation of a coating layer covering the active sites, is the primary mechanism behind the inhibitory activity of PYQX [18]. The η_P increases as the inhibitor PYQX concentration increases, peaking at 98.1 % at 1 mM. This result agrees well with the conclusions of the measures of atomic absorption and weight loss.

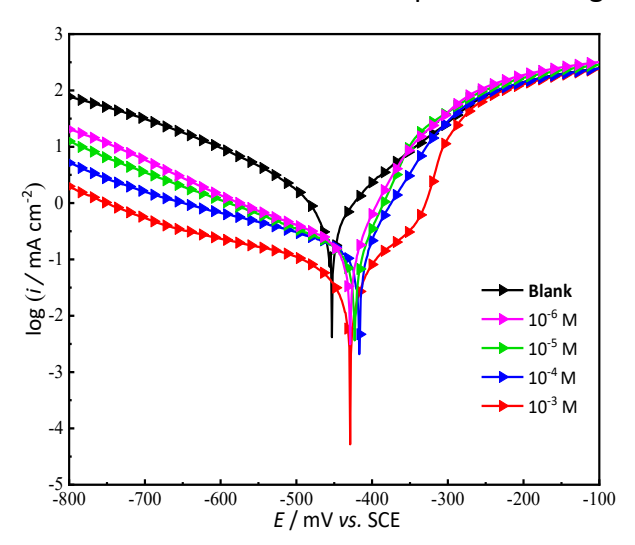


Figure 3. PDP curves for CS in uninhibited 1 M HCl electrolyte and with a variety of PYQX doses

with a variety of PYQX doses								
mM	-E _{corr} / mV vs. SCE	$-eta_{ m c}$ /mV dec $^{-1}$	eta_{a} / mV dec $^{ ext{-}1}$	i _{corr} /μA cm ⁻²	$\eta_{ extsf{P}}$			
000	456.3	155.4	112.8	1104.1				

Table 2. PDP factors and η_P for CS corrosion in the uninhibited 1 M HCl electrolyte and

C/ r / % 0.0 432.2 90.3 0.001 119.9 71.9 107.6 0.010 426.1 122.3 85.5 91.2 91.7 0.100 420.3 87.6 62.6 51.2 95.4 1.000 432.1 114.1 75.5 21.3 98.1

Electrochemical impedance spectroscopy analysis

Electrochemical impedance spectroscopy (EIS) is generally used to explore the mechanisms of charge transfer, surface passivation, and corrosion inhibition at the metal-electrolyte interface. Typically, Nyquist and Bode curves are employed to highlight these outcomes of EIS. The properties of corrosion prevention of quinoxaline derivative on CS have already been explored by EIS [19]. Nyquist impedance plots and Bode impedance modulus and phase angle plots of CS in the uninhibited electrolyte and with a variety of PYQX doses at 30 °C are shown in Figures 4 and 5, respectively.

Nyquist plots $(Z_i vs. Z_r)$ presented in Figure 4 show that just one capacitive loop has an identical form for all experienced inhibitor concentrations. These similar impedance responses indicate that the presence of PYQX did not alter the corrosion mechanism significantly, and the charge transfer is the primary factor controlling the process of corrosion. Similarly, Figure 4 reveals that the capacitive loop diameter rises with a rising dose, thus indicating inhibition efficiency. The obvious rise of impedance modulus |Z| at low frequencies, as evident in the Bode graphs (Figure 5), implies the rise of charge transfer resistance with the rise of the inhibitor concentration. This could be a confirmation of better coverage with the increase of PYQX dose, related to the planar geometry of the quinoxaline derivative, which may boost the adsorption of this substance on the CS surface by creating a barrier coat that prevents corrosion [19]. The phase angle diagrams present only one peak, revealing that the corrosion process requires only one stage and is governed by charge transfer. With increasing inhibitor concentration, the phase angles at corresponding peaks attained higher negative values due to considerable molecular adsorption, suggesting that the tested inhibitor PYQX may be involved in creating a protective layer on the metal substrate [20-22].

The experimental Nyquist and Bode diagrams for PYQX were adjusted using the equivalent electrical circuit depicted in Figure 6. The equivalent circuit in Figure 6 includes a solution resistance (R_s), a polarization resistance (R_p), and a constant phase element (CPE) describing a contribution of double-layer impedance. Equation (13) can be utilized to determine the expression for the impedance of the CPE [19]:

$$Z_{\text{CPE}} = \left| \frac{1}{Q(i\omega)^n} \right| \tag{13}$$

where Q, i, ω and n are CPE constant, imaginary number, angular frequency ($\omega = 2\pi f$, where f is frequency), and CPE exponent, which can be used to measure the roughness or heterogeneity of the surface, respectively.

The double layer capacity ($C_{\rm dl}$) of an adsorbed film is connected to the CPE settings in accordance with equation (14):

$$C_{\text{dl}} = \left[Q R_p^{1-n} \right]^{1/n} \tag{14}$$

The impedance parameter values retrieved and determined by fitting EEC in Figure 6 to EIS results in Figures 4 and 5 are presented in Table 3, together with calculated values for inhibitor efficacy using eq. (4), and chi-square (χ^2) values obtained after impedance data fitting procedure. Low values of χ^2 indicate a strong correlation between impedance data obtained by the chosen model and the measured outcomes. This suggests that there is a good concordance between the two sets of data.

Data in Table 3 generally show that the value of R_p rises as PYQX content does. This rise leads to the protection of the CS and reduces the number of active sites produced by binding the negatively charged Cl^- ions to the surface of CS. The simultaneous reduction in C_{dl} values can be ascribed to a decline in the local dielectric constant and/or an augmentation in the thickness of the electrical double layer, indicating the adsorption of the studied molecules onto the metal surface [12].

The EIS study gave an inhibitory efficiency of about 97.1 % for a concentration of 1.0 mM PYQX at 30 °C. This confirms the previous results obtained by WL, AAS and PDP.

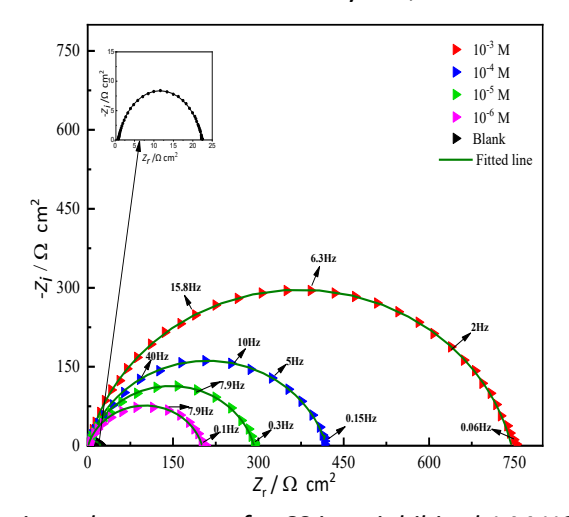


Figure 4. Nyquist impedance curves for CS in uninhibited 1 M HCl electrolyte and with a variety of PYQX doses

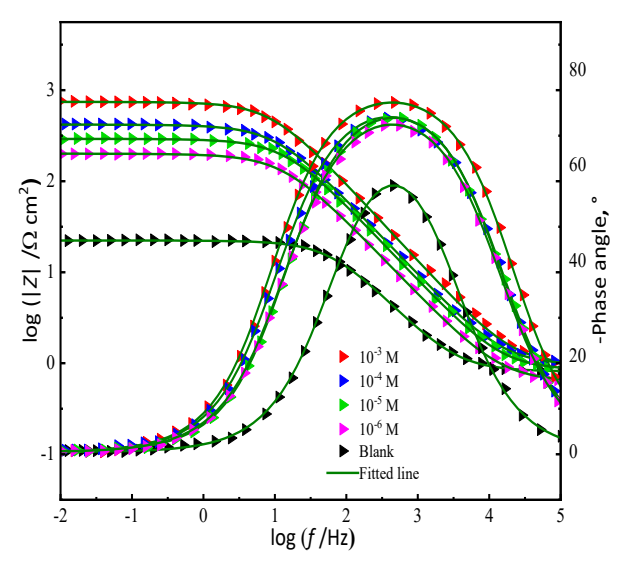


Figure 5. Bode graphs for CS in uninhibited 1 M HCl electrolyte and with a variety of PYQX doses

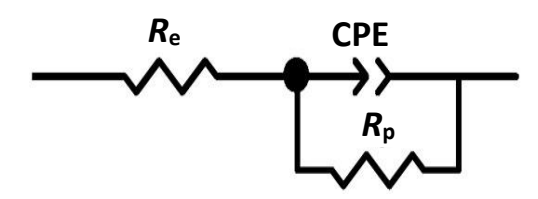


Figure 6. The electrical equivalent circuit model

Table 3. EIS variables and inhibitory effectiveness for CS in the uninhibited 1M HCl electrolyte and with a variety of PYQX doses

C/mM	$R_{\rm s}/\Omega{\rm cm}^2$	$R_{\rm p}/\Omega{\rm cm}^2$	$Q/10^{-6} \Omega^{-1} s^n \mathrm{cm}^{-2}$	n	C _{dl /} μF cm ⁻²	χ^2	η _R / %	θ
0.000	0.83	21.57	293.9	0.845	116.2	0.002		
0.001	0.80	200.5	78.0	0.847	36.8	0.004	89.2	0.892
0.010	0.86	291.5	64.1	0.850	31.8	0.003	92.6	0.926
0.100	1.01	418.6	49.3	0.854	25.4	0.006	94.8	0.948
1.000	0.96	743.8	35.5	0.866	20.2	0.009	97.1	0.971

Adsorption isotherm

After adhering to the metal/solution contact, organic molecules restrict the dissolution of C=S. Thus, it is needed to investigate the adhesion property of PYQX molecules on the C=S contact. To achieve this goal, a variety of adsorption models were investigated in the present research., including the Langmuir, Freundlich, El-Awady, Temkin, and Flory-Huggins isotherms. Finally, the results of this study indicate that the Langmuir model is the best-suited model for characterizing the adsorption of PYQX onto the CS contact, which can be expressed by equation (15):

$$\frac{\theta}{1-\theta} = K_{\text{ads}} C_{\text{inh}} \tag{15}$$

where C_{inh} , K_{ads} , and θ are the PYQX concentration, the equilibrium adsorption constant and the extent of surface coverage, respectively.

The standard Gibbs free energy of adsorption ΔG_{ads}^0 is related to the K_{ads} according to equation (16) [20]:

$$\Delta G_{\rm ads}{}^{0} = -RT \ln(55 \, K_{\rm ads}) \tag{16}$$

where 55.5 is the concentration of water in solution, R and T are gas constant and absolute temperature (303 K), respectively.

The Langmuir isotherm graph is illustrated in Figure 7. It has already been recognised that when $\Delta G_{\rm ads}{}^0 > -20~{\rm kJ~mol^{-1}}$, inhibitor molecules are adsorbed onto the CS surface by electrostatic interactions (physisorption), while when $\Delta G_{\rm ads}{}^0 < -40~{\rm kJ~mol^{-1}}$, inhibitor adsorption occurs through the formation of coordination bonds (chemisorption) between compound molecules and the CS surface. In cases where -40 kJ mol⁻¹ $< \Delta G_{\rm ads}{}^0 < -20~{\rm kJ~mol^{-1}}$, inhibitor adsorption occurs through both physisorption and chemisorption [20].

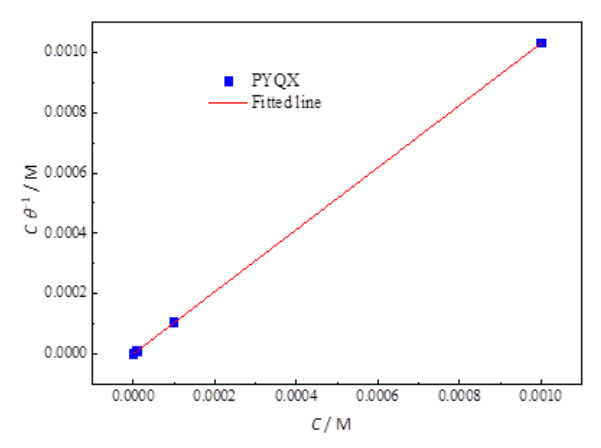


Figure 7. Langmuir isotherm graph for PYQX adsorption on the CS in 1 M HCl at 30 °C

 R^2 value of linear regression in Figure 7 is 1, indicating a close-to-perfect linear correlation. This affirms that the Langmuir adsorption model applies to the adsorption process of PYQX in the corrosion test. This data suggests that the adsorption process between PYQX and the corrosion system is highly efficient, allowing for consistent and reliable results. The negative value of $\Delta G_{\rm ads}^0$ and the high value of K, which takes on the value 988660.069 L mol⁻¹, demonstrate the durability of the bilayer taken up on the CS interface, resulting in a higher effectiveness of inhibition [21]. Additionally, the calculated value of $\Delta G_{\rm ads}$ in this study is equal to -44.89 kJ mol⁻¹, which reveals that adsorption of 2-phenyl-3-(prop-2-yn-1-yloxy) quinoxaline on the CS surface is mainly through chemisorption.

Temperature effect

In pickling, inhibitors are employed to guard against an acidic assault on metal equipment. Pickling processes are often carried out at high temperatures. For application, a corrosion inhibitor must maintain its effectiveness in a corrosive system at specific working temperatures. The research has clearly established that when temperature increases, organic molecules are desorbed from surfaces, which then results in increased corrosion of metals. This phenomenon has been documented and observed in numerous studies. Therefore, it is doubtful that higher temperatures can cause enhanced metal corrosion [21].

In the interest of investigating how temperature affects the efficiency of PYQX, PDP tests were carried out in the uninhibited electrolyte and with 1 mM PYQX at temperatures fluctuating between 30 to 60 °C (Figure 8). The inhibitor efficiency values (η) and electrochemical variables calculated for this study are presented in Table 4. The results show that an elevation in temperature produces higher i_{corr} values and this effect is greater in the uninhibited electrolyte. This means that the rise in temperature speeds up the disintegration of the CS by causing desorption of the PYQX molecules from the CS surface.

The η_p dropped from 98.1 to 91.6 %, demonstrating that PYQX underwent desorption from the CS surface, and consequently, the degree of surface coverage decreases as the adsorption-desorption equilibrium shifts in favour of inhibitory desorption [21].

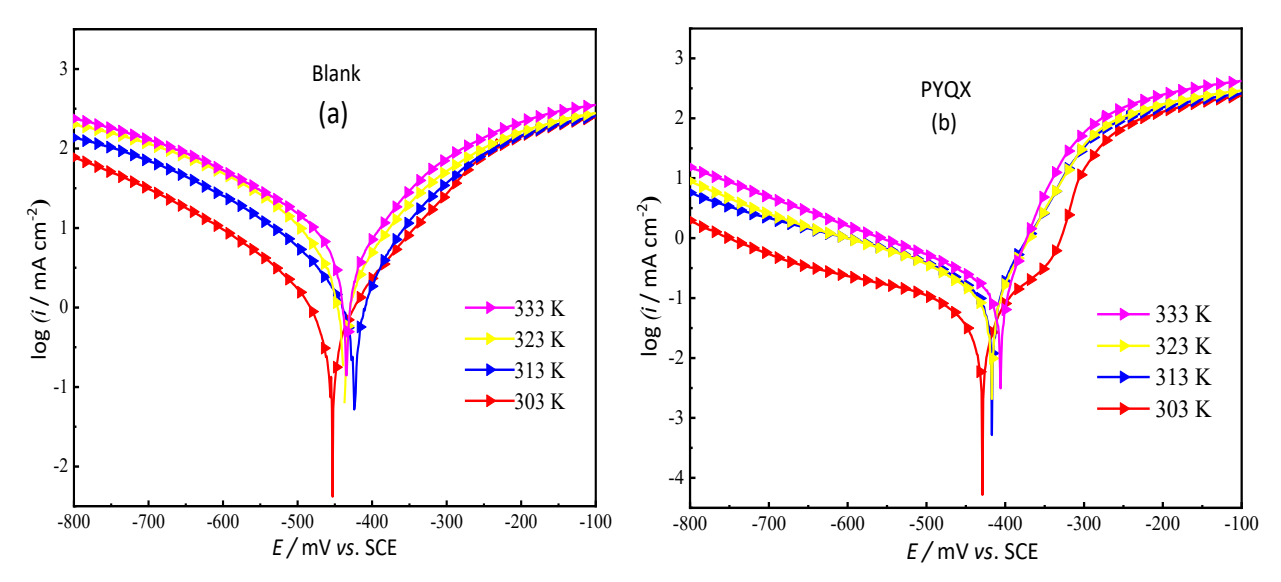


Figure 8. PDP graphs of CS in 1 M HCl electrolyte (a) - without and (b) - with 1.0 mM of PYQX, at different temperatures

Table 4. PDP electrochemical variables of CS in 1 M HCl electrolyte without and with 1 mM of PYQX, at
different temperatures

Medium	T/K	-E _{corr} / mV <i>vs.</i> SCE	- eta_c / mV dec $^{ ext{-}1}$	$eta_{\!\scriptscriptstyle a}$ / mV dec $^{\scriptscriptstyle extsf{-}1}$	i _{corr} / μA cm ⁻²	η _p / %
-	303	456.3	155.4	112.8	1104.1	
Dlank alastraluta	313	423.5	131.3	91.3	1477.4	
Blank electrolyte	323	436.3	117.8	91.4	2254.0	
	333	433.3	134.6	103.9	3944.9	
	303	432.1	114.1	75.5	21.3	98.1
DVOV	313	420.0	109.5	62.0	79.3	94.6
PYQX	323	420.5	127.0	71.5	138.4	93.9
	333	409.3	174.2	52.5	329.5	91.6

Activation parameters

The descriptors of the important indices, which are activation energy (E_a), enthalpy change (ΔH_a), and entropy change (ΔS_a), were determined in order to better understand how temperature affects the inhibition mechanism. The E_a value of the corrosion process at varying temperatures, both without and with 1 mM of PYQX was computed by applying the Arrhenius equation (17) [22]:

$$i_{corr} = A e^{\frac{-E_a}{RT}}$$
 (17)

 ΔH_a and ΔS_a were computed by using the following alternative Arrhenius equation (18) [22]:

$$i_{corr} = \frac{RT}{Nh} e^{\frac{\Delta S_a}{R}} e^{\frac{\Delta H_a}{RT}}$$
 (18)

where *A*, *R*, *T*, *N*, and *h* are the pre-exponential constant, gas constant, absolute temperature, Avogadro number, and Planck's constant, respectively.

The E_a value for CS oxidation was calculated without and with 1.0 mM of PYQX using the slope $(-E_a/R)$ of the plot presented in Figure 9, which shows the dependency of $\ln(i_{corr})$ on 1/T. Likewise, by

tracing $\ln(i_{corr}/T)$ as a function of 1/T under the same conditions (Figure 10), the slope calculates the values of ΔH_a , while the y-intercept calculates the values of ΔS_a . The activation energy and thermodynamic parameters resulting from the Arrhenius and the transition state plots are reported in Table 5.

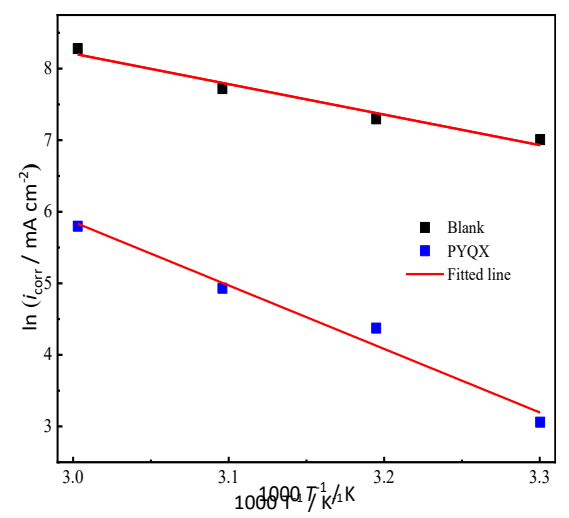


Figure 9. Arrhenius plots for CS in uninhibited 1 M HCl electrolyte and with 1 mM of PYQX

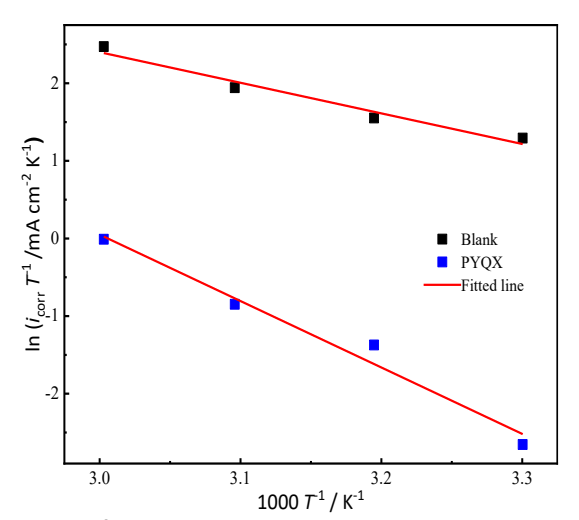


Figure 10. Transition-state plots for CS in uninhibited 1 M HCl electrolyte and with 1 mM of PYQX

It has been noted in Table 5, that when 10^{-3} M of PYQX is present, the E_a value is greater than that of the uninhibited electrolyte, suggesting that there is an energy barrier between the CS surface and inhibitor molecules under study. The oxidation process of the CS substrate is endothermic, as indicated by the positive sign of the activation enthalpy change (ΔH_a). In addition, the existence of PYQX increased the value of ΔH_a , stating that the dissolution of CS is difficult due to the adsorption of PYQX molecules on the CS surface. On the other side, ΔS_a value attains a high positive value compared to the uninhibited medium, indicating an increase in disorder of the system occurs throughout the adsorption process of the transformation from reactant molecules to activated complexes [23].

Table 5. Activation energy and thermodynamic parameters of CS in uninhibited 1 M HCl electrolyte and with 1 mM of PYQX

Medium	Ea∕kJ mol ⁻¹	ΔH_a / kJ mol ⁻¹	$\Delta S_a / J \text{ mol}^{-1} \text{ K}^{-1}$
Blank electrolyte	35.4	32.8	-79.2
PYQX	73.8	71.2	16.3

Scanning electron microscopy and energy-dispersive X-ray spectroscopy analysis

Surface examination by scanning electron microscopy (SEM) scanning technique was completed to generate evidence of the impact of inhibitor compounds on the microstructure of the CS surface and to confirm the creation of a protected layer by PYQX on the substrate. Figure 11 displays CS surface SEM micrographs after 24 h of soaking in the uninhibited medium [23] and with 1 mM of PYQX.

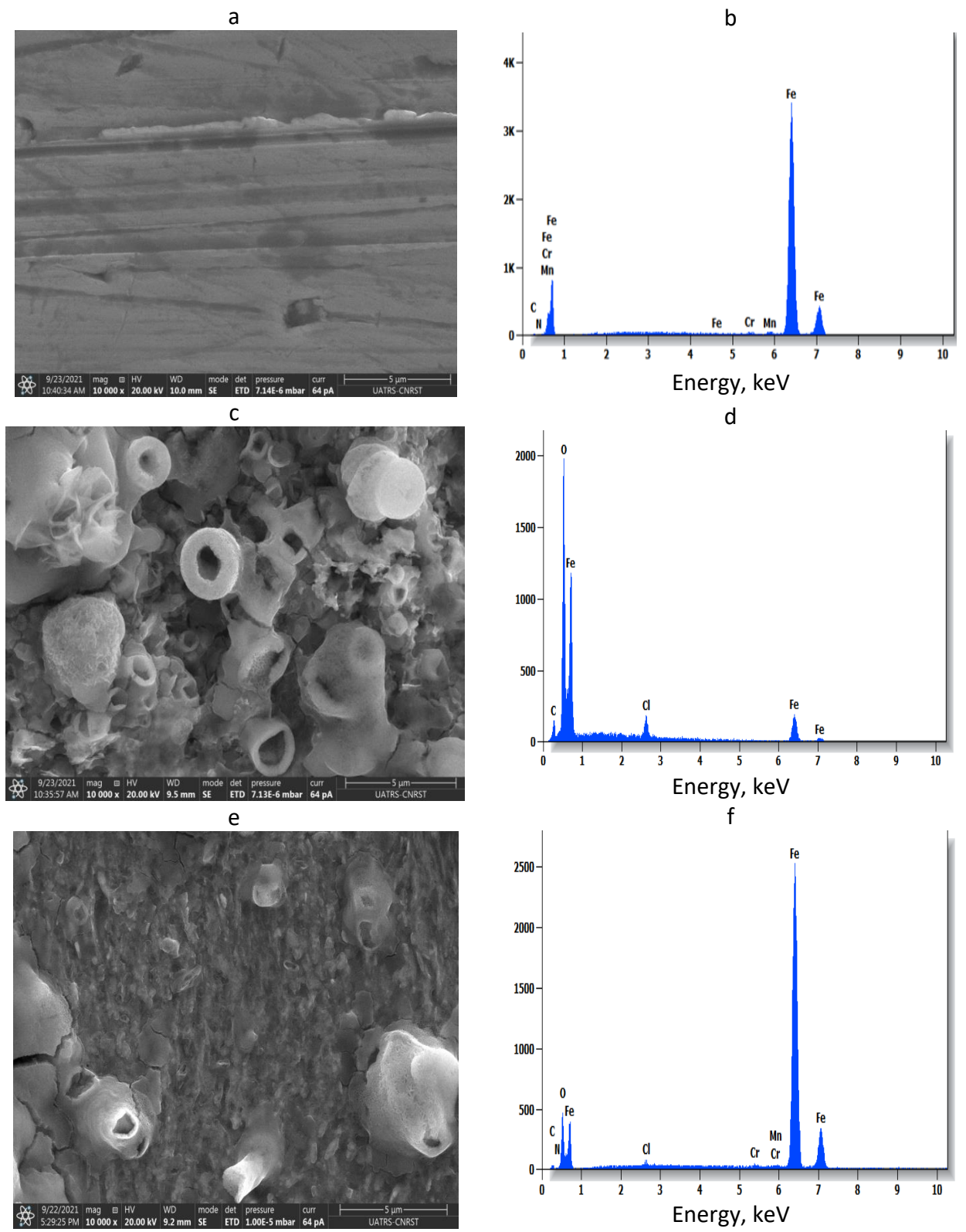


Figure 11. SEM/EDS photographs obtained: immediately after polishing (a/b), 24 hours after soaking in 1_M HCl media (c/d), and 24 hours after soaking in 1 M HCl media with 1 mM PYQX (e/f).

SEM images (a) and (c) are taken from [12]

Figure 11(a) shows that the polished CS surface has many scratches from polishing. It is clear from Figure 11(c) that the morphology of the entire CS area after immersion in the uninhibited medium is severely damaged, while Figure 11(e) shows that the surface morphology greatly improves when 1 mM PYQX is present in the solution. This shows that the inclusion of PYQX leads to a reduction in the number of active corrosion centres by adsorption of the molecules of PYQX on the surface of the CS substrate, thus creating a stable, protective film. The EDS spectrum for the polished CS presented in Figure 11(b) showed a strong iron peak and peaks characteristic for the chemical composition of the CS sample. After immersion of the CS in the HCl electrolyte, the EDS spectrum in Figure 11(d) shows strong Cl and O peaks, suggesting the existence of oxides and chlorides in the corrosion products. On the surface of the specimens exposed to the PYQX-inhibited acidic electrolyte, a remarkable reduction in Cl content is revealed in Figure 11(f), which confirms the adsorption of PYQX molecules on the area of CS.

UV- visible spectra analysis

UV-visible spectrometry was applied to see how CS and molecules of PYQX interact. The absorption spectra of corrosive media, including 1 mM of PYQX, before and after 72 h of CS soaking, are plotted in Figure 12. As in previous research [24], a change in the location of the absorbance peak or a change in the amplitude of the absorbance indicates the development of a complex between two species present in the acidic electrolyte. A careful examination of the absorption spectra showed a notable shift in the absorption bands from 252 to 254 nm and 321 to 327 nm. Furthermore, a remarkable increase in the absorption maximum (λ_{max}) and the appearance of an additional peak at 226 nm reflects the interaction between the studied PYQX compounds and Fe²⁺ ions in the solution. These findings demonstrate the development of a complex between quinoxaline molecules and Fe²⁺ ions in the acidic media [25].

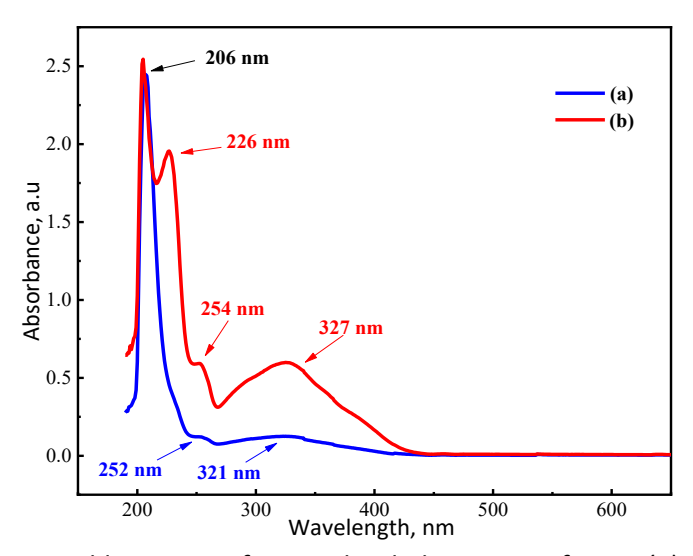


Figure 12. UV-visible spectra of 1 M HCl including 1 mM of PYQX (a) -before and (b) - after 72 hours of CS immersion

Density functional theory reactivity

A molecule with heteroatoms in its structure binds one or more H⁺ protons in an acidic medium, which can modify its chemical reactivity. Figure 13 shows the percentage distribution of the different protonated forms *vs.* pH using MarvinView software, suggesting that in dependence on pH, the PYQX molecule likely protonates in two forms.



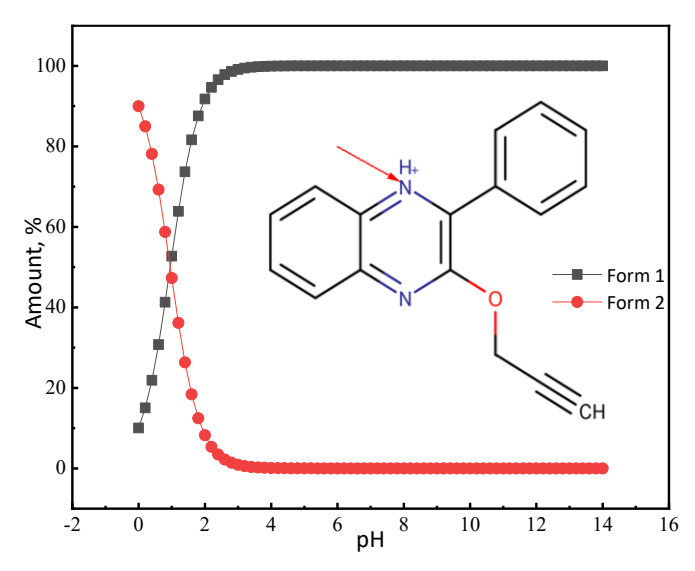


Figure 13. Content of different protonated forms of PYOX as a function of pH

The optimal protonation occurs at position 2, wherein the nitrogen atom (sp²-hybridized) within the foundational structure of quinoxaline is in closer proximity to the protons of the benzene ring, thereby inducing a change in the neutral state of PYQX. Therefore, the current analysis is intended to follow the reactivity behaviour of two forms, neutral and protonated.

To investigate the effectiveness of corrosion inhibition and evoke a plausible corrosion inhibition mechanism, the electronic properties, global activity descriptors and local activity indices of PYQX neutral and charged were calculated [26]. To maintain structural conformity, the absence of imaginary frequencies must be ascertained using the same level of theory. To plot the structure, HOMO and LUMO of the compounds, GaussView/5 software [27] was applied.

Figure 14 depicts the energy-minimized structures and FMOs (HOMO and LUMO) of the PYQX neutral and charged. For the two forms in question, it is noticeable that the distribution of FMOs is total over the structure of both forms of the PYQX, implying that the reactivity is very high with other species and especially with the metal surface.

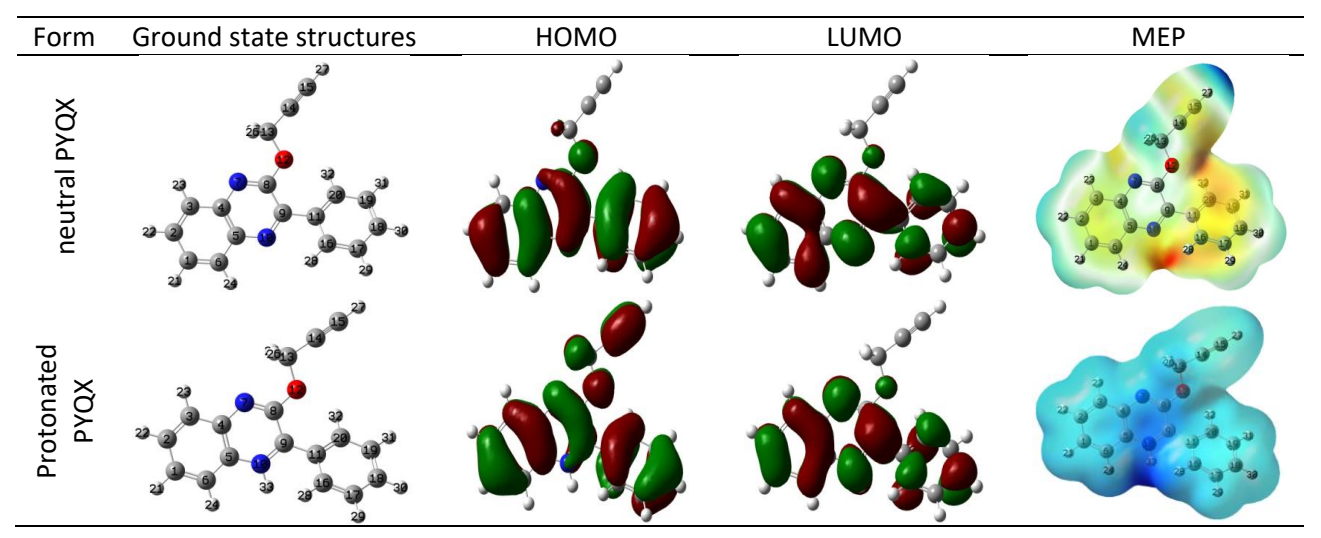


Figure 14. Optimized state structure (FMO), and molecular electrostatic potential (MEP) of the neutral and charged PYQX

 E_{HOMO} and E_{LUMO} values serve to assess the donor/acceptor ratio in the molecule/metal relationship [26]. In this study, the reactivity of the PYQX neutral and charged is followed by these two descriptors. Table 6 groups different values of the reactivity descriptors of both forms. It is

revealed in Table 6 that the PYQX neutral is more nucleophilic (E_{HOMO} =-6.103 eV) and the PYQX charged is more electrophilic (E_{LUMO} =-6.835 eV). Therefore, ΔE (E_{LUMO} - E_{HOMO}) allows to measure the reactivity of a molecule, as the most minimal value of this descriptor means that the specific reactivity is maximal [26]. The description comparison between the values for both forms of this descriptor (ΔE) shows that the charged PYQX is more reactive with a low value of 3.453 eV.

The electronegativity (χ) presents an attractive power of the electrons of a chemical species; the relevance of the descriptor translates the reactivity of interaction [26]. The value of 8.561 eV for the charged PYQX, as shown in Table 6, indicates that it is a more reactive inhibitor on surfaces with a negative charge. The reactivity and hardness (η) of a molecule are reciprocally proportional: a harder molecule implies lower reactivity [26]. The data in Table 6 show that charged PYQX (1.726 eV) is more reactive. The fraction of electron transferred (ΔN_{110}) values provide useful information on the tendency of electrons to flow from the inhibitor molecule to the CS surface ($\Delta N > 0$), or from the carbon steel to the inhibitor ($\Delta N < 0$) [28]. In this present computation, the neutral PYQX molecule ($\Delta N_{110} = 0.197$) is more likely to share its electrons in order to form coordination bonds with Fe (110).

Table 6. Chemical descriptors of neutral and charged PYQX molecules

Form	<i>E</i> _{номо} / eV	E _{LUMO} / eV	Δ <i>E</i> / eV	χ / eV	η / eV	ΔN_{110}
PYQX neutral	-6.103	-1.865	4.238	3.984	2.119	0.197
PYQX protonated	-10.288	-6.835	3.453	8.561	1.726	-1.084

The inhibitory efficacy of a molecule can be measured and assessed by the prevalence of active sites throughout its structure. In addition, the sites of high local reactivity support substantial inhibitory efficacy. These centres may bind with others located at the metal surface by chemical bonds [29]. In Table 7, the various sites of PYQX molecule neutral and charged are collected, respectively, with the most suitable atoms presenting the highest reactivity, giving the acceptor (nucleophilic attack (f^+)) and donor (electrophilic- attack (f^-)).

Table 7. Atoms of local reactivity for neutral and charged PYQX molecule

Atom	Atom PYQX molecule		PYQX mole	PYQX molecule charged		
Atom —	f-	$f^{\scriptscriptstyle +}$	f^{-}	$f^{\scriptscriptstyle +}$		
C (1)	0.034	0.052	0.019	0.047		
C (2)	0.062	0.054	0.030	0.057		
C (3)	0.056	0.050	0.023	0.037		
C (4)	0.024	0.038	0.016	0.045		
C (5)	0.034	0.038	0.019	0.047		
C (6)	0.063	0.051	0.027	0.042		
N (7)	0.040	0.107	0.017	0.078		
C (8)	0.023	0.056	0.016	0.087		
C (9)	0.035	0.065	0.015	0.047		
N (10)	0.057	0.106	0.032	0.107		
C (11)	0.055	0.012	0.054	0.008		
O (12)	0.015	0.025	0.016	0.037		
C (13)	0.007	0.007	0.023	0.010		
C (14)	0.011	0.004	0.109	0.010		
C (15)	0.030	0.022	0.148	0.032		
C (16)	0.048	0.030	0.041	0.021		
C (17)	0.039	0.022	0.038	0.019		
C (18)	0.074	0.036	0.069	0.028		
C (19)	0.041	0.020	0.039	0.017		
C (20)	0.034	0.023	0.022	0.016		

The condensed Fukui functions (f^+ and f^-) for PYQX neutral indicated that C2, C3, C6, N10, C11, C16, and C18 are the most electrophilic attacks centres, whereas the C1, C2, C3, C6, N7, C8, C9, and N10 are highest nucleophilic attacks centres. These sites are suitable for donating and accepting electrons. After protonation, the electron-donating effect decreased noticeably while the electron-attracting effect increased.

Molecular dynamics simulation

Molecular dynamics (MD) simulation is a valuable approach to describe better and understand the adsorption pattern of a molecular substance on a metallic material [30]. In this work, the simulation deals with the reactivity of quinoxaline molecules (neutral and charged) and Fe (110). This research also investigated the reactivity model of two molecule forms on the effectiveness of surface protection against attack by corrosive species contained in the molar HCl solution. Figure 15 illustrates the adsorption of the species of interest (lateral and top representations) onto Fe (110). Further analysis of these two configurations reveals that both molecules adsorb wholly and largely occupy the iron atomic layer, resulting in a high content of anticorrosive protection.

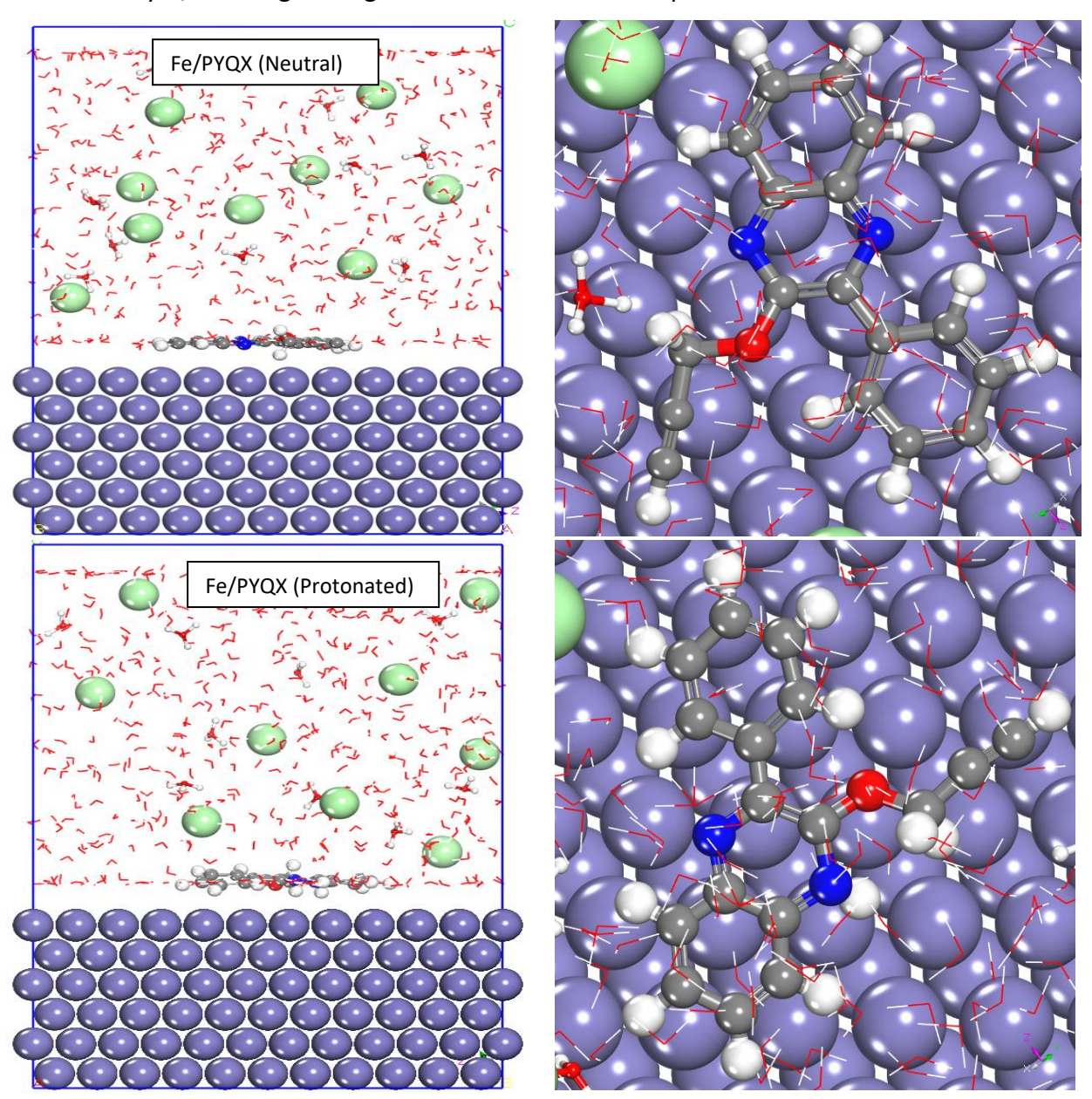


Figure 15. Adsorption configurations of neutral and charged PYQX molecule onto Fe (110)

The interaction energy (E_{inter}) value is established by the equation (19) [31]:

$$E_{\text{inter}} = -E_{\text{(surface+ solution)}} - E_{\text{inhibitor}} + E_{\text{total}}$$
(19)

The $E_{\rm inter}$ with a low value indicates the big interactions for both systems Fe/ PYQX (neutral) and Fe/PYQX (charged). It appears from the comparative study that the most negative value of Fe/PYQX (charged) with -889.929 kJ mol⁻¹ reflects a big interaction. These simulation data clearly prove the agreement compared with the quantum computations.

The primary objective of this model is to assess the significance of adsorption by utilizing interatomic distances for Fe/PYQX (neutral), which is equal to -888.428 kJ mol⁻¹, and Fe/PYQX (charged), which is equal to -889.929 kJ mol⁻¹, through the introduction of the radial distribution function (RDF). The published literature confirms that the likelihood of chemical adsorption is higher when the bond length is less than 0.35 nm (3.5 Å). By contrast, physical adsorption is more probable [31]. In Figure 16, the 1st peak displays the bond lengths for both systems are less than 0.35 nm.

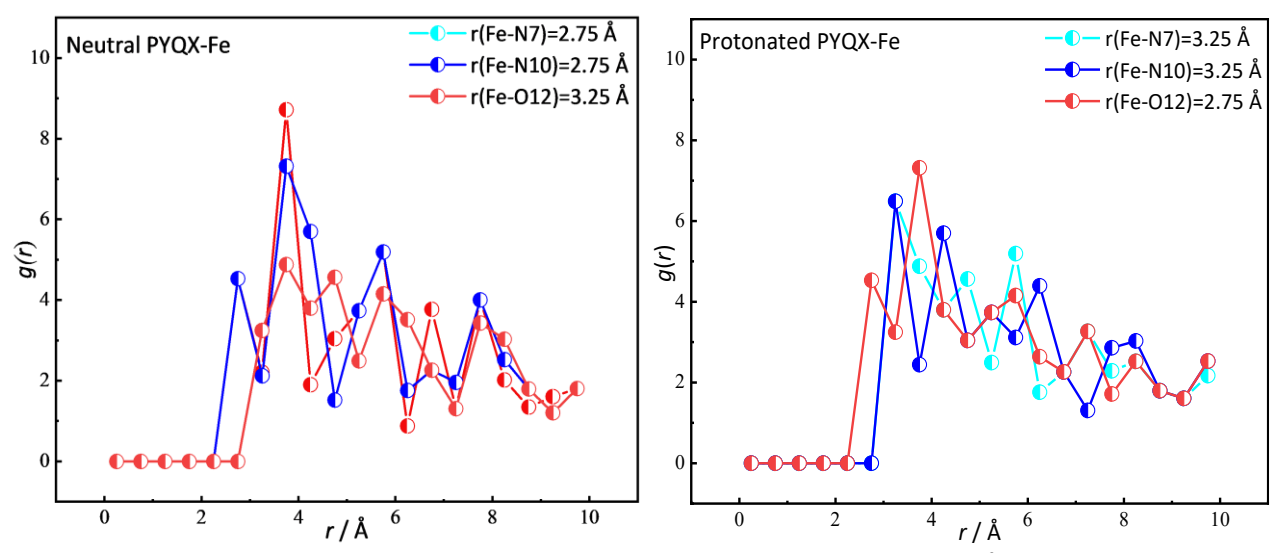


Figure 16. RDF (g(r)) of Fe/PYQX (neutral) and Fe/PYQX (charged) (1 \mathring{A} = 0.1 nm)

Inhibitory mechanism

The adsorption process of inhibitor on a metal surface explains the mechanism of corrosion inhibition. Figure 17 shows a possible mechanism for the adsorption of PYQX on the C•S surface in 1 M HCl. Organic molecules adsorb on metal surfaces primarily by chemisorption, physisorption, or both. In this study, PYQX has many functional groups, such as O and N heteroatoms and heterocycles, that can help the inhibitor stick to the surface. Organic compounds present both neutral and protonated forms when their heteroatoms undergo protonation in acidic environments. A positive charge may form on the metal surface as a result of fast metal oxidation. A negatively charged surface may emerge as a result of the positive charge attracting chloride ions present in the solution.

The protonated form then physically adheres to the newly formed negatively charged surface. This creates a protective layer that slows down the anodic corrosion process. Also, the positively charged ions that stick to the cathodic sites compete with H $^+$ for electrons, which lowers the production of H $_2$ [32]. The neutral form of PYQX chemisorbed to the metal surface through interactions between the empty d-orbital of Fe atoms and the free electron pairs of heteroatoms (N, O). The transfer of excess negative charge from the Fe d-orbital to the unoccupied π^* orbital of inhibitor molecules can occur on the CS surface, leading to greater inhibitor adsorption on the steel surface. Moreover, between the aromatic cycles and the d-orbitals of the CS surface, electron retro-donation

may occur [33]. At last, a barrier is created on the steel surface by an adsorbed inhibitor film to prevent metal corrosion from the corrosive medium.

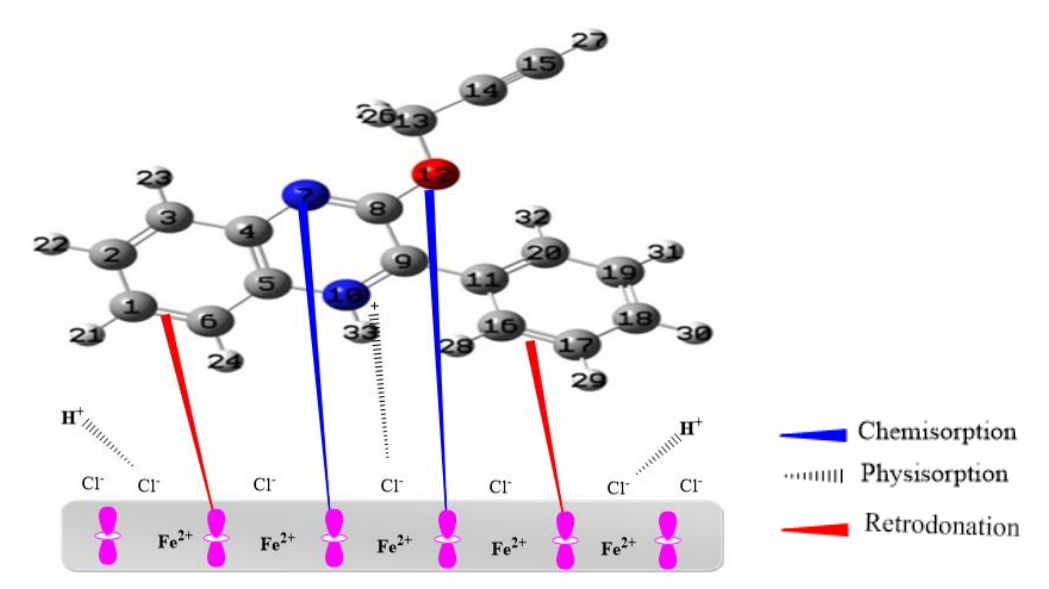


Figure 17. Schematic illustrating of PYQX adsorption mechanism on the C-S surface in chloride solution

Conclusion

Corrosion inhibition of carbon steel was investigated in a molar hydrochloric acid environment using a novel quinoxaline derivative. The study used a combination of chemical and electrochemical techniques, as well as some theoretical simulations. The main results of this research can be resumed as follows:

PYQX demonstrated exceptional inhibitory efficacy against CS corrosion in acidic electrolytes. As the concentration increases, its performance strengthens, reaching 98.1 % at 1 mM.

- PYQX is a mixed-type inhibitor with a cathodic inclination, as indicated by the PDP profiles, which show that it significantly inhibits cathodic hydrogen evolution processes and anodic metal dissolution. EIS analyses showed that when PYQX is present, R_p values go up and double-layer capacitance decreases. This shows that the inhibitor can slow down CS corrosion.
- The chemisorption mechanism of PYQX adsorption on the CS interface is consistent with the Langmuir adsorption isotherm.
- Surface and electrolyte investigations (SEM, EDS, and UV-visible) showed that a protective coating has formed over the surface of CS.
- DFT and MD simulations showed high reactivity with CS (Fe (110)).

References

- [1] M. M. Shaban, N. A. Negm, R. K. Farag, A. A. Fadda, A. E. Gomaa, A. A. Farag, M. A. Migahed, Anti-corrosion, antiscalant and anti-microbial performance of some synthesized trimeric cationic imidazolium salts in oilfield applications, *Journal of Molecular Liquids* **351** (2022) 118610. https://doi.org/10.1016/j.molliq.2022.118610
- [2] H. E. Hashem, A. A. Farag, E. A. Mohamed, E. M. Azmy, Experimental and theoretical assessment of benzopyran compounds as inhibitors to steel corrosion in aggressive acid solution, *Journal of Molecular Structure* **1249** (2022) 131641. https://doi.org/10.1016/j.molstruc.2021.131641
- [3] S. M. Shaban, E. Badr, M. A. Shenashen, A. A. Farag, Fabrication and characterization of encapsulated Gemini cationic surfactant as anticorrosion material for carbon steel

- protection in down-hole pipelines, *Environmental Technology and Innovation* **23** (2021) 101603. https://doi.org/10.1016/j.eti.2021.101603
- [4] E. A. Mohamed, H. E. Hashem, E. M. Azmy, N. A. Negm, A. A. Farag, Synthesis, structural analysis, and inhibition approach of novel eco-friendly chalcone derivatives on API X65 steel corrosion in acidic media assessment with DFT & MD studies, *Environmental Technology and Innovation* **24** (2021) 101966. https://doi.org/10.1016/j.eti.2021.101966
- [5] A. Zarrouk, A. Dafali, B. Hammouti, H. Zarrok, S. Boukhris, M. Zertoubi, Synthesis, characterization and comparative study of functionalized quinoxaline derivatives towards corrosion of copper in nitric acid medium, *International Journal of Electrochemical Science* 5 (2010) 46–55. https://doi.org/10.1016/S1452-3981(23)15266-7
- [6] F. Benhiba, R. Hsissou, Z. Benzekri, S. Echihi, J. El-blilak, S. Boukhris, A. Bellaouchou, DFT / electronic scale, MD simulation and evaluation of 6-methyl-2- (p-tolyl)-1, 4-dihydroquinoxaline as a potential corrosion inhibition, *Journal of Molecular Liquids* 335 (2021) 116539. https://doi.org/10.1016/j.molliq.2021.116539
- [7] M. Ouakki, M. Galai, Z. Benzekri, C. Verma, E. Ech-chihbi, S. Kaya, S. Boukhris, E. E. Ebenso, M. E. Touhami, M. Cherkaoui, Insights into corrosion inhibition mechanism of mild steel in 1 M HCl solution by quinoxaline derivatives: electrochemical, SEM/EDAX, UV-visible, FT-IR and theoretical approaches, *Colloids and Surfaces A* 611 (2021) 125810. https://doi.org/10.1016/j.colsurfa.2020.125810
- [8] T. Laabaissi, F. Benhiba, M. Missioui, Z. Roui, M. Rbaa, H. Oudda, Y. Ramli, A. Guenbour, I. Warad, A. Zarrouk, Heliyon Coupling of chemical, electrochemical and theoretical approach to study the corrosion inhibition of mild steel by new quinoxaline compounds in 1 M HCl, *Heliyon* 6 (2020) e03939. https://doi.org/10.1016/j.heliyon.2020.e03939
- [9] D. M. Mamand, T. M. K. Anwer, H. M. Qadr, Electronic structure and quantum chemical analysis of the corrosion inhibition efficiency of quinoxalines, *Journal of the Indian Chemical Society* **100** (2023) 101018. https://doi.org/10.1016/J.JICS.2023.101018
- [10] Q. Deng, S. Jeschke, R. K. Mishra, S. Spicher, S. Darouich, E. Schreiner, P. Eiden, P. Deglmann, J. N. Gorges, X. B. Chen, P. Keil, I. Cole, Design of alkyl-substituted aminothiazoles to optimise corrosion inhibition for galvanised steel: A combined experimental and molecular modelling approach, *Corrosion Science* 227 (2024) 111733. https://doi.org/10.1016/j.corsci.2023.111733
- [11] ASTM, Standard Practice for Preparing, Cleaning, and Evaluating Corrosion Test Specimens. Designation: G1-03, ASTM Special Technical Publication (2017) 505-510.
- [12] F. Benhiba, Z. Benzekri, Y. Kerroum, N. Timoudan, R. Hsissou, A. Guenbour, M. Belfaquir, S. Boukhris, A. Bellaouchou, H. Oudda, A. Zarrouk, Assessment of inhibitory behavior of ethyl 5-cyano-4-(furan-2-yl)-2-methyl-6-oxo-1,4,5,6-tetrahydropyridine-3-carboxylate as a corrosion inhibitor for carbon steel in molar HCl: Theoretical approaches and experimental investigation, *Journal of the Indian Chemical Society* **100** (2023) 100916. https://doi.org/10.1016/j.jics.2023.100916
- [13] A. Thoume, D. B. Left, A. Elmakssoudi, F. Benhiba, A. Zarrouk, N. Benzbiria, I. Warad, M. Dakir, M. Azzi, M. Zertoubi, Chalcone oxime derivatives as new inhibitors corrosion of carbon steel in 1 M HCl solution, *Journal of Molecular Liquids* **337** (2021) 116398. https://doi.org/10.1016/j.molliq.2021.116398
- [14] R. G. Parr, W. Yang, Density Functional Approach to the Frontier-Electron Theory of Chemical Reactivity, *Journal of the American Chemical Society* **106** (1984) 4049-4050. https://doi.org/10.1021/ja00326a036
- [15] H. Sun, Compass: An ab initio force-field optimized for condensed-phase applications Overview with details on alkane and benzene compounds, *Journal of Physical Chemistry B* **102** (1998) 7338-7364. https://doi.org/10.1021/jp980939v



- [16] W. Sun, H. Wang, Moisture effect on nanostructure and adhesion energy of asphalt on aggregate surface: A molecular dynamics study, *Applied Surface Science* **510** (2020) 145435. https://doi.org/10.1016/j.apsusc.2020.145435
- [17] M. El Faydy, F. Benhiba, N. Timoudan, B. Lakhrissi, I. Warad, S. Saoiabi, A. Guenbour, F. Bentiss, A. Zarrouk, Experimental and theoretical examinations of two quinolin-8-ol-piperazine derivatives as organic corrosion inhibitors for C35E steel in hydrochloric acid, *Journal of Molecular Liquids* 354 (2022) 118900. https://doi.org/10.1016/j.molliq.2022.118900
- [18] W. L. Xu, X. Wang , G. A. Zhang, Efficient inhibition of mild steel corrosion in acidic medium by novel pyrimidine derivatives: Inhibitive effect evaluation and interface, *Journal of Molecular Structure* **1291** (2023) 136005. https://doi.org/10.1016/j.molstruc.2023.136005
- [19] X. Liu, Y. Gao, J. Guan, Q. Zhang, Y. Lin, C. Shi, Y. Wang, J. Du, N. Ma, Corrosion inhibition properties of spinach extract on Q235 steel in a hydrochloric acid medium, *Arabian Journal of Chemistry* **16** (2023) 105066. https://doi.org/10.1016/j.arabjc.2023.105066
- [20] Y. Qiang, L. Guo, H. Li, X. Lan, Fabrication of environmentally friendly Losartan potassium film for corrosion inhibition of mild steel in HCl medium, *Chemical Engineering Journal* **406** (2021) 126863. https://doi.org/10.1016/j.cej.2020.126863
- [21] K. Raviprabha, R. S. Bhat, Corrosion inhibition of mild steel in 0.5 M HCL by substituted 1,3,4-oxadiazole, *Egyptian Journal of Petroleum* **32** (2023) 1-10. https://doi.org/10.1016/j.ejpe.2023.03.002
- [22] X. Wang, W.L. Xu, Z.Y. Liu, G.A. Zhang, Unraveling the corrosion inhibition mechanism of triazine derivatives for carbon steel: Experimental and theoretical insights into interfacial adsorption, *Corrosion Science* 220 (2023) 111288. https://doi.org/10.1016/j.corsci.2023.111288
- [23] A. Salhi, S. Tighadouini, M. El-Massaoudi, M. Elbelghiti, A. Bouyanzer, S. Radi, S. El Barkany, F. Bentiss, A. Zarrouk, Keto-enol heterocycles as new compounds of corrosion inhibitors for carbon steel in 1 M HCl: Weight loss, electrochemical and quantum chemical investigation, *Journal of Molecular Liquids* 248 (2017) 340-349. https://doi.org/10.1016/j.molliq.2017.10.040
- [24] M. El Faydy, M. Galai, A. El Assyry, A. Tazouti, R. Touir, B. Lakhrissi, M. Ebn Touhami, A. Zarrouk, Experimental investigation on the corrosion inhibition of carbon steel by 5-(chloromethyl)-8-quinolinol hydrochloride in hydrochloric acid solution, *Journal of Molecular Liquids* **219** (2016) 396-404. https://doi.org/10.1016/j.molliq.2016.03.056
- [25] A. Berrissoul, E. Loukili, N. Mechbal, F. Benhiba, A. Guenbour, B. Dikici, A. Zarrouk, A. Dafali, Journal of Colloid and Interface Science Anticorrosion effect of a green sustainable inhibitor on mild steel in hydrochloric acid, *Journal of Colloid and Interface Science* **580** (2020) 740-752. https://doi.org/10.1016/j.jcis.2020.07.073
- [26] J. Lazrak, E. Ech-chihbi, B. El Ibrahimi, F. El Hajjaji, Z. Rais, M. Tachihante, M. Taleb, Colloids and Surfaces A: Physicochemical and Engineering Aspects Detailed DFT / MD simulation, surface analysis and electrochemical computer explorations of aldehyde derivatives for mild steel in 1.0 M HCl, Colloids and Surfaces A 632 (2022) 127822. https://doi.org/10.1016/j.colsurfa.2021.127822
- [27] J. M. Frisch, G.W. Trucks, H. B. Schlegel, G. E. Scuseria, M. A. Robb, J. R. Cheeseman, G. Scalmani, V. B arone, B. Mennucci, G. A. Petersson, H. Nakatsuji, M. Caricato, X. Li, H. P. Hratchian, A. F. Izmaylov, J. Bloino, G. Zheng, J. L. Sonnenberg, M. Hada, GAUSSIAN 09 Révision., Gaussian, Inc., Wallingford CT,. (2009).
- [28] K. S. Miled Ferigita, M. Saracoglu, M. G. Kadhim AlFalah, M. I. Yilmazer, Z. Kokbudak, S. Kaya, F. Kandemirli, Corrosion inhibition of mild steel in acidic media using new oxo-

- pyrimidine derivatives: Experimental and theoretical insights, *Journal of Molecular Structure* **1284** (2023) 135361. https://doi.org/10.1016/j.molstruc.2023.135361
- [29] T. H. El-Mokadem, A. I. Hashem, Nour E. A. Abd El-Sattar, E. A. Dawood, N. S. Abdelshaf, Green synthesis, electrochemical, DFT studies and MD simulation of novel synthesized thiourea derivatives on carbon steel corrosion inhibition in 1.0 M HCl, *Journal of Molecular Structure* **1274** (2023) 134567. https://doi.org/10.1016/j.molstruc.2022.134567
- [30] M. El Faydy, F. Benhiba, I. Warad, S. Saoiabi, A. Alharbi, A. A. Alluhaybi, B. Lakhrissi, M. Abdallah, A. Zarrouk, Bisquinoline analogs as corrosion inhibitors for carbon steel in acidic electrolyte: Experimental, DFT, and molecular dynamics simulation approaches, *Journal of Molecular Structure* 1265 (2022) 133389. https://doi.org/10.1016/J.MOLSTRUC.2022.133389
- [31] J. Saranya, F. Benhiba, N. Anusuya, R. Subbiah, A. Zarrouk, S. Chitra, Experimental and computational approaches on the pyran derivatives for acid corrosion, *Colloids and Surfaces A* **603** (2020) 125231. https://doi.org/10.1016/J.COLSURFA.2020.125231
- [32] N. Anusuya, J. Saranya, P. Sounthari, A. Zarrouk, S. Chitra, Corrosion inhibition and adsorption behaviour of some bis-pyrimidine derivatives on mild steel in acidic medium, *Journal of Molecular Liquids* **225** (2017) 406-417. https://doi.org/10.1016/j.molliq.2016.11.015
- [33] X. Yang, X. Lang, W. Dong, L. Yu, G. Chen, X. Li, Experimental and theoretical investigations on the inhibition of mild steel corrosion by capsaicin derivatives in hydrochloric acid, *Journal of Molecular Structure* **1283** (2023) 135341. https://doi.org/10.1016/j.molstruc.2023.135341

©2024 by the authors; licensee IAPC, Zagreb, Croatia. This article is an open-access article distributed under the terms and conditions of the Creative Commons Attribution license (https://creativecommons.org/licenses/by/4.0/)





Open Access:: ISSN 1847-9286 www.jESE-online.org

Original scientific paper

Walnut (Juglans regia L.) fruit septum alcoholic extract as corrosion inhibitor for Fe B500B steel bars in mixed acidic solution

Alketa Lame[™], Muhamed Farruku, Efrosini Kokalari, Klodian Xhanari, Nensi Isak, Kledi Xhaxhiu and Alma Shehu

Faculty of Natural Sciences, University of Tirana, Boulevard "Zogu I", 1001, Tirana, Albania

Corresponding author: \square alketa.lame@fshn.edu.al

Received: February 23, 2024; Accepted: July 3, 2024; Published: July 16, 2024

Abstract

The corrosion inhibition performance of the walnut fruit (Juglans regia L.) septum alcoholic extract for Fe B500B steel bars in a mixed acidic solution (H_2SO_4/HCl) is reported. Weight loss, potentiodynamic polarization, and electrochemical impedance spectroscopy measurements were performed at 298 to 318 K, with the addition of various extract concentrations. Results showed the maximum corrosion inhibition efficiency of 86.99 % for 300 mg L^{-1} extract added. The extract acts as a mixed-type inhibitor, predominantly affecting the anodic side, following Flory-Huggins adsorption isotherm. Thermodynamic analysis indicated an endothermic process with both chemisorption and physisorption on the steel bar surface. Surface characterization was conducted using ATR-FTIR, UV-vis and SEM techniques to prove the adsorption of the inhibitor molecules on the steel bar surface. Also, a possible adsorption mechanism of inhibitor molecules was proposed.

Keywords

Green corrosion inhibitor, corrosion rate; inhibition efficiency, Flory-Huggins isotherm, inhibitor adsorption mechanism

Introduction

Corrosion is an issue that costs economies billions of dollars worldwide [1]. Several techniques are used to mitigate corrosion, such as materials selection and isolation, design improvement, environment modification, *etc*. Different kinds of carbon steels used as reinforcements in constructions are susceptible to corrosion in aggressive environments. It is known that concrete with a basic media protects all types of carbon steel. The problem arises when concrete is damaged due to various chemical or physical causes. In contact with concrete, an aggressive environment migrates through the cracks on the surface of the reinforcement. Such aggressive environments include acid rain containing chloride ions in coastal urban industrial areas or acidic solutions used for pickling metals. According to the paper published by C. J. Brown and D.R. Olsen [2], "Pickling is, and likely will remain, very much an art". Based on this paper, adding H₂SO₄ to HCl (traditional

pickling) increases the pickling rate. Furthermore, the inhibitors used to avoid attack in HCl pickling remain effective with mixed acids. All of these are the impetus of the scientific motivation to use a mixture of 0.5 M H₂SO₄/0.5 M HCl as an aggressive acidic environment (blank solution), which provides both the acidic environment with chloride ions and the corrosion situation during the pickling process. Both H₂SO₄ and HCl are strong corrosive acids [3,4].

Changing the environment using different additives as corrosion inhibitors is an effective solution to mitigate corrosion. Corrosion inhibitors are generally grouped into inorganic, organic, and environmentally friendly compounds extracted from plants [5-9]. Different parts of the plants have been extracted, such as bark, roots, seeds, fruit peels, and leaves [10-14]. The corrosion-protective properties of these extracts are attributed to flavonoids, phenolic compounds, tannins, etc. These active compounds added to the corrosive medium protect metals from corrosion due to heteroatoms such as N, O, as well as double bonds and aromatic rings, capable of adsorbing on the metal surface physically or chemically [15,16].

The high inhibition efficiency was previously reported for the extracts obtained from different parts of *Juglans regia* L, such as leaves, green husk, and walnut shell, in the corrosion of carbon steel, mild steel, and aluminum in aggressive media [17-21]. Several scientific publications were reported on the pharmaceutical and medical uses of the septum extract of the walnut fruit, thanks to its anti-inflammatory and antimicrobial properties. These properties are due to the presence of active compounds such as gallic acid, catechin, isoquercitrin, quercitrin, *etc.* [22,23]. The reason for selecting walnut septum extract as a corrosion inhibitor is the presence of compounds mentioned above and the low cost of this recyclable material in the fruit processing industry. These are the genesis for the design of the walnut fruit septum extract as an inhibitor against corrosion of Fe B500B steel bars in the acidic mixture (0.5 M $H_2SO_4/0.5$ M HCl).

The corrosion rate of the Fe B500B samples was evaluated using the weight loss method, potentiodynamic polarization, and electrochemical impedance spectroscopy (EIS). The measurements were carried out at room temperature with and without the addition of different concentrations of the extract and for the optimum concentration at 298 to 318 K range. Adsorption isotherms were used to find the type of adsorption on the metal solution interface. The activation energy was determined with the Arrhenius-type dependence. The walnut fruit septum extract was characterized by FTIR and UV-vis techniques. Scanning electron microscope (SEM) was used to investigate the surface morphology of the Fe B500B samples for blank and optimum concentration of the solution after 100 h of immersion in the 298 to 318 K temperature range.

Experimental

Preparation and characterization of the walnut fruit septum extract

The walnut fruit septum was obtained from domestic production in Albania and dried at 40 °C for 5 days. The dried walnut fruit septum was ground in a blender and then extracted for 24 h in 70 % ethanol under reflux at 298 K. The extract was filtered and stored at 277 K. HPLC-DAD was used to confirm the presence of gallic acid, catechin, isoquercitrin, and quercitrin which are the main compounds present in walnut septum extract as previously reported [22], and suitable for use as corrosion inhibitors.

Solution preparation

The mixed acidic corrosive medium (0.5 M $H_2SO_4/0.5$ M HCl) was prepared by diluting the 37 % HCl and 96 % H_2SO_4 solutions provided by Sigma Aldrich. The concentration of the extract was

calculated based on the difference of the dried plant mass before and after extraction divided by the volume of the solvent after reflux. The brown walnut fruit septum extract was added to the corrosive solution in the concentration range of 100 to 300 mg L⁻¹ (*i.e.* 100, 200 and 300 mg L⁻¹).

Materials

The hot-rolled deformed steel bars Fe B500B used in this study were provided by Diler Demir Celik Endustri Ve Ticaret A.S. (Gebze, Turkey) has the following composition: 0.20 wt.% C, 0.22 wt.% Si, 0.023 wt.% S, 0.014 wt.% P, 0.84 wt.% Mn, 0.11 wt.% Ni, 0.10 wt.% Cr, 0.017 wt.% Mo, 0.30 wt.% Cu, 0.0012 wt.% V, 0.0095 wt.% N, 0.0002 wt.% B and balance Fe.

Weight loss measurement

For weight loss measurements, Fe B500B samples were cut into cylinders of 5 cm in length and 0.8 cm in diameter. They were ground with different emery papers (*i.e.*, 180, 240, 320, 500, and 1000 grit), washed with bi-distilled water, and degreased with acetone in an ultrasonic bath for 5 minutes. The samples were measured and marked before weighing with an accuracy of 0.0001 g and then immersed in the 0.5 M $H_2SO_4/0.5$ M HCl solution without and with the walnut fruit septum extract at 298 K. Before immersing the samples, the solutions were deaerated for 30 min. The kinetics of the corrosion process for the optimum concentration of walnut fruit septum extract was also investigated within the 298 to 318 K temperature range. A water bath was used to keep the temperature constant (± 0.5 °C). Adsorption isotherms were also used to find the type of adsorption of the inhibitor on the surface of Fe B500B samples.

After 100 h of immersion, the samples were washed with bi-distilled water, cleaned from corrosion products with 1 M HCl containing 2 g L⁻¹ urotropine solution, degreased with acetone, and weighed accurately. Experiments were carried out in triplicates. The corrosion rate (C.R., g m⁻² h⁻¹) was calculated by Equation (1):

$$C.R. = W / St \tag{1}$$

where W is the average weight loss of the samples in g, S is the total surface of the samples in m^2 , and t is the immersion time in hours.

The corrosion rate (CR, mm year⁻¹) was calculated using converting Equation (2):

$$CR = (8.76 / d_{Fe}) C.R.$$
 (2)

where d is the density of Fe / g cm⁻³ and 8.76 is the conversion coefficient.

The corrosion inhibition efficiency (IE, %) and degree of surface coverage (θ) of the walnut fruit septum extract were calculated by Equations (3) and (4):

$$IE = \frac{C.R.^{\circ} - C.R.}{C.R.^{\circ}} 100$$
(3)

$$\theta = \frac{\text{C.R.}^{\circ} - \text{C.R.}}{\text{C.R.}^{\circ}}$$
 (4)

where C.R. and C.R.⁰ represent the corrosion rates with and without the walnut fruit septum extract, respectively.

Electrochemical methods

Open circuit potential (OCP), potentiodynamic polarization (PD), and electrochemical impedance spectroscopy (EIS) experiments were carried out with IS-CCS Corrosion Cell Set from PalmSens, consisting of a three-electrode cell with a platinum counter electrode (CE) and saturated calomel electrode (SCE) coupled to a Luggin capillary as a reference electrode. The working electrode samples

were coupons with a surface area of $0.785\,\mathrm{cm^2}$. The coupons were cut from hot-rolled deformed steel bars (Fe B500B) in discs of 5 mm in height and 15 mm in diameter that were ground with different emery papers (*i.e.*, 180, 240, 320, 500, and 1000 grit), washed with bi-distilled water and degreased with acetone. Potentiodynamic polarization and electrochemical impedance spectroscopy measurements were carried out using Palmsens 4 potentiostat. The open circuit potential (OCP) of the Fe B500B samples immersed in the mixed acidic medium (0.5 M $_2$ SO₄/ 0.5 M $_2$ SO₄/ 0.5 M HCl) solution was measured for 30 min, with and without additions of the walnut fruit septum extract. Potentiodynamic polarization curves were obtained with a scan rate of 0.1 mV s⁻¹ in the potential range OCP ±120 mV. Electrochemical impedance spectroscopy (EIS) was carried out at OCP condition with an amplitude of 10 mV and a frequency range from 1 MHz to 0.01 Hz. The effect of the concentration of the walnut fruit septum extract on the corrosion susceptibility of the Fe B500B samples was tested at 298 K. Meanwhile, the impact of temperature on the corrosion rate and charge transfer resistance of the Fe B500B samples immersed in the mixed acidic medium (0.5 M $_2$ SO₄/0.5 M HCl) containing the optimum concentration of walnut fruit septum extract was also tested at 308 and 318 K.

From potentiodynamic results, corrosion rates (CR, mm y⁻¹) were calculated using Equation (5):

$$CR = \frac{Kai}{nd} \tag{5}$$

where K is the conversion coefficient (0.00327), a is the atomic mass of Fe (g mol⁻¹), i is corrosion current density in μ A cm⁻², d is the density of Fe (g cm⁻³), and n is the valence of Fe (n=2).

The corrosion inhibition efficiency (IE) of the walnut fruit septum extract was calculated by Equation (6):

$$IE = \frac{i_{corr}^0 - i_{corr}}{i_{corr}^0} 100 \tag{6}$$

where i_{corr} and i_{corr}^0 represent the corrosion current density of the samples in the mixed acidic medium (0.5 M H₂SO₄/0.5 M HCl) with and without the addition of the walnut fruit septum extract, respectively.

Surface characterization of Fe B500B steel bars

The scanning electron microscope (SEM) experiments were conducted using Zeiss EVO MA10. Samples were immersed for 24 h in a blank and 300 mg L⁻¹ extract solution of the inhibitor over a temperature range (298 to 318 K). To characterize the surface of Fe B500B samples in the 400 to 4000 cm⁻¹ range, attenuated total reflection Fourier transform infrared (ATR-FTIR) spectroscopy with an ALPHA II spectrometer from Bruker was used.

UV-vis spectroscopy analysis

UV-Vis model VWR type UV-1600PC was employed to qualitatively analyze the walnut fruit septum extract's composition. It was performed after 24 h of immersion of Fe B500B samples in the absence and presence of walnut fruit septum extract.

Results and discussion

Weight loss measurements

As shown in Table 1, the corrosion rates (C.R.) of the Fe B500B samples immersed in the mixed acidic medium (0.5 M $H_2SO_4/0.5$ M HCl) at 298 K decreased gradually with the increase of the inhibitor concentration. The corrosion rate decreased from 1.4117 to 0.2893 g m⁻² h⁻¹ in terms of weight loss

over time or decreased from 1.5713 to 0.3220 mm y $^{-1}$ in terms of penetration in the Fe B500B samples surface samples over time at 298 K. Inhibitor efficiency and surface coverage increased with increasing the extract concentration, reaching a maximum value of 79.51 % for 300 mg L $^{-1}$ of walnut fruit septum extract added. Further increase of inhibitor concentration (*i.e.*, 400 mg L $^{-1}$, results are not displayed) does not improve the inhibitor efficiency, suggesting that 300 mg L $^{-1}$ is the optimum concentration. This will be further confirmed by SEM analysis. The addition of the inhibitor changes the type of corrosion to the uniform type.

Table 1. Weight loss results of Fe B500B samples immersed for 100 h at 298 K in the mixed acidic medium (0.5 M $H_2SO_4/0.5$ M HCl) without and with different concentrations of walnut fruit septum extract

Concentration, mg L ⁻¹	C.R., g m ⁻² h ⁻¹	CR, mm y ⁻¹	IE, %
0.0 (blank)	1.4117	1.5713	-
100.0	0.7966	0.8866	43.58
200.0	0.4831	0.5377	65.78
300.0	0.2893	0.3220	79.51

Adsorption isotherm

It is generally known that inhibitor molecules adsorb on the metal surface by chemisorption (involving coordination bonds or covalent bonds between inhibitor molecules and unfilled d orbitals of iron) in the case of Fe B500B samples, or physical adsorption on the surface of the metal (involving electrostatic forces). Therefore, adsorption isotherms are used to gain information on the type of interaction on the surface of the metal. Various isotherms, such as Temkin, Freundlich, Langmuir, Frumkin, El-Awady, and Flory-Huggins, were used to fit the data reported in Table 1. Nonetheless, the best-obtained fit was Flory-Huggins adsorption isotherm, as shown in Figure 1. The data for adsorption isotherms were fitted according to Equation (7):

$$\ln\left(\frac{\theta}{C_{\text{inh}}}\right) = \ln K_{\text{ads}} + x \ln(1-\theta) \tag{7}$$

where θ is the surface coverage assessed from weight loss measurement at 298 K (Table 1). The intercept and the slope from the plot presented in Figure 1 are ln K_{ads} and x, respectively, where K_{ads} is the adsorption equilibrium constant, and x represents the number of water molecules substituted by a single inhibitor molecule [24]. The intercept value of the Flory-Huggins isotherm presented in Figure 1, which corresponds to ln K_{ads} was found to be 1.78 and is further used to calculate the standard Gibbs free energy of the adsorption according to Equation (8):

$$\Delta G^{\circ}_{ads} = -RT \ln (55.5 \Delta K_{ads})$$
 (8)

where R is the universal gas constant in 8.314 J mol⁻¹ K⁻¹, T is the temperature in Kelvin, 55.5 mol L⁻¹ is the concentration of water in solution at 298 K. Based on the literature [25], if the value of Gibbs free energy of the adsorption (ΔG°_{ads}) is less negative or equal to -20 kJ mol⁻¹, the interaction between the charged metal surface and the inhibitor molecules is by physical adsorption (electrostatic). In the case when $\Delta G^{\circ}_{ads} \ge$ -40 kJ mol⁻¹, we have the occurrence of chemisorption (charge transfer between the inhibitor molecules and metal surface) [25]. The calculated value in this case is -14.38 kJ mol⁻¹, confirming physisorption. The x value is 0.49, which indicates the replacement of water molecules.

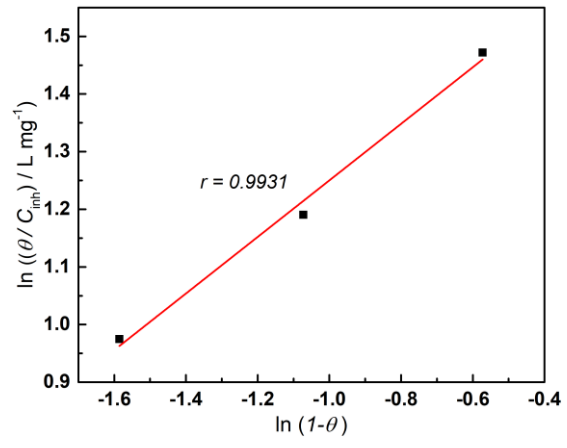


Figure 1. Adsorption isotherm of Flory-Huggins plotted from the weight loss measurements data at 298 K

Effect of temperature and thermodynamic activation parameter

Temperature has a significant effect on the kinetics of the corrosion processes. It also impacts the behaviour of the corrosion inhibitors. To study these effects, weight loss measurements at different temperatures (298 to 318 K) with and without the addition of the optimum concentration of the walnut fruit septum extract (300 mg L⁻¹) were performed. As shown in Table 2, the corrosion rate increases significantly with the increase of the temperature for blank and inhibited solutions that corresponds to the Arrhenius equation (9).

Table 2. Corrosion rate of Fe B500B samples and inhibitor efficiency of walnut fruit septum extract for optimum concentration and blank after 100 h immersion at 298 to 318 K

			Temperatui	re, K		
C / mg L^{-1}	298		308		318	
	C.R., g m ⁻² h	IE, %	C.R., g m ⁻² h	IE, %	C.R., g m ⁻² h	IE, %
0.0 (blank)	1.4117	-	6.5271	-	18.2326	-
300.0	0.2893	79.51	2.5262	61.29	8.3767	54.05

To further investigate this process, the Arrhenius-type dependence between temperature and corrosion rate was used, from which we were able to calculate the activation energy of the corrosion process (E_a) at different temperatures for the blank and optimum concentration of the inhibitor, using Equation (9) [26]:

$$C.R.=k e^{\left(\frac{-E_a}{RT}\right)}$$
 (9)

By using the transition state energy equation (10), thermodynamic parameters for the corrosion processes, such as entropy (ΔS_a) and enthalpy (ΔH_a) were calculated [26]:

$$C.R. = \frac{RT}{Nh} e^{\left(\frac{\Delta S_a}{RT}\right)} e^{\left(\frac{-\Delta H_a}{RT}\right)}$$
(10)

where C.R., *k*, *N*, and *h* are the corrosion rate, pre-exponential factor, Avogadro number and Planck's constant, respectively.

From the slope in Figure 2a, which is according to the linearized form of Equation (9), equal to $-E_a/R$, the activation energy of the metal dissolution was calculated for the blank and optimum concentration of the inhibitor (300 mg L⁻¹). Figure 2b shows the plot of ln [C.R. T^{-1}) vs. T^{-1} from which the intercept and slope were found and used to calculate (ΔS_a) and (ΔH_a) values, respectively.

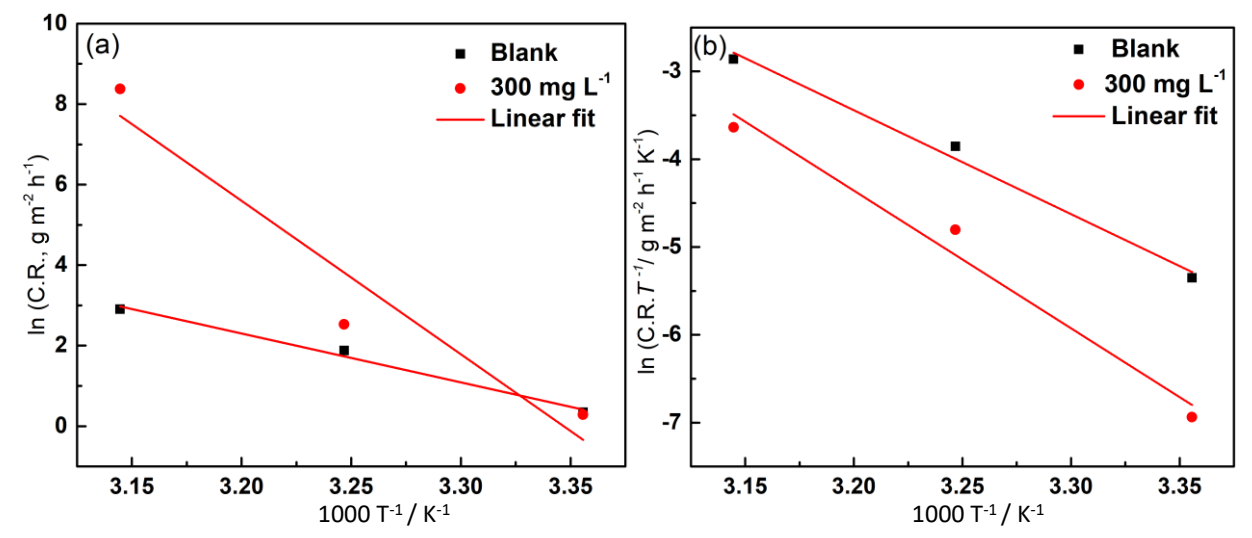


Figure 2. (a) Plot of In C.R. vs. 1/T for the activation energy of corrosion reaction, (b) Arrhenius plot of In (C.R./T) vs. 1/T for Fe B500B samples in the absence and presence of optimum concentration (300 mg L^{-1}) of walnut fruit septum extract

Table 3 shows the activation parameters obtained from Arrhenius and transition state plots. From the calculated data listed in Table 3, the activation energy for the inhibitor optimum concentration was higher than the blank solution. The activation energy for optimum concentration (300 mg L⁻¹) and blank solution were 316.92 and 100.93 kJ mol⁻¹, respectively. This indicates that walnut fruit septum extract forms a thin protection layer for corrosion mitigation in the inhibited medium [27]. This increase in the E_a value suggests a physisorption that occurs at the first stage of the inhibition mechanism [28]. The enthalpy of activation (ΔH_a) has a positive sign, which implies an endothermic corrosion process in the Fe B500B samples. Interestingly, both activation energy E_a values for the blank and optimum inhibitor concentration are greater than the corresponding ΔH_a values. This indicates the involvement of a gaseous reaction in the corrosion process, that is, the reduction of the hydrogen ions [29]. The positive value of entropy shows an increase in the disorder.

Table 3. The values of E_a , ΔH_a , and ΔS_a for Fe B500B samples immersed for 100 h in the mixed acidic medium (0.5 M $H_2SO_4/0.5$ M HCI) in the absence and the presence of 300 mg L^{-1} of walnut fruit septum extract

C / mg L ⁻¹	E_a / kJ mol ⁻¹)	$\Delta H_{\rm a}$ / kJ mol ⁻¹	ΔS_a / J mol ⁻¹ K ⁻¹
0.0 blank	100.93	98.35	286.08
300.0	316.92	130.19	379.86

Potentiodynamic polarization curves

Figure 3 shows the potentiodynamic polarization curves for Fe B500B samples in the mixed acidic medium (0.5 M $H_2SO_4/0.5M$ HCl) at 298 K without and with different concentrations of the walnut fruit septum extract. The addition of the walnut fruit septum extract lowers both cathodic and anodic branches of the potentiodynamic polarization curves, with more dominance on the anodic side. All cathodic and anodic branches are parallel, suggesting that the inhibition mechanism has not been changed [30].

Table 4 presents the Tafel extrapolation data, including corrosion potential (E_{corr}), corrosion current density (i_{corr}), polarization resistance (R_p) and the respective calculated corrosion rates and inhibitor efficiencies.

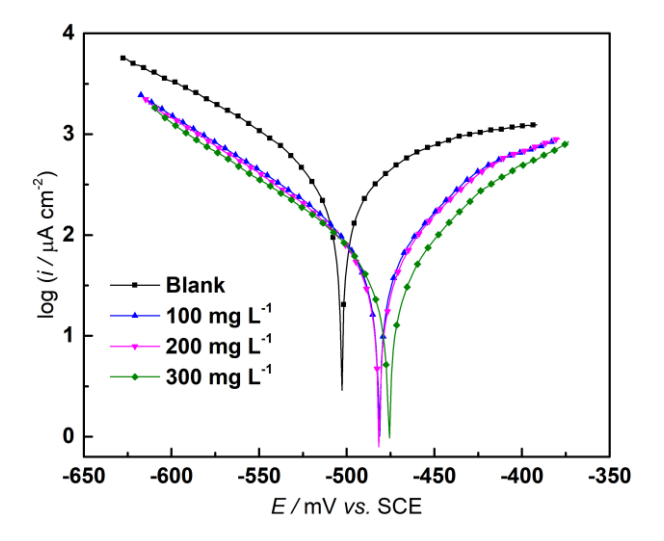


Figure 3. Potentiodynamic polarization curves of Fe B500B samples in the mixed acidic medium (0.5 M $H_2SO_4/0.5$ M HCl) solution without and with different concentrations of the walnut fruit septum extract at 298 K

Table 4. Kinetic parameters obtained from potentiodynamic polarization curves of Fe B500B samples immersed in the mixed acidic medium (0.5 M $H_2SO_4/0.5$ M HCl) at 298 K, without and with different concentrations of walnut fruit septum extract

C / mg L ⁻¹	E _{corr} / mV	b _c / mV dec ⁻¹	ba/ mV dec⁻¹	i _{corr} / μAcm ⁻²	CR, mm year ⁻¹	IE, %	f_{a}	f_{c}	$R_{\rm p}$ / Ω cm ²	IE _{Rp} / %
0	-504.79	-84.65	138.8	316.04	3.695	-			72.24	-
100	-475.68	-89.719	60.688	65.660	0.714	80.68	0.13	0.15	239.40	69.82
200	-476.98	-80.8	55.516	51.222	0.596	83.88	0.09	0.11	278.95	74.10
300	-466.79	-88.012	49.528	41.324	0.481	86.99	0.06	0.085	333.01	78.31

As shown in Table 4, $E_{\rm corr}$ value shifts positively compared to the blank solution. Based on the literature, when the difference in corrosion potential between the inhibited solution and blank is less than 85 mV in absolute value, this inhibitor is considered a mixed-type inhibitor with anodic dominance [31]. Cathodic (b_c) and anodic (b_a) Tafel slopes decrease in their absolute values, indicating adsorption of the inhibitor on both cathodic and anodic sites [32]. Current density (i_{corr}) values decrease significantly with the increase of walnut fruit septum extract concentration from 316.04 μ A cm⁻² for the blank solution to 41.32 μ A cm⁻² for the optimum inhibitor concentration of 300 mg L⁻¹. Corrosion rates also decrease from 3.695 mm year⁻¹ for blank solution to 0.481 mm year⁻¹ for the optimum concentration. These results are in general agreement with corrosion rates obtained from weight loss results (Table 1), except for the blank solution, what is probably due to pitting corrosion occurring in this aggressive condition. In such a case, CR cannot be estimated by the weight loss method. The repeatability of the results regarding the corrosion rate refers to the uniform corrosion, not the pitting corrosion. Increasing the exposure time and temperature in weight loss measurements, as well as adding the inhibitor, converts pitting corrosion to uniform corrosion.

Regarding penetration measurements, the corrosion rate decreased from 3.69 mm year⁻¹ for the blank solution to 0.48 mm year⁻¹ for the optimum concentration (300 mg L⁻¹). The inhibitor efficiency increases remarkably with the increase of the inhibitor concentration, reaching a maximum value for optimum concentration (300 mg L⁻¹) of 86.99 %. Further increase of inhibitor concentration (*i.e.*, 400 mg L⁻¹ results not displayed) did not result in increased inhibition efficiency.

To clarify the complexity of the corrosion process that occurred at the metal/solution interface in the presence of the inhibitor (supposed electrochemical inhibition mechanism), Cao [33]

suggested two exponents of the cathodic (f_c) and anodic (f_a) reaction, calculated by equations (11) and (12):

$$f_{c} = \left(\frac{\dot{I}_{corr}^{inh}}{\dot{I}_{corr}^{0}}\right) e^{\frac{E_{corr}^{inh} - E_{corr}^{0}}{b_{c}}}$$
(11)

$$f_{\rm a} = \left(\frac{\dot{I}_{\rm corr}^{\rm inh}}{\dot{I}_{\rm corr}^0}\right) e^{\frac{E_{\rm corr}^0 - E_{\rm corr}^{\rm inh}}{b_{\rm a}}} \tag{12}$$

where the super-indexes (0) and (inh) represent the corrosive medium without and with walnut fruit septum extract, respectively. The inhibitive mechanism is attributed to the geometric blocking effect if $f_c = f_a$, and if $f_c < 1$ or $f_a < 1$, the blocking effect of active sites is attributed to the adsorption of the inhibitor.

The calculated values of f_a and f_c are also displayed in Table 4. Both coefficients, f_c and f_a , are less than one, and furthermore, $f_c > f_a$. This indicates that the inhibition process is related to the adsorption on the active sites of the metal surface. Meanwhile, the inhibitor retards the anodic reaction. This confirms the shift of E_{corr} , shown in Figure 3 and Table 4.

In addition, the Stearn-Geary equation was used to calculate the polarization resistance (R_p) by equation (13):

$$R_{\rm p} = \frac{b_{\rm c}b_{\rm a}}{2.303 i_{\rm corr} \left(b_{\rm c} + b_{\rm a}\right)} \tag{13}$$

Inhibitor efficiency for R_p values was calculated by equation (14):

$$IE_{R_{p}} = \frac{R_{p \text{ inh}} - R_{p \text{ 0}}}{R_{p \text{ inh}}} 100 \tag{14}$$

where $R_{p \text{ inh}}$ is polarization resistance with the presence of the inhibitor, and $R_{p 0}$ is the polarization resistance of the blank solution.

Table 4 shows that R_p values increase with the increase of walnut fruit septum extract concentration from 72.24 Ω cm² for the blank solution to 333.0 Ω cm² for optimum concentration (300 mg L⁻¹). The increase in concentration of the inhibitor corresponds to the increase in polarization resistance. This indicates the reduction of the electroactive area by the adsorption film formed by the inhibitor on the surface of Fe B500B steel bar samples.

Effect of temperature on the corrosion rate of Fe B500B samples

Potentiodynamic polarization was also used to investigate the effect of temperature on corrosion rate. Figure 4 presents polarization curves for Fe B500B samples in the mixed acidic medium (0.5 M $H_2SO_4/0.5$ M HCl) for blank and optimum concentration (300 mg L^{-1}) at different temperatures. Both anodic and cathodic branches of polarization curves followed the same trend with the increase in temperature. It is clearly seen that with the addition of the optimum concentration of the inhibitor, the corrosion current density significantly decreases compared to the corresponding blank solutions at all tested temperatures.

All relevant data evaluated from potentiodynamic polarization curves are summarized in Table 5, where it is seen that corrosion current density values decrease with the increase of temperature, and this is also reflected in the variation of the inhibition efficiency values. The shift of corrosion potential toward the anodic side decreases with the increase in temperature. At 318 K, the corrosion potential shifts slightly to the cathodic side, referred to the corresponding blank solution (Figure 4).

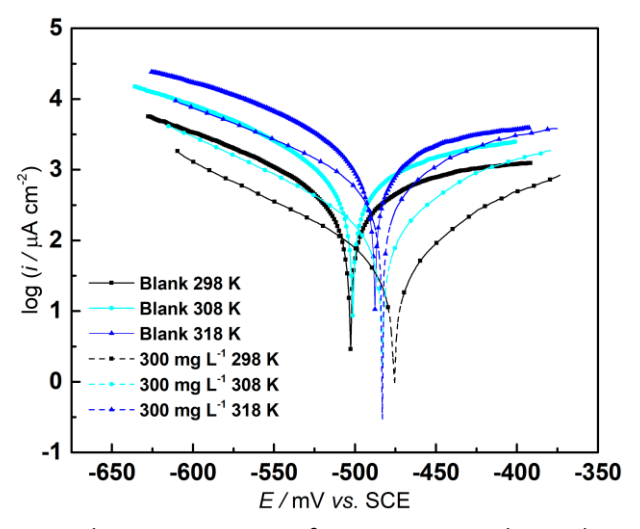


Figure 4. Potentiodynamic polarization curves of Fe B500B samples in the mixed acidic medium (0.5 M $H_2SO_4/0.5$ M HCl) without and with the optimum concentration (300 mg L^{-1}) of the walnut fruit septum extract at different temperatures (298 to 318 K)

This confirms that walnut fruit septum extract acts as a mixed-type inhibitor with dominance on the anodic side, which decreases with the increase in temperature. As a consequence of the increase in temperatures, the density of the pits (active centres of adsorption) increases until the formation of uniform corrosion [25]. This justifies again the mechanism of inhibition of walnut fruit septum alcoholic extract suggested by weight loss to convert pitting corrosion into uniform corrosion [34].

Table 5. Data obtained from Tafel extrapolation of potentiodynamic polarization curves for Fe B500B samples immersed in the mixed acidic medium (0.5 M $H_2SO_4/0.5$ M HCl) without and with the optimal concentration of 300 mg L⁻¹ walnut fruit septum extract at different temperatures (298-318 K)

C / mg L ⁻¹	E _{corr} / mV	b _c / mV dec ⁻¹	<i>b</i> _a / mV dec ⁻¹	i _{corr} / μΑ cm ⁻²	CR, mm year ¹	IE, %	$R_{\rm p}$ / Ω cm ²	IE _{Rp} %
0.0 (blank) 298 K	-504.79	- 84.65	138.8	316.04	3.695	-	72.24	-
0.0 (blank) 308 K	- 483.34	- 95.85	205.41	851.14	9.87	-	33.34	-
0.0 (blank) 318 K	- 487.69	- 109.90	280.44	1854.90	21.52	-	18.48	-
300.0 298 K	- 466.79	- 88.012	49.528	41.324	0.481	86.99	333.02	78.31
300.0 308 K	- 496.17	- 90.79	115.73	217.82	2.53	74.4	101.42	67.1
300.0 318 K	- 485.28	- 100.66	113.52	608.84	7.06	67.2	38.05	51.4

To investigate further, the Stearn-Geary equation (equation 13) was also used here to calculate polarization resistance. Since polarization resistance is the inverse of current density, its decrease means an increase in current density or, in other words, an increase in the corrosion rate. Inhibitor efficiency calculated from R_p values decreases with the increase in temperature. This indicates a decrease in the performance of the inhibitor at high temperatures.

Electrochemical impedance spectroscopy measurements

Electrochemical impedance spectroscopy was conducted for Fe B500B samples immersed in the mixed acidic medium (0.5 M $H_2SO_4/0.5$ M HCl) without and with different concentrations of the



inhibitor at 298 K, and also at 308 and 318 K for the optimum inhibitor concentration (300 mg L⁻¹) with respective to blank solution.

Figure 5a shows the Nyquist diagrams of Fe B500B samples in the presence and absence of the walnut fruit septum at 298 K. The obtained semicircle impedance responses indicate that the process occurring at the metal interface with the solution is mainly charge transfer [35]. Furthermore, all semicircles appear slightly depressed. This may be related to the inhomogeneous surface of Fe B500B samples that causes frequency dispersion of the interfacial impedance [36]. At lower frequencies, an inductive loop that may be related to the adsorption-desorption of the inhibitor molecules due to electrode surface instability is observed. Nevertheless, this inductive loop decreases with the increase of the inhibitor concentration, indicating the increase of stability in the adsorption-desorption equilibrium process at the electrode surface [36]. The Nyquist plots display a significant increase in diameters with the addition of the walnut fruit septum extract. This indicates an increase in the adsorption of the inhibitor with the increase of the concentration, resulting in a lower electroactive region on the surface of the Fe B500B samples. Bode modulus and phase angle diagrams for Fe B500B samples immersed in the mixed acidic medium (0.5 M H₂SO₄/0.5 M HCl) without and with different concentrations of the inhibitor at 298 K are displayed in Figure 5b. As shown in Bode curves at lower frequencies, the impedance magnitude increases with the concentration of walnut fruit septum extract. This reveals higher charge transfer resistance at the metal solution interface. It seems that the corrosion mechanism does not change with the increase of the inhibitor concentration, which is shown by forms of Bode curves that are similar in shape for all measured samples. Only one peak appearing in phase angle plots indicates the presence of only one time constant. With the increase of the inhibitor concentration, the phase angle peak increases, which suggests continuous adsorption of inhibitor molecules on the Fe B500B samples at higher concentrations of the inhibitor. The increase in phase angle value with the increase of inhibitor concentration indicates that the metal dissolution decreased [37].

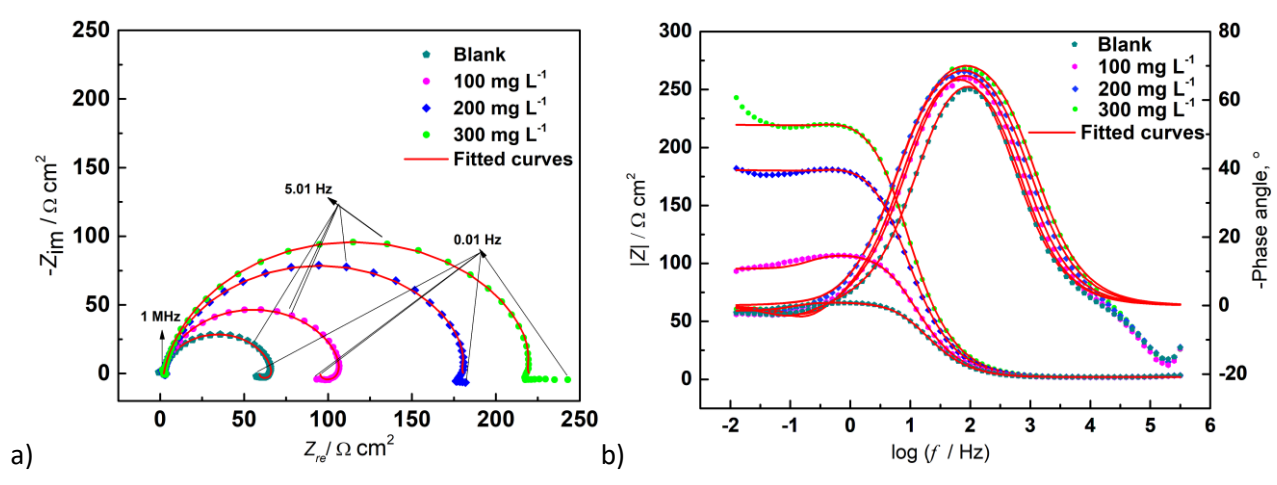


Figure 5. (a) Nyquist plots and (b) Bode phase angle and modulus plots for Fe B500B samples in the mixed acidic medium (0.5 M $H_2SO_4/0.5$ M HCl) without and with different concentrations of the walnut fruit septum extract at 298 K

Figure 6 shows Nyquist and Bode diagrams at different temperatures for the optimum concentration of the walnut fruit septum extract (300 mg L⁻¹) and blank solution. The capacitive loops increase for optimum concentration compared to respective blank solutions at all studied temperatures, indicating the formation of the protective layer on the surface of Fe B500B samples. Nevertheless, the capacitive loops decrease with the increase of the temperature both for blank and

optimum concentration, implying acceleration of corrosion rate. The respective Bode modulus plots show an increase in the magnitude of impedance for optimum concentration (300 mg L⁻¹) compared with corresponding blank solutions. However, the increase in temperature decreases the magnitude of the impedance, indicating the desorption of inhibitor molecules with the increased temperature.

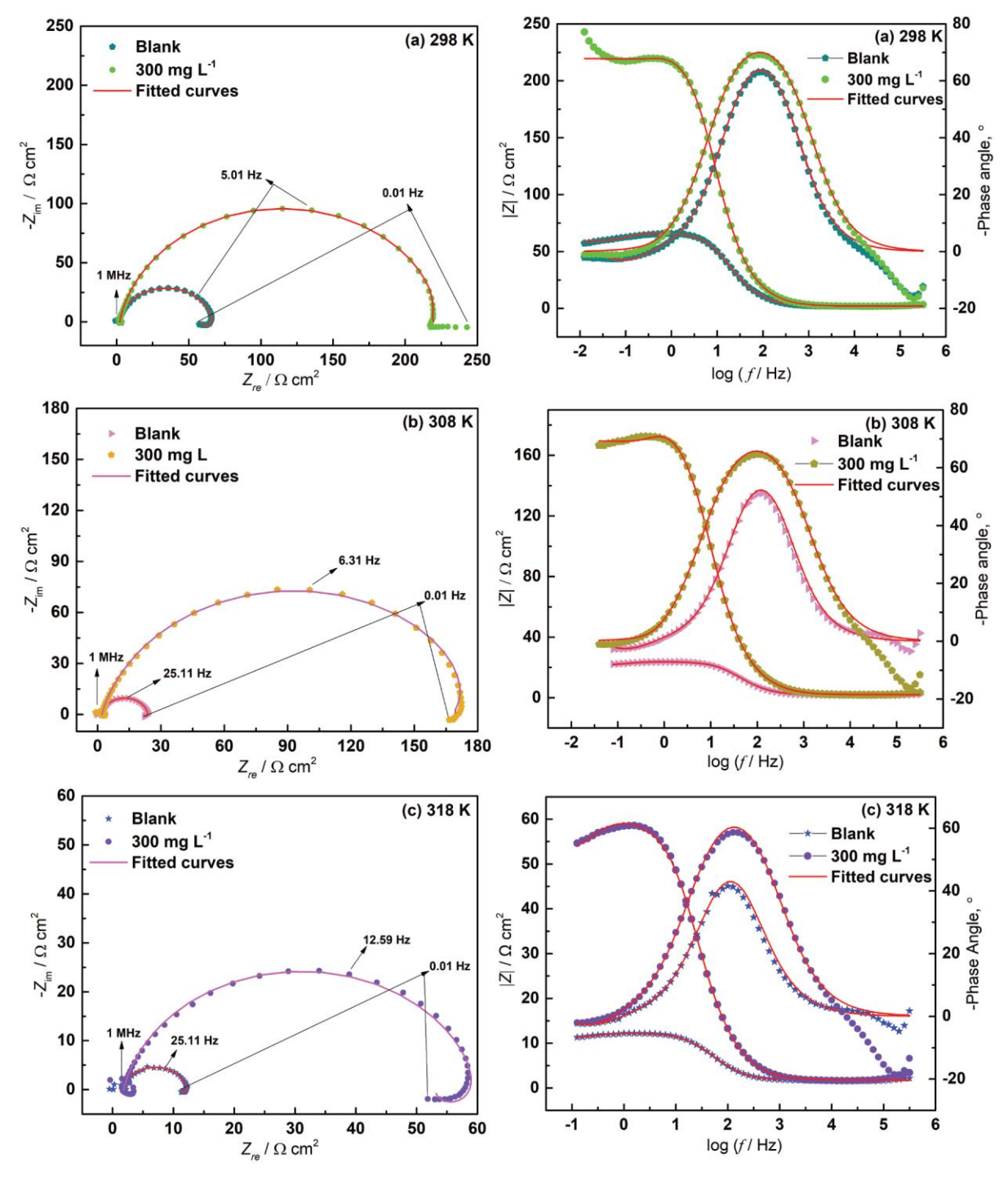


Figure 6. Nyquist plots (left), and Bode phase and-modulus plots (right) for Fe B500B samples in the mixed acidic medium (0.5 M $H_2SO_4/0.5$ M HCl) without and with the optimum concentration (300 mg L^{-1}) of the walnut fruit septum extract at: (a) 298 K; (b) 308 K; (c) 318 K

The equivalent circuit shown in Figure 7 was used to fit the data of EIS measurements. Experimental data obtained from Palmsens 4 potentiostat were imported to Aftermath software version 1.6.10523 from Pine Research to make fittings of EIS spectra.

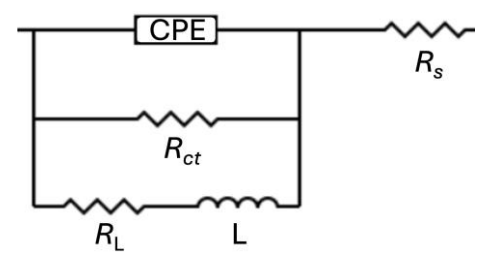


Figure 7. Equivalent circuit used to fit the EIS experimental data

The solution resistance (R_s), constant phase element (CPE), which is related to double layer capacitance, charge transfer resistance (R_{ct}), inductance (L), and resistance of inductance (R_L) were used to fit the experimental data of EIS measurements. Equation (15) determines the impedance of constant phase element (Z_{CPE}) [38]:

$$Z_{\text{CPE}} = \frac{1}{Y_0 \left(j\omega\right)^{\alpha}} \tag{15}$$

where Y_0 represents the CPE constant, ω (ω = $2\pi f$) is the angular frequency, and α is the CPE exponent, which represents a deviation from the ideal semicircle response and takes value in a range of -1 < α <1. When α is equal to 1, 0 and -1 represent a pure capacitor, resistor, and inductor, respectively. The CPE was further converted to double-layer capacitance (C_{cl}) by equations (16) and (17):

$$C_{\rm dl} = Y_0 \, \omega_{\rm max}^{\alpha - 1} \tag{16}$$

$$\omega_{\text{max}} = 2\pi f_{\text{max}} \tag{17}$$

where f_{max} is the frequency for the maximum value of the imaginary component in the plot of - Z_{im} vs. log f (12.62, 7.95, 6.30, and 6.31 Hz for the walnut fruit septum extract concentration of 0 (blank), 100, 200 and 300 mg L⁻¹ respectively), whereas ω_{max} is the maximum angular frequency calculated from f_{max} .

The results of the equivalent circuit fitting to experimental impedance data presented in Figures 5 and 6 are shown in Tables 6 and 7.

Table 6 presents impedance parameter values for Fe B500B samples in a blank solution and for different concentrations of the walnut fruit septum extract at 298 K.

Table 6. Fitted experimental parameter values of EIS spectra (Fig.5) for Fe B500B samples immersed in the mixed acidic medium (0.5 M $H_2SO_4/0.5$ M HCl), without and with different concentrations of walnut fruit septum extract at 298 K

C / mg L ⁻¹	$R_{\rm s}$ / Ω cm ²	$R_{\rm ct}$ / Ω cm ²	$C_{\rm dl}$ / μF cm ⁻²	α	$L/H cm^2$	$R_L / \Omega \text{ cm}^2$	IE, %
0.0 (blank)	1.99	64.82	185.66	0.92	772.01	478.81	-
100.0	2.33	111.17	164.47	0.91	1044.05	860.50	41.69
200.0	2.11	186.33	135.64	0.89	1338.08	4212.50	65.21
300.0	2.10	225.94	111.91	0.90	1953.93	5863.68	71.31

It is shown in Table 6 that the addition of walnut fruit septum extract increases the value of charge transfer ($R_{\rm ct}$), indicating the adsorption of the inhibitor molecules at the metal-solution interface with the increase of the inhibitor concentration. As a consequence, the corrosion rate is decreased. The double-layer capacitance ($C_{\rm cl}$) decreases as the corrosion inhibitor concentration increases. The behaviour of the double-layer capacitance can be investigated further by using the following equation [39]:

$$C_{\rm dl} = \frac{\varepsilon^0 \varepsilon}{d} S \tag{18}$$

where ε^0 and ε are vacuum dielectric permittivity constant and double layer dielectric constant, respectively. S is the exposed area of material in the corrosive medium, and d is the thickness of the double layer. The dielectric constant of water is bigger than that of inhibitor molecules. The decrease of the double-layer capacitance values suggests a continuous replacement of water molecules at the metal solution interface by adsorption of the inhibitor molecules with the increase of the inhibitor concentration. The molecules of the inhibitor are bigger than the molecules of water, indicating an increase in d, which results in a decrease of capacitance [40]. The inductance values increase with the increase of the inhibitor concentration to resist the current changes. This is further supported by the corresponding values of R_L , which also increase with the increase of the inductance values. This phenomenon may result from either the surface of the metal becoming less tense or from the formation of unstable corrosion products, such as FeCl₂, at the boundary between the metal and the solution, causing the inductive loop (R L) at low frequencies [41].

Table 7 lists impedance parameter values for Fe B500B samples measured in blank solution and for the optimal concentration of the walnut fruit septum extract (300 mg L^{-1}) at different temperatures (298 to 318 K). The parameter values were obtained by fitting EEC in Figure 7 to impedance spectra presented in Figure 6. As shown in Table 7, the charge transfer resistance (R_{ct}) increases at the optimum inhibitor concentration compared to the respective blank solution, displaying the moderate performance of the inhibitor at higher temperatures. The increase in the temperature decreases charge transfer resistance both for blank and optimum concentration. This suggests increased desorption of the inhibitor molecules from the metal solution interface. Double-layer capacitance (C_{dl}) value decreases compared to the blank solution and increases with the increase of the temperature. The values of inductance (L) decrease with the increase in temperature, indicating increased current at the metal/solution interface. Also, resistance R_{L} follows the same trend as inductance with the increase in temperature.

Table 7. Fitted experimental parameter values of EIS spectra (Fig.6) for Fe B500B samples immersed in the mixed acidic medium (0.5 M $H_2SO_4/0.5$ M HCl) without and with 300 mg L^{-1} walnut fruit septum extract at different temperatures (298-318 K)

Inhibitor concentration, mg L	$R_{\rm s}/\Omega~{\rm cm}^2$	$R_{\rm ct}$ / Ω cm ²	$C_{\rm dl}$ / μF cm ⁻²	α	L/H cm ²	$R_{\rm L}$ / Ω cm ²
0.0 (blank) - 298 K	1.99	64.82	185.66	0.92	772.01	478.81
0.0 (blank) - 308 K	1.83	22.09	248.98	0.91	182.35	185.86
0.0 (blank) - 318 K	1.68	10.65	396.60	0.90	49.58	84.19
300.0 - 298 K	2.10	225.94	111.91	0.90	1953.93	5863.68
300.0 - 308 K	2.05	182.86	122.79	0.86	526.83	2044.81
300.0 - 318 K	1.83	58.56	151.79	0.88	261.51	411.88

SEM analysis

Scanning electron microscope (SEM) was used to evaluate the protective properties of walnut fruit septum extract on the surface of Fe B500B samples immersed in the mixed acidic medium (0.5 M $H_2SO_4/0.5$ M HCl), without and with optimum inhibitor concentration (300 mg L^{-1}), in the temperature range 298-318 K.

Figure 8a shows the Fe B500B sample surface previously polished with emery paper and cleaned with bi-distilled water before immersion. From the observation of the image, some white lines appear on the surface of the sample that are inherent from the polishing machine. At 298 K, the SEM image of the sample in the blank solution shows local corrosion (Figure 8b).

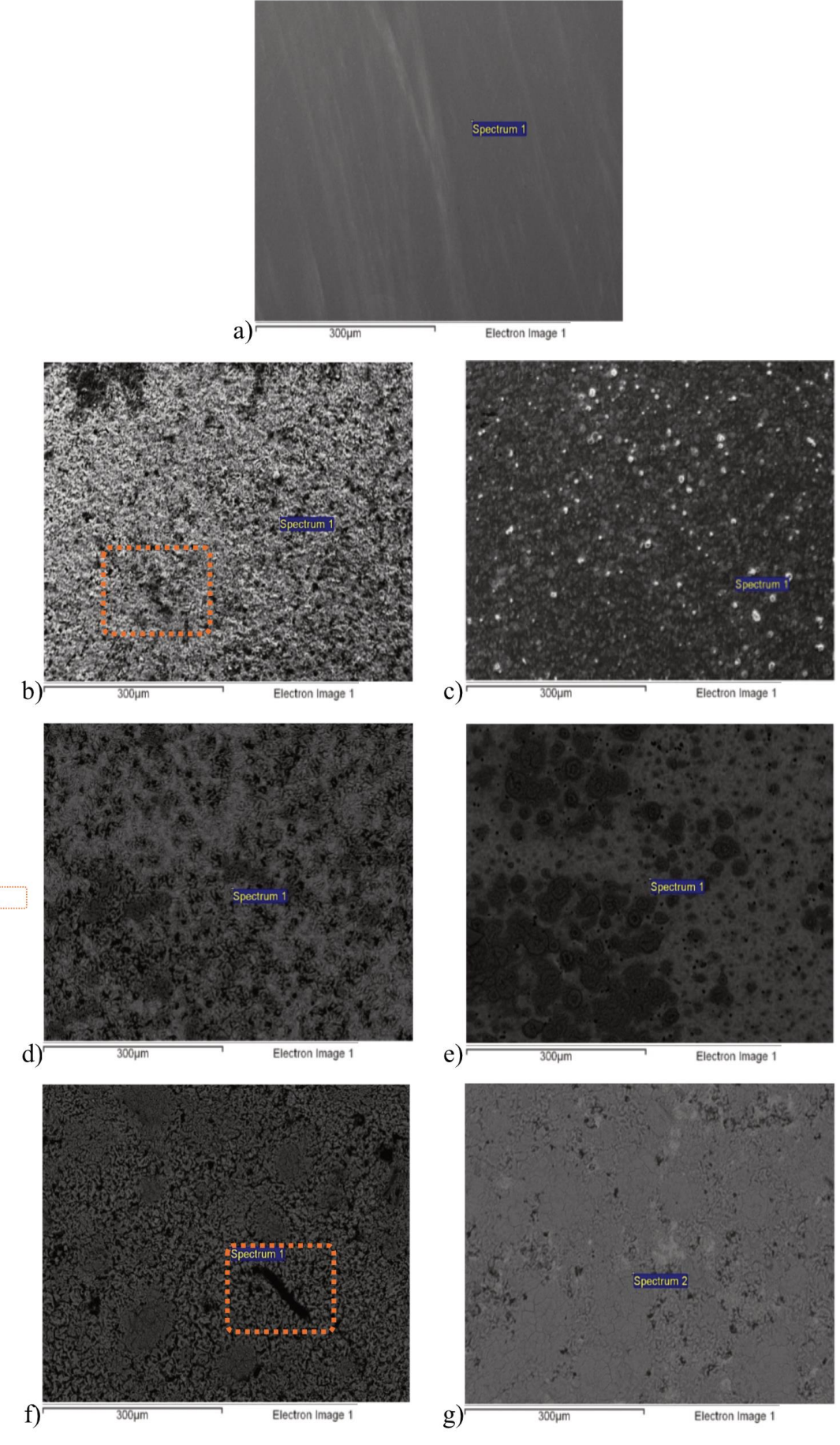


Figure 8. SEM images of Fe B500B samples: (a) polished, (b, d, f) immersed in blank solution, (c, e, g) in optimum concentration (300 mg L^{-1}) of walnut septum fruit extract, for 24 h at 298, 308 and 318 K

The sample immersed in the solution with optimum inhibitor concentration at 298 K displays a homogeneous and uniform surface (Figure 8c), conforming the results from weight loss and electrochemical measurements. The SEM images confirm once more the good protection performance of the inhibitor, as we observe the conversion with time of the localised corrosion to uniform corrosion. This validates the adsorption of the walnut fruit septum extract on the surface of the Fe B500B sample. With the increase in temperature, the protection properties of the walnut fruit septum extract weakened, but the samples immersed in the solution with optimum inhibitor concentration showed improvements compared to the respective samples immersed in blank solutions at the corresponding temperatures (as seen in Figure 8). Namely, the walnut fruit septum extract significantly impedes corrosion processes on the surface of the Fe B500B samples.

ATR-FTIR spectroscopy analysis of the walnut fruit septum extract

Based on previously published works on green inhibitors, the presence of heteroatoms (*i.e.*, O, N and S), aromatic rings, double bonds, and conjugated bonds gave the inhibitors the ability to be adsorbed on the surface of the metals [42,43]. To confirm qualitatively the presence of those groups in walnut fruit septum extract, ATR-FTIR was carried out on Fe B500B samples in polished form, immersed in blank and optimum concentration of the inhibitor and pure alcoholic extract, and shown in Figure 9. The ATR-FTIR of the dried alcoholic extract (Figure 9d) displays the strongest and broader band at 3237 cm⁻¹, which is attributed to O-H stretching [44]. The bands at 2922 and 2852 cm⁻¹ are related to C-H stretching vibration [44]. The 1706 cm⁻¹ peak is attributed to the carbonyl group, C=O stretching [45]. The strong bands at 1604 and 1518 cm⁻¹ could be assigned as aromatic rings supported by weak peaks at 2114 cm⁻¹ [44]. The ATR-FTIR spectra for the non-treated specimen (only ground) and the specimen immersed in blank solution show no characteristic bands (Figure 9a and 9b). The FTIR spectrum of the Fe B500B immersed in the optimum concentration of the inhibitor (300 mg L⁻¹) for 24 h displays bands at 1618 and 1018 cm⁻¹, attributed to the stretching vibration of C=C, C=O double bonds and C-O bonds, respectively (Figure 9c).

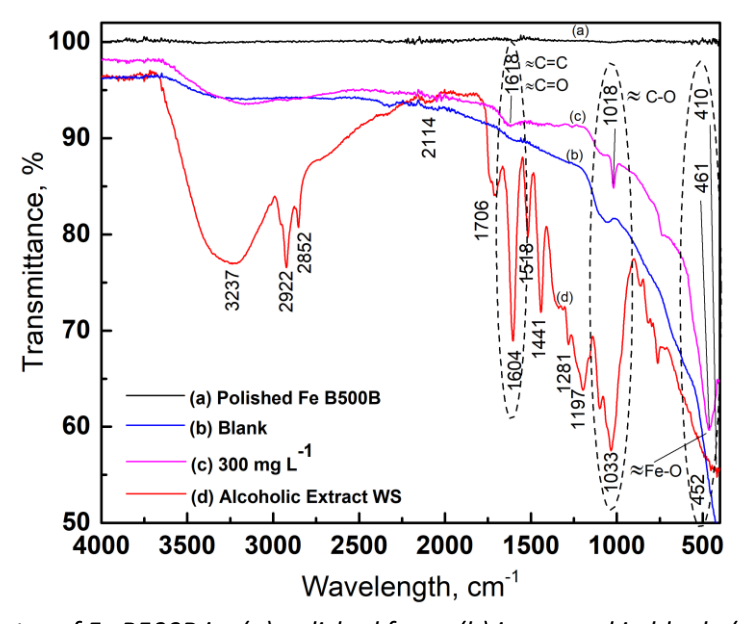


Figure 9. ATR-FTIR spectra of Fe B500B in: (a) polished form, (b) immersed in blank, (c) at optimum inhibitor concentration (300 mg L-1); (d) of pure alcoholic inhibitor extract

These bands are approximately in the same range as the bands for C=C, C=O, and C-O of phenolic compounds on the alcoholic extract of the walnut septum (Figures 9 c,d) [46,47]. This suggests the presence of phenolic compounds on the surface of the Fe B500B sample. Also, the bands at 461 and

410 cm⁻¹ are attributed to the stretching modes of the Fe-O bonds, resulting from the interaction of iron with the oxygen of polyphenols present in the extract [47]. Based on the presence of these bands, it can be concluded that walnut septum extract molecules are chemisorbed on the surface of the Fe B500B specimen.

UV-Vis spectroscopy analysis of the walnut fruit septum extract

Organic compounds in walnut fruit septum extract can reveal characteristic peaks. The alcoholic extract and blank solution (0.5 M $H_2SO_4/0.5$ M HCl), with and without the addition of 300 mg L^{-1} (optimum concentration), were used for the analysis. The absorbance peaks are displayed in Figure 10. The immersion of Fe B500B steel bar in the solution that contains the optimum concentration of the inhibitor (300 mg L^{-1}) decreases the absorbance peak compared to the optimum (300 mg L^{-1}) solution without immersion of the Fe B500B samples. This clearly indicates the adsorption of the inhibitor molecules on the active sites on the surface of Fe B500B samples [48].

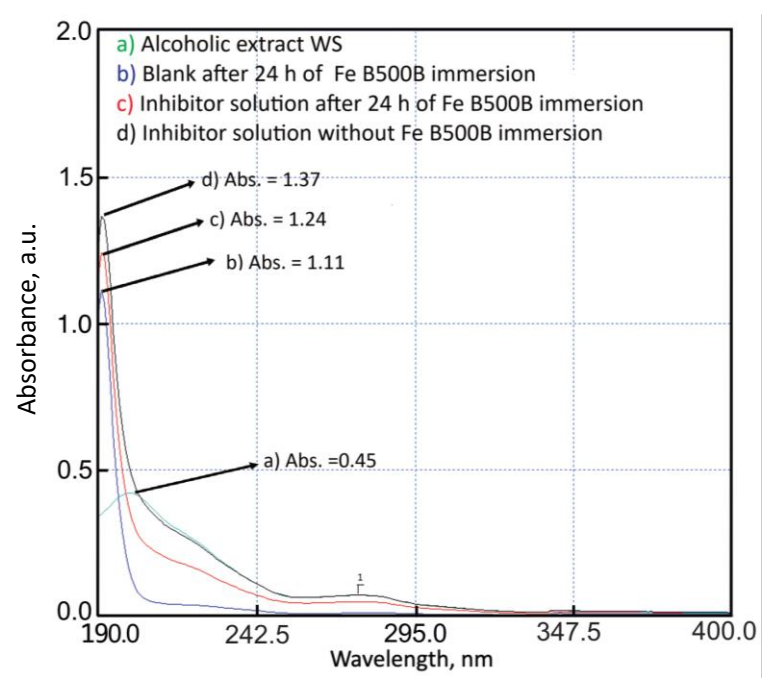


Figure 10. UV-vis spectra of: (a) alcoholic walnut fruit septum extract; solutions after 24 h immersion of Fe B500B in (b) blank, and (c) inhibitor (300 mg L^{-1}); (d) inhibitor solution without immersion of Fe B500B

Suggested mechanism of corrosion and inhibition by walnut fruit septum extract

According to the above discussion based on weight loss and electrochemical measurements, walnut fruit septum extract acts as a mixed-type inhibitor (anodic-cathodic) that is adsorbed spontaneously on the surface of the metal (hot rolled steel Fe B500B samples), according to the mixed physical-chemical mechanism. It is well known that carbon steel has a positive surface charge in an acidic solution [49]. According to the potential of the zero-charge adsorption mechanism, for Fe B500B samples, pH of zero charge (pHzch) is almost 8.8. When immersed in acidic solutions (pH <8.8), the Fe B500B sample is charged positively. In such conditions, Cl⁻ ions and other negative ions are likely to get adsorbed. Another important principle proposed by Pearson HSAB (Hard and Soft Acids and Bases) explains the adsorption of Cl⁻ (as a weak base) and bulk metals, which act as a weak acid [50,51].

The proposed mechanism for anodic and cathodic corrosion reaction on the surface of carbon steel (hot rolled steel Fe B500B samples) immersed in mixed acidic solution (0.5 M $H_2SO_4/0.5$ M HCl) contains the following steps [52-54]:

In water solution, H_2SO_4 and HCl dissociate to H^+ , HSO^{4-} , SO_4^{2-} and Cl^- ions. Corrosion of hot-rolled steel Fe B500B in mixed acidic solution is considered as localized corrosion in the form of pitting with hydrogen evolution at the cathodic sites and anodic dissolution of Fe, where HSO_4^{--} , SO_4^{2--} and Cl^- ions react and form corrosion products as $FeCl_2$, $FeSO_4$, and $Fe(HSO_4)_2$. The presence of Cl^- in concentration 0.5 M with autocatalytic action, the small radius, and easy penetration in the passivation layer accelerates the pitting corrosion, where the presence of SO_4^{2--} ions can act as a pitting corrosion accelerator [53].

The general cathodic reaction is (Equation (19)):

$$2H^{+}_{(ag)} + 2e^{-} \rightarrow H_{2(g)}$$
 (19)

This reaction can be described by the following steps (Equations (20) to (22)):

$$Fe + H^+ \rightarrow (FeH^+)_{aq} \tag{20}$$

$$(FeH^+)_{aq} + e^- \rightarrow (FeH)_{ads}$$
 (21)

$$(FeH)_{ads} + H^{+} + e^{-} \rightarrow Fe + H_{2(g)}$$
(22)

The general anodic reaction is (Equation (23)):

$$Fe \rightarrow Fe^{2+} + 2e^{-} \tag{23}$$

The anodic reaction mechanism is more complicated than the cathodic reaction mechanism, especially in mixed acidic solutions. After immersion of the metal (hot rolled steel Fe B500B samples) in the above corrosive water solution, it is soaked with water molecules, which are adsorbed initially in a competitive manner with chlorine ions [52].

The anodic reaction can be described by the following steps:

In the part of anodic surface area where chlorine ions are adsorbed, pitting corrosion is initiated according to equations (24) to (26):

$$Fe + Cl^{-} + H_2O \leftrightarrow [FeCl(OH)]^{-}_{ads} + H^{+} + e^{-}$$
(24)

$$[FeCI(OH)]^{-}_{ads} \leftrightarrow FeCIOH + e^{-}$$
 (25)

$$FeCIOH + H^+ \leftrightarrow Fe^{2+} + CI^- + H_2O \tag{26}$$

In the remaining part of the anodic surface area, the dissolution of iron may occur by the following steps (equations (27) to (29)):

$$Fe +H_2O \leftrightarrow (FeOH)_{ads} + H^+ + e^- \tag{27}$$

$$(FeOH)_{ads} \rightarrow (FeOH)^+ + e^-$$
 (28)

$$(FeOH)^{+} + H^{+} \leftrightarrow Fe^{2+} + H_{2}O$$
 (29)

When walnut septum extract (WSE) is added to the mixed acidic solution, the corrosion rate of hot rolled steel Fe B500B is inhibited moderately. The inhibition mechanism is explained by the adsorption of compounds contained in the walnut septum extract. Rusu *et al.* [22] reported that the main compounds found in walnut septum extract are phenolic compounds presented in Figure 11. Their HPLC-DAD quantitative analysis of the extract confirmed the presence and the respective concentrations of these main compounds, *i.e.*, gallic acid (7.249 mg L⁻¹); catechin (25.005 mg L⁻¹); isoquercitrin (5.701 mg L⁻¹) and quercitrin (87.520 mg L⁻¹).

These compounds contain many polar groups of oxygen atoms, which can be protonated in the acidic medium according to:

$$WSE + xH^{+} \rightarrow WSEH_{x}^{x+}$$
 (30)

Figure 11. Main compounds found in walnut septum extract: a) gallic acid, b) catechin, c) isoquercitrin, d) quercitrin

In mixed acidic solution (0.5 M $H_2SO_4/0.5$ M HCl), WSE compound exists in two main forms: WSE and WSE H_x^{x+} . During the corrosion process of hot rolled steel Fe B500B samples surface would be covered by HSO_4^{-} , SO_4^{-2} and Cl^{-} ions (the last one is adsorbed on the surface), converting the surface of the metal from the positively charged into the negatively charged [49].

The physisorption of the WSE occurred between the surface of Fe B500B samples of negatively charged and protonated compounds WSEH $_x^{x+}$. This possibly occurred on the active anodic side of the metal as electrostatic attraction [55].

The chemisorption of the WSE compounds (protonated and unprotonated) occurred on the interface of the cathodic site of the metal surface Fe B500B samples through coordinate bonds and back-donating bonds due to the presence of heteroatoms like oxygen that provide electron lone pairs to the Fe vacant 3d orbitals [55]. The scheme of the suggested adsorption of main inhibitor compounds is shown in Figure 12.

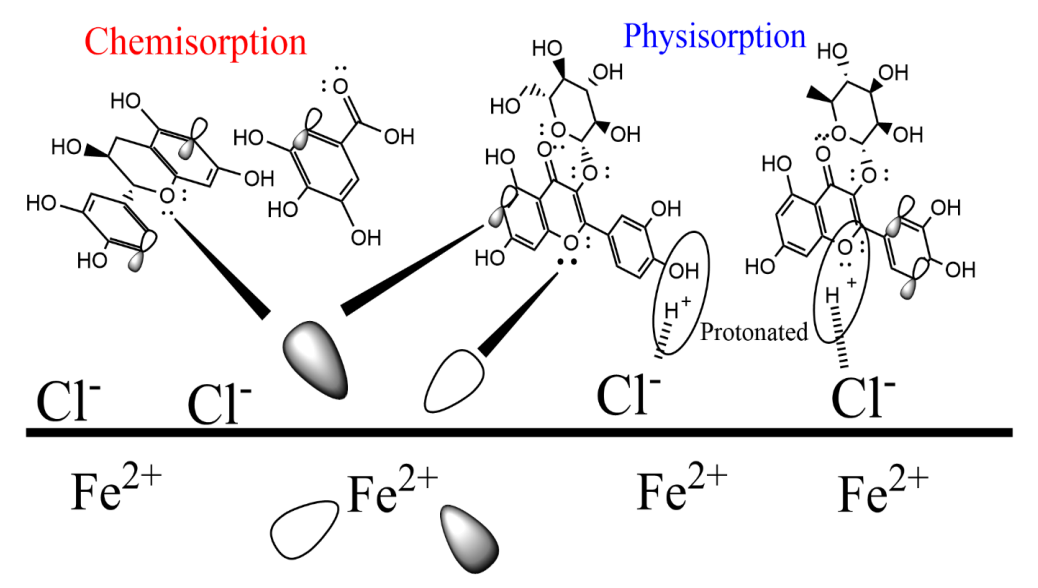


Figure 12. Suggested mechanism for the adsorption of main compounds of walnut septum extract on Fe B500B samples in mixed acidic solution

Conclusions

The present work evaluated the inhibition properties of walnut fruit septum alcoholic extract for Fe B500B samples in the presence of the mixed acidic medium (0.5 M H₂SO₄/0.5 M HCl) at temperatures from 298 to 318 K. The inhibitor molecules were easily extracted under reflux. The presence of gallic acid, catechin, isoquercitrin, and quercitrin (suitable for corrosion inhibitors) was qualitatively and quantitatively confirmed by HPLC-DAD spectroscopy. The classical weight loss method results displayed very good performance of the inhibitor at 298 K, reaching a maximum inhibitor efficiency of 79.51 % for 300 mg L⁻¹ of the extract added. The adsorption of the inhibitor molecules obeys the Flory-Huggins isotherm that indicated the physisorption on the surface of Fe B500B samples. ATR-FTIR spectra of the Fe B500B in polished form, immersed in the blank and optimum concentration of the inhibitor and pure alcoholic extract, confirmed the presence of phenolic compounds on the surface of the Fe B500B samples, indicating the adsorption of the walnut septum extract molecules on the sample surfaces. The Arrhenius equation displays an endothermic dissolution process at the surface of the Fe B500B samples. The increase in temperature accelerates the corrosion processes, and with the increase of inhibitor concentration at 298 K, the corrosion rates decrease. Potentiodynamic polarization curves displayed inhibition of both anodic and cathodic reactions when increasing the inhibitor concentration. This indicates that the walnut fruit septum extract acts as a mixed-type inhibitor. From the kinetic calculation, inhibition efficiency resulted in 86.99 %. The increase in the temperature decreases the inhibition efficiency. The Nyquist plots present slightly depressed capacitive loops, showing an increase in diameters with an increase of the inhibitor concentration due to an increase of charge transfer resistance, indicating the adsorption of walnut fruit septum extract at the metal solution interface. The charge transfer resistance decreases with the increase in temperature, indicating desorption of the inhibitor molecules. Surface characterization with SEM further confirms the adsorption of the inhibitor molecules on the surface of the Fe B500B samples. This work modestly contributes to more sustainable sources of corrosion inhibition for a safer and cleaner environment.

Acknowledgements: We appreciate the contribution of the Albanian Institute of The Scientific Police for SEM surface characterization of our samples.

References

- [1] G. Koch, Cost of corrosion, in Trends in Oil and Gas Corrosion Research and Technologies, A. M. El-Sherik Ed., Woodhead Publishing, Boston, 2017, pp. 3-30. https://doi.org/10.1016/B978-0-08-101105-8.00001-2
- [2] C. J. Brown, D. R. Olsen, Regeneration of hydrochloric acid pickle liquors by crystallization, Iron control technologies: proceedings of the Third International Symposium on Iron Control in Hydrometallurgy, Montreal, Canada, October 1-4, 2006. ISBN: 189447564X. https://www.yumpu.com/en/document/read/11519218/regeneration-of-hydrochloric-acid-pickle-liquors-by-
- [3] M. Abdallah, K. A. Soliman, B. A. Al Jahdaly, J. H. Al-Fahemi, H. Hawsawi, H. M. Altass, M. S. Motawea, S. S. Al-Juaid, Natural parsley oil as a green and safe inhibitor for corrosion of X80 carbon steel in 0.5 M H₂SO₄ solution: a chemical, electrochemical, DFT and MC simulation approach, RSC Advances 12 (5) (2022) 2959-2971. https://doi.org/10.1039/D1RA08855F
- [4] M. Abdallah, H. M. Altass, A. S. Al-Gorair, J. H. Al-Fahemi, B. A. A. L. Jahdaly, K.A. Soliman, Natural nutmeg oil as a green corrosion inhibitor for carbon steel in 1.0 M HCl solution:



- Chemical, electrochemical, and computational methods, *Journal of Molecular Liquids* **323** (2021) 115036. https://doi.org/10.1016/j.molliq.2020.115036
- [5] L. Chen, D. Lu, Y. Zhang, Organic Compounds as Corrosion Inhibitors for Carbon Steel in HCl Solution: A Comprehensive Review, *Materials* 15(6) (2022) 2023. https://www.mdpi.com/1996-1944/15/6/2023
- [6] A. Ait Aghzzaf, D. Veys-Renaux, E. Rocca, Pomegranate peels crude extract as a corrosion inhibitor of mild steel in HCl medium: Passivation and hydrophobic effect, *Materials and Corrosion* **71(1)** (2020) 148-154. https://doi.org/10.1002/maco.201911049
- [7] G. I. Ramírez-Peralta, U. León-Silva, M. E. Nicho Díaz, M. G. Valladares-Cisneros, Effect of Equisetum arvense extract as corrosion inhibitor of A36 steel in sulfuric acid solution, Materials and Corrosion 69(11) (2018) 1631-1637. https://doi.org/10.1002/maco.201810119
- [8] S. E. Adeniji, B. A. Akindehinde, Comparative analysis of adsorption and corrosion inhibitive properties of ethanol extract of Dialium Guineense leaves for mild steel in 0.5 M HCl, *Journal of Electrochemical Science and Engineering* **8(3)** (2018) 219-226. https://doi.org/10.5599/jese.486
- [9] F. E. Abeng, V. Anadebe, P. Y. Nkom, K. J. Uwakwe, E. G. Kamalu, Experimental and theoretical study on the corrosion inhibitor potential of quinazoline derivative for mild steel in hydrochloric acid solution, *Journal of Electrochemical Science and Engineering* **11(1)** (2020) 11-26. https://doi.org/10.5599/jese.887
- [10] I. H. Ali, A. M. Idris, M. H. A. Suliman, Evaluation of Leaf and Bark Extracts of Acacia tortilis as Corrosion Inhibitors for Mild Steel in Seawater: Experimental and Studies, *International Journal of Electrochemical Science* 14(7) (2019) 6406-6419. https://doi.org/10.20964/2019.07.10
- [11] H. S. Gadow, M. M. Motawea, Investigation of the corrosion inhibition of carbon steel in hydrochloric acid solution by using ginger roots extract, *RSC Advances* **7(40)** (2017) 24576-24588. https://doi.org/10.1039/C6RA28636D
- [12] K. Hjouji, E. Ech-chihbi, I. Atemni, M. Ouakki, T. Ainane, M. Taleb, Z. Rais, Datura stramonium plant seed extracts as a new green corrosion inhibitor for mild steel in 1M HCl solution: Experimental and surface characterization studies, *Sustainable Chemistry and Pharmacy* **34** (2023) 101170. https://doi.org/10.1016/j.scp.2023.101170
- [13] F. Kaya, R. Solmaz, İ. H. Geçibesler, Investigation of adsorption, corrosion inhibition, synergistic inhibition effect and stability studies of Rheum ribes leaf extract on mild steel in 1 M HCl solution, *Journal of the Taiwan Institute of Chemical Engineers* **143** (2023) 104712. https://doi.org/10.1016/j.jtice.2023.104712
- [14] A. Jano, A. Lame, E. Kokalari, Test of inhibitors for preventing corrosion of steel reinforcement in concrete, *Ovidius University Annals of Chemistry* **32(2)** (2021) 110-113. https://doi.org/10.2478/auoc-2021-0016
- [15] X. Wang, L. Chen, F. Yang, Q. Xiang, J. Liu, Corrosion inhibition mechanism and extraction technology of plant corrosion inhibitors: a review, *Journal of Adhesion Science and Technology* **37(21)** (2023) 2919-2943. https://doi.org/10.1080/01694243.2023.2172993
- [16] M. Abdallah, K. A. Soliman, M. Alfakeer, A. M. Al-bonayan, M. T. Alotaibi, H. Hawsawi, O. A. Hazazi, R. S. Abdel Hameed, M. Sobhi, Mitigation effect of natural lettuce oil on the corrosion of mild steel in sulfuric acid solution: chemical, electrochemical, computational aspects, *Green Chemistry Letters and Reviews* 16(1) (2023) 2249019. https://doi.org/10.1080/17518253.2023.2249019
- [17] A. R. Shahmoradi, M. Ranjbarghanei, A.A. Javidparvar, L. Guo, E. Berdimurodov, B. Ramezanzadeh, Theoretical and surface/electrochemical investigations of walnut fruit green husk extract as effective inhibitor for mild-steel corrosion in 1M HCl electrolyte,

- Journal of Molecular Liquids **338** (2021) 116550. https://doi.org/10.1016/j.molliq.2021.116550
- [18] M. Okutan, A. Asan, H. E. Singer, The Effect of the Oğuzlar Walnut Extract as a Green Corrosion Inhibitor on AISI 1010 Mild, Steel *Hittite Journal of Science and Engineering* **10(1)** (2023) 33-41. https://doi.org/10.17350/HJSE19030000288
- [19] S. A. Haddadi, E. Alibakhshi, G. Bahlakeh, B. Ramezanzadeh, M. Mahdavian, A detailed atomic level computational and electrochemical exploration of the Juglans regia green fruit shell extract as a sustainable and highly efficient green corrosion inhibitor for mild steel in 3.5 wt% NaCl solution, *Journal of Molecular Liquids* **284** (2019) 682-699. https://doi.org/10.1016/j.mollig.2019.04.045
- [20] X. Gu, H. Zhang, Z. Zhang, W. Du, S. Zhu, G. Chen, Modification and Application of Walnut Peel Extract as Acidic Corrosion Inhibitor, *Journal of Biobased Materials and Bioenergy* **15(6)** (2021) 820-825. https://doi.org/10.1166/jbmb.2021.2138
- [21] M. Akin, S. Nalbantoglu, O. Cuhadar, D. Uzun, N. Saki, *Juglans regia* L. extract as green inhibitor for stainless steel and aluminium in acidic media, *Research on Chemical Intermediates* **41(2)** (2015) 899-912. https://doi.org/10.1007/s11164-013-1241-x
- [22] M. E. Rusu, I. Fizesan, A. Pop, A. Mocan, A.-M. Gheldiu, M. Babota, D. C. Vodnar, A. Jurj, I. Berindan-Neagoe, L. Vlase, D.-S. Popa, Walnut (*Juglans regia* L.) Septum: Assessment of Bioactive Molecules and In Vitro Biological Effects, *Molecules* 25(9) (2020) 2187. https://doi.org/10.3390/molecules25092187
- [23] M. E. Rusu, A.-M. Gheldiu, A. Mocan, C. Moldovan, D.-S. Popa, I. Tomuta, L. Vlase, Process Optimization for Improved Phenolic Compounds Recovery from Walnut (*Juglans regia* L.) Septum: Phytochemical Profile and Biological Activities, *Molecules* **23(11)** (2018) 2814. https://doi.org/10.3390/molecules23112814
- [24] S. E. Nataraja, T. V. Venkatesha, K. Manjunatha, B. Poojary, M. K. Pavithra, H. C. Tandon, Inhibition of the corrosion of steel in hydrochloric acid solution by some organic molecules containing the methylthiophenyl moiety, *Corrosion Science* **53(8)** (2011, 2651-2659. https://doi.org/10.1016/j.corsci.2011.05.004
- [25] E. E. El-Katori, S. Al-Mhyawi, Assessment of the *Bassia muricata* extract as a green corrosion inhibitor for aluminum in acidic solution, *Green Chemistry Letters and Reviews* **12(1)** (2019) 31-48. https://doi.org/10.1080/17518253.2019.1569728
- [26] A. Khadraoui, A. Khelifa, M. Hadjmeliani, R. Mehdaoui, K. Hachama, A. Tidu, Z. Azari, I.B. Obot, A. Zarrouk, Extraction, characterization and anti-corrosion activity of *Mentha pulegium* oil: Weight loss, electrochemical, thermodynamic and surface studies, *Journal of Molecular Liquids* **216** (2016) 724-731. https://doi.org/10.1016/j.molliq.2016.02.005
- [27] P. Kannan, P. Jithinraj, M. Natesan, Multiphasic inhibition of mild steel corrosion in H₂S gas environment, *Arabian Journal of Chemistry* **11(3)** (2018) 388-404. https://doi.org/10.1016/j.arabjc.2014.10.032
- [28] M. Kaddouri, M. Bouklah, S. Rekkab, R. Touzani, S.S. Al-Deyab, B. Hammouti, A. Aouniti, Z. Kabouche, Thermodynamic, Chemical and Electrochemical Investigations of Calixarene Derivatives as Corrosion Inhibitor for Mild Steel in Hydrochloric Acid Solution, *International Journal of Electrochemical Science* 7(9) (2012) 9004-9023. https://doi.org/10.1016/S1452-3981(23)18047-3
- [29] E.A. Noor, Temperature Effects on the Corrosion Inhibition of Mild Steel in Acidic Solutions by Aqueous Extract of Fenugreek Leaves, *International Journal of Electrochemical Science* **2(12)** (2007) 996-1017. https://doi.org/10.1016/S1452-3981(23)17129-X
- [30] C. M. Fernandes, T. da S. Ferreira Fagundes, N. Escarpini dos Santos, T. Shewry de M. Rocha, R. Garrett, R. M. Borges, G. Muricy, A. L. Valverde, E. A. Ponzio, *Ircinia strobilina*



- crude extract as corrosion inhibitor for mild steel in acid medium, *Electrochimica Acta* **312** (2019) 137-148. https://doi.org/10.1016/j.electacta.2019.04.148
- [31] X. Wang, H. Yang, F. Wang, An investigation of benzimidazole derivative as corrosion inhibitor for mild steel in different concentration HCl solutions, *Corrosion Science* **53(1)** (2011) 113-121. https://doi.org/10.1016/j.corsci.2010.09.029
- [32] X. Li, X. Xie, S. Deng, G. Du, Two phenylpyrimidine derivatives as new corrosion inhibitors for cold rolled steel in hydrochloric acid solution, *Corrosion Science* **87** (2014) 27-39. https://doi.org/10.1016/j.corsci.2014.05.017
- [33] C. Cao, On electrochemical techniques for interface inhibitor research, *Corrosion Science* **38(12)** (1996) 2073-2082. https://doi.org/10.1016/S0010-938X(96)00034-0
- [34] Y. Wang, G. Cheng, Y. Li, Observation of the pitting corrosion and uniform corrosion for X80 steel in 3.5wt.% NaCl solutions using in-situ and 3-D measuring microscope, *Corrosion Science* **111** (2016), 508-517. https://doi.org/10.1016/j.corsci.2016.05.037
- [35] Y. Qiang, L. Guo, S. Zhang, W. Li, S. Yu, J. Tan, Synergistic effect of tartaric acid with 2,6-diaminopyridine on the corrosion inhibition of mild steel in 0.5 M HCl, *Scientific Reports* **6(1)** (2016) 33305. https://doi.org/10.1038/srep33305
- [36] Z. Tao, W. He, S. Wang, G. Zhou, Electrochemical Study of Cyproconazole as a Novel Corrosion Inhibitor for Copper in Acidic Solution, *Industrial & Engineering Chemistry Research* **52(50)** (2013) 17891-17899. https://doi.org/10.1021/ie402693d
- [37] T. Vennila, T. Muneeswaran, M. Manjula, B. Stalin, J. Vairamuthu, Synergism between sodium molybdate and binary inhibitor (BHI + Zn²⁺) on corrosion inhibition of mild steel in aqueous medium containing 60 ppm Cl⁻ion, *Materials Research Express* **6(11)** (2019) 1165g6. https://doi.org/10.1088/2053-1591/ab5233
- [38] Y. Qiang, S. Zhang, B. Tan, S. Chen, Evaluation of *Ginkgo* leaf extract as an eco-friendly corrosion inhibitor of X70 steel in HCl solution, *Corrosion Science* **133** (2018) 6-16. https://doi.org/10.1016/j.corsci.2018.01.008
- [39] P. Du, S. Deng, G. Du, D. Shao, D. Xu, X. Li, Synergistic inhibition effect of *Mikania micrantha* extract with potassium iodide on the corrosion of cold rolled steel in methanesulfonic acid solution, *Corrosion Science* **220** (2023) 111296. https://doi.org/10.1016/j.corsci.2023.111296
- [40] G. Sığırcık, D. Yildirim, T. Tüken, Synthesis and inhibitory effect of N,N'-bis(1-phenylethanol)ethylenediamine against steel corrosion in HCl Media, *Corrosion Science* **120** (2017) 184-193. https://doi.org/10.1016/j.corsci.2017.03.003
- [41] Q. Wang, R. Wang, X. Sun, R. Aslam, X. Zhou, Q. Zhang, C. Zhao, Y. Sun, Z. Yan, X. Li, Protein-derived carbon dots as green corrosion inhibitors for carbon steel in sulfuric acid solution, *Diamond and Related Materials* **145** (2024) 111135. https://doi.org/10.1016/j.diamond.2024.111135
- [42] A. K. Badawi, I. S. Fahim, A critical review on green corrosion inhibitors based on plant extracts: Advances and potential presence in the market, *International Journal of Corrosion and Scale Inhibition* **10(4)** (2021) 1385-1406. https://doi.org/10.17675/2305-6894-2021-10-4-2
- [43] A. Miralrio, A. Espinoza Vazquez, Plant Extracts as Green Corrosion Inhibitors for Different Metal Surfaces and Corrosive Media: A Review, *Processes* **8(8)** (2020) 942. https://doi.org/10.3390/pr8080942
- [44] A. B. D. Nandiyanto, R. Oktiani, R. Ragadhita, How to read and interpret FTIR spectroscope of organic material, *Indonesian Journal of Science and Technology* **4(1)** (2019) 97-118. http://dx.doi.org/10.17509/ijost.v4i1.15806
- [45] D. I. Njoku, Y. Li, H. Lgaz, E. E. Oguzie, Dispersive adsorption of *Xylopia aethiopica* constituents on carbon steel in acid-chloride medium: A combined experimental and

- theoretical approach, *Journal of Molecular Liquids* **249** (2018) 371-388. https://doi.org/10.1016/j.molliq.2017.11.051
- [46] R. N. Oliveira, M. C. Mancini, F. C. Salles de Oliveira, T. M. Passos, B. Quilty, R. M. da Silva Moreira Thire, G. B. McGuinness, FTIR analysis and quantification of phenols and flavonoids of five commercially available plants extracts used in wound healing, *Revista Matēria* **21(3)** (2016) 767-779. https://doi.org/10.1590/S1517-707620160003.0072
- [47] A. Espina, M. V. Cañamares, Z. Jurasekova, S. Sanchez-Cortes, Analysis of iron complexes of tannic acid and other related polyphenols as revealed by spectroscopic techniques: Implications in the identification and characterization of iron gall inks in historical manuscripts, *ACS Omega* **7(32)** (2022) 27937-27949. https://doi.org/10.1021/acsomega.2c01679
- [48] N. Errahmany, M. Rbaa, A. S. Abousalem, A. Tazouti, M. Galai, E. H. E. Kafssaoui, M. E. Touhami, B. Lakhrissi, R. Touir, Experimental, DFT calculations and MC simulations concept of novel quinazolinone derivatives as corrosion inhibitor for mild steel in 1.0 M HCl medium, *Journal of Molecular Liquids* **312** (2020) 113413. https://doi.org/10.1016/j.molliq.2020.113413
- [49] A. Toghan, H. S. Gadow, H. M. Dardeer, H. M. Elabbasy, New promising halogenated cyclic imides derivatives as potential corrosion inhibitors for carbon steel in hydrochloric acid solution, *Journal of Molecular Liquids* **325** (2021) 115136. https://doi.org/10.1016/j.molliq.2020.115136
- [50] P. M. Natishan, E. McCafferty, G. K. Hubler, The Effect of pH of Zero Charge on the Pitting Potential, Journal of The Electrochemical Society 133(5) (1986) 1061. https://doi.org/10.1149/1.2108708
- [51] R. G. Pearson, Hard and soft acids and bases, HSAB, part II: Underlying theories, *Journal of Chemical Education* **45(10)** (1968) 643. https://doi.org/10.1021/ed045p643
- [52] X. Li, S. Deng, G. Du, X. Xie, Synergistic inhibition effect of walnut green husk extract and sodium lignosulfonate on the corrosion of cold rolled steel in phosphoric acid solution, *Journal of the Taiwan Institute of Chemical Engineers* **114** (2020) 263-283. https://doi.org/10.1016/j.jtice.2020.09.010
- [53] S. M. Sayed, H. A. E. Shayeb, The measurement of pitting corrosion currents of steel in neutral aqueous solutions, *Corrosion Science* 28(2) (1988) 153-162. https://doi.org/10.1016/0010-938X(88)90092-3
- [54] K. V. Akpanyung, R. T. Loto, Pitting corrosion evaluation: a review, *Journal of Physics: Conference Series* 1378(2) (2019) 022088. https://doi.org/10.1088/1742-6596/1378/2/022088
- [55] A. Toghan, M. Khairy, M. Huang, A. A. Farag, Electrochemical, chemical and theoretical exploration of the corrosion inhibition of carbon steel with new imidazole-carboxamide derivatives in an acidic environment, *International Journal of Electrochemical Science* **18(3)** (2023) 100072. https://doi.org/10.1016/j.ijoes.2023.100072

© 2024 by the authors; licensee IAPC, Zagreb, Croatia. This article is an open-access article distributed under the terms and conditions of the Creative Commons Attribution license (https://creativecommons.org/licenses/by/4.0/)





Open Access : : ISSN 1847-9286

www.jESE-online.org

Original scientific paper

Bidens pilosa extract as a corrosion inhibitor on 1008 carbon steel in neutral medium

José Dávila¹, Karin Paucar¹, Abel Vergara¹, Idalina V. Aoki², Keidy Cancino³ and Jesus M. Falcón^{3,⊠}

¹Corrosion Laboratory, Chemical Engineering and Textile Faculty, National University of Engineering, Av. Tupac Amaru, No. 210, Rimac, Lima, Perú

²Chemical Engineering Department, Polytechnic School, University of São Paulo, Av. Prof. Luciano Gualberto, travessa 3, no. 380, CEP 05508-010 São Paulo, Brazil

³Environmental Engineering Department, San Ignacio de Loyola University, Av. La Fontana, No. 550, La Molina, Lima, Perú

Corresponding author: [□]<u>jesus.falcon@usil.pe</u>; Tel.: +51-1-972089777; Fax: +51-1-972089777

Received: March 22, 2024; Accepted: July 8, 2024; Published: July 23, 2024

Abstract

The aim of this work is to evaluate the performance of Bidens pilosa extract as a corrosion inhibitor for 1008 carbon steel in a neutral medium of 0.1 M NaCl. The research has been accomplished by weight loss measurements, linear polarization resistance (R_p) monitoring and electrochemical impedance spectroscopy (EIS). Phytochemical analysis and Fourier transform infrared spectroscopy were performed to determine bioactive components and detect the main functional groups of Bidens pilosa extract, respectively. The morphological characterization of the substrate was carried out by optical microscopy (OM). Different isotherms were evaluated to understand more clearly the adsorption mechanism of the inhibitor extract molecules on the surface of the 1008 carbon steel substrate, and the best fit was obtained for the Langmuir isotherm. The results showed that the corrosion rate decreased with an increase of the concentration of the inhibitor up to 1000 ppm, reaching a maximum efficiency value of 82.9 % from gravimetric tests, and 73.1 % from the fitting of EIS data to an equivalent electric circuit. The calculated thermodynamic parameters suggested the formation of a monolayer of inhibitor molecules on the metal surface. The ΔG^{o}_{ads} value (-22.8 kJ mol⁻¹) determined from the Langmuir isotherm model indicated that adsorption of the inhibitor molecules on the substrate surface follows a physisorption mechanism. This research revealed that Bidens pilosa extract can be used as a corrosion inhibitor and emerges as an alternative to replace synthetic corrosion inhibitors that are harmful to health and cause damage to the environment.

Keywords

Green corrosion inhibitor, corrosion resistance; phytochemical screening; electrochemical impedance spectroscopy; adsorption isotherms

Introduction

Carbon steel is an alloy formed by Fe-C, which is widely used in the industrial field due to its low cost and a variety of useful properties suitable for numerous engineering applications [1]. It is also known that Fe-C material is very susceptible to corrosion, particularly if not alloyed with some additional elements, which implies a need to use coatings or corrosion inhibitors.

Corrosion inhibitors are chemical substances that, added in small quantities, can significantly reduce corrosion rate of a metal [1,2]. One of the main mechanisms of their action is the adsorption of inhibitor molecules on the metal surface, reducing the electrically active areas and hindering the progress of oxidation-reduction reactions [3,4]. This adsorption depends mainly on the presence of functional groups and heteroatoms such as N, O, P and S that contain lone pairs of electrons, which favour the interaction of inhibitor with the metal surface [5]. However, most of these synthetic inhibitors are expensive and highly toxic, causing harm to both humans and the environment [2,6]. Due to this drawback, researchers have been concerned with finding eco-friendly inhibitors with low or no toxicity to the environment, such as inhibitors from natural products. This class of inhibitors, called "green inhibitors" contains a variety of organic compounds, such as pigments, alkaloids, tannins, polyphenols and amino acids, where most of these substances have an effective inhibitory action. In recent years, it has been possible to find in the literature a series of investigations where the efficiency of extracts from medicinal plants in the protection of metal substrates has been verified, in most cases using acid solutions as aggressive media. However, there are still extracts that have not been studied in relation to their anticorrosive properties, which represents an opportunity to continue exploring novel inhibitors with low toxicity and low cost. For example, the extract of Ceratonia Siliqua L. seeds was tested as corrosion inhibitor of carbon steel in 1 M HCl medium, reaching an efficiency of around 95 % [7]. On the other hand, Cucumis Sativus L., with a concentration of 0.3 g L⁻¹, presented an inhibition efficiency of 92.8 % in the protection of carbon steel when immersed in 0.5 mol L-1 H₂SO₄ solution [8]. Another study was carried out on the extract from almond flowers (Prunus dulcis), where it was possible to verify the reduction in the corrosion rate of carbon steel when it was immersed in 1 M HCl solution, reaching inhibition efficiency up to 96 % [9]. A variety of recent research on the application of natural extracts as corrosion inhibitors in the protection of carbon steel and other metallic substrates can be found in the literature [10-13].

Bidens pilosa is a plant that belongs to the Asteraceae family and is native to the Americas and some parts of Africa. This plant is used in traditional medicine for the treatment of at least 40 diseases, among them are diabetes, pharyngitis, laryngitis, influence and hypertension [14,15]. The presence of bioactive components, such as tannins and flavonoids, classifies Bidens pilosa as a plant with a high potential to present considerable inhibitory properties against corrosion [14,16]. It is also important to emphasize that there is little information in the literature on the use of natural inhibitors in neutral media since most of the studies were performed in acidic media. Therefore, the novelty of this work lies in verifying the effectiveness of the Bidens pilosa extract as an inhibitor in the protection against corrosion of carbon steel in a neutral medium of 0.1 M NaCl.

The present study is focused on evaluating the potential performance of the extract from *Bidens pilosa* as a corrosion inhibitor of SAE 1008 carbon steel in the neutral medium of 0.1 M NaCl by gravimetric tests and electrochemical techniques such as linear polarization resistance and electrochemical impedance spectroscopy. Different adsorption isotherms were also analyzed to better understand the adsorption mechanism of extract molecules on the metal substrate.

Experimental

Materials and solutions

In this study, SAE 1008 carbon steel plates were used with the following composition, 0.04 % C, 0.01 % Si, 0.18 % Mn, 0.018 % P, 0.007 % S, 0.029 % Al, 0.0008 % B and 99.72 % Fe). The corrosion inhibitor used in this study was the ethanolic extract of *Bidens Pilosa*. A solution of 0.1 mol L-1 sodium chloride (NaCl) (pH 7) was used as a corrosion medium for gravimetric and electrochemical tests.

Preparation of carbon steel surface

Carbon steel samples with quadrangular geometry and cut to the dimensions of $3\times3\times0.2$ cm and treated with silicon carbide (SiC) emery papers with a grit size of 80, 220, 400 and 600 # for the removal of corrosion products. This procedure was followed by washing it with distilled water, alcohol, and acetone, and finally, it was dried in hot air.

Preparation of Bidens pilosa extract

The fresh leaves of the *Bidens pilosa* plant obtained from the Chilca district - Peru (Figure 1), were cut and separated from the stems, flowers and roots to later be dried at room temperature. The previously dried leaves passed through a grinding process to be transformed into powder, which was placed in contact with 96 % ethyl alcohol solvent for 3 days without agitation. The extract was then separated, and the process was repeated 4 times using the same leaves with the purpose of increasing the solid-liquid extraction efficiency. In order to concentrate the extract, an evaporation process was carried out at 45 °C and at reduced pressure (1.38×10⁴ Pa) in an equipment called BUCHI R-100 rotary evaporator for a period of 4 h. The resulting extract was finally used to prepare five different concentrations in the range of 350 ppm to 1750 ppm in a neutral 0.1 mol L-1 NaCl solution.

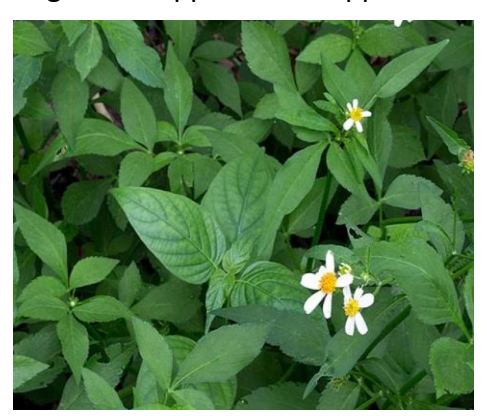


Figure 1. Leaves of the Bidens pilosa plant

Phytochemical screening

A phytochemical is a term that refers to a variety of compounds produced naturally in plants. They are classified into six main types based on their chemical structure and properties. These include carbohydrates, lipids, phenols, terpenoids, alkaloids and other nitrogen-containing compounds. Phytochemicals are mainly classified into primary and secondary metabolites. Phytochemical analysis is a qualitative analytical study that, by certain standardized procedures, can be used to determine the main constituents of a plant extract [17]. Thin layer chromatography (TLC) is a technique generally used to analyse the number and types of components present in a mixture. In TLC, the extracts are loaded in a glass coated with silica gel or other adsorbent, which is then kept in a chromatographic chamber containing a suitable running solvent. This technique mainly consists of a mobile phase and a stationary phase, separating the compounds based on their polarity [18].

Weight loss measurements

For the gravimetric tests, previously sanded and cleaned SAE 1008 carbon steel plates were used, which were cut to the dimensions of $40\times10\times2$ mm and weighed on an analytical balance (Sartorius, Model TE214S) with 0.1 mg precision. Next, the plates were immersed in the 0.1 M NaCl solution in the presence and absence of *Bidens pilosa* extract. Five concentrations of *Bidens pilosa* extract were prepared (350, 700, 1000, 1400 and 1750 ppm) and the immersion time of the samples was 15 days. After this time, they were removed from the immersion, cleaned with a soft brush and washed with distilled water, alcohol, acetone, and then dried and weighed. The tests were carried out in an aerated solution, not stirred, and in duplicate.

Electrochemical tests

In order to evaluate the inhibition efficiency of the *Bidens pilosa* extract, electrochemical techniques such as measurements of open circuit or corrosion potential (E_{oc}), polarization resistance (R_p) and electrochemical impedance spectroscopy (EIS) were used. The inhibitor concentrations evaluated were 350, 700, 1000, 1400 and 1750 ppm in the neutral medium of 0.1 M NaCl. The tests were carried out in a three-electrode electrochemical cell, where Ag|AgCl|KCl_{sat} was used as the reference electrode, a graphite electrode as the counter electrode and a working electrode (SAE 1008 carbon steel) with exposed area of 1.085 cm². Electrochemical impedance measurements were performed after 60 min of immersion in the 0.1 M NaCl solution to achieve a steady-state potential. A sinusoidal potential perturbation with an amplitude of 10 mV (root mean square) was used in relation to the open circuit potential and a frequency range of 10 kHz to 10 mHz with 10 measurements for each frequency decade. Linear polarization resistance measurements were obtained at room temperature and after EIS measurements, with a scan rate value of 0.167 mV s⁻¹ and scan potential range of -0.01 V < η < +0.01 V, relative to the open circuit potential. All tests were carried out on a Gamry Interface 1010 B potentiostat/galvanostat controlled by Gamry Framework software.

Morphological characterization

The morphological characterization of the surface of the metal substrate in the absence and presence of the inhibitor was carried out by an optical microscope ZEISS Axio Lab. A1, with the help of the ZEN software.

Infrared spectroscopy

The infrared spectroscopy analyzes were carried out on a Bruker Alpha II model, operating in ATR mode and with the help of the OPUS software. The spectrum was obtained at room temperature in the range of 4000 to 400 cm⁻¹.

Results and discussion

Phytochemical analysis

The results of the phytochemical constituents of the ethanolic extract of *Bidens pilosa* are shown in Table 1. Based on the results obtained, it can be observed that the *Bidens pilosa* extract mainly contains compounds such as alkaloids, tannins, reducing sugars, phenols, and in smaller amounts, anthocyanins, lactones, flavonoids and cardenolides. On the other hand, the presence of saponins and amino acids could not be detected. However, the finding of these main bioactive organic compounds reveals the inhibitory characteristics of the *Bidens pilosa* extract due to the presence of potential functional groups and long chains of high molecular weight, which are absorbed on the

surface of the substrate. Thus, the adsorbed film forms a protective barrier against the aggressive environment. Similar results were also found in the literature for the protection of aluminum in an acid medium using *Bidens pilosa* extract as corrosion inhibitor [16].

One of the main drawbacks in the use of plant extracts as corrosion inhibitors is the difficulty of identifying the main active component responsible for the inhibitory action due to the complex matrix of the plant extract. However, the synergism of several of these bioactive components contained in the extract was reached, effectively inhibiting the corrosion of the substrate [19].

Phytochemical groups	Result
Anthocyanins	++
Alkaloids	+++
Lactones	++
Flavonoids	++
Cardenolides	++
Tannins	+++
Reducing sugars	+++
Phenols	+++
Saponins	-
Aminoacids	_

Table 1. Phytochemical analysis of the ethanolic extract of Bidens pilosa

+++: very obvious reaction; ++: obvious reaction; -: no reaction

Fourier transform infrared spectroscopy

Fourier transform infrared spectroscopy (FTIR) is a powerful analytical tool that allows determination of the main chemical functional groups contained in a natural or synthetic sample. Figure 2 represents the FTIR spectrum of the liquid extract of *Bidens pilosa* where the most representative absorption peaks were identified.

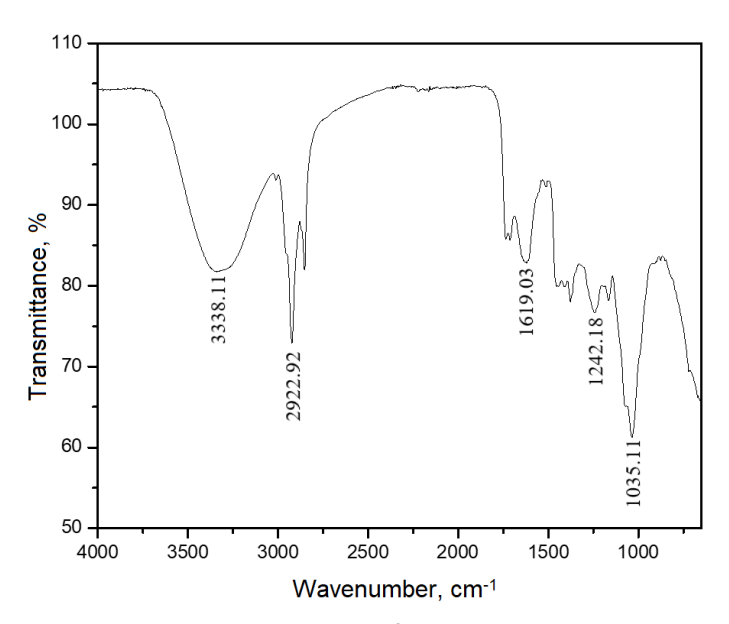


Figure 2. FTIR spectrum of Bidens pilosa extract

The first broad and strongly pronounced peak around 3338.11 cm⁻¹ can be attributed to a tension vibration between the O-H group bonds and could correspond to the presence of simple phenolic compounds and tannins [1,13,20-22], which is confirmed by phytochemical analysis (Table 1). The peaks located around 2922.92 and 1619.03 cm⁻¹, can be attributed to tension vibrations of the -CH and C=C groups, respectively, due to the presence of aromatic rings as part of the flavonoid structure

or alkaloids [20,23,24]. The peak at 1242.18 cm⁻¹ is related to the vibration of the C-N group and finally, the peak located at 1035.11 cm⁻¹ can be attributed to the C-O group [25].

According to the results of the analysis by FTIR, it was possible to detect the presence of heteroatoms such as C, N and O, which belong to different functional groups found in the structure of the *Bidens pilosa* extract and which are responsible for the corrosion inhibition process on metal substrates. In the literature, it is possible to find several research works on natural inhibitors where the presence of these heteroatoms is reported [4,26-29].

Weight loss measurements

The results of the gravimetric tests were obtained by immersing 1008 carbon steel samples for a period of 15 days in 0.1 M NaCl solution in the absence and presence of different concentrations of *Bidens pilosa* extract. Important parameters such as corrosion rate (C_R), inhibition efficiency (η) and degree of surface coverage (θ) were obtained from this gravimetric study and are presented in Table 2. The corrosion rate expressed in mm year⁻¹ (1 mm year⁻¹ = 39.37 mpy (mils per year)) was calculated using Equation (1), where ΔW / g is the change in mass, A /cm² is the total area exposed to the solution, D is density of the metal equal to 7.86 g cm⁻³, t / h is immersion time in the solution and K is a conversion factor equal to 8.76x10⁴.

$$C_{\rm R} = K \left(\frac{\Delta W}{ADt} \right) \tag{1}$$

The inhibition efficiency was calculated using Equation (2) where C_{Ro} is corrosion rate in the absence of an inhibitor and C_{Ri} is corrosion rate in the presence of an inhibitor. The degree of surface coverage θ was calculated based on the inhibition efficiency values using Equation (3).

$$\eta = \frac{\left(C_{\text{Ro}} - C_{\text{Ri}}\right)}{C_{\text{Ro}}} 100 \tag{2}$$

$$\theta = \frac{\eta}{100} \tag{3}$$

Table 2. Corrosion rate, inhibition efficiency and degree of coverage calculated from gravimetric tests for SAE 1008 carbon steel during immersion time of 15 days in 0.1 M NaCl in the absence and presence of different concentrations of Bidens pilosa extract

Concentration of inhibitor (ppm)	C _R / mpy	C _R / mm year ⁻¹	η/%	θ
0.0 (blank)	3.1233 ± 0.012	0.0793 ± 0.0003	-	-
350.0	1.321 + 0.011	0.0336 ± 0.0002	57.7	0.577
700.0	0.584 ± 0.008	0.0148 ± 0.0002	81.3	0.8129
1000.0	0.531 ± 0.013	0.0135 ± 0.0003	83.0	0.8299
1400.0	0.604 ± 0.014	0.0153 ± 0.0004	80.7	0.8067
1750.0	0.670 ± 0.001	0.0170 ± 0.00003	78.5	0.7854

The results presented in Table 2 show an increase in the inhibition efficiency up to the maximum value of 83.0 %, obtained for the inhibitor concentration of 1000 ppm. As seen in the FITR analysis, this can be attributed to the presence of *Bidens pilosa* extract molecules on the surface of the substrate, generating a protective barrier layer that inhibits the corrosion process. Similar results were also reported in the literature for the protection of carbon steel using natural corrosion inhibitors [24,27].

Furthermore, the degree of coverage also increases with the *Bidens pilosa* extract concentration, which indicates a possible increase in the adsorption effectiveness of the *Bidens pilosa* extract

molecules on the substrate surface. However, for the last two concentrations (1400 ppm and 1750 ppm) a slight increase in the corrosion rate is observed (Figure 3).

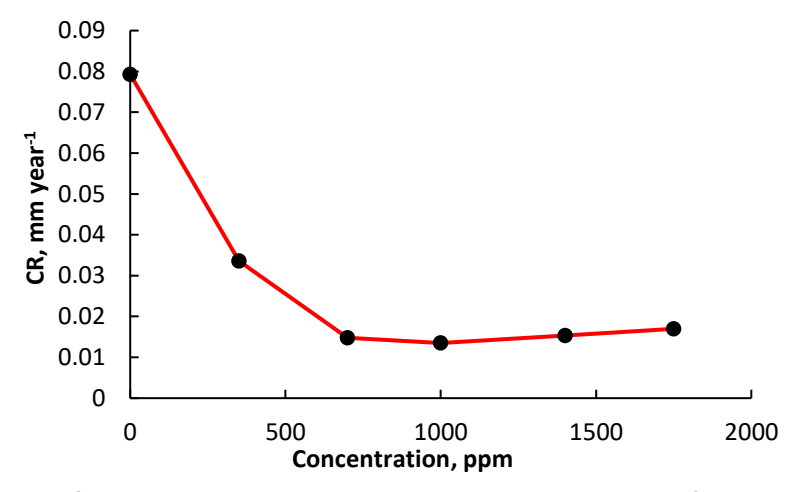


Figure 3. Corrosion rate of 1008 carbon steel immersed in a neutral solution of 0.1 M NaCl from gravimetric tests at different concentrations of Bidens pilosa extract

A possible explanation for this fact is related to the repulsive forces between the inhibitor molecules which causes a desorption of the inhibitor. Therefore, the unprotected sites are formed, that are prone to corrosion and generate an increase in corrosion rate values [27,30]. Other investigations argue that when high amounts of inhibitor are added, the adsorption on the surface of the substrate is perpendicular due to the repulsion between molecules and this generates unprotected sites since the parallel adsorption of the inhibitor molecules normally covers a greater area of the substrate [27]. For higher concentrations of inhibitor molecules beyond the optimal one, some of the adsorbed and self-assembled inhibiting molecules undergo a kind of disorder provoked by repulsive interactions among them, diminishing the inhibitor efficiency.

Open circuit potential

Open circuit potential (OCP) measurements for carbon steel 1008 were carried out during 3600 s of immersion time in 0.1 M NaCl solution in the absence and presence of different concentrations of *Bidens pilosa* extract. In Figure 4 it is possible to observe the same trend of decreasing potential for all inhibitor concentrations in reaching steady state values at longer immersion time.

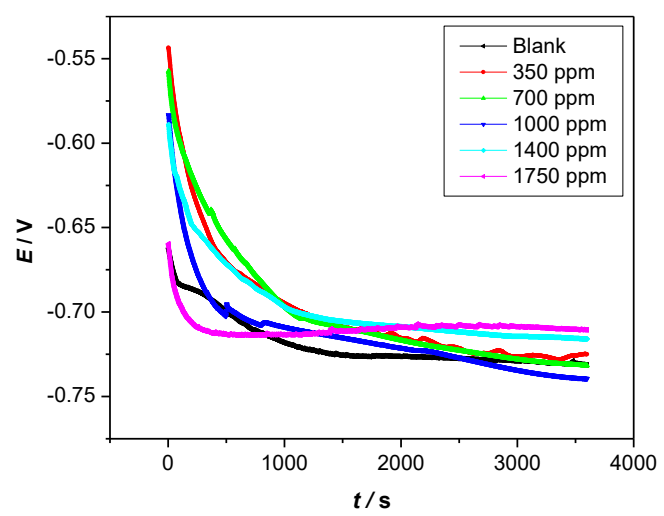


Figure 4. Time changes of open circuit potential for 1008 carbon steel in 0.1 M NaCl solution in the absence and presence of different concentrations of Bidens pilosa extract

For the concentrations of 350, 700 and 1000 ppm the steady state was reached in approximately 3300 s, while for other concentrations of 1400 and 1750 ppm the stabilization time was shorter, reaching a steady-state value within approximately 1500 s. The addition of the inhibitor to the corrosive medium changes the behaviour of the OCP, leading to more positive steady-state potentials in the case of 1400 and 1750 ppm, and to the most negative potential for the concentration of 1000 ppm. It is known that when the differences in the corrosion potential values in relation to the blank are at least 85 mV, the inhibitor can be classified as a cathodic or anodic type inhibitor for negative or positive differences, respectively. A mixed type of inhibitor is assumed for slight differences, less than 85 mV [28,30,31], as this would be the case in present experiments.

Electrochemical impedance spectroscopy

Figure 5 represents the Nyquist (a) and Bode ((b) and (c)) plots for 1008 carbon steel in 0.1 M NaCl solution in the absence and presence of different concentrations of *Bidens pilosa* inhibitor extract. In all Nyquist diagrams, the presence of a single capacitive arc was observed, indicating that the corrosion kinetics is controlled by the charge transfer resistance and the corrosion mechanism is not affected by the presence of the inhibitor [9,25,32,33]. It is also possible to observe an increase in the diameters of capacitive arcs up to a concentration value of 1000 ppm, which indicates an increase in the charge transfer resistance due to the formation of adsorbed film on the metal surface with protective properties against corrosion [1,8,30,34].

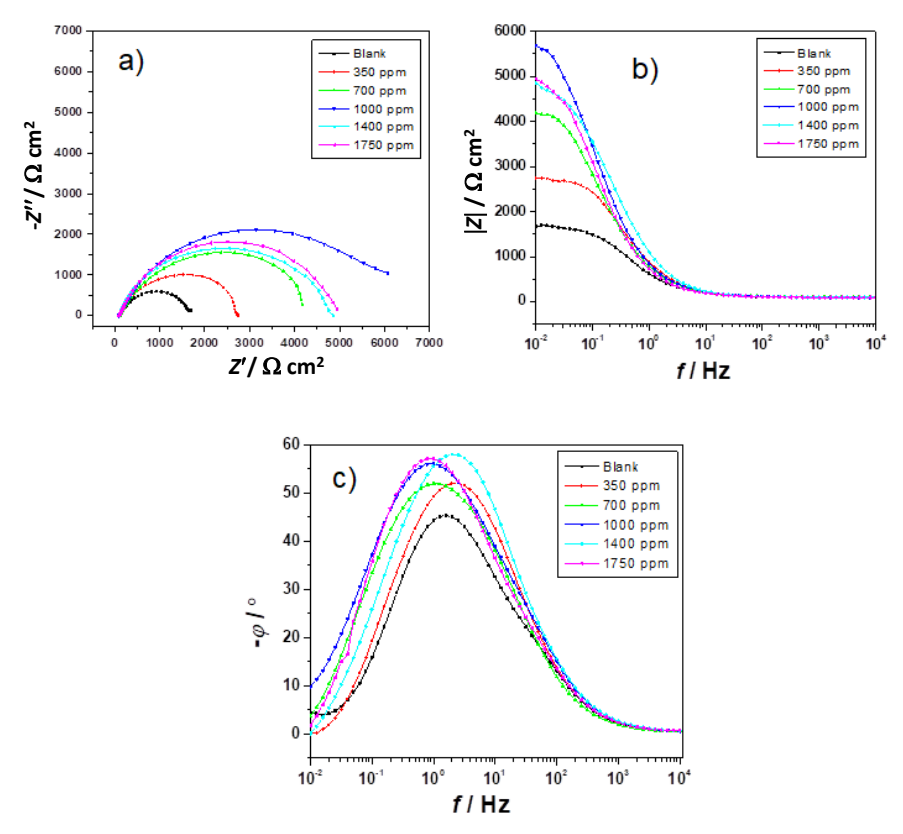


Figure 5. Nyquist (a) and Bode (b) and (c) diagrams for 1008 carbon steel in 0.1 M NaCl solution in the absence and presence of different concentrations of Bidens pilosa extract

In relation to the Bode modulus diagrams (Figure 5b), it is possible to observe that at low frequencies, there is an increase in the value of the impedance modulus as the concentration of the inhibitor increases up to 1000 ppm and then there is a decay of impedance modulus values as the concentration of the inhibitor is further increased. It is important to mention that the Bode phase

diagrams in Figure 5c, show the presence of a single time constant for all the conditions studied, which is related to the formation of an electrical double layer at the metal-solution interface [13,25].

The values obtained in the electrochemical impedance measurements were fitted to an equivalent electric circuit with the objective of obtaining the electrochemical parameters and, thus, quantitatively comparing the effects of the different concentrations of the *Bidens pilosa* extract in the protection of 1008 carbon steel. Figure 6 represents the classic Randles equivalent circuit, which was used to simulate the metal/electrolyte system, where $R_{\rm S}$ corresponds to the resistance of the electrolyte, $R_{\rm ct}$ is the resistance to charge transfer in parallel with the capacitance of the electrical double layer represented by a constant phase element (CPE_{dl}). The consideration of a CPE is due to the inhomogeneities found in the steel surface. This equivalent circuit has already been found in the literature to fit properly EIS data for studies of different corrosion inhibitors [7,13,35,36].

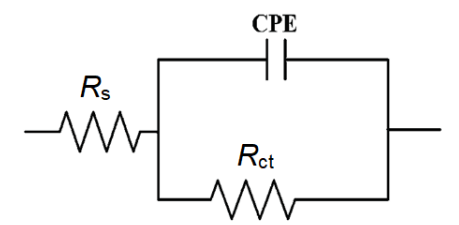


Figure 6. Equivalent electrical circuit used to fit EIS data of carbon steel in 0.1 M NaCl solution in the absence and presence of different concentrations of Bidens pilosa extract

The CPE_{dl} element was introduced to replace the pure capacitor representing the electrical double layer. The impedance of CPE_{dl} is expressed mathematically according to Equation (4) [1,30,32,33,37].

$$Z_{\text{CPE}} = Y_0 (j\omega)^{-\alpha} \tag{4}$$

In Equation (4) Y_0 is the constant parameter of CPE_{dl}, ω the angular frequency, j^2 is equal to -1 and α is the dispersion factor, which values are between 0 and 1. Previous studies have reported that the value of α can inform on different physical defects on the metal surface, such as surface inhomogeneity, impurities, inhibitor adsorption, formation of layers with porosity, *etc.* [26,30,37,38].

The impedance parameter values obtained from the adjustment of the EIS data to the proposed equivalent circuit are presented in Table 3. The χ^2 values were also calculated to provide support for the adjustment made. The χ^2 values were mostly lower than 10⁻³, indicating a good fit for the proposed equivalent circuit [25,32].

Table 3 shows that the values of α range between 0.749 and 0.808, which leads to using a CPE_{dl} and not a pure capacitor. In relation to the R_{ct} values, it is possible to observe an increase as the inhibitor is added to the solution, where the maximum R_{ct} value was obtained for a concentration of 1000 ppm of inhibitor. This behaviour is related to an increase in the degree of coverage of the substrate due to the inhibitor molecules adsorption, indicating a decrease in the area exposed to the corrosive medium due to the displacement of water molecules and/or chloride ions by the inhibitor molecules [21,28,39]. The inhibition efficiency (IE) values shown in Table 3 were calculated using Equation (5), where $R_{ct,0}$ is the charge transfer resistance in the absence of an inhibitor and R_{ct} represents the charge transfer resistance in the presence of the inhibitor.

$$IE = \frac{R_{\rm ct} - R_{\rm ct,o}}{R_{\rm ct}} 100 \tag{5}$$

Table 3. Corrosion parameters obtained from fits of EIS data (Fig. 5) to Randles equivalent circuit model (Fig. 6) for 1008 carbon steel immersed in 0.1 M NaCl solution in the absence and presence of different concentrations of Bidens pilosa extract

C (ppm)	$R_{\rm s}$ / Ω cm ²	$R_{ m ct}/\Omega{ m cm}^2$	CPE _{dl} , μF cm ⁻² s ^(α-1)	α	χ^2	IE, %	θ
Blank	103.00	1587	381.6×10 ⁻⁶	0.766	7.399×10 ⁻⁴	-	-
350	93.84	2636	251.0×10 ⁻⁶	0.794	4.248×10 ⁻⁴	39.8	0.398
700	99.60	4303	330.8×10 ⁻⁶	0.749	7.035×10 ⁻⁴	63.1	0.631
1000	112.10	5894	301.0×10 ⁻⁶	0.774	1.365×10 ⁻⁴	73.1	0.731
1400	92.30	4443	207.2×10 ⁻⁶	0.806	4.148×10 ⁻⁴	64.2	0.642
1750	105.80	4632	323.8×10 ⁻⁶	0.808	1.908×10 ⁻³	65.7	0.657

Based on the inhibition efficiency values determined by Equation (5), it is possible to observe that the efficiencies were in the range of 39.8 to 73.1 %, where the best result (73.1 %) was achieved for the concentration of 1000 ppm of inhibitor. It is interesting to mention that for the conditions studied (neutral NaCl medium), an efficiency value greater than 70 % was determined, which, according to what is reported in the literature, is the minimum value that all types of corrosion inhibitors must show to be considered as effective [1,25,32,40]. It is important to stress that EIS results are in close agreement with weight loss measurements.

Linear polarization resistance measurements

Linear polarization resistance (R_p) measurements were obtained after 80 min of immersion of the 1008 carbon steel substrate in 0.1 M NaCl solution in the absence and presence of different concentrations of the *Bidens pilosa* extract. The corrosion rate expressed in mm year⁻¹ was calculated using Equation (6), where i_{corr} / A is the corrosion current, Eq_{metal} /g is the equivalent weight of the metal, A / cm² is the total area exposed to the solution, D is the density of the metal equal to 7.86 g cm⁻³ and K' is conversion factor equal to 3.27×10³.

$$C_{\rm R} = K' \left(\frac{i_{\rm corr} E q_{\rm metal}}{AD} \right) \tag{6}$$

The value of the corrosion current (i_{corr}) is obtained by the Stern-Geary Equation (7):

$$i_{corr} = \frac{b_{a} |b_{c}|}{2.3(b_{a} + |b_{c}|)} \frac{1}{R_{p}}$$
 (7)

where the values of b_a and b_c are Tafel slopes, whose values are 0.12 V decade⁻¹.

Figure 7 shows the experimental measurements of R_p , adjusted to straight lines with the purpose of obtaining slopes that represent the values of R_p . It is seen that for the solution containing 1000 ppm of *Bidens pilosa* extract, a higher polarization resistance ($R_p = 7070.96 \Omega$) compared to the other concentrations is obtained, which is due to the barrier effect caused by the adsorption of inhibitor molecules on the surface of carbon steel.

In relation to Table 4, which summarizes measured polarization resistance values, it is possible to observe an increase in the value of the polarization resistance and, therefore, a decrease in the corrosion rate as the concentration of *Bidens pilosa* extract in the 0.1 M NaCl solution increases up to 1000 ppm concentration. For higher concentration values (1400 and 1750 ppm), the R_p value began to decrease due to the inhibitor's low corrosion protection efficiency.

This fact can be attributed to the change in orientation that some adsorbed *Bidens pilosa* extract molecules may have from the flat or parallel to a vertical orientation (>1000 ppm). This reorientation causes some parts of the substrate to be exposed to the aggressive solution and causes an increase in the corrosion rate and, consequently, a decrease in the polarization resistance [24].

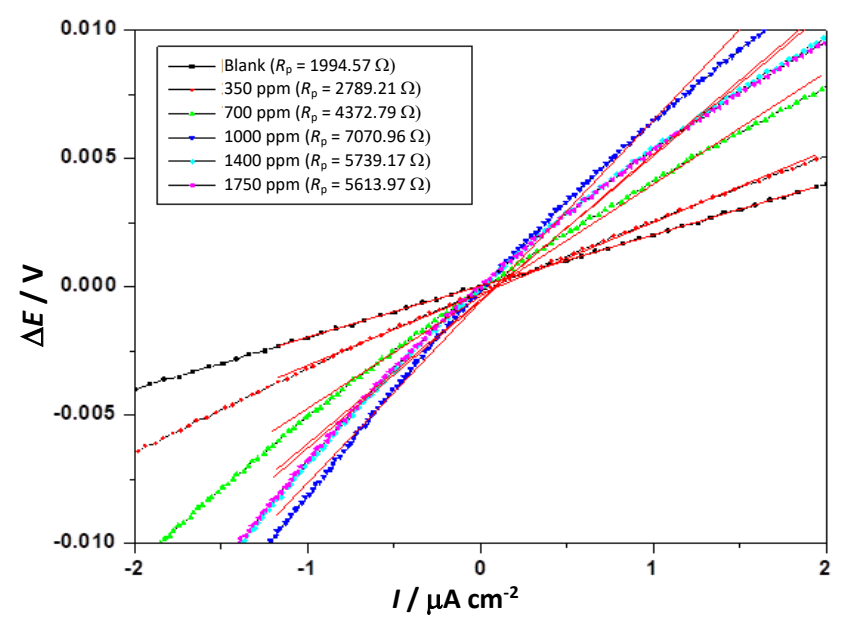


Figure 7. Linear polarization resistance measurements (R_p) for carbon steel in 0.1 M NaCl solution in the absence and presence of different concentrations of Bidens pilosa extract

It is important to highlight that the results obtained from R_p follow a similar trend to those obtained in the mass loss and electrochemical impedance spectroscopy tests, confirming the inhibitory properties of *Bidens pilosa* extract on the 1008 carbon steel substrate.

Table 4. Polarization resistance and corrosion rate values of 1008 carbon steel obtained from R_p measurements after 80 min immersion in 0.1 M NaCl solution in the absence and presence of different concentrations of Bidens pilosa extract

Concentration of inhibitor, ppm	$R_{ m p}/\Omega$	C_R / mpy	C _R / mm year ⁻¹	IE, %
0.0 (blank)	1994.57 ± 117.33	5.51 ± 0.38	0.14 ± 0.01	-
350.0	2789.21 ± 610.14	3.94 ± 0.89	0.10 ± 0.02	28.5
700.0	4372.79 ± 406.77	2.51 ± 0.26	0.06 ± 0.01	54.4
1000.0	7070.96 ± 1584.87	1.55 ± 0.35	0.04 ± 0.01	71.8
1400.0	5739.17 ± 1291.31	1.91 ± 0.42	0.05 ± 0.01	65.2
1750.0	5613.97 ± 249.51	1.96 ± 0.07	0.05 ± 0.002	64.5

Adsorption isotherms

The use of adsorption isotherms is a very useful tool to understand the adsorption mechanism of the inhibitor on the surface of carbon steel in the aggressive medium. Generally, values around -20 kJ mol⁻¹ or less negative are related to electrostatic interactions between the inhibitor molecules and the charged surface of the metal (physisorption) and those values around -40 kJ mol⁻¹ or more negative involve a sharing or transfer of charge from the inhibitor molecules towards the metal surface to form coordinated covalent type bonds [25,41,42].

Several isotherm models exist, such as Temkin, Freundlich and Langmuir, but the latter is the most frequently used [9]. In this model, it is assumed that the inhibitor molecules occupy a single active site on the metal surface and that there is no interaction between neighbouring molecules. Equation (8) represents the Langmuir isotherm model

$$\frac{C}{\theta} = \frac{1}{k_{\text{ads}}} + C \tag{8}$$

where C, k_{ads} and θ are the concentration of the inhibitor, the equilibrium constant of the adsorption process and the covered surface of the metal, respectively.

Figure 8 was plotted with the values of concentration (expressed in g L⁻¹) and θ obtained from Table 2 corresponding to the gravimetric tests, which fits perfectly to a straight line with a value of R^2 = 0.9868, proving that the adsorption of the inhibitor follows the Langmuir model ($C/\theta vs. C$) due to the adsorption of a monolayer of inhibitory molecules on the surface of carbon steel [19]. The value of the equilibrium constant (k_{ads}) was determined from the intercept of the Langmuir isotherm at the y axis is 9.94 L g⁻¹, where this k_{ads} value obtained suggests strong adsorption of the *Bidens pilosa* extract molecules on the substrate surface. k_{ads} shows the interaction strength between the adsorbate and adsorbent in the electrolyte. Higher values of k_{ads} indicate effective adsorption of inhibitor molecules on the metal surface and high inhibition efficiency [28,34,43].

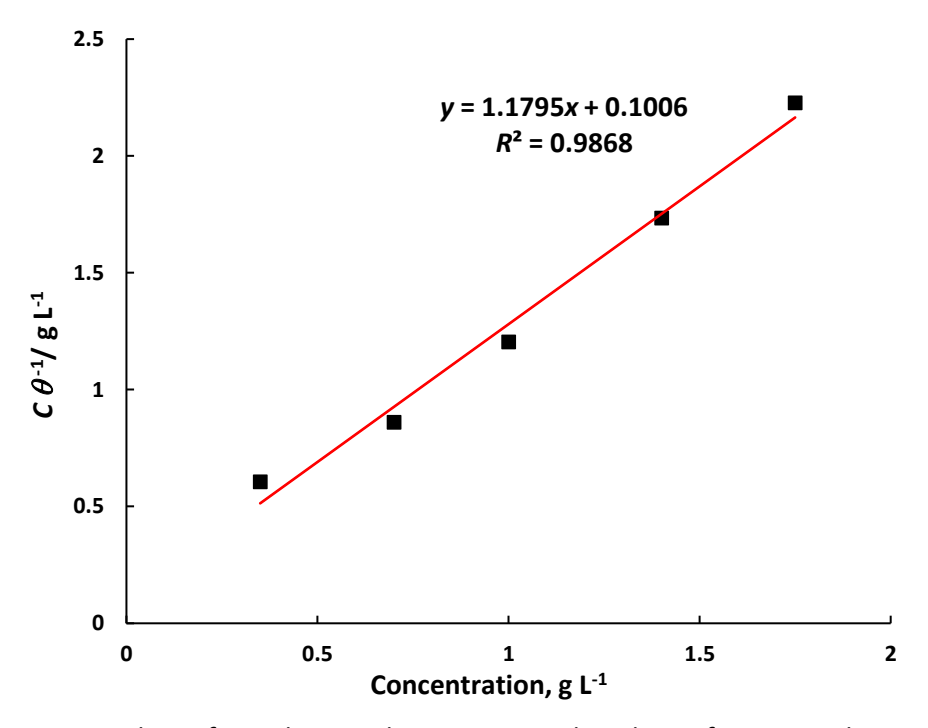


Figure 8. Langmuir isotherm for carbon steel 1008 in neutral medium of 0.1 M NaCl containing different concentrations of Bidens pilosa extract

With the value of the adsorption constant k_{ads} the Gibbs free energy of adsorption (ΔG^{o}_{ads}) was determined using Equation (9) [25]:

$$\Delta G^0_{ads} = -RT \ln(C_{H_2O} k_{ads}) \tag{9}$$

where T is the absolute temperature of the system under study, R is the universal gas constant (8.3147 J mol⁻¹ K⁻¹), C_{H2O} is the concentration of water, and its value is 1000 g L⁻¹ (55.5 mol L⁻¹) [25]. Substituting all needed values into Equation (9), a value of ΔG^{o}_{ads} = -22.8 kJ mol⁻¹ is obtained. The negative value of the Gibbs adsorption free energy indicates that the inhibitor molecules spontaneously adsorb on the surface of the carbon steel. On the other hand, it can be observed that the value of ΔG^{o}_{ads} is around -20 kJ mol⁻¹, indicating that the inhibitory molecules coming from functional groups contained in the *Bidens pilosa* extract and being responsible for the decrease in the corrosion rate are physically adsorbed on the surface of the substrate [44].

In the case of the Freundlich and Temkin isotherms, the fitting was also carried out with θ values taken from Table 2, and the results are presented in Table 5, where the correlation coefficient values (R^2) were far from 1 (0.6092 and 0.5925, respectively), and therefore they will not be considered for this particular study.

Isotherms	Equations	Linear fit and correlation coefficient (R ²)
Langmuir (C/Auc. C)	$C/\theta = 1/k + C$	C/θ = 0.1006 + 1.1795C
Langmuir (C/θ vs. C)	C/ 0 - 1/K + C	$R^2 = 0.9868$
Fraundlish (log (lug log C)	log 0-1/k + /1/n) log C	$\log \theta$ = -0.1133 + 0.1876 $\log C$
Freundlich (log θ vs. log C)	$Log \theta = 1/k_f + (1/n) log C$	$R^2 = 0.6092$
Tambin (Over lag C)	0 12 202/5) 5 - 1	θ = 0.7754 + 0.2935 log <i>C</i>
Temkin (θ vs. log C)	θ = (-2.303/a) log k + (-2.303/a) log C	$R^2 = 0.5925$

Table 5. Parameters obtained for different adsorption isotherms

The results in Table 5 clearly show that the Langmuir isotherm presented the highest correlation coefficient value (0.9868) compared to the Freundlich (0.6092) and Temkin (0.5925) isotherms. In the literature, it is possible to find other studies using natural corrosion inhibitors for the protection of carbon steel where the adsorption mechanism was adequately adjusted to the Langmuir isotherm model [9,19,45,46].

Morphological characterization

In Figure 9, the surface of the 1008 carbon steel before immersion in the solution of 0.1 M NaCl is presented, where it is possible to see the scratches produced by the grinding process.

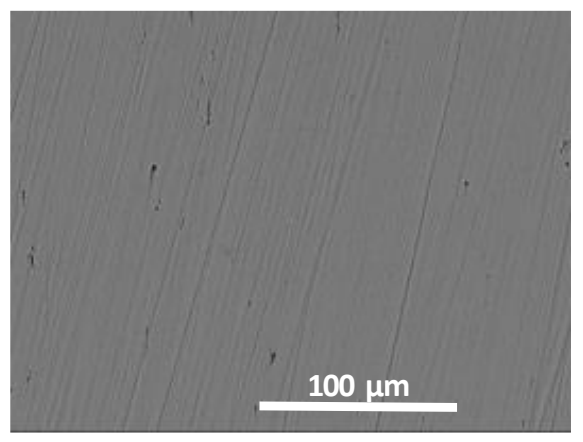
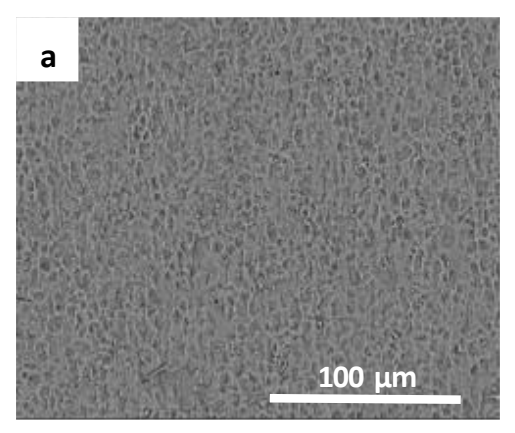


Figure 9. Micrograph for carbon steel 1008 before the immersion in the electrolyte

Figure 10a shows the appearance of the carbon steel surface after 60 min of immersion in the electrolytic solution in the absence of the inhibitor. In this condition, it is possible to observe a rough surface due to the drastic attack of the corrosive medium. In contrast, Figure 10b shows a surface with little corrosion products on the sample surface and no attack morphology even after 60 min of immersion. The few spots accentuated in Figure 10b can be associated with previous defects on the steel surface, and the inhibitor was adsorbed all over the steel surface, which forms an efficient protective film on the substrate.

Table 6 compares the efficiencies already obtained with the *Bidens pilosa* extract in relation to the efficiencies obtained using commercial phosphate-based inhibitors for carbon steel in NaCl neutral medium. As can be seen from Table 6, the majority of these commercial inhibitors present a higher efficiency compared to the *Bidens pilosa* extract, but it is important to highlight that our inhibitor is of the natural type and not synthetic, biodegradable and less harmful to health and environment. Another important detail to mention about Table 6 is that the commercial inhibitors chosen to compare the inhibition efficiencies were phosphate-based because the media in which they were tested were also neutral. Most commercial inhibitors present a better performance in an acidic medium than in a neutral medium and in the literature, there is not much information on inhibitors that can present high inhibitor efficiency when the medium is neutral.



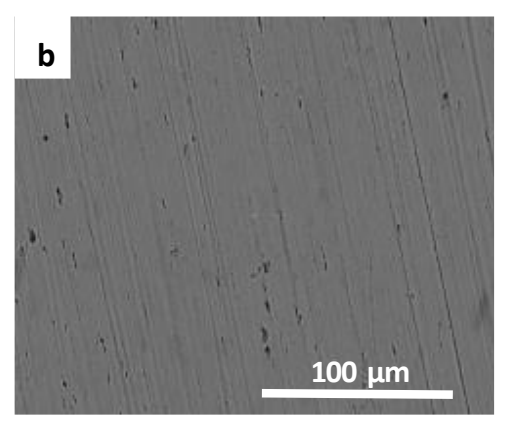


Figure 10. Micrographs for carbon steel 1008 after immersion in the electrolyte, in the absence (a) and in the presence of Bidens pilosa extract inhibitor (b)

Table 6. Efficiencies obtained from EIS measurements for commercial phosphate-based inhibitors on carbon steel in NaCl solutions

Inhibitor	Concentration	Immersion solution	Type of inhibition	IE, %	Ref.
Bidens pilosa extract	1000 ppm	0.1 M NaCl	Mixed	73.1	-
Na ₃ PO ₄ .12H ₂ O	0.4 mol per kg	3.5 wt.% NaCl	Cathodic	95	[47]
Na ₃ PO ₄ .12H ₂ O	7 %	0.5 M NaCl	Mixed	95.9	[48]
Na ₃ PO ₄	0.6 M	0.6 M NaCl	Cathodic	88.6	[49]
Bis(2-ehylhexyl) phosphate (BEP)	500 ppm	1 wt.% NaCl	-	93.07	[50]

Conclusions

- According to the results obtained, it is possible to conclude that the *Bidens pilosa* extract is a potential and eco-friendly corrosion inhibitor for carbon steel 1008 in 0.1 M NaCl.
- The phytochemical analysis showed the presence of bioactive organic compounds, which confer that *Bidens pilosa* extract has inhibitory properties against corrosion.
- Gravimetric test results showed that the inhibition efficiency increases to a maximum value of 83.0 % for an optimal inhibitor extract concentration of 1000 ppm. The results of electrochemical impedance spectroscopy and polarization resistance (R_p) measurements also confirmed this trend, reaching maximum efficiency values of 73.1 and 75.6 % respectively.
- The thermodynamic study showed that the molecules of the *Bidens pilosa* extract are physically adsorbed (physisorption) on the surface of the carbon steel substrate due to the interaction of the heteroatoms such as carbon, nitrogen and oxygen found in the analyses by FITR.
- The adsorption process obeys the Langmuir isotherm, which assumes that each site is occupied by only one molecule of the inhibitor.
- The images obtained by optical microscopy indicate the reduction of the corrosive process in the presence of the *Bidens pilosa* extract.

Acknowledgements: The authors would like to acknowledge to USIL for the financial support provided through the special research project 040-2022-01-PID and to the Corrosion Laboratory of Chemical Engineering and Textile Faculty of UNI for the support provided in the electrochemical tests and the characterization tests. The author also acknowledges to National Counsel of Technological and Scientific Development (CNPq), Brazil, for research grant to Idalina V. Aoki (Process nr. 308564/2023-50).

References

- [1] A. De Mendonça Santos, T. F. De Almeida, F. Cotting, I. V. Aoki, H. G. De Melo, V. R. Capelossi, Evaluation of castor bark powder as a corrosion inhibitor for carbon steel in acidic media, *Materials Research* **20** (2017) 492-505. https://doi.org/10.1590/1980-5373-MR-2016-0963
- [2] G. Khan, K. M. Salim Newaz, W. Jefrey Basirun, H. Binti, M. Ali, F. L. Faraj, G. M. Khan, Application of Natural Product Extracts as Green Corrosion Inhibitors for Metals and Alloys in Acid Pickling Processes, *International Journal of Electrochemical Science* **10** (2015) 6120-6134. https://doi.org/10.1016/S1452-3981(23)06707-X
- [3] M. Belkhaouda, L. Bammou, R. Salghi, A. Zarrouk, E. E. Ebenso, H. Zarrok, B. Hammouti, K. Morocco, Inedible Avocado Extract: An Efficient Inhibitor of Carbon Steel Corrosion in Hydrochloric Acid, *International Journal of Electrochemical Sci*ence **8** (2013) 10987-10999. https://doi.org/10.1016/S1452-3981(23)13164-6
- [4] A. M. Salim, N. M. Dawood, R. Ghazi, Pomegranate Peel Plant Extract as Potential Corrosion Inhibitor for Mild Carbon Steel in a 1 M HCl Solution, *IOP Conference Series: Materials Science and Engineering* **987** (2020) 012019. https://doi.org/10.1088/1757-899X/987/1/012019
- [5] A. Rodríguez-Torres, M. G. Valladares-Cisneros, C. Cuevas-Arteaga, M.A. Veloz-Rodríguez, Study of Green Corrosion Inhibition on AISI 1018 Carbon Steel in Sulfuric Acid Using *Crataegus mexicana* as Eco-Friendly Inhibitor, *Journal of Materials and Environmental Sciences* 10 (2019) 101-112. https://www.jmaterenvironsci.com/Document/vol10/vol10 N2/12-JMES-Rodri%CC%81guez-Torres-2019.pdf
- [6] R. S. A. Hameed, G. M. S. Aleid, D. Mohammad, M. M. Badr, B. Huwaimel, M. S. Suliman, F. Alshammary, M. Abdallah, *Spinacia oleracea* Extract as Green Corrosion Inhibitor for Carbon Steel in Hydrochloric Acid Solution, *International Journal of Electrochemical Sci*ence **17** (2022) 221017. https://doi.org/10.20964/2022.10.31
- [7] S. Abbout, D. Chebabe, M. Zouarhi, M. Rehioui, Z. Lakbaibi, N. Hajjaji, *Ceratonia Siliqua* L seeds extract as eco-friendly corrosion inhibitor for carbon steel in 1 M HCl: Characterization, electrochemical, surface analysis, and theoretical studies, *Journal of Molecular Structure* 1240 (2021) 130611. https://doi.org/10.1016/j.molstruc.2021.130611
- [8] L. Feng, S. Zhang, L. Hao, H. Du, R. Pan, G. Huang, H. Liu, Cucumber (*Cucumis sativus* L.) Leaf Extract as a Green Corrosion Inhibitor for Carbon Steel in Acidic Solution: Electrochemical, Functional and Molecular Analysis, *Molecules* **27** (2022) 3826. https://doi.org/10.3390/molecules27123826
- [9] S. Lahmady, O. Anor, I. Forsal, H. Hanin, K. Benbouya, Electrochemical Examination of an Eco-friendly Corrosion Inhibitor "Almond Flower Extract" for Carbon Steel in Acidic Medium (1 M HCl), Analytical and Bioanalytical Electrochemistry 14 (2022) 303-318. https://www.abechem.com/article 251274.html
- [10] A. Sabea, Iraqi orange peel extract inhibits corrosion of metallic alloys in hydrochloric acid solution, *Journal of Engineering Science and Technology* **15** (2020) 3433-3448. https://jestec.taylors.edu.my/Vol%2015%20issue%205%20October%202020/15 5 40.pdf
- [11] F. Kaya, R. Solmaz, İ.H. Geçibesler, The Use of *Rheum Ribes* (Işgın) Extracts for Copper Protection in Acidic Media, *Turkish Journal of Nature and Science* **11** (2022) 94-101. https://doi.org/10.46810/tdfd.1166367
- [12] T. A. Salman, M. Sabri, C. Taghried, A. Salman, Pomegranate Peel Extract as Green Corrosion Inhibitor for α-Brass in 2M HCl Solution, *Journal of Materials Science and Surface Engineering* 5 (2017) 597-601. https://www.jmsse.in/files/545 Mustafa Sabri Cheyad et al.PDF
- [13] A. F. Shoair, M. M. A. H. Shanab, M. H. H. Mahmoud, Z. I. Zaki, H. M. Abdel-Ghafar, M. M. Motawea, Investigation on Effects of Avocado Extract as Eco-friendly Inhibitor for 201

- Stainless Steel corrosion in Acidic Environment, *International Journal of Electrochemical Sci*ence **17** (2022) 220642. https://doi.org/10.20964/2022.06.31
- [14] D. C. Bilanda, P. D. D. Dzeufiet, L. Kouakep, B. F. O. Aboubakar, L. Tedong, P. Kamtchouing, T. Dimo, *Bidens pilosa* Ethylene acetate extract can protect against L-NAME-induced hypertension on rats, *BMC Complementary Alternative Medicine* **17** (2017) 479. https://doi.org/10.1186/s12906-017-1972-0
- [15] D. V. Mtenga, A. S. Ripanda, A review on the potential of underutilized Blackjack (*Biden Pilosa*) naturally occurring in sub-Saharan Africa, *Heliyon* **8** (2022) E09586. https://doi.org/10.1016/j.heliyon.2022.e09586
- [16] K. K. Alaneme, B. Osasona, E. A. Okotete, S. J. Olusegun, U. Donatus, Corrosion Inhibition Behaviour of Biden Pilosa Extract on Aluminium Matrix Composites in 1 M HCl Solution, *The Journal of the Association of Professional Engineers of Trinidad and Tobago* 44 (2016) 35-42. https://www.researchgate.net/publication/311495204 Corrosion Inhibition Behaviour of Biden Pilosa Extract on Aluminium Matrix Composites in 1M HCl Solution
- [17] D. S. H. S. Peiris, D. T. K. Fernando, S. P. N. N. Senadeera, C.B. Ranaweera, Phytochemical Screening for Medicinal Plants: Guide for Extraction Methods, *Asian Plant Research Journal* 11 (2023) 13-34. https://doi.org/10.9734/aprj/2023/v11i4216
- [18] P. Srivastava, M. Singh, G. Devi, R. Chaturvedi, Herbal Medicine and Biotechnology for the Benefit of Human Health, *Animal Biotechnology: Models in Discovery and Translation* **30** (2013) 563-575. https://doi.org/10.1016/B978-0-12-416002-6.00030-4
- [19] A. M. Santos, I.P. Aquino, F. Cotting, I. V. Aoki, H. G. de Melo, V.R. Capelossi, Evaluation of Palm Kernel Cake Powder (*Elaeis guineensis Jacq.*) as Corrosion Inhibitor for Carbon Steel in Acidic Media, *Metals and Materials International* **27** (2021) 1519-1530. https://doi.org/10.1007/s12540-019-00559-x
- [20] S. J. Olusegun, M. Bodunrin, S. Aribo, S. J. Olusegun, T. S. Joshua, M. O. Bodunrin, S. Aribo, Inhibition of mild steel corrosion in HCl solution by plant extract of *Biden pilosa*, *Nature and Science* **16** (2018) 1-8. https://doi.org/10.7537/marsnsj160118.01
- [21] X. Wang, H. Jiang, D. X. Zhang, L. Hou, W. J. Zhou, *Solanum lasiocarpum* L. extract as green corrosion inhibitor for A3 steel in 1 M HCl solution, *International Journal of Electrochemical Sci*ence **14** (2019) 1178-1196. https://doi.org/10.20964/2019.02.06
- [22] N. Hossain, M.A. Chowdhury, M. Rana, M. Hassan, S. Islam, *Terminalia arjuna* leaves extract as green corrosion inhibitor for mild steel in HCl solution, *Results in Engineering* **14** (2022) 100438. https://doi.org/10.1016/j.rineng.2022.100438
- [23] M. Alimohammadi, M. Ghaderi, A. Ramazani S. A. M. Mahdavian, *Falcaria vulgaris* leaves extract as an eco-friendly corrosion inhibitor for mild steel in hydrochloric acid media, *Scientific Reports* **13** (2023) 3737. https://doi.org/10.1038/s41598-023-30571-6
- [24] M. A. Deyab, M. M. Osman, A. E. Elkholy, F. El-Taib Heakal, Green approach towards corrosion inhibition of carbon steel in produced oilfield water using lemongrass extract, RSC Advances 7 (2017) 45241-45251. https://doi.org/10.1039/c7ra07979f
- [25] M. C. F. De Carvalho, N. M. S. De Almeida, I. M. F. C. R. Silva, F. Cotting, I. V. Aoki, V. R. Capelossi, Electrochemical and Economic Evaluation of the Cocoa Bean Shell as a Corrosion Inhibitor in Acidic Medium, *Materials Research* 25 (2022) e20210125. https://doi.org/10.1590/1980-5373-MR-2021-0125
- [26] A. Rodríguez-Torres, O. Olivares-Xometl, M. G. Valladares-Cisneros, J. G. González-Rodríguez, Effect of green corrosion inhibition by *Prunus persica* on AISI 1018 carbon steel in 0.5 M H₂SO₄, *International Journal of Electrochemical Sci*ence **13** (2018) 3023-3049. https://doi.org/10.20964/2018.03.40
- [27] O. Sotelo-Mazon, S. Valdez, J. Porcayo-Calderon, M. Casales-Diaz, J. Henao, G. Salinas-Solano, J.L. Valenzuela-Lagarda, L. Martinez-Gomez, Corrosion protection of 1018 carbon



- steel using an avocado oil-based inhibitor, *Green Chemistry Letters and Reviews* **12** (2019) 255-270. https://doi.org/10.1080/17518253.2019.1629698
- [28] H. Mobtaker, M. Azadi, N. Hassani, M. Neek-Amal, M. Rassouli, M. A. Bidi, The inhibition performance of quinoa seed on corrosion behavior of carbon steel in the HCl solution; theoretical and experimental evaluations, *Journal of Molecular Liquids* **335** (2021) 116183. https://doi.org/10.1016/j.molliq.2021.116183
- [29] Z. Xia, X. Zhang, Study on Corrosion Resistance of Carbon Steel in HF/HCl Acid Mixture in Presence of *Lycoris radiata* and *Lycoris chinensis* Leaf Extract as Environmentally Friendly Corrosion Inhibitor, *International Journal of Electrochemical Science* **17** (2022) 220921. https://doi.org/10.20964/2022.09.20
- [30] G. Salinas-Solano, J. Porcayo-Calderon, L. M. Martinez de la Escalera, J. Canto, M. Casales-Diaz, O. Sotelo-Mazon, J. Henao, L. Martinez-Gomez, Development and evaluation of a green corrosion inhibitor based on rice bran oil obtained from agro-industrial waste, *Industrial Crops and Products* **119** (2018) 111-124. https://doi.org/10.1016/j.indcrop.2018.04.009
- [31] M. S. Al-Otaibi, A. M. Al-Mayouf, M. Khan, A. A. Mousa, S. A. Al-Mazroa, H. Z. Alkhathlan, Corrosion inhibitory action of some plant extracts on the corrosion of mild steel in acidic media, *Arabian Journal of Chemistry* 7 (2014) 340-346. https://doi.org/10.1016/j.arabjc.2012.01.015
- [32] M. E. S. de Jesus, A. de M. Santos, M. S. Tokumoto, F. Cotting, I. P. Aquino, V. R. Capelossi, Evaluation of efficiency of avocado seed powder (*Persea Americana*) as a corrosion inhibitor in SAE 1008 carbon steel in acidic medium, *Brazilian Journal of Development* **6** (2020) 77197-77215. https://doi.org/10.34117/bjdv6n10-227
- [33] N. M. S. de Almeida, I. M. F. C. R. e Silva, B. P. da Silva, F. Cotting, I. V. Aoki, T. C. Veloso, V. R. Capelossi, Use of the hydrodistillation residue of the essential oil of pink pepper (*Schinus terebinthifolius Raddi*) in the corrosion protection of carbon steel in HCl medium, *Research, Society and Development* 11 (2022) e433111335797. https://doi.org/10.33448/rsd-v11i13.35797
- [34] Z. Golshani, H. C. Moezabad, M. Amiri, G. S. Sajadi, R. Naghizade, S. M. A. Hosseini, Effect of *Thyme* extract as an ecofriendly inhibitor for corrosion of mild steel in acidic media, *Materials and Corrosion* **73** (2022) 460-469. https://doi.org/10.1002/maco.202112769
- [35] A. Berrissoul, A. Ouarhach, F. Benhiba, A. Romane, A. Guenbour, B. Dikici, F. Bentiss, A. Zarrouk, A. Dafali, Assessment of corrosion inhibition performance of origanum compactum extract for mild steel in 1 M HCl: Weight loss, electrochemical, SEM/EDX, XPS, DFT and molecular dynamic simulation, *Industrial Crops and Products* **187** (2022) 115310. https://doi.org/10.1016/j.indcrop.2022.115310
- [36] O. S. Shehata, A. H. A. Fatah, H. Abdelsalm, A. M. Abdel-Karim, Crispy Dry Chili Extract as an Eco-Friendly Corrosion Inhibitor for Mild Steel in Chloride Solutions: Experimental and Theoretical Studies, *Journal of Bio-and Tribo-Corrosion* **8** (2022) 97. https://doi.org/10.1007/s40735-022-00691-z
- [37] G. A. De Oliveira, V. M. Teixeira, J. N. da Cunha, M. R. dos Santos, V. M. Paiva, M. J. C. Rezende, A. F. do Valle, E. D'Elia, Biomass of Microalgae *Chlorella Sorokiniana* as Green Corrosion Inhibitor for Mild Steel in HCl Solution, *International Journal of Electrochemical Sci*ence **16** (2021) 210249. https://doi.org/10.20964/2021.02.42
- [38] A. D. Arulraj, J. Prabha, R. Deepa, B. Neppolian, V. S. Vasantha, Effect of components of solanum trilobatum-L extract as corrosion inhibitor for mild steel in acid and neutral medium, *Materials Research Express* **6** (2019) 036527. https://doi.org/10.1088/2053-1591/aaf267

- [39] M.A. Bidi, M. Azadi, M. Rassouli, A new green inhibitor for lowering the corrosion rate of carbon steel in 1 M HCl solution: *Hyalomma* tick extract, *Materials Today Communications* **24** (2020) 100996. https://doi.org/10.1016/j.mtcomm.2020.100996
- [40] R. W. Revie, H.H. Uhlig, *Corrosion and corrosion control: An Introduction to Corrosion Science and Engineering*, 4th ed., Wiley-Interscience, New Jersey, 2008, pp. 15-19. ISBN: 978-0-471-73279-2
- [41] Z. Zipeng, Y. Yan, Z. Gao, Betel Nut Shell Water Extract as a Green Corrosion Inhibitor for Q235 Steel in 1 M HCl, International Journal of Electrochemical Science 17 (2022) 221151. https://doi.org/10.20964/2022.11.47
- [42] R. S. A. Hameed, G. M. S. Aleid, D. Mohammad, M. M. Badr, B. Huwaimel, M.S. Suliman, F. Alshammary, M. Abdallah, *Spinacia oleracea* Extract as Green Corrosion Inhibitor for Carbon Steel in Hydrochloric Acid Solution, *International Journal of Electrochemical Sci*ence **17** (2022) 221017. https://doi.org/10.20964/2022.10.31
- [43] D. K. Verma, F. Khan, Corrosion inhibition of mild steel in hydrochloric acid using extract of glycine max leaves, *Research on Chemical Intermediates* **42** (2016) 3489-3506. https://doi.org/10.1007/s11164-015-2227-7
- [44] I. Ekemini, A. Onyewuchi, J. Abosede, Evaluation of performance of corrosion inhibitors using adsorption isotherm models: an overview, *Chemical Science International Journal* **18** (2017) 1-34. http://dx.doi.org/10.9734/CSJI/2017/28976
- [45] L. A. Al Juhaiman, A. A. Mustafa, W. K. Mekhamer, Polyvinyl Pyrrolidone as a Green Corrosion Inhibitor of Carbon Steel in Neutral Solutions Containing NaCl: Electrochemical and Thermodynamic Study, *International Journal of Electrochemical Sci*ence **7** (2012) 8578-8596. https://doi.org/10.1016/S1452-3981(23)18017-5
- [46] E. A. Flores-Frias, V. Barba, M. A. Lucio-Garcia, R. Lopez-Cecenes, J. Porcayo-Calderon, J.G. Gonzalez-Rodriguez, Use of Curcuma and curcumin as a green corrosion inhibitor for carbon steel in sulfuric acid, *International Journal of Electrochemical Science* **14** (2016) 5026-5041. https://doi.org/10.20964/2019.06.53
- [47] J. J. Shi, W. Sun, Effects of phosphate on the chloride-induced corrosion behavior of reinforcing steel in mortars, *Cement and Concrete Composites* **45** (2014) 166-175. https://doi.org/10.1016/j.cemconcomp.2013.10.002
- [48] L. Yohai, M. B. Valcarce, M. Vázquez, Testing phosphate ions as corrosion inhibitors for construction steel in mortars, *Electrochimica Acta* **202** (2016) 316-324. https://doi.org/10.1016/j.electacta.2015.12.124
- [49] A. Mohamed, U. Martin, D. M. Bastidas, Adsorption and Surface Analysis of Sodium Phosphate Corrosion Inhibitor on Carbon Steel in Simulated Concrete Pore Solution, *Materials* **15** (2022) 7429. https://doi.org/10.3390/ma15217429
- [50] J. Hu, Q. Xiong, L. Chen, C. Zhang, Z. Zheng, S. Geng, et al. Corrosion inhibitor in CO₂-O₂-containing environment: Inhibition effect and mechanisms of Bis(2-ehylhexyl) phosphate for the corrosion of carbon steel, *Corrosion Science* **179** (2021) 109173. https://doi.org/10.1016/j.corsci.2020.109173





Open Access :: ISSN 1847-9286 www.jESE-online.org

Original scientific paper

Development of electrode by using gold-platinum alloy nanoparticles for electrochemical detection of serum amyloid A protein

Kalpana Ladi and Aditya Sharma Ghrera[⊠]

The NorthCap University, Applied Science Department, Gurugram, Haryana, India, 122017 Corresponding author:

□ adityasghrera@gmail.com

Received: August 23, 2023; Accepted: February 11, 2024; Published: April 29, 2024

Abstract

Gold-platinum alloy nanoparticles (AuPtNP) were electrochemically deposited on the surface of indium-tin-oxide (ITO) modified with (3-aminopropyl)triethoxysilane (APTES), after optimizing deposition conditions for the electroplating solution and number of deposition cycles. Different part ratios of Au/Pt used were 4/0, 3/1, 2/2, 1/3 and 0/4 (AuNP, Au_3Pt_1 , Au_2Pt_2 , Au_1Pt_3 and PtNP, respectively) in preparation of 1 mM solutions. FE-SEM, EDAX and XRD surface characterization techniques were used to confirm the presence of deposited AuPt alloy nanoparticles on the modified ITO surface. Electrochemical methods (CV, DPV and EIS) were used to investigate the electrochemical properties of prepared electrodes in the presence of ferri/ferrocyanide redox couple, which indicated the following increasing order of electrocatalytic peak current: $Au < Au_2Pt_2 < Pt < Au_1Pt_3 < Au_3Pt_1$. The most active electrode, $Au_3Pt_1NP/APTES/ITO$ (with Au/Pt part ratio 3:1), was further used to fabricate the immunoelectrode SAA-Ab/Au₃Pt₁NP/APTES/ITO. The prepared immunoelectrode was tested for detection of serum amyloid A protein biomarker (APO-SAA) by immobilising SAA-specific antibodies (SAA 1/2 Ab) on its surface. Sensing studies on this immunoelectrode, performed by DPV technique, revealed the SAA biomarker detection in the linear range of 10 to 10^6 fg ml⁻¹. The limit of detection was calculated as 7.0 fg ml⁻¹.

Keywords

Electrochemical biosensing; bimetallic nanoparticles; electrocatalysts; immunoelectrode; inflammatory biomarker

Introduction

Bimetallic nanoparticles have gained great attention due to their unique catalytic efficiency, low cost, high stability, high electronic and optical properties. The presence of the second metal affects many parameters of prepared alloys like particle size, composition alterations, shape, surface morphologies, chemical and physical properties of materials, including catalytic activities and selectivity. Bimetallic nanoparticles of platinum and gold have proven their extraordinary electrocatalytic properties and are used for various applications, including fuel cells and biosensing [1-4].

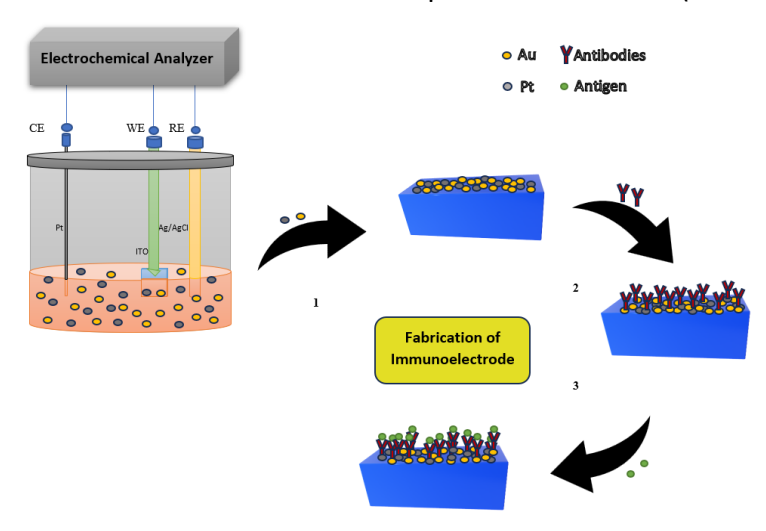
Pt with outstanding electrocatalytic properties and Au with more electronegativity and less reactivity produce synergistic catalytic effects due to their interaction in their alloy [5-7]. The greater availability of gold at a lower price than platinum favors this combination of metal nanoparticles to tap the benefits of both in one alloy besides reducing the cost of preparation of electrode [8-11]. Electrochemical deposition of Au-Pt nanoparticles is a simple, easy, and direct method to fabricate electrodes with AuPtNP alloy film.

Indium tin oxide (ITO) has a wide range of applications and can be used in fields such as biosensors, transistors, electroluminescence devices, light-emitting diodes, solar cells and displays. Its surface can be modified in different ways to enhance its electrocatalytic activity [5,12,13]. Due to high transparency, excellent electrical conductivity and large conducting surface area, ITO has wide potential to be used as a working electrode for electrochemical deposition of AuPtNP alloy film. As it can be easily etched and patterned, electrochemical biosensors can be fabricated using modified ITO surfaces to detect various biomolecules of interest [12].

Serum amyloid A (SAA) protein, an inflammatory biomarker, has recently gained attention as its concentration in human serum increases manifolds immediately after viral infection in the human body, which helps in the early detection of viral diseases. Its concentration may increase many times its original concentration and decrease at a faster rate during recovery from the infection [14-16]. Fabricating an electrochemical biosensor to detect biomarkers is easy, cost-effective, less time-consuming, and non-invasive as compared with the other techniques to detect SAA biomarker. These biosensors are sensitive, reproducible, reliable, selective, and stable towards target biomolecules and hence possess wide potential in clinical diagnosis [17,18].

Xia et al. reported SAA electrochemical immunoassay [19] to detect SAA as a chronic inflammatory biomarker, while Lee et al. reported the fabrication of anodic aluminum oxide (AAO) chip for the detection of SAA 1 as a lung cancer biomarker [20]. Antibody array-based immunosensor was developed by Timucin et al. [21] to detect SAA as a cardiovascular disease biomarker, [11,22] presented the detection of SAA as a renal cell carcinoma biomarker in their report. SAA as an inflammatory rheumatic disease biomarker and for allograft rejection was reported by Sorić Hosman et al. [23], while SAA as a prominent acute phase reactant biomarker was reported by Malle et al. [16].

In the present manuscript, electrochemical deposition condition parameters were firstly optimized for the alloy of gold-platinum nanoparticles (AuPtNP) on the ITO surface. AuPtNP hybrids were electrochemically deposited on the ITO surface with different part ratios of Au and Pt salts in the electrolyte. Electrode with part ratio 3:1 for Au and Pt, respectively (Au₃Pt₁NP) was found to be of greater electrocatalytic activity and was further used to detect SAA biomarker by immobilizing antibodies on the surface of the optimized electrode (Scheme 1).



Scheme 1. Scheme for fabrication of SAA-Ab/AuPtNP/APTES/ITO immunoelectrode

The procedures for modification of ITO surface with APTES, preparation of electrolytic solutions and antibody immobilization have already been reported in our previous works [24,25].

Experimental

Chemicals and reagents

Hexachloroplatinic acid hexahydrate ($H_2PtCl_6\cdot 6H_2O$) was purchased from SRL (Sisco Research Laboratories) and hydrogen tetrachloroaurate(III) ($HAuCl_4\cdot 3H_2O$) was purchased from CDH. (3-aminopropyl)triethoxysilane (APTES) (Himedia make), SAA $^1/_2$ antibodies (Affinity Biosciences), and Prospec make serum amyloid A protein (APO-SAA) were used. Solution of 100 mM PBS (pH 7.4) containing 5 mM [Fe(CN)6] $^{3-/4-}$ was prepared by using 0.2 M sodium phosphate dibasic dihydrate ($Na_2HPO_4\cdot 2H_2O$) and 0.2M sodium phosphate monobasic dihydrate ($NaH_2PO_4\cdot 2H_2O$) on 100 ml ultrapure water along with adding 0.9 % NaCl. For 5 mM [Fe(CN)6] $^{3-/4-}$, 0.211 g of potassium ferrocyanide and 0.165 g of potassium ferricyanide were added to the 100 ml PBS solution prepared. Other chemicals were supplied and prepared, as reported previously [24,25].

Instrumentation

For electrochemical deposition and characterization, an advanced Metrohm potentiostat/gal-vanostat 204 was used with a three-electrode system [24,25] containing Ag/AgCl/3 M KCl reference electrode and Pt wire as a counter electrode. Electrochemical characterization techniques used were cyclic voltammetry (CV), electrochemical impedance spectroscopy (EIS) and differential pulse voltammetry (DPV) in 100 mM PBS buffer solution with 0.9 % NaCl and 5 mM [Fe(CN) $_6$]^{3-/4-} (pH 7.4). EIS measurements were performed using alternating signal amplitude of 10 mV, dc potential of 0.03 V and frequency range of 10 5 to 0.1 Hz.

For morphological characterization of AuPtNP-modified electrodes, FE-SEM (JEOL JSM-7610F Plus with attached EDX analysis tool) was Shimadzu UV2600sed. A 20 kV operation voltage was used over a collection period of 164 seconds to obtain the EDX spectrum. To determine the crystalline structures of the deposits, an X-ray diffraction (XRD) analyzer (Rigaku SmartLab StudioII, λ = 0.1541 nm, Cu K α radiation) was used. UV measurements were performed by Shimadzu UV2600 spectrophotometer.

Optimization of electrochemical deposition parameters for AuPtNP deposition on ITO surface

AuPtNP were deposited electrochemically from two different solutions (labelled as solution A and B, both containing platinum salts $H_2PtCl_6\cdot 6H_2O$ and $HAuCl_4\cdot 3H_2O$) on the surface of ITO with and without its modification with APTES. The CV technique was applied in the potential range of -0.6 to 1.0 V and a scan rate of 100 mV s⁻¹ for 20 cycles. Only slight changes were observed in redox peak currents after depositing AuPtNP for more than 60 cycles on the electrode surface.

AuPtNP were first deposited on ITO surface (with/without modification with APTES) from solution A (0.01 M Na₂SO₄, 0.01 M H₂SO₄ and 1 mM total concentration of H₂PtCl₆·6H₂O and HAuCl₄·3H₂O), and then from solution B (0.05 M PBS (pH 7.0) and 1 mM total concentration of H₂PtCl₆·6H₂O and HAuCl₄·3H₂O) [26]. The procedure for cleaning and modification of bare ITO electrodes of size 1×1 cm² with APTES was reported in previous works [24,25], along with a procedure for solution condition optimization.

Fabrication of different AuPtNP/APTES/ITO electrodes

To optimize Au and Pt metal salt proportion in deposition solution, AuPt nanoparticles were electrochemically deposited for 60 cycles on APTES/ITO electrodes from solution A containing noble metal salts of Au/Pt in different part ratios of 4:0, 3:1, 2:2, 1:3 and 0:4, respectively (with their total

molar concentration in deposition solution taken as 1mM) (Table 1). The corresponding electrodes are denoted as AuNP/APTES/ITO, $Au_3Pt_1NP/APTES/ITO$, $Au_2Pt_2NP/APTES/ITO$, $Au_1Pt_3NP/APTES/ITO$ and PtNP/APTES/ITO, respectively.

Table 1. Detailed information about the Au and Pt salts concentrations used for the deposition
of AuPTNP on APTES/ITO electrodes

Terminology adopted	Part of actual concentration of metallic salt (out of 1 mM concentration) in the electrolyte solution (Au salt + Pt salt)	Concentrations of metallic salts in 20 ml solution (Au salt + Pt salt), mM	Molar ratio of salts in solution
4:0	4:0	1.0 + 0.0	1:0
0:4	0:4	0.0 + 1.0	0:1
2:2	2:2	0.5 + 0.5	1:1
3:1	3:1	0.75 + 0.25	3:1
1:3	1:3	0.25 + 0.75	1:3

Results and discussion

Electrochemical characterization of variously deposited AuPtNP on ITO and APTES/ITO electrodes

AuPtNP (Au₂Pt₂) deposited for 20 cycles on bare ITO and APTES/ITO electrodes from solutions A and B were characterized by CVs recorded at 50 mV/s scan rate within -0.5 to 1.0 V potential range in 100 mM PBS buffer solution containing 5 mM [Fe(CN)₆]^{3-/4-} (Figure 1a). The highest redox peak current was obtained for the AuPtNP/APTES/ITO electrode when AuPt nanoparticles were deposited from solution A. The reason for this could be easier electrochemical deposition in acidic conditions containing H_2SO_4 .

Characterization of bare ITO and APTES/ITO modified with Au, Pt and AuPt metal nanoparticles was performed using CVs (at 50 mV/s scan rate and -0.6 V to 1.5 V potential range) in 0.05 M H₂SO₄ (Figure 1b) for electrodes AuNP/APTES/ITO, Au₂Pt₂NP/APTES/ITO and PtNP/APTES/ITO. The reduction peaks were observed at potentials 0.61 and 0.02 V for electrodes AuNP/APTES/ITO and PtNP/APTES/ITO, respectively. For electrode AuPtNP/APTES/ITO, two reduction peaks were observed at potentials 0.57 V and 0.07 V, corresponding to deposited AuNP and PtNP. These two peaks confirm the deposition of two noble metal alloy nanoparticles on ITO [27].

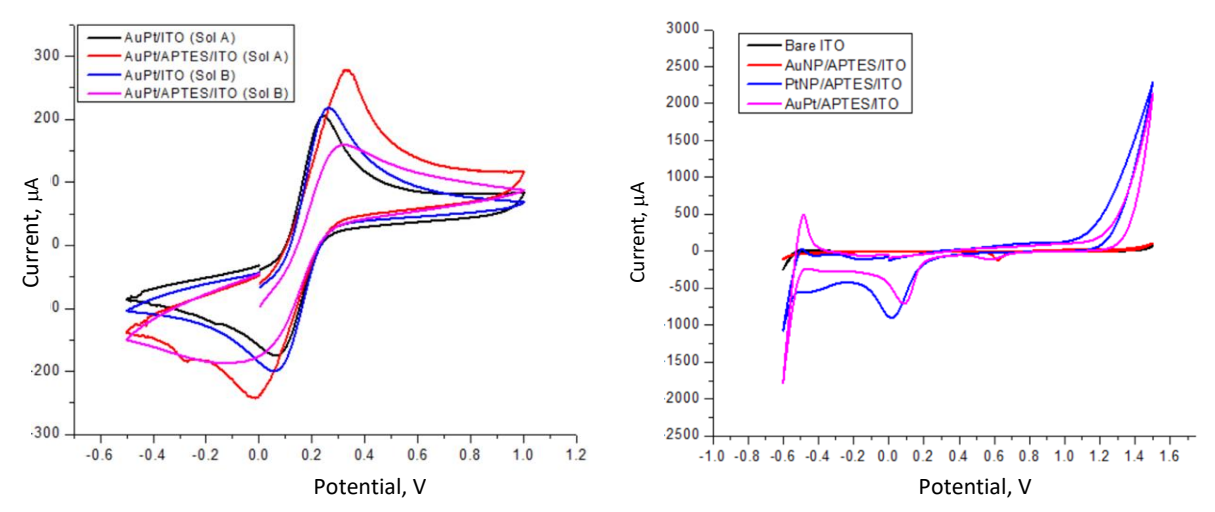


Figure 1. CVs (50 mV s⁻¹) of: (a) AuPtNP (Au₂Pt₂) on ITO (with/without APTES on ITO surface) electrochemically deposited from solutions A and B for 20 cycles, recorded in 100 mM PBS, pH 7.4 containing 5 mM [Fe(CN)₆]^{3-/4-}; (b) bare ITO, AuNP/APTES/ITO, PtNP/APTES/ITO and AuPtNP/APTES/ITO recorded in 0.05 M H₂SO₄ (AuNP, PtNP, AuPtNP deposited for 20 cycles from solution A on APTES/ITO)

Since the highest oxidation and reduction peak currents due to ferricyanide/ferrocyanide redox reaction were obtained for the APTES-modified ITO with AuPtNP deposited from solution A, solution A has been used throughout this study for deposition of AuPtNP.

FE-SEM and EDX (including elemental X-ray mapping) of deposited AuPt nanoparticles

FE-SEM surface morphological studies were conducted for $Au_2Pt_2NP/APTES/ITO$, $Au_1Pt_3NP/APTES/ITO$ and $Au_3Pt_1NP/APTES/ITO$ electrodes [1]. Electrodes with deposition of alloys of metal nanoparticles, $Au_2Pt_2NP/APTES/ITO$ (Figure 2a), $Au_1Pt_3NP/APTES/ITO$ (Figure 2b) and $Au_3Pt_1NP/APTES/ITO$ (Figure 2c) electrodes, show cauliflower-like nanoparticles with numerous grains conglomeration which undergoes three step growth process of nuclei formation, aggregation of tiny particles on nuclei and then growth into crystal grains.

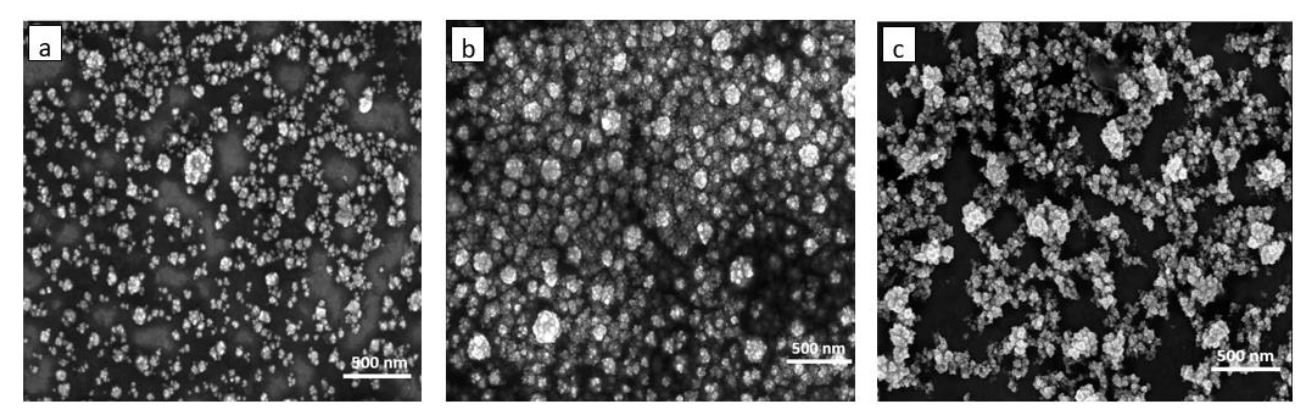


Figure 2. FE-SEM images of: (a) $Au_2Pt_2NP/APTES/ITO$, (b) $Au_1Pt_3NP/APTES/ITO$, (c) $Au_3Pt_1NP/APTES/ITO$ electrodes

EDX analysis (along with elemental X-ray mapping) was also performed for all alloy deposited nanoparticles ($Au_2Pt_2NP/APTES/ITO$, $Au_1Pt_3NP/APTES/ITO$ and $Au_3Pt_1NP/APTES/ITO$) which provided a more detailed elemental composition of these electrodes (Figure 3).

EDX results for various AuPtNP hybrids deposited on APTES/ITO confirm the presence of deposited Au and Pt on the electrode surfaces. Further, the varying content of Au and Pt in different hybrids follows their varying composition in the salt solution. EDX of the electrode with an electrochemically deposited film of Au₃Pt₁NP shows a higher content of Au as compared to Pt, whereas EDX of Au₁Pt₃NP electrode shows less elemental presence of Au as compared to Pt. It is worth noting that in the case of the Au₂Pt₂NP electrode, where the same molar concentrations of Au and Pt in the salt solution were used, the EDX presents a content of Pt as compared to Au. This may be because Pt tends to get deposited on the electrode surface better than Au. The increased tendency of PtNP deposition compared to AuNP deposition is also reflected for Au₁Pt₃ and Au₃Pt₁ electrodes, where the content is not directly correlated with the parts of their respective salts in the solution. Rather, the weight of PtNP deposited is higher compared to its part ratio in the salt solution.

XRD analysis of deposited AuPt metal nanoparticles

X-ray diffraction spectra of different AuPtNP/APTES/ITO electrodes are presented in Figure 4.

XRD diffraction patterns acquired for all prepared electrodes show different peaks, as listed in Table 2. In the 2ϑ range of 10 to 80°, different distinctive peaks have been obtained with (111), (200), (220) and (311) as their crystallographic planes, respectively. A fairly symmetric and single peak (111) face is shown by XRD profiles of the Au-Pt bimetallic system, which is intermediate of Au and Pt (111) peaks [24,25].

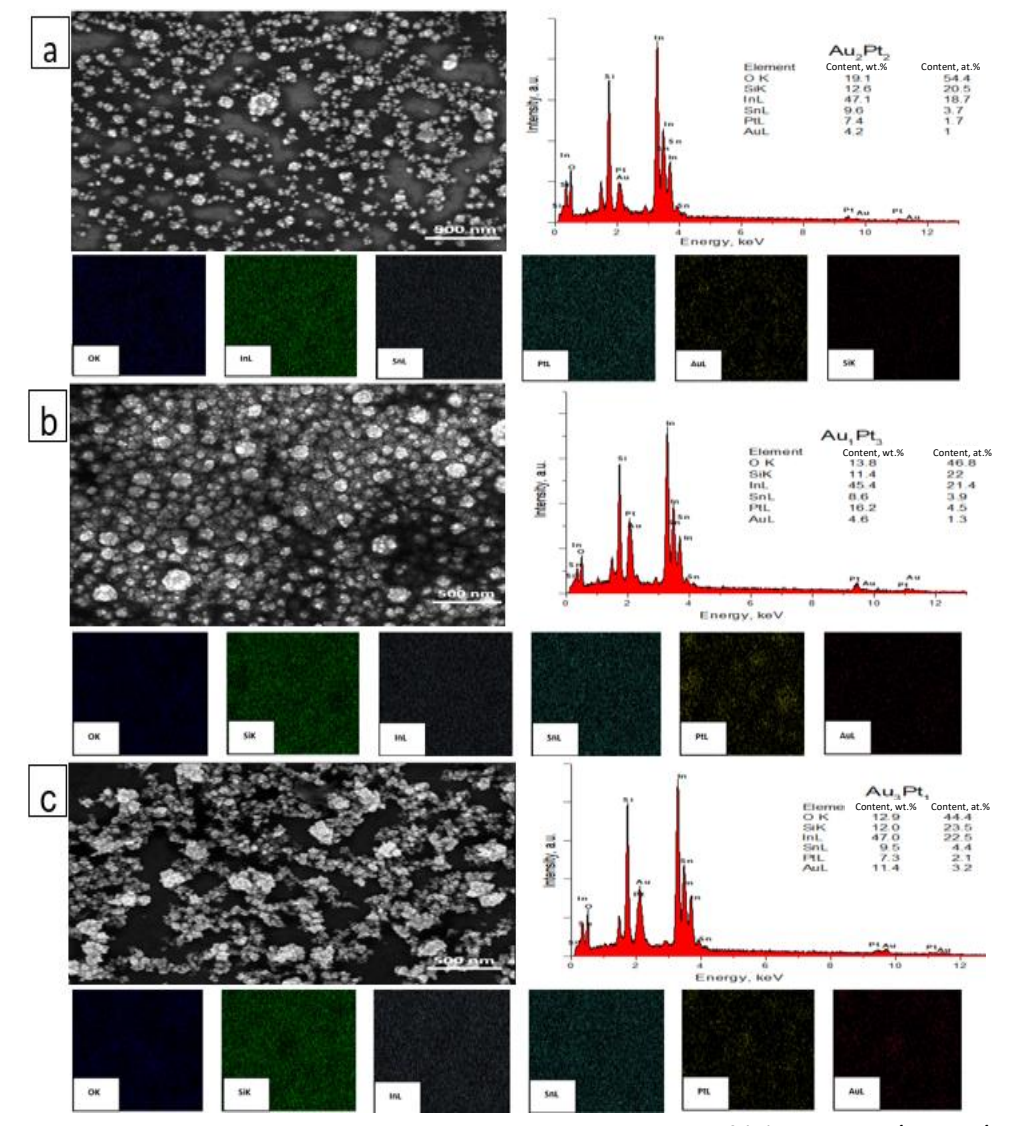


Figure 3. FE-SEM, EDX analysis and elemental X-ray mapping of (a) $Au_2Pt_2NP/APTES/ITO$, (b) $Au_1Pt_3NP/APTES/ITO$, (c) $Au_3Pt_1NP/APTES/ITO$ electrodes

Moreover, the values of Au-Pt hybrid nanoparticles lattice constant (*d*) are in between values of monometallic gold (0.407 nm) and platinum (0.392 nm) and increase linearly on increasing mole fraction of platinum in the electrolyte solution. Vegard's law was used to calculate lattice constant (d), which suggests an alloy feature in deposited Au-Pt hybrid where Au and Pt atoms are mixed tightly [28].

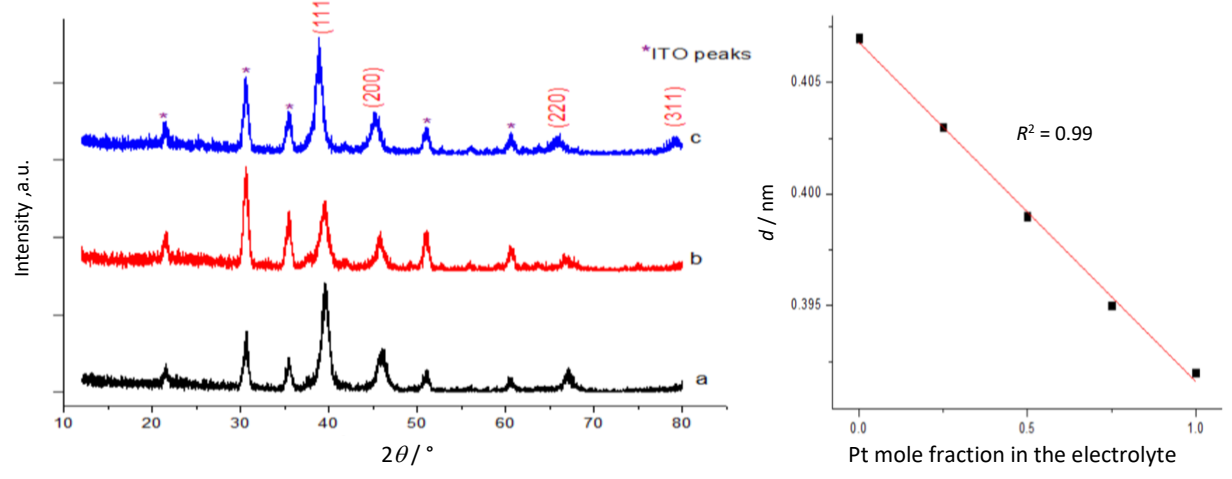


Figure 4. (Left) XRD of (a) $Au_1Pt_3NP/APTES/ITO$, (b) $Au_2Pt_2NP/APTES/ITO$, (c) $Au_3Pt_1NP/APTES/ITO$ electrodes, and (right) plot for their lattice constant

Electrode type	2 <i>θ</i> /°				- <i>d</i> / nm	Au:Pt part ratio	DD card number	
Electrode type	111	200	220	311	<i>u</i> / IIIII	in electrolyte	DB card number	
AuNP/APTES/ITO [25]	38.18	44.36	64.60	77.61	0.407	4:0	00-001-1172	
Au₃Pt₁NP/APTES/ITO	38.98	45.42	65.75	79.17	0.403	3:1	00-015-0043	
Au ₂ Pt ₂ NP/APTES/ITO	39.41	45.74	66.97	-	0.399	2:2	00-015-0043	
Au₁Pt₃NP/APTES/ITO	39.67	46.11	66.03	79.56	0.395	1:3	00-015-0043	
PtNP/APTES/ITO [24]	39.75	46.33	67.69	-	0.392	0:4	00-001-1194	

Table 2. Peak positions and d values for various prepared electrodes

Absorption spectra analysis of deposited AuPt nanoparticles

UV absorption spectra for AuNP, PtNP and their alloys electrochemically deposited on APTES/ITO electrode surfaces in different ratios were compared in a range of 400 to 800 nm wavelength (Figure 5). No absorption peak was observed for PtNP (Figure 5a), while different broad peaks for AuNP, Au₂Pt₂NP and Au₁Pt₃NP were observed at maximum wavelengths of 567 nm (Figure 5b), 557 nm (Figure 5e), 551 nm (Figure 5c) and 515 nm (Figure 5d), respectively. A left shift of wavelength peaks in the obtained spectrum was observed with the increase of Pt content in the alloy [1].

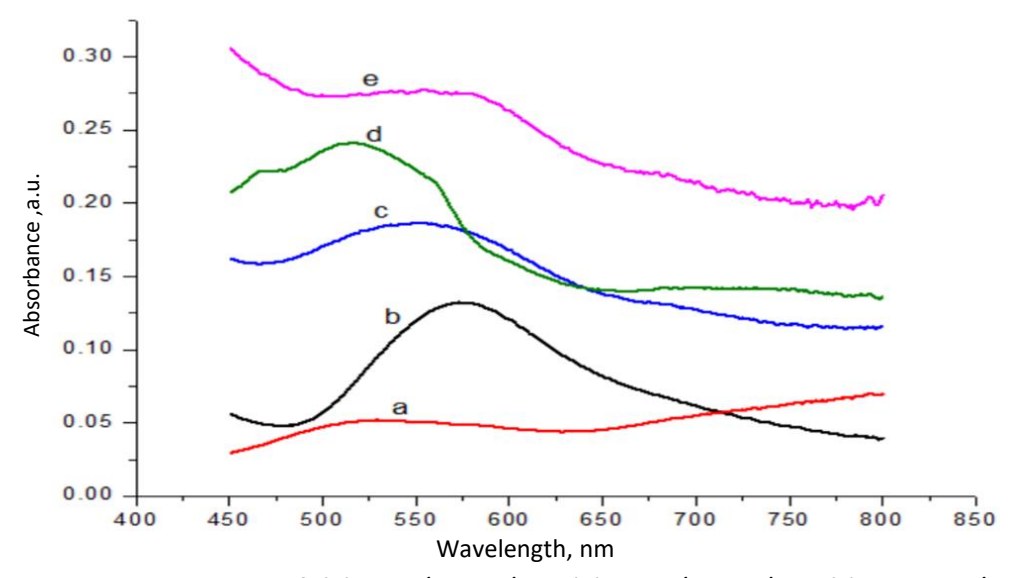


Figure 5. UV absorption spectra of: (a) PtNP/APTES/ITO, (b) AuNP/APTES/ITO, (c) Au₂Pt₂NP/APTES/ITO, (d) Au_1 Pt₃NP/APTES/ITO, (e) Au_3 Pt₁NP/APTES/ITO electrodes

Electrochemical characterization of different AuPtNP/APTES/ITO-modified electrodes

Further electrochemical investigations were done for all prepared AuPtNP-modified electrodes (Au₃Pt₁NP/APTES/ITO, Au₂Pt₂NP/APTES/ITO and Au₁Pt₃NP/APTES/ITO) in 100 mM PBS buffer solution containing 5 mM of [Fe(CN)₆]^{3-/4-} redox couple. An increase in redox peak currents and a decrease in the separation of peak potential values were observed with the deposition of noble metal alloy nanoparticles on APTES/ITO (Figure 6a), which is reconfirmed by DPV peak current (Figure 6b) and a decrease in resistance of charge transfer (Figure 6c). The corresponding parameters for AuPtNP/APTES/ITO electrodes are summarized in Table 3 and compared with those already obtained for Au and Pt-modified APTES/ITO electrodes [24,25]. Among AuPtNP-modified electrodes, an increase in anodic and cathodic current is maximal for Au₃Pt₁NP/APTES/ITO with ΔI_p 1271.97 μ A, for which the lowest charge transfer resistance (R_{ct}) of 319.78 Ω was obtained (Table 3). So, for the preparation of the biosensing electrode, Au₃Pt₁NP/APTES/ITO was used and modified by depositing SAA biomarker-specific antibodies.

Table 3. CV redox peak potentials (E_{oxi} and E_{red}), their difference (ΔE_p), peak currents difference (ΔI_p) and charge transfer resistance (R_{ct}) of APTES/ITO modified with metal nanoparticles and their alloys

Electrode type	E_{oxi} / V	E_{red} / V	ΔE_{p} / V	$\Delta I_p / \mu A$	$R_{ m ct}$ / Ω
AuNP/APTES/ITO [25]	0.27	-0.09	0.36	1029.30	258.65
Au ₃ Pt ₁ NP/APTES/ITO	0.30	-0.01	0.31	1271.97	319.78
Au ₂ Pt ₂ NP/APTES/ITO	0.25	-0.01	0.27	1102.11	333.88
Au ₁ Pt ₃ NP/APTES/ITO	0.26	0.03	0.23	1235.57	407.65
PtNP/APTES/ITO [24]	0.25	0.06	0.19	1130.31	430.68

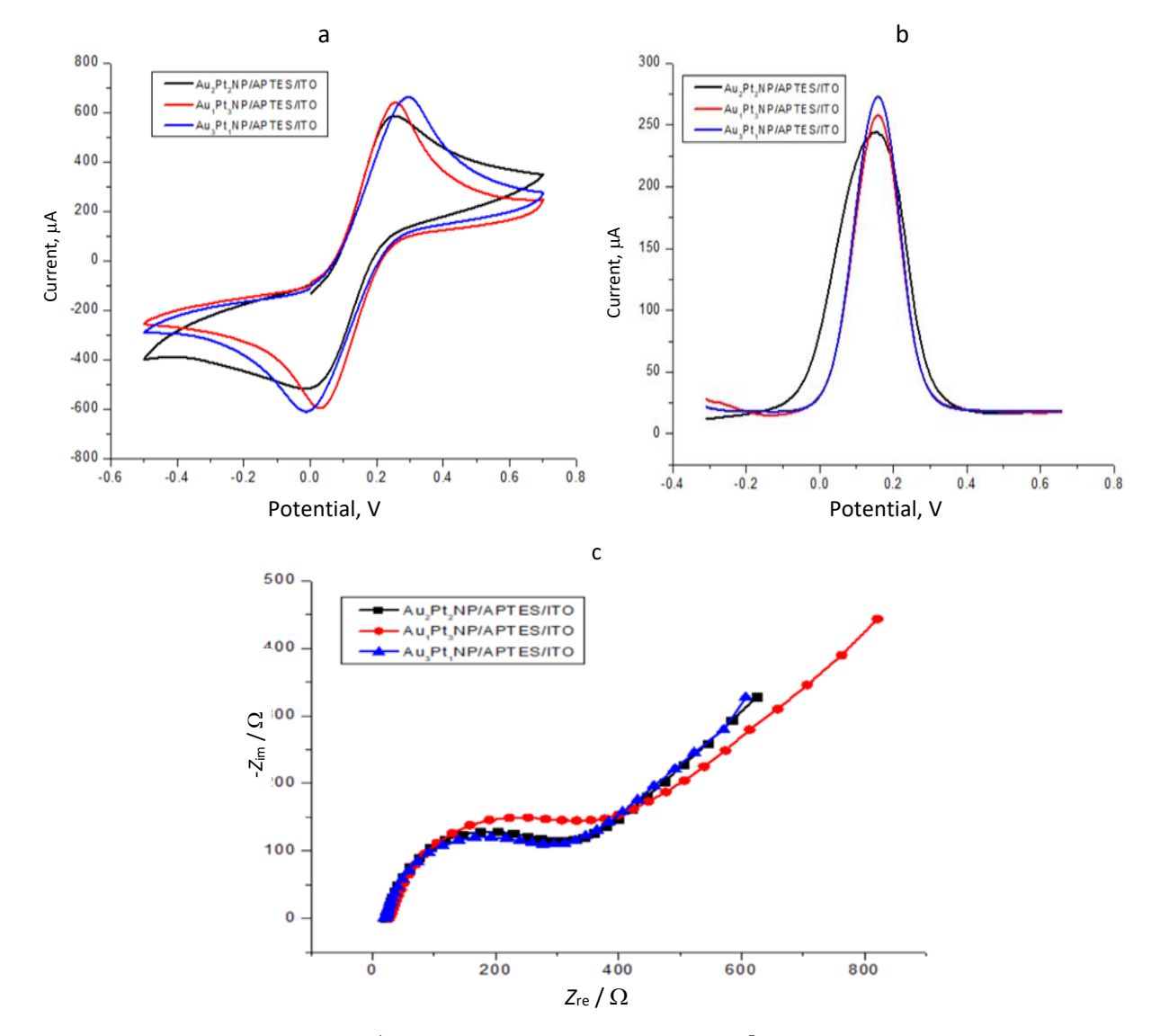


Figure 6. (a) CVs at 50 mV s⁻¹, (b) DPVs and (c) EIS at 0.03 V (10^5 -0.1 Hz) of different AuPtNP alloys (deposited for 60 cycles from solution A on APTES/ITO in various ratios) in 100 mM PBS, pH 7.4 containing 5 mM [Fe(CN)₆]^{3-/4-}

SAA ½ antibodies immobilization on Au₃Pt₁NP/APTES/ITO

Solution of SAA ½ antibodies of concentration 10 μg ml⁻¹ was prepared as reported in our previous work [24,25], and 20 μ l were poured on the surface of Au₃Pt₁NP/APTES/ITO electrode and left for the whole day for immobilizing antibodies by self-assembled monolayer (SAM). Such prepared immunoelectrode (SAA-Ab/Au₃Pt₁NP/APTES/ITO) was further used for biosensing of biomarker SAA by various electrochemical techniques [24,25].



Electrochemical properties of SAA-Ab/Au₃Pt₁NP/APTES/ITO electrode

The electrochemical properties of bare $Au_3Pt_1NP/APTES/ITO$ and $SAA-Ab/Au_3Pt_1NP/APTES/ITO$ electrodes in the presence of the $[Fe(CN)_6]^{3-/4-}$ redox couple were defined by different electrochemical techniques, *i.e.* CV, differential pulse voltammetry (DPV) and EIS (Figure 7). The observed variations in peak potential difference (ΔE_p) and peak redox currents (ΔI_p) for recorded CVs profiles in 100 mM PBS buffer solution containing 5 mM $[Fe(CN)_6]^{3-/4-}$ in -0.5 to 0.7 V potential range and at 50 mV/s scan rate, have indicated variations in current values and other parameters, not only between two electrodes, but for ITO and APTES/ITO electrodes [24,25] too. CV of bare ITO showed ΔE_p of 0.27 V, oxidation and reduction peak potentials at 0.26 and -0.02 V, respectively, and ΔI_p of 1078.68 μ A [24,25]. Decreased ΔI_p value (775.21 μ A) was obtained when ITO was modified with APTES with an increased (ΔE_p) value of 0.59 V. This decrease in ΔI_p value could be due to inhibition in electron transfer between the redox probe and the surface of the electrode, which also confirms the modification with APTES [24,25]. An increased ΔI_p value (1271.97 μ A) was seen for Au_3Pt_1NPs modified APTES/ITO electrode with ΔE_p 0.31 V, which can be due to the large surface area and increased conductivity provided by electrochemical deposition of AuPtNPs. This led to faster electron transfer between the redox probe and AuPtNPs modified ITO electrode.

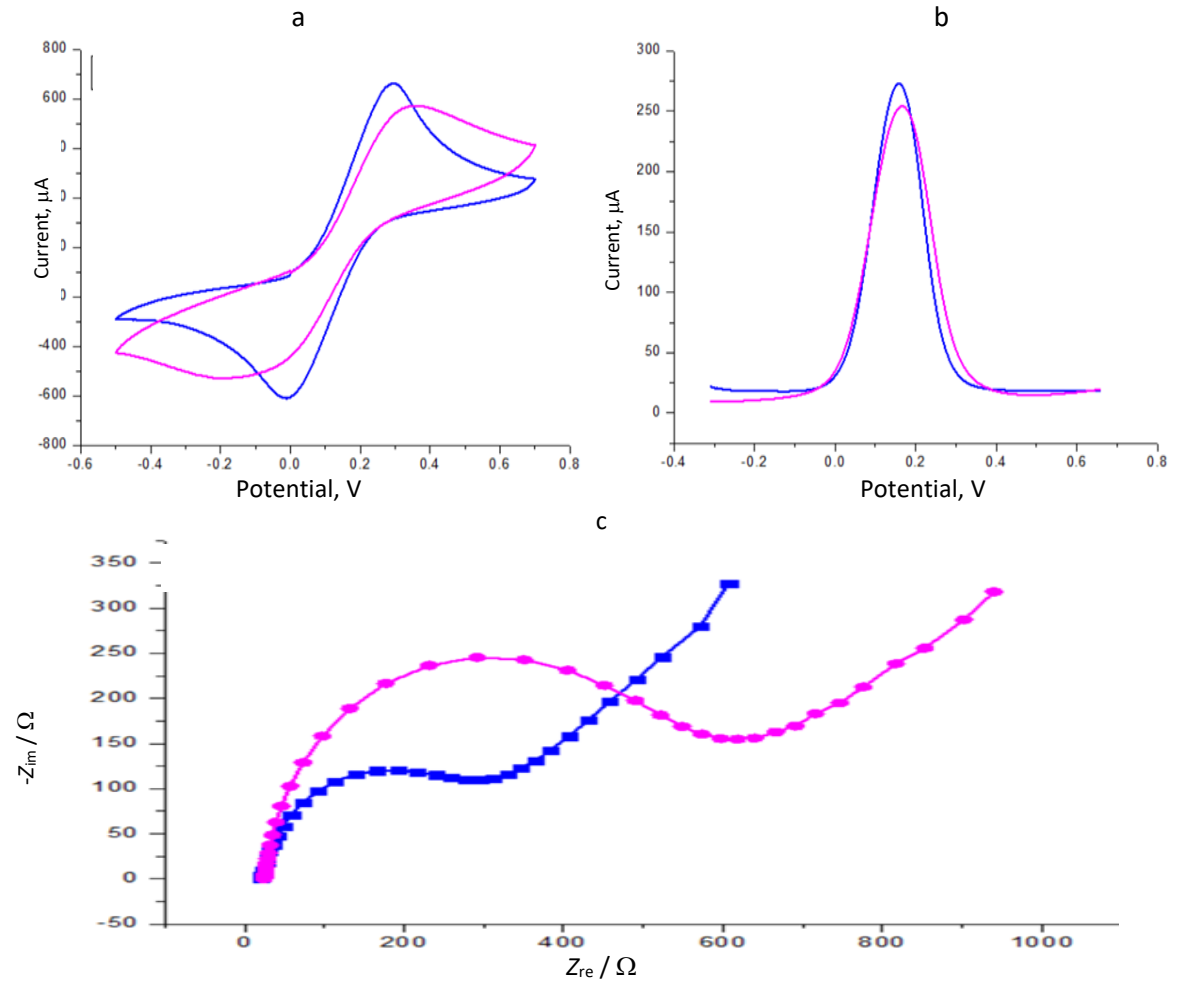


Figure 7. (a) CV at 50 mV s⁻¹, (b) DPV and (c) EIS at 0.03 V (10^5 -0.1 Hz) of ■ Au₃Pt₁NP/APTES/ITO and ● SAA-Ab/Au₃Pt₁NP/APTES/ITO electrodes in 100 mM PBS, pH 7.4 containing 5 mM [Fe(CN)₆]^{3-/4-}. Au₃Pt₁NP were deposited for 60 cycles from solution A on APTES/ITO electrode

Decreased ΔI_p (1100.10 μ A) and increased ΔE_p (0.55 V) values were obtained with redox peak potential at -0.20 and 0.36 V, respectively, when the Au₃Pt₁NP/APTES/ITO electrode was modified

with specific antibodies (SAA-Ab/Au₃Pt₁NP/APTES/ITO). This could be ascribed to the insulating layer formation after antibodies immobilization on the electrode surface, which hinders electron transfer between immunoelectrode and redox probe. The pattern of variations obtained for redox peak currents was similar to the pattern of current variations in DPV scans (Figure 7b) of all these modifications of ITO (in -0.3 to 0.7 V potential range) [1,27].

Further, the electrochemical impedance spectroscopy (EIS) technique was used to compare the electrochemical properties of Au₃Pt₁NP/APTES/ITO and SAA-Ab/Au₃Pt₁NP/APTES/ITO electrodes. The Nyquist plots obtained after EIS measurements (Figure 7c) indicated variations in impedance spectra for each modification of ITO [29]. In Nyquist plots, a semicircle diameter represents the electron transfer resistance (R_{ct}), which helps to investigate the interfacial properties of the modified electrode [30,31]. The corresponding R_{ct} values for bare ITO, APTES/ITO [24,25], and two ITO modifications presented in Figure 7c are given in Table 4. It was already shown that bare ITO and APTES/ITO showed R_{ct} values of 677.14 and 1728.64 Ω , respectively [24,25]. However, the smallest $R_{\rm ct}$ value (319.78 Ω) was obtained for APTES/ITO modified with Au3Pt1NPs, indicating excellent conductivity of AuPt alloy nanoparticles. After immobilization of SAA ½ antibodies on the surface of the Au₃Pt₁NP/APTES/ITO electrode, the R_{ct} value was increased (568.77 Ω), which refers to the decreased conductivity of electrode SAA-Ab/Au₃Pt₁NP/APTES/ITO due to the insulating layer formation after antibodies immobilization. These resulted in higher impedance of charge exchange due to the insulation property of protein molecules. Variations in R_{ct} values and obtained impedance spectra with different sizes of semicircle region in Nyquist plots confirm different modifications of ITO and are also in conformity with obtained ΔI_p values of CV measurements (Table 4).

Table 4. CV oxidation and reduction peak potentials, their difference (ΔE_p), peak current difference (ΔI_p) and charge transfer resistance (R_{ct}) for ITO modifications

Electrode type	E_{oxi} / V	E_{red} / V	ΔE_{p} / V	$\Delta I_p / \mu A$	$R_{ m ct}/\Omega$
ITO [24,25]	0.26	-0.02	0.27	1078.68	677.14
APTES/ITO [24,25]	0.24	-0.34	0.59	775.21	1728.64
Au ₃ Pt ₁ NP/APTES/ITO	0.30	-0.01	0.31	1271.97	319.78
SAA-Ab/Au ₃ Pt ₁ NP/APTES/ITO	0.36	-0.20	0.55	1100.10	568.77

Scan rate studies of fabricated electrodes

Scan rate studies were also performed for $Au_3Pt_1NP/APTES/ITO$ and $SAA-Ab/Au_3Pt_1NP/APTES/ITO$ modified electrodes in 100 mM PBS buffer solution containing 5 mM [Fe(CN)₆]^{3-/4-} in the scan rates range of 10 to 200 mV/s (Figure 8). As seen in Figures 8a and c, with every increase in the scan rate, an increase in redox peak current is observed [7]. The ratio of redox peak currents (I_{pc} and I_{pa}) was near one. The quasi-reversible nature of CV and electron transfer kinetics were confirmed by this ratio, which is supported by an increase in peak potential difference, ΔE_p , with an increase in the scan rate. Linear plots of redox peak currents (I_{pa} and I_{pc}) and square root of scan rate (ν) were obtained for all examined modified electrodes in the scan rates range of 10 to 200 mV/s (Figures 8b and 8d).

Electrochemical response to SAA biomarker

A stock solution of concentration 100 μg ml⁻¹ of SAA biomarker was prepared as was reported in our previous work [24,25]. DPV technique was used to investigate the electrochemical current in a potential range of -0.3 to 0.7 V. As seen in Figure 9a, the oxidation peak current response of immuno-electrode SAA-Ab/Au₃Pt₁NP/APTES/ITO as a function of concentration of SAA biomarker revealed

linear decrease in recorded DPVs, when 10 μ l of SAA biomarker was poured from concentrations range of 10, 10^2 , 10^3 , 10^4 , 10^5 and 10^6 fg ml⁻¹, and kept on the immunoelectrode for 10 minutes every time. The current decrease could be due to the formed SAA/SAA-Ab, which hinders the electron transfer. The linear relationship between DPV peak current values (with negative slope) and the concentration range of the SAA biomarkers can be seen in the obtained calibration plot (Figure 9b) [32]. The linearity is defined by equation (1):

$$I = -24.08703 \log c_{SAA} + 263.91593 \tag{1}$$

The regression coefficient for the linearity equation (R^2) is 0.94. Using equation 3σ /sensitivity (where σ is the standard deviation, which indicates a "typical" deviation from the mean), the limit of detection (LOD) was calculated as 7.0 fg ml⁻¹. The sensitivity of fabricated bioelectrodes was determined by linearity curve slope [33-35].

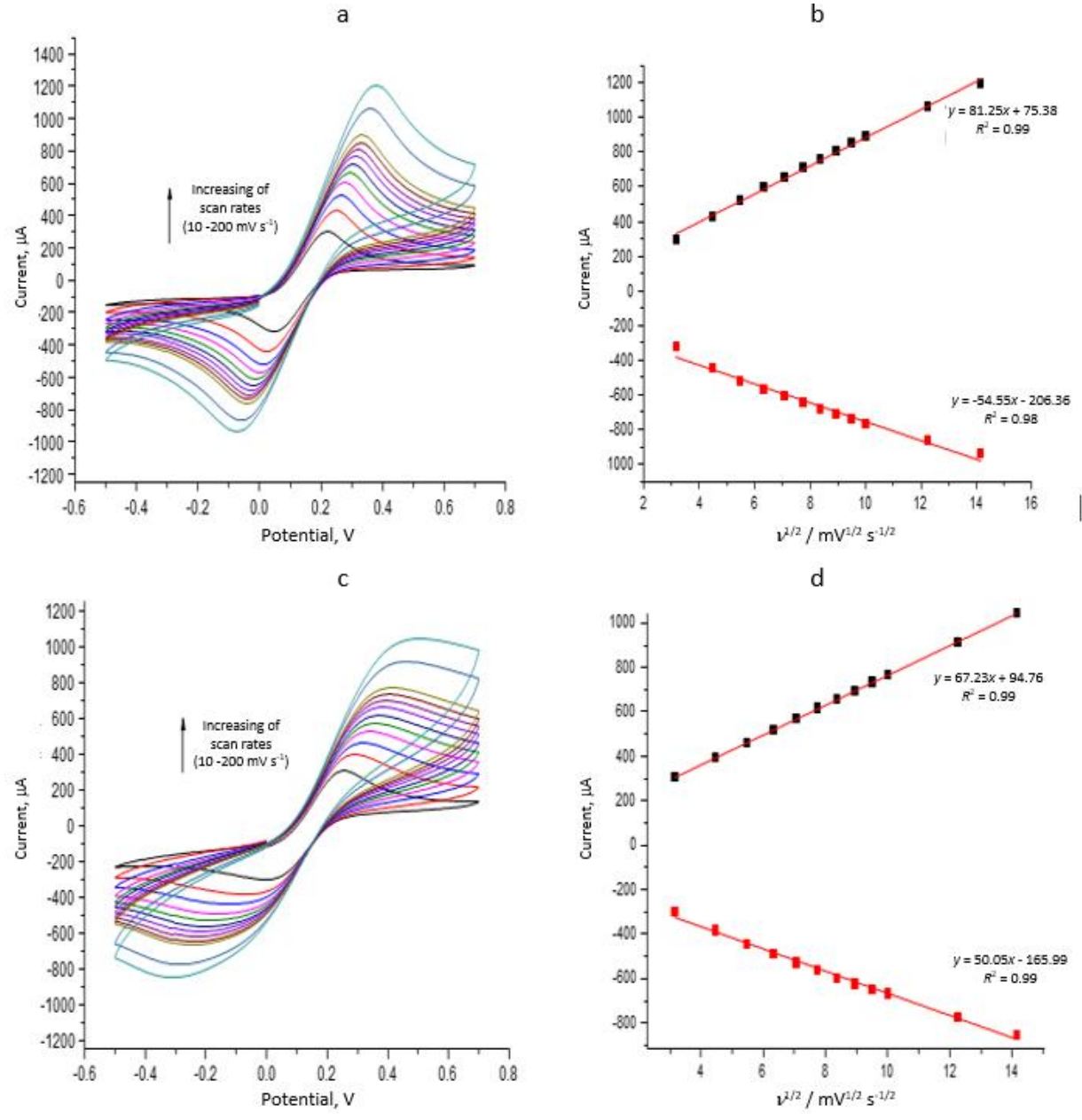


Figure 8. CV plots at scan rates from 10 mV to 200 mV s^{-1} (left) and linear plots of reduction and oxidation peak currents against square root of scan rate, with indicated linear equations and R^2 values (right) of (a) and (b) $Au_3Pt_1NP/APTES/ITO$; (c) and (d) $SAA-Ab/Au_3Pt_1NP/APTES/ITO$ electrodes in 100 mM PBS containing 5 mM [Fe(CN)₆]^{3-/4-}. Au_3Pt_1NP were deposited for 60 cycles from solution A on APTES/ITO electrode

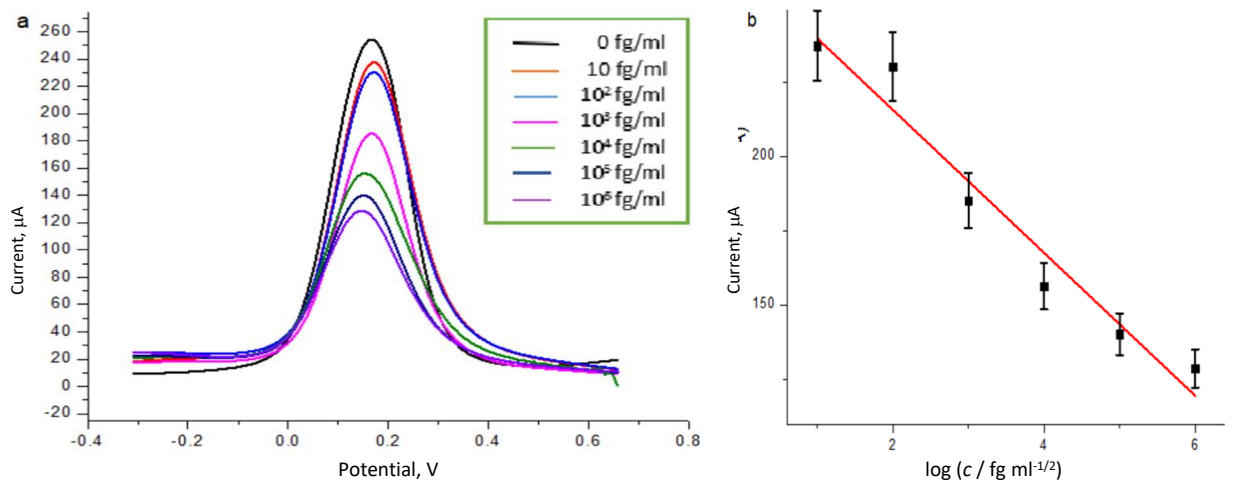


Figure 9. DPVs (a) and calibration plot (b) for SAA-Ab/Au₃Pt₁NP/APTES/ITO immunoelectrode for SAA biomarker in the concentration range from 10 to 10^6 fg ml⁻¹

Conclusion

Parameters for electrochemical deposition of AuPt nanoparticles (AuPtNP) alloy from solutions containing different molar fractions of Au and Pt salts on ITO modified by 3-aminopropyltriethoxysilane (APTES) surfaces were optimized. The prepared AuPtNPs/APTES/ITO electrodes, having different part ratios of Au and Pt, were characterized by XRD, FESEM, EDAX and UV absorption techniques, confirming different morphologies and the presence of two metals in various modifications at electrode surfaces. Electrochemical testing of electrodes performed by CV and EIS techniques using a redox probe showed that Au/Pt alloy with the part ratio of 3:1, *i.e.*, Au₃Pt₁NP/APTES/ITO electrode displayed excellent electrocatalytic activity. This electrode was used for SAA-specific antibody immobilization to fabricate the immunoelectrode SAA-Ab/Au₃Pt₁NP/APTES/ITO, successfully detecting SAA biomarkers in the 10 to 106 fg ml⁻¹ concentration range. A linear relationship was obtained between increasing SAA concentrations and decreasing peak current values of recorded DPVs, with a calculated LOD of 7.0 fg ml⁻¹.

Conflict of interest: There is no conflict of interest as per the authors declaration.

Acknowledgements: The authors acknowledge gratefully the support of The NorthCap University & CRF laboratory (Central Research Facility laboratory) for their infrastructure facilities and instrumentation. Authors also thank for financial support received by A. S. Ghrera from Science and Engineering Board (DST), India under Young Scientist research project (YSS/2015/001330).

References

- [1] Y. Song, Y. Ma, Y. Wang, J. Di, Y. Tu, Electrochemical deposition of gold-platinum alloy nanoparticles on an indium tin oxide electrode and their electrocatalytic applications, *Electrochimica Acta* **55** (2010) 4909-4914. https://doi.org/10.1016/j.electacta.2010.03.089
- [2] F. Xiao, F. Zhao, Y. Zhang, G. Guo, B. Zeng, Ultrasonic Electrodeposition of Gold-Platinum Alloy Nanoparticles on Ionic Liquid-Chitosan Composite Film and Their Application in Fabricating Nonenzyme Hydrogen Peroxide Sensors, *The Journal of Physical Chemistry C* **113** (2009) 849-855. https://doi.org/10.1021/jp808162g
- [3] Y. Zhou, G. Yu, F. Chang, B. Hu, C.-J. Zhong, Gold-platinum alloy nanowires as highly sensitive materials for electrochemical detection of hydrogen peroxide, *Analytica Chimica Acta* **757** (2012) 56-62. https://doi.org/10.1016/j.aca.2012.10.036
- [4] H. Shen, M. Wang, W. Zhang, Y. Zhang, W. Wang, X. Cao, The bimetallic heterostructure Pt-Au nanoparticle array on Indium Tin Oxide electrode by electrodeposition and their high activity



- for the electrochemical oxidation of methanol, *Journal of Alloys and Compounds* **895** (2022) 162581. https://doi.org/10.1016/j.jallcom.2021.162581
- [5] A. Kathalingam, K.P. Marimuthu, K. Karuppasamy, Y.-S. Chae, H. Lee, H.-C. Park, H.-S. Kim, Structural and Mechanical Characterization of Platinum Thin Films Prepared Electrochemically on ITO/Glass Substrate, *Metals and Materials International* 27 (2021) 1554-1564. https://doi.org/10.1007/s12540-019-00527-5
- [6] H. Yu, J. Yu, L. Li, Y. Zhang, S. Xin, X. Ni, Y. Sun, K. Song, Recent Progress of the Practical Applications of the Platinum Nanoparticle-Based Electrochemistry Biosensors, *Frontiers in Chemistry* **9** (2021) 677876. https://doi.org/10.3389/fchem.2021.677876
- [7] R. Chauhan, B. Nagar, P. R. Solanki, T. Basu, Development of Triglyceride Biosensor Based on a Platinum Nano Particle and Polypyrrole Nano Composite Electrode, *Materials Focus* **2** (2013) 316-323. https://doi.org/10.1166/mat.2013.1096
- [8] P. Si, N. Razmi, O. Nur, S. Solanki, C. M. Pandey, R. K. Gupta, B. D. Malhotra, M. Willander, A. de la Zerda, Gold nanomaterials for optical biosensing and bioimaging, *Nanoscale Advances* **3** (2021) 2679-2698. https://doi.org/10.1039/D0NA00961J
- [9] T. Ahuja, V. K. Tanwar, S. K. Mishra, D. Kumar, A. M. Biradar, A. M. Rajesh, Immobilization of Uricase Enzyme on Self-Assembled Gold Nanoparticles for Application in Uric Acid Biosensor, Journal of Nanoscience Nanotechnology 11 (2011) 4692-4701. https://doi.org/10.1166/jnn.2011.4158
- [10] H. H. Kyaw, S. H. Al-Harthi, A. Sellai, J. Dutta, Self-organization of gold nanoparticles on silanated surfaces, *Beilstein Journal of Nanotechnology* **6** (2015) 2345-2353. https://doi.org/10.3762/bjnano.6.242
- [11] G. Zhao, G. Liu, Electrochemical Deposition of Gold Nanoparticles on Reduced Graphene Oxide by Fast Scan Cyclic Voltammetry for the Sensitive Determination of As(III), *Nanomaterials* **9** (2018) 41. https://doi.org/10.3390/nano9010041
- [12] M. Z. H. Khan, Nanoparticles Modified ITO Based Biosensor, *Journal of Electronic Materials* **46** (2017) 2254-2268. https://doi.org/10.1007/s11664-016-5172-3
- [13] Md. Z. H. Khan, Effect of ITO surface properties on SAM modification: A review toward biosensor application, *Cogent Engineering* **3** (2016) 1170097. https://doi.org/10.1080/23311916.2016.1170097
- [14] G. H. Sack, Serum amyloid A, *Molecular Medicine* **24** (2018) 46. https://doi.org/10.1186/s10020-018-0047-0
- [15] H. Miwata, T. Yamada, M. Okada, T. Kudo, H. Kimura, T. Morishima, Serum amyloid A protein in acute viral infections, *Archives of Disease Childhood* 68 (1993) 210-214. https://doi.org/10.1136/adc.68.2.210
- [16] E. Malle, F. C. De Beer, Human serum amyloid A (SAA) protein: a prominent acute-phase reactant for clinical practice, *European Journal of Clinical Investigation* **26** (1996) 427-435. https://doi.org/10.1046/j.1365-2362.1996.159291.x
- [17] B. Rezaei, N. Irannejad, *Electrochemical detection techniques in biosensor applications*, in *Electrochemical Biosensors*, A. A. Ensafi, Ed., Elsevier Inc., 2019, 11-43. https://doi.org/10.1016/B978-0-12-816491-4.00002-4
- [18] K. Y. Goud, K. K. Reddy, A. Khorshed, V. S. Kumar, R. K. Mishra, M. Oraby, A. H. Ibrahim, H. Kim, K. V. Gobi, Electrochemical diagnostics of infectious viral diseases: Trends and challenges, *Biosensors and Bioelectronics* **180** (2021) 113112. https://doi.org/10.1016/j.bios.2021.113112
- [19] C. Xia, Y.n Li, G. Yuan, Y. Guo, C. Yu, Immunoassay for serum amyloid A using a glassy carbon electrode modified with carboxy-polypyrrole, multiwalled carbon nanotubes, ionic liquid and chitosan, *Microchimica Acta* **182** (2015) 1395-1402. https://doi.org/10.1007/s00604-015-1465-0
- [20] J.-S. Lee, S.-W. Kim, E.-Y. Jang, B.-H. Kang, S.-W. Lee, G. Sai-Anand, S.-H. Lee, D.-H. Kwon, S.-W. Kang, Rapid and Sensitive Detection of Lung Cancer Biomarker Using Nanoporous Biosensor

- Based on Localized Surface Plasmon Resonance Coupled with Interferometry, *Journal of Nanomaterials* **2015** (2015) 183438. https://doi.org/10.1155/2015/183438
- [21] C. Timucin, O. Gul, O. Kutuk, H. Basaga, antibody array-based immunosensor for detecting cardiovascular disease risk markers, *Journal of Immunoassay and Immunochemistry* **33** (2012) 275-290. https://doi.org/10.1080/15321819.2011.638407
- [22] A. L. Pastore, G. Palleschi, L. Silvestri, D. Moschese, S. Ricci, V. Petrozza, A. Carbone, A. Di Carlo, Serum and Urine Biomarkers for Human Renal Cell Carcinoma, *Disease Markers* **2015** (2015) 251403. https://doi.org/10.1155/2015/251403
- [23] I. Sorić Hosman, I. Kos, L. Lamot, Serum Amyloid A in Inflammatory Rheumatic Diseases: A Compendious Review of a Renowned Biomarker, *Frontiers in Immunology* **11** (2021) 631299. https://doi.org/10.3389/fimmu.2020.631299
- [24] Kalpana, A. S. Ghrera, Electrochemical Investigation of Viral Respiratory Infection Inflammatory Biomarker Serum Amyloid A Protein by Using PtNP Modified Electrode, *Chemistry Select* **8** (2023) e202203532. https://doi.org/10.1002/slct.202203532
- [25] Kalpana, A. S. Ghrera, Electrochemical Investigation of Viral Respiratory Infection Inflammatory Biomarker Protein by Using AuNPs Modified Electrode, *Analytical and Bioanalytical Chemistry Research* **10** (2023) 289-300. https://doi.org/10.22036/ABCR.2023.367377.1849
- [26] M.-C. Tsai, P.-Y. Chen, Voltammetric study and electrochemical detection of hexavalent chromium at gold nanoparticle-electrodeposited indium tin oxide (ITO) electrodes in acidic media, *Talanta* **76** (2008) 533-539. https://doi.org/10.1016/j.talanta.2008.03.043
- [27] N. Tavakkoli, N. Soltani, Z. K. Tabar, M. R. Jalali, Determination of dopamine using the indium tin oxide electrode modified with direct electrodeposition of gold-platinum nanoparticles, *Chemical Papers* **73** (2019) 1377-1388. https://doi.org/10.1007/s11696-019-00690-4
- [28] W. Ye, H. Kou, Q. Liu, J. Yan, F. Zhou, C. Wang, Electrochemical deposition of Au-Pt alloy particles with cauliflower-like microstructures for electrocatalytic methanol oxidation, *International Journal of Hydrogen Energy* **37** (2012) 4088-4097. https://doi.org/10.1016/j.ijhydene.2011.11.132
- [29] M. A. MacDonald, H. A. Andreas, Method for equivalent circuit determination for electrochemical impedance spectroscopy data of protein adsorption on solid surfaces, *Electrochimica Acta* **129** (2014) 290-299. https://doi.org/10.1016/j.electacta.2014.02.046
- [30] A. S. Ghrera, C. M. Pandey, B. D. Malhotra, Multiwalled carbon nanotube modified microfluidic-based biosensor chip for nucleic acid detection, *Sensors and Actuators B: Chemical* **266** (2018) 329-336. https://doi.org/10.1016/j.snb.2018.03.118
- [31] A. Sharma, Z. Matharu, G. Sumana, P. R. Solanki, C. G. Kim, B. D. Malhotra, Antibody immobilized cysteamine functionalized-gold nanoparticles for aflatoxin detection, *Thin Solid Films* **519** (2010) 1213-1218. https://doi.org/10.1016/j.tsf.2010.08.071
- [32] Y. G. Gupta, Kalpana, A. Sharma Ghrera, Electrochemical studies of lateral flow assay test results for procalcitonin detection, *Journal of Electrochemical Science and Engineering* **12** (2021) 265–274. https://doi.org/10.5599/jese.1127
- [33] Y. Gupta, C. M. Pandey, A. S. Ghrera, Reduced Graphene Oxide-Gold Nanoparticle Nanohybrid Modified Cost-Effective Paper-Based Biosensor for Procalcitonin Detection, *ChemistrySelect* **7** (2022) e202202642. https://doi.org/10.1002/slct.202202642
- [34] Y. Gupta, C. M. Pandey, A. S. Ghrera, Development of conducting cellulose paper for electrochemical sensing of procalcitonin, *Microchimica Acta* **190** (2023) 32. https://doi.org/10.1007/s00604-022-05596-9
- [35] Y. Gupta, A. S. Ghrera, Development of conducting paper-based electrochemical biosensor for procalcitonin detection, *ADMET & DMPK* **11** (2023) 263-275. https://doi.org/10.5599/admet.1575

© 2024 by the authors; licensee IAPC, Zagreb, Croatia. This article is an open-access article distributed under the terms and conditions of the Creative Commons Attribution license (https://creativecommons.org/licenses/by/4.0/)





Open Access :: ISSN 1847-9286 www.jESE-online.org

Original scientific paper

Supercapacitive performance of self-assembled thin film of liquid catocene/basal plane pyrolytic graphite electrode

Sajjad Damiri[™], Zahra Samiei and Hamid R. Pouretedal

Department of Applied Chemistry, Malek-Ashtar University of Technology, Shahin-shahr, Esfahan, I.R. Iran

Corresponding author: [□]sajjaddamiri@chmail.ir; Tel: +98-314-591-2253; Fax: +98-314-522-0420

Received: March 21, 2024; Accepted: July 4, 2024; Published: July 23, 2024

Abstract

Reasonable design of electrode material with low cost, lightweight, and excellent electrochemical properties is of great significance for future large-scale energy storage applications. Herein, we report the electrochemical and supercapacitive behaviour of the liquid redox of catocene, 2,2'-bis(ethyl-ferroceneyl) propane, self-assembled on a basal plane pyrolitic graphite electrode in comparison to the solid ferrocene thin film in aqueous sodium sulfate electrolyte. The modified electrode surfaces were evaluated to assess the iron content and the formation of thin film using scanning electron microscopy, laserinduced breakdown spectroscopy, and attenuated total reflectance method. Also, the supercapacitive performances of the related modified electrodes were assessed and compared using cyclic voltammetry and galvanostatic charge-discharge in a threeelectrode system and an asymmetric two-electrode supercapacitor system. Electrochemical results showed that the electrode processes are diffusion-controlled with battery-like behaviour, and the liquid catocene exhibits more effective interaction with the graphite surface in comparison to solid ferrocene. The catocene surface coverage on graphite is nearly 50-75 % higher than ferrocene, leading to improved interaction and charge transfer resistance, observed in electrochemical impedance spectroscopy studies. In galvanostatic charge-discharge evaluations, the supercapacitor based on catocene modified electrode shows a specific capacitance of 141.2 F g^{-1} at a current density of 1.0 A g^{-1} , with a specific energy density of 56.7 Wh kg^{-1} at a power density of 2.9 kW kg^{-1} .

Keywords

Supercapacitor; ferrocene; liquid redox; thin films; self-assembly

Introduction

Nowadays, with the development of new technologies and environmental concerns, there is an ever-increasing demand for clean, lightweight, high-capacity and cyclically stable electrical energy storage resources. In this regard, research and development on electrochemical supercapacitors (SCs)

have garnered special attention due to their high power density and long cycle life (>100,000 cycles), as well as rapid charge-discharge rates compared to batteries and fuel cells [1-3]. Electrochemical supercapacitors are classified into two main categories based on their energy storage mechanisms: 1) electrochemical double-layer capacitors, with the electric charge accumulating at the electrode/electrolyte interface, and 2) pseudo-capacitors, where charge is stored on electrochemically active sites through reversible redox reactions [4]. The research in designing new electrode materials is crucial to SCs because they play a pivotal role in the capacitive performance of SCs [5-7]. In the recent decade, various electrode active materials such as conducting polymers, transition metal oxides [4], metal complexes and metal-organic frameworks (MOFs) [8] have garnered attention due to their electrochemical behaviour and relatively desirable charge storage capacity. Furthermore, to lighten the weight and improve the surface area and electrical conductivity of the electrodes, various carbonaceous materials such as graphite, graphene, carbon nanotubes, carbon nanofibers [9], or porous metallic microstructures [10] have been developed.

Thin-film electrodes (TFEs), with relatively high charge-discharge rates and low equivalent series resistances (ESR), are a category of intelligent supercapacitor electrodes mainly used in portable and/or miniaturized devices [11]. However, the overall specific capacitance decreases due to the low loading of active material on these electrode surfaces. In this context, transition metal oxide (TMOs) thin films are usually high-capacity materials with high redox activity. However, their cyclability and poor rate performance are persistent challenges because of their dissolution in aqueous electrolytes and mediocre conductivity. A thin layer of RuO₂ as a noble metal oxide, with a thickness of 400 nm, shows a capacity of 4.5 F cm⁻² at 2.0 mV s⁻¹, and it maintains nearly 90 % of the initial charge capacity after 10,000 charge-discharge cycles in micro-supercapacitors [12].

Nowadays, 2D metallic materials, including transition metal dichalcogenides (TMDs) [13] and MXene, with the general formula M_n+1X_n (M is an early transition metal, and X is C or N) [14], have been introduced as excellent options in TFEs. The TaS₂-based TMD electrode exhibits a high volumetric capacity close to 508 F cm⁻³ at a scan rate of 10 mV s⁻¹ and its energy density in micro-supercapacitors is 58.5 Wh L⁻¹ [15]. Ti₃C₂Tx MXene film with a Fe₃O₄ porous layer on a flexible Ni strip demonstrates electrochemical performance of 46.4 mF cm⁻² at a current density of 0.5 mA cm⁻², and energy density of 0.970 μ Wh cm⁻² at a power density of 0.176 mW cm⁻², with good cycle stability [16].

Organometallic compounds such as metal coordination polymers and molecular complexes based on Fe, Ni, Co, Mn, Cu, or other metals have also garnered considerable attention due to their reversible electrochemical behaviour, light atom weight, availability, environmental friendliness, non-toxicity, low cost, and their ability to form various thin films and electrode composites [17]. Iron and various iron-based compounds have also been used in electrode-active materials due to their multiple reversible redox reactions and high specific capacity [18]. Ferrocene-based coordination polymers have relatively high thermal stability, two stable redox states, fast electron transfer, and excellent charge-discharge efficiency [19]. By employing modified multi-walled carbon nanotubes (MWCNTs) functionalized with ferrocene, a specific capacity of 50.0 F g⁻¹ at 0.25 A g⁻¹ was achieved with high cycle stability [20]. Furthermore, reduced graphene oxide (rGO) functionalized with 1,1'-bis(4-isobutyl) ferrocene displayed better electrical conductivity than rGO and demonstrated good charge-discharge performance with stable cycling [21].

In the development of TFEs or composite electroactive materials for fast charge-discharge supercapacitors, the most common method is the chemical functionalization of redox materials such as ferrocene derivatives on porous conductive electrodes. However, this synthesis process is often expensive, and the surface coverage of the bonded material is relatively low [19-21]. In surface

adsorption methods, solid active materials such as crystalline ferrocene derivatives are usually used, leading to a decrease in electrochemical efficiency. The use of liquid redox materials compared to solids can provide a more desirable interaction with carbonaceous electrodes and crystalline particles [22-24].

In this research, an attempt has been made to compare and analyse the electrochemical behaviour and energy storage capacity of two redox materials, solid ferrocene and liquid 2,2'-bis(ethyl-ferrocenyl) propane (catocene), self-assembled on the basal plane pyrolytic graphite (BPPG) electrodes. Catocene is a dark brownish-orange liquid with the chemical formula $C_{27}H_{32}Fe_2$ and an atomic mass of 282.2 g mol^{-1} , which is used as an effective catalyst in solid propellants containing ammonium perchlorate [25].

Experimental

Chemicals and apparatus

All chemical materials, such as ferrocene, sodium sulphate (Na₂SO₄), and the solvent N,N-dimethyl-formamide (DMF) with analytical grade purity, were purchased from Merck. A BPPG sheet with high electrical conductivity containing 98.69 wt.% graphite powder and 1.31 wt.% polymer with a thickness of 0.5 mm was obtained from Redoxkala Co. (Iran). Catocene liquid with 97.5 % purity containing 23.3 -to 24.4 wt.% iron was purchased from Tanyun Aerospace Materials (Yingkou) Technology Co. (China).

Electrochemical measurements, cyclic voltammetry (CV), galvanostatic charge-discharge (GCD), and electrochemical impedance spectroscopy (EIS) were performed by EG&G potentiostatgalvanostat instrument (PARSTAT 2273, Princeton Applied Research, USA), in a 1.0 M sodium sulphate solution using a three-electrode system consisting an Ag/AgCl (saturated KCl) reference electrode, a platinum auxiliary electrode with a 2.0 cm² surface area, and a BPPG working electrode with a geometric area of 0.2 cm² immersed in the electrolyte and coated with the catocene or ferrocene film. For the evaluation of the coated films on the electrode and the detection of active electrode materials, Fourier-transform infrared spectroscopy (FT-IR), attenuated total reflectance (ATR), scanning electron microscopy (SEM), energy-dispersive X-ray spectroscopy (EDS) and laserinduced breakdown spectroscopy (LIBS) elemental analysis were employed. FT-IR/ATR measurements were performed using an Infralum-FT08 spectrometer (Lumex, Russia) equipped with a DTGS detector and MIRacle™ Single Reflection ATR accessory with a diamond/ZnSe crystal plate. LIBS spectra were recorded using the LIBSCAN100 system (Photonic Applied Ltd.), which includes an Nd:YAG laser with a wavelength of 1064.0 nm, output energy of 100.0 mJ, pulse width of 2±7 ns, and a repetition rate of 1.0 to 20.0 Hz. The emitted LIBS plasma radiations were collected and transferred to the system detector capable of recording spectra in the range of 182.0 to 1057.0 nm with an accuracy of 0.04 nm. EIS studies were conducted over a frequency range of 100.0 kHz to 10.0 mHz at a DC potential of 0.5 V with a sinusoidal potential amplitude of 10.0 mV and 10 points per frequency decade.

Preparation of thin film electrodes

Working electrodes with a coating of a thin layer of catocene on BPPG electrode (Cat/BBPG) or ferrocene thin film on BPPG (Fc/BPPG) were prepared by first cleaning the graphite electrode with acetone and keeping it in a vacuum at 45.0 °C for one hour to remove surface impurities. The electrodes were then cooled to room temperature and weighed. Subsequently, 2.0 molar concentrations of redox reactants, catocene or ferrocene, were prepared in the DMF solvent. The graphite sheet

with a geometric area of 0.2 cm² was then immersed in the solution for 5.0 minutes. Afterwards, the solvent-soaked electrode was dried and cooled for 10.0 minutes to stabilize the catocene or ferrocene films on the surface of the graphite electrode. The weight of the electrode materials was calculated by measuring the weight difference between the initial graphite electrode and the coated electrode using a 5-digit analytical balance (Balance XPR105DR, Model). The average weight of self-assembled catocene and ferrocene on the graphite electrode was near 16.0 and 11.0 mg cm⁻², respectively.

Electrochemical tests

Cyclic voltammetry measurements were conducted in a three-electrode cell in $0.1 \text{ M Na}_2\text{SO}_4$ electrolyte solution at potential scan rates ranging from 20 to 140 mV s⁻¹ and at the ambient temperature of 28-30 °C. The specific capacitance of the working electrode can be obtained from the voltammetry surface area according to equation (1) [1,28]:

$$C_{\rm sp} = \frac{1}{2mv\Delta V} \int i(V) dV \tag{1}$$

In equation (1), C_{sp} / F g⁻¹is the specific capacitance, m / g is the mass of self-assembled catocene or ferrocene on the working electrode, v / V s⁻¹ is the potential scan rate, $\int i(V)dV$ is the area under the cyclic voltammetry curve in ampere-volts, and ΔV / V is the potential window.

Galvanostatic charge-discharge tests were conducted at current densities ranging from 1.0 to 10.0 A g⁻¹, and the specific capacitance was calculated according to equation (2) [1]:

$$C_{\rm sp} = \frac{I\Delta t}{m\Delta V} \tag{2}$$

where I/A is the discharge current and $\Delta t/s$ is the discharge time. Additionally, the specific energy density ($E/Wh kg^{-1}$) can be calculated using equation (3)[27]:

$$E = \frac{1}{2 \times 3.6} C_{\rm sp} \left(\Delta V \right)^2 \tag{3}$$

Here, ΔV is the operational potential window, and C_{sp} is the specific capacitance of the fabricated electrode. Also, the specific power density P / kW kg⁻¹ is described in equation (4) [29]:

$$P = \frac{3.6 E}{\Delta t} \tag{4}$$

where E / Wh kg⁻¹ and t / s are specific energy density and discharge time, respectively.

Furthermore, an asymmetric supercapacitor was assembled using a graphite electrode as the negative electrode, Cat/BPPG or Fc/BPPG as the positive electrode, and a cellulose filter paper as the dielectric. Before electrochemical tests, the electrodes and dielectric were soaked in $0.1~M~Na_2SO_4$ electrolyte, and all experiments were conducted under laboratory temperature conditions. For potentiostaic or galvanostatic tests in the two-electrode configurations, the reference and auxiliary electrodes were connected, and GCD tests were recorded in the voltage window of 0.0~to~1.7~V.

Results and discussion

Characterization of electrode materials

Various surface techniques, including SEM, EDS, LIBS, and FT-IR/ATR, were utilized to assess the quality and quantity of catocene and ferrocene films formed on the relatively smooth surface of BPPG electrodes. SEM images and the distribution of Fe element with EDS mapping on the surfaces of Cat/BPPG and Fc/BPPG electrodes are depicted in Figure 1. It can be observed that iron atoms



from catocene and ferrocene are distributed with relatively low concentrations and almost uniform distribution across the entire mapped window. Upon closer evaluation of SEM images, crystalline solid particles of ferrocene with partial iron enrichment are also observed. The self-assembled liquid catocene on graphite is expected to exhibit a more uniform distribution than solid ferrocene. A homogeneous and thin layer distribution can accelerate the kinetics of electrochemical reactions, leading to increased efficiency in redox reactions.

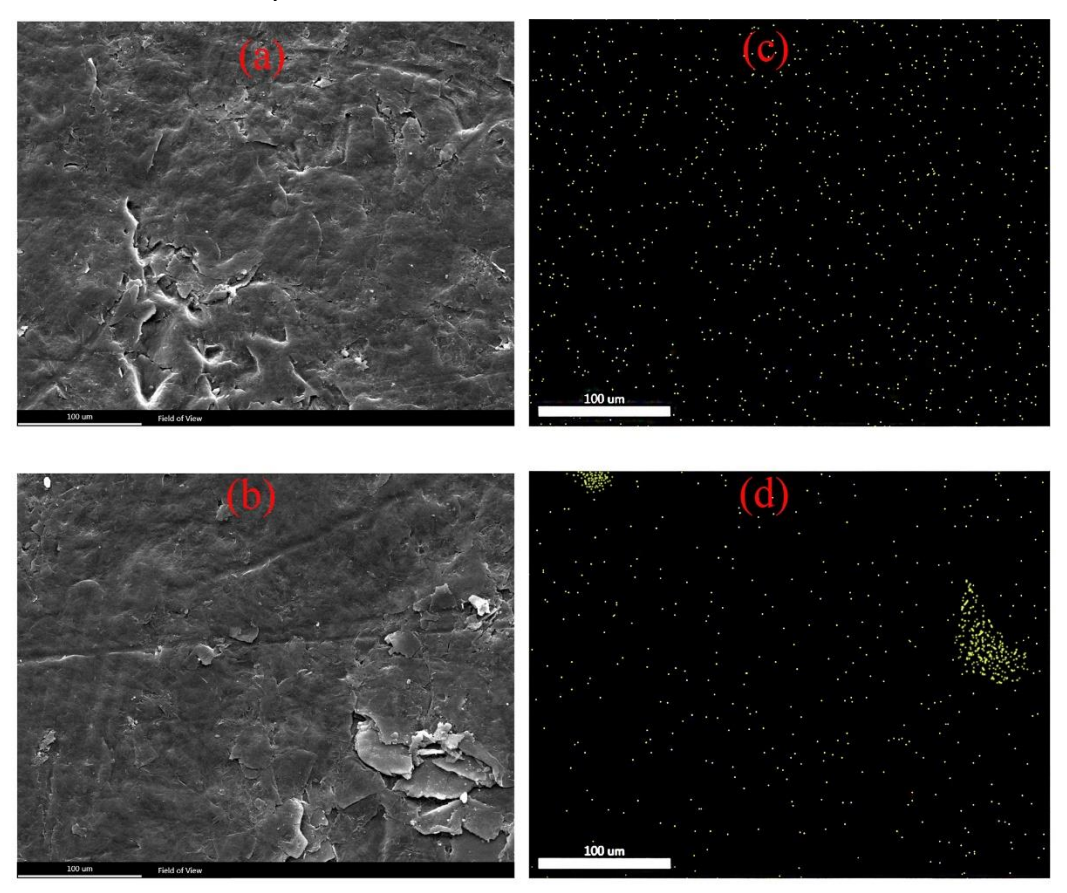


Figure 1. SEM images of Cat/BPPG (a) and Fc/BPPG (b) and EDS mappings for Fe atoms of catocene (c) and ferrocene (d) thin films on the BPPG electrode

Elemental analysis using EDS and LIBS of the two prepared electrodes is presented in Figure 2. EDS analysis provides a more accurate assessment of the elemental content and metal components of the films on surfaces due to the lower penetration ability of electrons into solid surfaces compared to X-ray photons. Impurities of some elements such as Ca, Mn, Fe, Ni, Zn, or others have been reported in graphite powders and their composites, depending on the production process [28]. According to Figure 2, EDS on the Cat/BPPG and Fc/BPPG surface indicates a nearly 6.0±2.0 atomic percent of iron on the electrode surfaces with dimensions of 500×500 μm. Furthermore, the surface analysis of electrodes using the highly sensitive LIBS technique equipped with an Nd: YAG laser with a wavelength of 1064 nm, output energy of 100.0 mJ, and pulse width of 2±7 nanoseconds was conducted in air. For the iron element, around 27 emission lines were reported, including 20 atomic emission lines (Fe I) and 7 ionic emission lines (Fe II), with the strongest emission line observed at 374.55 nm for Fe I [29]. Analysis of atomic spectra with the NIST LIBS database and NIST atomic spectra database on the LIBS spectra of various samples in Figure 2 shows that the presence of Fe element in BPPG surface is negligible. However, in the two electrodes modified with ferrocene and catocene, the presence of iron is noticeable in the wavelengths of 374 nm and the range of 230 to 275 nm. Atomic iron has various emission lines at wavelengths 249, 252, 272, 302, 357, 374, and 383 nm, and iron ion emission lines at 238, 259 and 274 nm. At about 390 nm, broad emission peaks due to carbon atoms or CN bonds resulting from the reaction with carbon and nitrogen in the air are observed. Atomic emission ranges of various carbon types at 248, 251, 284, 392, 426, 659 and 722 nm have been reported. Additionally, emission peaks at 600, 575, 567, 520 and 500 nm correspond to nitrogen [30].

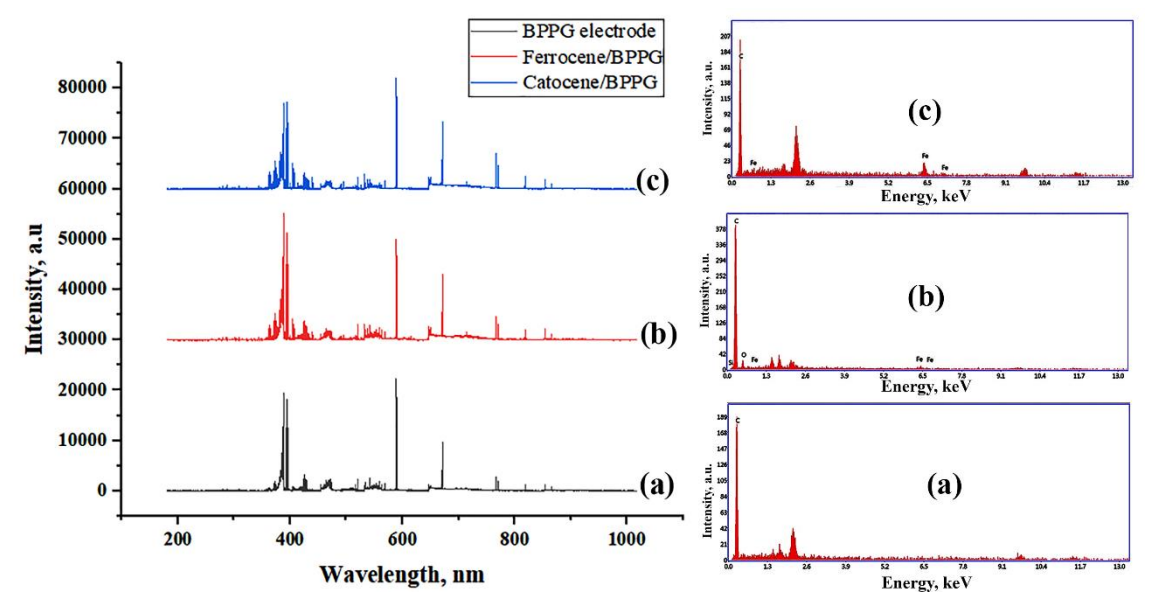


Figure 2. Elemental analysis by energy dispersive x-ray spectroscopy (EDS) (right) and laser-induced breakdown spectroscopy (LIBS) (left) of: a) BPPG, b) BPPG coated with ferrocene thin film, and c) BPPG coated with catocene thin film

Fourier transform infrared spectroscopy (FT-IR) is also suitable for detecting molecular functional groups and films created on electrodes. By examining the attenuated total reflectance (ATR) spectra of Fc/BPPG and Cat/BPPG electrodes (see Figure 3), the presence of components was not well-detected due to the low concentration of ferrocene or catocene films on the electrode surfaces, and some weak peaks were observed near 3000 cm⁻¹ wave number. Figure 3 presents FT-IR spectra of pure ferrocene and catocene, as well as ATR spectra of the modified electrodes.

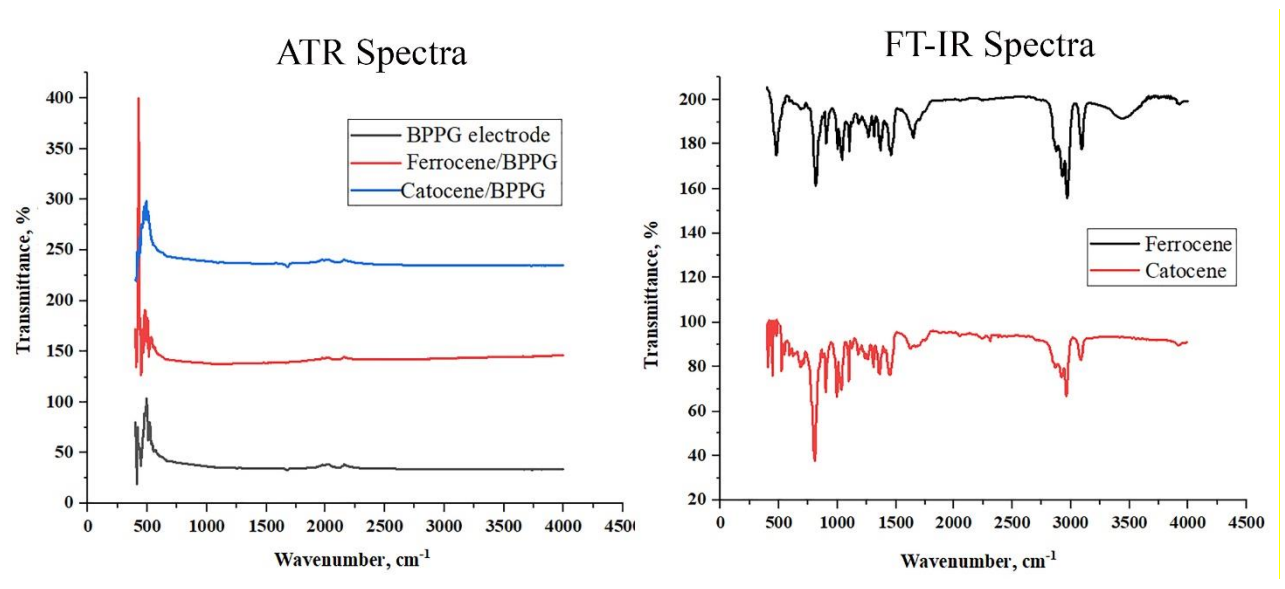


Figure 3. FT-IR spectra of pure catocene and ferrocene (right) and ATR spectra of modified BPPG electrodes (left)



For ferrocene, the features observed are consistent with the vibrational characteristics of cyclopentadienyl moieties, including C-H stretching (2840 to 3100 cm⁻¹), aromatic C-H asymmetric stretching vibrations (1566 to 1750 cm⁻¹), C=C phenyl stretching vibrations (1375 / 1465 cm⁻¹), C-H bending of methylene groups (985 to 995 / 905 to 915 cm⁻¹), C=C bending (815 cm⁻¹), and C-H bending vibrations (1030 cm⁻¹) [31]. Similar peaks are also observed for catocene FT-IR spectrum.

Voltammetry studies

Cyclic voltammetry was performed on liquid catocene-coated graphite electrode (Cat/BPPG), ferrocene-coated graphite electrode (Fc/BPPG), and bare graphite electrode (BPPG) in a three-electrode system with 1.0 M Na_2SO_4 electrolyte solution. The investigation covered the potential range of -0.5 to 2.0 V vs. Ag/AgCl at different scan rates from 20.0 to 140 mV s⁻¹. Figure 4 illustrates typical CV curves of the samples at various scan rates, showing two main peaks associated with the oxidation-reduction processes on Fc/BPPG and Cat/BPPG electrodes.

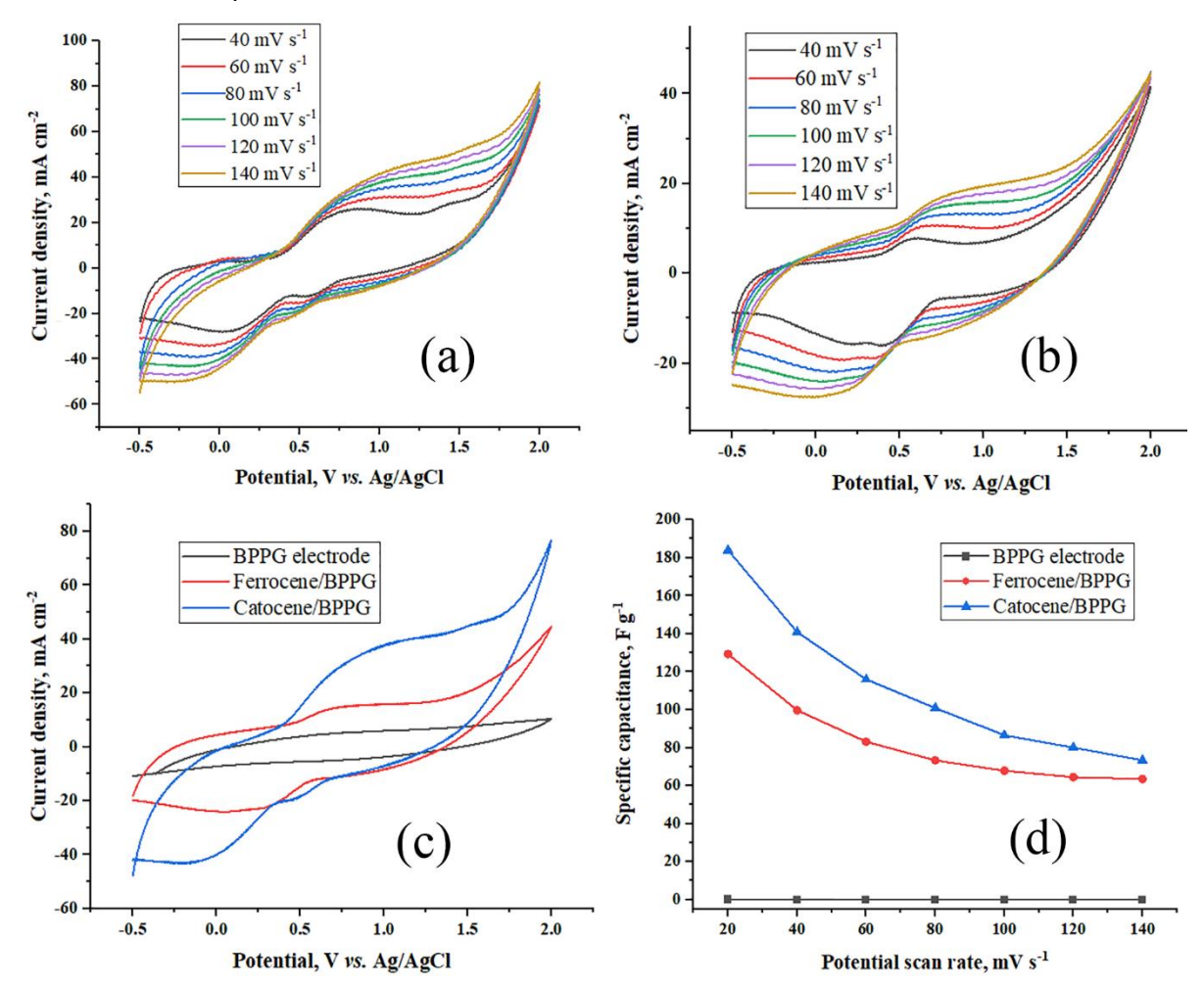


Figure 4. Supercapacitive performance of modified BPPG electrodes assessed from three-electrode measurements in 1.0 M Na₂SO₄. CV curves of (a) catocene thin film BPPG electrode and (b) ferrocene thin film BPPG electrode at different scan rates, and (c) comparison of CV curves at 100.0 mV s⁻¹. (d) Specific capacitance derived from (a) and (b)

Similar to the redox processes of ferrocene derivatives [23-32], ferrocene is usually oxidized to $Fe(C_2H_5)_2^+$ with an initial oxidation potential around 0.4 V. The Fe oxidation state in ferrocene or catocene is +2, and the cyclopentadienyl (C_5H_5) ligands carry a -1 charge. The reverse potential scan also exhibits a quasi-reversible reduction of $Fe(C_2H_5)_2^+$. Similar behaviour is observed for catocene. This substance is commonly used in defence and aerospace industries. It contains a small amount

of four isomeric compounds with different substitution positions for ethyl groups and di-ferrocenyl propane compounds, making their separation challenging due to nearly identical physical and chemical properties [33]. The presence of these impurities in catocene leads to an increase in the oxidation-reduction potential range of this iron complex and the appearance of a weak oxidation peak after 1.0 V and its corresponding reduction at +0.5 V. Of course, the generation of consecutive peaks in capacitors can improve their charge-discharge behaviour. With an increase in the potential scan rate, the oxidation peaks shift towards more positive potentials, and reduction peaks shift towards more negative potentials. This is because working electrodes have a low internal resistance, and a shorter time is available for the redox reactions. Additionally, with increasing scan rates, the area under CV curves and their currents increases. The anodic peak currents of catocene and ferrocene increased linearly with the square root of the scan rate. The following equations were obtained, respectively: $I = 118.49 \, v^{1/2} + 2.07$, $R^2 = 0.9942$, and $I = 61.67 \, v^{1/2} - 4.62$, $R^2 = 0.9985$, suggesting that the electrochemical reactions of modified electrodes are diffusion-controlled processes with quasi-reversible behaviour [34], and the related supercapacitor can be classified as a battery-like capacitor [28,36].

Trasatti's analysis method was utilized to further evaluate the contribution of EDLC and the quasireversible redox process with diffusion-controlled behaviour [37,46-47]. As mentioned in the literature [27], EDLC occurs on the outer surface of the electrode and contributes to the outer capacitance (C_{out}), which is assumed to be constant across the range of potential scanning rates. The redox contribution of capacitance is inner capacitance (C_{in}), controlled by semi-infinite linear diffusion with a rate proportional to $V^{-1/2}$. Also, the entire capacitive behaviour (C_{total}) is assumed to be divided into the contribution of the outer surface and inner surfaces of the electrode, as shown in equation 5 [27]:

$$C_{\text{total}} = C_{\text{out}} + C_{\text{in}} \tag{5}$$

Table 1 shows the capacitance contribution ratio analyzed based on the Trasatti method and the calculated areal capacitances at various potential scan rates obtained from Figure 4. It can be clearly seen that the charge storage in the Cat/BPPG and Fc/BPPG electrodes originates mainly from the battery-like contributions (93.75 and 78.02 %, respectively).

Table 1. Capacitance contribution of the electrodes as analyzed by the Trasatti method and the areal capacitance (F cm⁻²) based on CV curves shown in Fig. 4 (a-b)

Detential coop rate m)/	Areal capacitance, F cm ⁻²				
Potential scan rate, mV	BPPG electrode	Cat/BPPG	Fc/BPPG		
20.0	0.08	2.94	1.42		
40.0	0.06	2.25	1.1		
60.0	0.05	1.86	0.91		
80.0	0.044	1.61	0.81		
100.0		0.035	1.38	0.75	
$C_{\rm total}$ / F cm ⁻²		0.16	44.64	5.60	
C _{out} / F cm ⁻²		0.14	2.79	1.23	
$C_{\rm in}$ / F cm ⁻²		0.020	41.85	4.37	
Canaditanes contribution 0/	Battery like	12.70	93.75	78.02	
Capacitance contribution, %	EDLC	87.30	6.25	21.98	

In the rate-determining step of the oxidation reactions, the value of αn_{α} (where α is the charge transfer coefficient and n_{α} is the number of electrons involved in the rate-determining step) was calculated at a typical scan rate potential of 40.0 mV s⁻¹, according to the equation αn_{α} =0.048/(E_p - $E_{p/2}$).



In this equation, E_p is the potential of the anodic peak, and $E_{p/2}$ is the potential at half the anodic peak current. Calculations indicated that the value of αn_{α} for the oxidation of catocene and ferrocene on the BPPG electrode were 0.16 and 0.48, respectively. The higher value of α for ferrocene indicates a lower energy barrier path for forming the activated complex, overcoming the activation energy of electrochemical reactions. On the other hand, according to the voltammetry curves in Figure 4c, it is observed that the anodic current density for catocene oxidation is almost doubled compared to ferrocene. Figure 4d also shows that the specific capacitance of the electrode with a catocene film is higher than that with a ferrocene film. Here, the surface concentration of electroactive materials or surface coverage (Γ) was calculated according to equation (6) [38]:

$$\Gamma = \frac{Q}{nFA} \tag{6}$$

In this equation, Q is the area under the oxidation peak in the CV of the modified electrodes, n is the number of electrons participating in the reaction (n = 1 in the present case), A is the electrode surface area, and F is the Faraday constant. The surface coverage (Γ) for the electrodes modified with catocene or ferrocene at different potential scan rates is presented in Table 2. It is observed that as the scan rate increases, the value Γ decreases. Furthermore, the molar coverage of catocene on graphite is approximately 50 to 75 % higher than that of ferrocene.

The electrode substrate and porosity are the same for both Cat/BPPG and Fc/BPPG electrodes. However, the faradaic reaction efficiency and capacity of liquid catocene, despite having a higher molar mass (282.2 g mol⁻¹) compared to ferrocene (186.04 g mol⁻¹), have increased. The main factors contributing to the enhanced performance of the liquid redox material catocene are more uniform distribution and more effective interaction of the liquid catocene thin film than solid ferrocene film on the graphite BPPG electrode.

Table 2. Effect of potential scan rate on the surface coverage of catocene and ferrocene thin films on BPPG in $1.0 \text{ M Na}_2\text{SO}_4$

v/ mV s ⁻¹	Q,	′ mC	$arGamma$ / μ mol cm $^{ extstyle 2}$		
V/ IIIV S	Catocene	Ferrocene	Catocene	Ferrocene	
40.0	677.22	389.14	7.02	4.03	
60.0	560.28	326.84	5.81	3.39	
80.0	469.76	286.32	4.87	2.97	
100.0	400.95	254.03	4.16	2.63	
120.0	351.86	225.62	3.65	2.34	
140.0	310.48	208.05	3.22	2.16	

Electrochemical impedance spectroscopy and galvanostatic charge-discharge studies

Electrochemical impedance spectroscopy studies at a potential of +0.5 V, as depicted in the Nyquist diagram in Figure 5a, show a slightly depressed capacitive semicircles at high frequencies related to the charge-transfer resistance and double-layer capacitance. Table 3 lists the values of impedance parameters calculated by fitting the electrical equivalent circuit (EEC) in Figure 5a to the experimental results. The goodness of the fit can be judged by the estimated relative errors presented in the parentheses. According to the values of the electrical equivalent elements reported in this table, the charge transfer resistance ($R_{\rm ct}$) for ferrocene and catocene is 235.1 (±2.7 %) Ω cm² and 164.9 (±2.7 %) Ω cm², respectively. The apparent electron transfer rate constant ($K_{\rm app}$) has an inverse relationship with $R_{\rm ct}$ on Nyquist diagrams. In other words, with a decrease in $R_{\rm ct}$, the electrode reaction rates increase [34]. Therefore, the reaction rate at a constant potential for

catocene is nearly 40 % higher than that for ferrocene. In EIS studies, an appropriate equivalent circuit for the recorded Nyquist semicircles for modified electrodes is plotted in the inset of Figure 5a. The modelled equivalent circuits contain the solution resistance (R_s), the charge-transfer resistance of the oxidation step (R_{ct}), and a constant phase element corresponding to the double-layer capacitance (CPE_{dl}). The impedance of CPE_{dl} (Z_{CPE}) and infinite Warburg (Z_w) elements can be expressed as in equations (7) and (8) [38-40]:

$$Z_{\rm CPE} = Y_0^{-1} j^{-n} \tag{7}$$

$$Z_{W} = \sigma^{-1/2}(1-j) \tag{8}$$

In equation (7), Y_0 (the CPE parameter, S cm⁻² sⁿ) and n (dimensionless CPE exponent reflecting the roughness of the electrode surface) are two parameters independent of frequency, σ the Warburg impedance coefficient (Ω s^{-1/2} cm²) associated with the diffusivity in the electronic system; $j = -1^{1/2}$ and $\omega = 2\pi f$ is the angular frequency.

Figure 5 also presents the galvanostatic charge/discharge curves of the samples at different current densities within the potential window -0.5 to +1.2 V. It is observed that the discharge time of the samples increases with a decrease in current density.

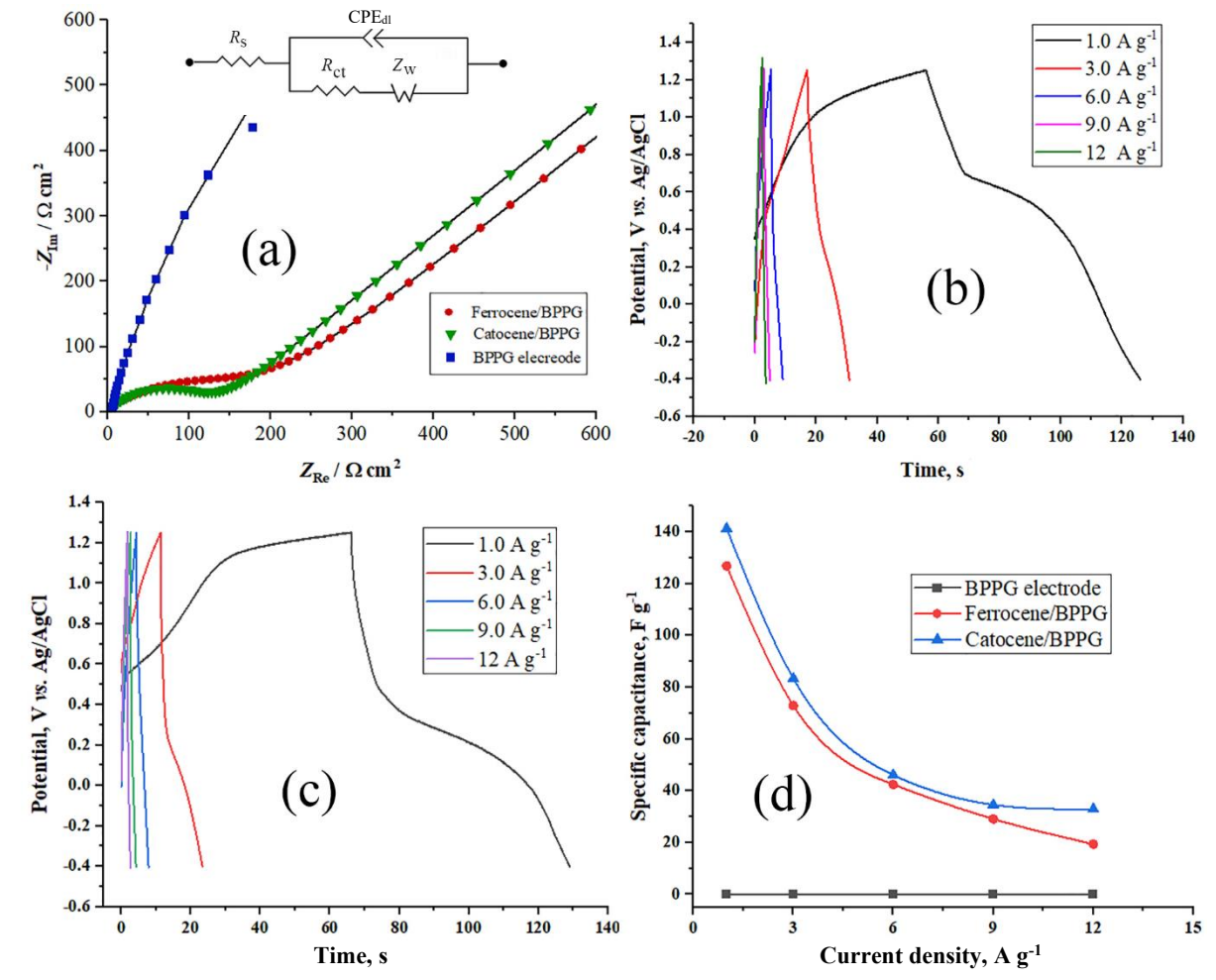


Figure 5. a) Nyquist diagram and equivalent circuit of modified electrodes for EIS studies by applying a bias of +0.5 V and an AC voltage of 10.0 mV amplitude in a frequency range from 100.0 kHz to 10 Hz in 1.0 M Na₂SO₄; b) GCD curves of Cat/BPPG, and c) Fc/BPPG at various current densities; d) specific capacitance versus current density for electrodes with the geometric area of 0.2 cm²

The specific capacitance (F g⁻¹) of the electrodes is calculated from their discharge curves at different current densities, and the results are presented in Figure 5d. By comparing GCD curves of

Cat/BPPG and Fc/BPPG samples at different current densities, the specific capacitance and performance of catocene-based film electrodes are 10-15 F g⁻¹ higher. The specific capacitance decreases with an increase in current density, likely due to mass transfer limitations and the diffusive mechanism of redox materials. The solid nature of ferrocene compared to the liquid catocene may lead to the formation of crystalline particles and aggregation of iron complex concentrations on the BPPG electrode surface, leading to reduced availability and performance of solid particles. SEM images of the Fc/BPPG electrode presented in Figure 1 also qualify the presence of some crystalline particles and localized iron concentrations on EDS mappings. Additionally, it appears that the van der Waals interaction of catocene molecules with the graphite surface is higher than that of ferrocene due to the more hydrophobic nature of ethyldicyclopentadienyl ligands compared to cyclopenta-1,3-diene.

Table 3. The values of electrode impedance parameters and the corresponding percentage relative errors for the oxidation of self-assembled catocene and ferrocene thin films on BPPG in 1.0 M Na_2SO_4

Clastus da	D / O ama?	D / O ares?	СР	PE	- /O a-1/2 amp?
Electrode	$R_s / \Omega \text{ cm}^2$	$R_{\rm ct}/\Omega~{\rm cm}^2$	Y ₀ / μS cm ⁻² s ⁿ	n	σ/Ω s ^{-1/2} cm ²
BPPG electrode	6.48	4645.6 (4.3 %)	0.01340 (3.2 %)	0.5500 (2.8 %)	
Fc/BPPG	7.10	235.1 (3.0 %)	0.06447 (1.9 %)	0.5480 (3.3 %)	1753.1 (2.6 %)
Cat/BPPG	6.90	164.9 (4.4 %)	0.08553 (3.1 %)	0.7041 (2.7 %)	1156.9 (0.25 %)

Due to the favourable performance of the liquid redox material catocene at a positive potential, it was decided to construct an asymmetrical supercapacitor by pairing it with a graphite negative electrode saturated with electrolyte, as described in the experimental section, and evaluate its performance. The aim was solely to compare the behaviour of the new redox material catocene with ferrocene. According to studies mentioned in the previous section, at a potential scan rate of 20.0 mV s⁻¹, a specific capacitance close to 185 F g⁻¹ for catocene and 125.0 F g⁻¹ for ferrocene thin film electrodes can be achieved.

Galvanostatic charge/discharge tests were performed on a two-electrode setup in the voltage window of 0.0-1.7 V. The energy and power densities of the samples were calculated according to equations (3) and (4). Ragone plots (energy density versus power density) of the supercapacitors are presented in Figure 6.

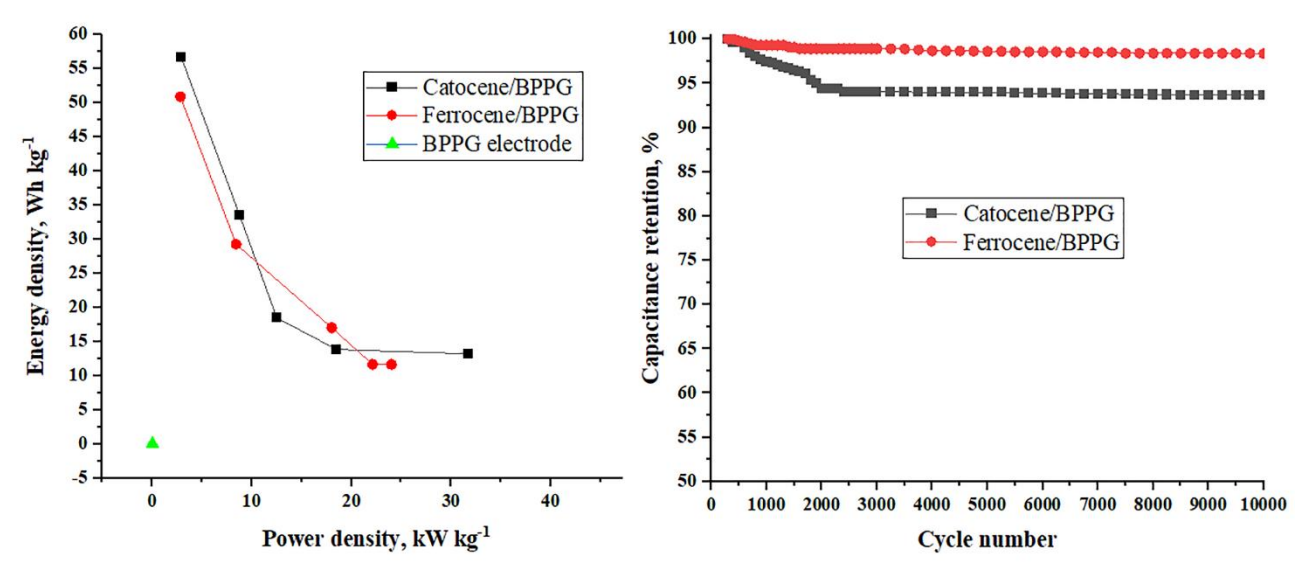


Figure 6. (a) Ragone plots of Cat/BPPG and Fc/BPPG asymmetrical supercapacitor; (b) cycling stability of two asymmetrical supercapacitors at a current density of 5.0 A g^{-1} and 1.0 M Na₂SO₄ electrolyte

Additionally, cyclic stability tests were conducted at a current density of 5.0 A g⁻¹ for 10000 GCD cycles. The constructed capacitor with catocene exhibited an energy density of 56.7 Wh kg⁻¹ at a power density of 2.9 kW kg⁻¹, while the capacitor based on ferrocene showed an energy density of 50.9 Wh kg⁻¹ at a power density of 2.8 kW kg⁻¹. Moreover, with an increase in power density, the energy density values exhibit a decreasing trend. The overall capacitance of the capacitors in consecutive charge-discharge cycles shows a slight reduction over 10000 cycles. After these GCD cycles, the electrode capacity of Cat/BPPG decreases by approximately 6.3 %, and Fc/BPPG decreases by nearly 3 %. The irreversible oxidation products often cause electrode surface fouling, reducing the effectiveness of redox reactions at working electrodes [41]. The lower performance of Cat/BPPG in GCD cycles tests can be caused by the partial destruction of the catocene molecule compared to ferrocene at high oxidation potentials and its conversion to Fe₂O₃ with a more irreversible electrochemical behaviour [42-43].

Here, the supercapacitance efficiency of some similar electrodes is compared in Table 4. It is observed that the self-assembled catocene on the BPPG electrode has a relatively high power density and discharge kinetics with suitable specific capacity. Of course, the main goal of this research is to compare the electrochemical efficiency of liquid catocene with solid ferrocene on the flat surface of BPPG. Certainly, by using more efficient carbon electrodes such as rGO or MWCNTs, the performance of these materials can be expected to be increased. By utilizing multi-walled carbon nanotubes (MWCNTs) functionalized with ferrocene, a specific capacitance of 50.0 F g⁻¹ at discharge current density of 0.25 A g⁻¹ has been recorded [20]. Cat/BPPG shows the specific capacitance of 141.2 and 57.0 F g⁻¹ at current densities of 1.0 and 5.0 A g⁻¹, respectively. Considering the high production stages and expensive cost of functionalized electrode materials and the limited amount of redox materials adhering under these conditions, it seems that the use of liquid catocene could also be a suitable approach for enhancing the performance of electrochemical capacitors.

Table 4. Supercapacitor performances of some carbon-modified electrodes taken from the literature

Electrode material	Electrolyte	Current	Specific	Energy den-	Power density,	Cyclos	Stability,	Ref.	
	Liectrolyte	density, A g ⁻¹	capacity, F g ⁻¹	sity, Wh kg ⁻¹	kW kg ⁻¹	Cycles	%	Rei.	
Mac/CO/DANI/CE3	3 М КОН	3.8	484					[44]	
MnS/GO/PANI/GE ^a	3 IVI KUH	1.0	773				-	[44]	
Ag-Ag ₂ O/PPy/GE ^b	0.1 M H ₂ SO ₄	2.0	500	23.6	0.51	5000	62	[45]	
ssDNA/rGO ^c	1 M KOH		129	-	-	10000	92	[46]	
MnO ₂ /CF ^d	2.0 M Li ₂ SO ₄	0.2	187.5	-	-	10000	99.0	[47]	
NiFe ₂ O ₄ /CF ^e	3.0 M KOH	1.0	490	39	0.41	5000	94.2	[48]	
Fc-MWCNTs ^f	2.0 M KOH	0.25	50	-	-	5000	90.8	[20]	
Cat/PDDC	1.0 M	1.0	141.2	56.7	2.9	10000	93.7	This	
Cat/BPPG	Na ₂ SO ₄	5.0	57.0	25.5	11.8	10000	93.7	work	

^aManganese sulfide (MnS)/graphene oxide (GO)/ polyaniline (PANI) nanocomposites on graphite electrode

Conclusion

In summary, this study compared the super-capacitive behaviour of two redoxes of liquid catocene, and solid ferrocene, on a basal plane pyroletic graphite electrode. Thin layers of these materials were self-assembled on the graphite electrode, and their super-capacitive behaviours were compared in an aqueous sodium sulphate electrolyte. The liquid catocene demonstrated a more uniform distribution



^bAg-Ag₂O/polypyrrole (PPy) nano composite on graphite electrode

^cSingle-stranded deoxyribonucleic acid (ssDNA) functionalized reduced graphene oxide

^dBinder-free electro-deposited MnO₂ @3D carbon felt network

^eNickel ferrite coated on carbon felt

^fFerrocene functionalized multi-walled carbon nanotubes

and better interaction with the BPPG surface than ferrocene, with its surface molar coverage up to 75 % higher. In voltammetric studies, this material exhibited a specific capacitance close to 185.0 F g⁻¹ at a potential scan rate of 20.0 mV s⁻¹, compared to 125.0 F g⁻¹ for ferrocene, and provided lower charge transfer resistance during oxidation. In a way, the energy density of the asymmetrical capacitor based on catocene was measured at 56.7 Wh kg⁻¹ at a power density of 2.9 kW kg⁻¹, while the ferrocene-based capacitor showed an energy density of 50.9 Wh kg⁻¹ at a power density of 2.8 kW kg⁻¹, and both capacitors maintained nearly 93.7 and 97.0 % of their overall capacitance in consecutive 10000 charge-discharge cycles, respectively. The calculation of capacitance contribution ratio analysed by Trasatti's method, showed that the charge storage in the Cat/BPPG and Fc/BPPG electrodes originates mainly from the battery-like contributions (93.75 and 78.02 %, respectively). Considering the high production stages and expensive cost of chemically functionalized carbonaceous electrodes with redox materials, the use of liquid redox materials such as catocene appears to be a suitable solution for improving the performance of electrochemical capacitors.

Acknowledgements: The authors are grateful for the financial support of this work by Malek-Ashtar University of Technology (I.R. Iran).

Disclosure statement: The authors declare that they have no known competing financial interests or personal relationships that could have appeared to influence the work reported in this paper.

References

- [1] S. Sharma, P. Chand, Supercapacitor and electrochemical techniques, *Results in Chemistry* **5** (2023) 100885. https://doi.org/10.1016/J.RECHEM.2023.100885
- [2] J. Qiu, H. Zhao, Y. Lei, Emerging smart design of electrodes for micro-supercapacitors, SmartMat 3 (2022) 447-473. https://doi.org/10.1002/SMM2.1094
- [3] N. S. Shaikh, S. B. Ubale, V. J. Mane, J. S. Shaikh, V. C. Lokhande, S. Praserthdam, C. D. Lokhande, P. Kanjanaboos, Novel electrodes for supercapacitor: Conducting polymers, metal oxides, chalcogenides, carbides, nitrides, MXenes, and their composites with graphene, *Journal of Alloys and Compounds* **893** (2022) 161998. https://doi.org/10.1016/J.JALLCOM.2021.161998
- [4] S. S. Shah, M. A. Aziz, W. Mahfoz, M. Akhtaruzzaman, *Types of Supercapacitors, in: Biomass-Based Supercapacitors Design, Fabrication and Sustainability,* John Wiley & Sons, Ltd, 2023, pp. 93-104. https://doi.org/10.1002/9781119866435.CH6
- [5] S. S. Rajaputra, N. Pennada, A. Yerramilli, N. M. Kummara, Graphene based sulfonated polyvinyl alcohol hydrogel nanocomposite for flexible supercapacitors, *Journal of Electrochemical Science and Engineering* **11** (2021) 197-207. https://doi.org/10.5599/JESE.1031
- [6] V. N. K. S. K. Nersu, B. R. Annepu, S. S. B. Patcha, S. S. Rajaputra, Rice husk char as a potential electrode material for supercapacitors, *Journal of Electrochemical Science and Engineering*, **12** (2022) 451-462. https://doi.org/10.5599/JESE.1310
- [7] M. S. Khan, P. Shakya, N. Bhardwaj, D. Jhankal, A. K. Sharma, M. K. Banerjee, K. Sachdev, Chemical vapor deposited graphene-based quasi-solid-state ultrathin and flexible sodium-ion supercapacitor, *Journal of Electrochemical Science and Engineering* **12** (2022) 799-813. https://doi.org/10.5599/JESE.1411
- [8] S. Tomar, V. K. Singh, Cobalt and copper-based metal-organic frameworks synthesis and their supercapacitor application, *Journal of Electrochemical Science and Engineering* **14** (2024) 163–175. https://doi.org/10.5599/JESE.2096

- [9] R. Maheswaran, B. P. Shanmugavel, A Critical Review of the Role of Carbon Nanotubes in the Progress of Next-Generation Electronic Applications, *Journal of Electronic Materials* **51** (2022) 2786-2800. https://doi.org/10.1007/S11664-022-09516-8/FIGURES/12
- [10] S. Damiri, H. Y. Varzaneh, H. R. Ebrahimi, PEG-assisted electrochemical growth of lead oxide nanodendrites with strongly enhanced charge storage capacity, *Materials Letters* **65** (2011) 2598-2600. https://doi.org/10.1016/J.MATLET.2011.06.024
- [11] M. Yu, X. Feng, Thin-Film Electrode-Based Supercapacitors, *Joule* **3** (2019) 338-360. https://doi.org/10.1016/J.JOULE.2018.12.012
- [12] B. Asbani, G. Buvat, J. Freixas, M. Huvé, D. Troadec, P. Roussel, T. Brousse, C. Lethien, Ultrahigh areal capacitance and high rate capability RuO₂ thin film electrodes for 3D microsupercapacitors, *Energy Storage Materials* **42** (2021) 259-267. https://doi.org/10.1016/J.ENSM.2021.07.038
- [13] S. Tanwar, A. Arya, A. Gaur, A. L. Sharma, Transition metal dichalcogenide (TMDs) electrodes for supercapacitors: a comprehensive review, *Journal of Physics: Condensed Matter*, **33** (2021) 303002. https://doi.org/10.1088/1361-648X/ABFB3C
- [14] S. Panda, K. Deshmukh, S. K. Khadheer Pasha, J. Theerthagiri, S. Manickam, M. Y. Choi, MXene based emerging materials for supercapacitor applications: Recent advances, challenges, and future perspectives, *Coordination Chemistry Reviews* **462** (2022) 214518. https://doi.org/10.1016/J.CCR.2022.214518
- [15] J. Wu, J. Peng, Z. Yu, Y. Zhou, Y. Guo, Z. Li, Y. Lin, K. Ruan, C. Wu, Y. Xie, Acid-Assisted Exfoliation toward Metallic Sub-nanopore TaS₂ Monolayer with High Volumetric Capacitance, *Journal of the American Chemical Society* **140** (2018) 493-498. https://doi.org/10.1021/JACS.7B11915
- [16] H. Li, Y. Liu, S. Lin, H. Li, Z. Wu, L. Zhu, C. Li, X. Wang, X. Zhu, Y. Sun, Laser crystallized sandwich-like MXene/Fe₃O₄/MXene thin film electrodes for flexible supercapacitors, *Journal of Power Sources* **497** (2021) 229882. https://doi.org/10.1016/J.JPOWSOUR.2021.229882
- [17] B. Chen, L. Xu, Z. Xie, W. Y. Wong, Supercapacitor electrodes based on metal-organic compounds from the first transition metal series, *EcoMat* **3** (2021) e12106. https://doi.org/10.1002/EOM2.12106
- [18] X. Chen, K. Chen, H. Wang, D. Xue, Composition Design Upon Iron Element Toward Supercapacitor Electrode Materials, *Materials Focus* 4 (2015) 78-80. https://doi.org/10.1166/MAT.2015.1213
- [19] M. L. Hu, M. Abbasi-Azad, B. Habibi, F. Rouhani, H. Moghanni-Bavil-Olyaei, K. G. Liu, A. Morsali, Electrochemical Applications of Ferrocene-Based Coordination Polymers, ChemPlusChem 85 (2020) 2397-2418. https://doi.org/10.1002/CPLU.202000584
- [20] G. A. M. Ali, E. Megiel, P. Cieciórski, M. R. Thalji, J. Romański, H. Algarni, K. F. Chong, Ferrocene functionalized multi-walled carbon nanotubes as supercapacitor electrodes, *Journal of Molecular Liquids* 318 (2020) 114064. https://doi.org/10.1016/J.MOLLIQ.2020.114064
- [21] R. Teimuri-Mofrad, R. Hadi, H. Abbasi, Synthesis and characterization of ferrocene-functionalized reduced graphene oxide nanocomposite as a supercapacitor electrode material, *Journal of Organometallic Chemistry* **880** (2019) 355-362. https://doi.org/10.1016/J.JORGANCHEM.2018.11.033
- [22] P. Saha, V. K. Yadav, V. Gurunarayanan, R. Ramapanicker, J. K. Singh, T. G. Gopakumar, Revealing the Limits of Intermolecular Interactions: Molecular Rings of Ferrocene Derivatives on Graphite Surface, *Journal of Physical Chemistry Letters* **11** (2020) 297-302. https://doi.org/10.1021/acs.jpclett.9b03357



- [23] N. Kurapati, P. Pathirathna, C. J. Ziegler, S. Amemiya, Adsorption and Electron-Transfer Mechanisms of Ferrocene Carboxylates and Sulfonates at Highly Oriented Pyrolytic Graphite, *ChemElectroChem* **6** (2019) 5651-5660. https://doi.org/10.1002/CELC.201901664
- [24] S. Damiri, H. R. Pouretedal, M. Mahmoudi, Sensitive Electrocatalytic Assay of Cyclotetramethylene Tetranitramine (HMX) Explosive on Carbon Nanotube/Ag Nanocomposite Electrode, *Iranian Journal of Catalysis* **12** (2022) 69-76. https://doi.org/10.30495/ijc.2022.689576
- [25] M. Sa'at, M. Yarmohammadi, M. Zamani Pedram, M. Shahidzadeh, M. S. Amini-Fazl, Evaluation of the catocene/graphene oxide nanocomposite catalytic activity on ammonium perchlorate thermal decomposition, *International Journal of Chemical Kinetics* **51** (2019) 337-345. https://doi.org/10.1002/KIN.21257
- [26] A. Noori, M. F. El-Kady, M. S. Rahmanifar, R. B. Kaner, M. F. Mousavi, Towards establishing standard performance metrics for batteries, supercapacitors and beyond, *Chemical Society Reviews* **48** (2019) 1272-1341. https://doi.org/10.1039/C8CS00581H
- [27] K. Liu, Z. Hu, R. Xue, J. Zhang, J. Zhu, Electropolymerization of high stable poly(3,4-ethylenedioxythiophene) in ionic liquids and its potential applications in electrochemical capacitor, *Journal of Power Sources* **179** (2008) 858-862. https://doi.org/10.1016/J.JPOWSOUR.2008.01.024
- [28] M. Ghosh, K. K. Swain, P. S. Remya Devi, T. A. Chavan, A. K. Singh, M. K. Tiwari, R. Verma, Determination of impurities in graphite using synchrotron radiation based X-ray fluorescence spectrometry, *Applied Radiation and Isotopes* **128** (2017) 210-215. https://doi.org/10.1016/J.APRADISO.2017.07.025
- [29] N. Idris, K. Lahna, Fadhli, M. Ramli, Study on Emission Spectral Lines of Iron, Fe in Laser-Induced Breakdown Spectroscopy (LIBS) on Soil Samples, *Journal of Physics: Conference Series* 846 (2017) 012020. https://doi.org/10.1088/1742-6596/846/1/012020
- [30] Y. Ralchenko, A. Kramida, Development of NIST Atomic Databases and Online Tools, *Atoms* **8** (2020) 56. https://doi.org/10.3390/ATOMS8030056
- [31] J. Shimei, W. Yue, Vibrational spectra of an open ferrocene and a half-open ferrocene. Spectrochimica Acta Part A: Molecular and Biomolecular Spectroscopy **55** (1999) 1025-1033. https://doi.org/10.1016/S1386-1425(98)00246-7
- [32] N. G. Tsierkezos, Cyclic voltammetric studies of ferrocene in nonaqueous solvents in the temperature range from 248.15 to 298.15, *Journal of Solution Chemistry* **36** (2007) 289-302. https://doi.org/10.1007/s10953-006-9119-9
- [33] L. Xiaoju, S. Qi, F. Haitao, Z. Chi, M. Xiaoyan, L. Xiaoju, S. Qi, F. Haitao, Z. Chi, M. Xiaoyan, Theoretical and experimental study on synthesis of high-content catocene. *Journal of Beijing University of Aeronautics and Astronautics* **47** (2021) 2514-2520. https://doi.org/10.13700/J.BH.1001-5965.2020.0497
- [34] A. J. Bard, L. R. Faulkner, *Electrochemical Methods: Fundamentals and Applications, 2nd Edition, John Wiley & Sons,* 2001.
- [35] Y. Gogotsi, R. M. Penner, Energy Storage in Nanomaterials Capacitive, Pseudocapacitive, or Battery-like? *ACS Nano* **12** (2018) 2081-2083. https://doi.org/10.1021/acsnano.8b01914
- [36] M. R. Thalji, G. A. M. Ali, P. Liu, Y. L. Zhong, K. F. Chong, W₁₈O₄₉ nanowires-graphene nanocomposite for asymmetric supercapacitors employing AlCl₃ aqueous electrolyte. *Chemical Engineering Journal* **409** (2021) 128216. https://doi.org/10.1016/J.CEJ.2020.128216
- [37] W. Pholauyphon, P. Charoen-amornkitt, T. Suzuki, S. Tsushima, Perspectives on accurately analyzing cyclic voltammograms for surface- and diffusion-controlled contributions, *Electrochemistry Communications* **159** (2024) 107654. https://doi.org/10.1016/J.ELECOM.2023.107654

- [38] S. Damiri, H. R. Pouretedal, A. Heidari, Fabrication of a nanostructured TiO₂/carbon nanotube composite electrode for voltammetric and impedimetric determination of NTO explosive in the water and soil samples, *International Journal of Environmental Analytical Chemistry* **96** (2016) 1059-1073. https://doi.org/10.1080/03067319.2016.1232722
- [39] K. M. Košiček, K. Kvastek, V. Horvat-Radošević, Different charge storage mechanisms at some carbon electrodes in redox active electrolyte revealed by electrochemical impedance spectroscopy, *Electrochimica Acta* **195** (2016) 77-84. https://doi.org/10.1016/J.ELECTACTA.2016.02.140
- [40] C. P. Zimmermann, G. M. Kranz, J. P. Eckert, L. Fadani, M. Zanetti, J. M. M. de Mello, P. R. Innocente, G. L. Colpani, M. A. Fiori, C. H. Scuracchio, Ionic Polymer-Metal Composite Coated with Polyaniline Film by Electrodeposition: A Promising IPMC/PANI Junction for Applications in Robotics and Bioengineering, *Materials Research* 26 (2023) e20220609. https://doi.org/10.1590/1980-5373-MR-2022-0609
- [41] J. Jang, H. U. Cho, S. Hwang, Y. Kwak, H. Kwon, M. L. Heien, K. E. Bennet, Y. Oh, H. Shin, K. H. Lee, D. P. Jang, Understanding the different effects of fouling mechanisms on working and reference electrodes in fast-scan cyclic voltammetry for neurotransmitter detection, *Analyst* **149** (2024) 3008-3016. https://doi.org/10.1039/D3AN02205F
- [42] B. Z. Jiang, T. P. Wang, Oxidation of Catocene in AP/Catocene Mixture at Low Temperature, *Propellants, Explosives, Pyrotechnics* **44** (2019) 513-518. https://doi.org/10.1002/PREP.201800168
- [43] S. K. Patil, M. M. Vadiyar, S. C. Bhise, S. A. Patil, D. V. Awale, U. V. Ghorpade, J. H. Kim, A. V. Ghule, S. S. Kolekar, Hydroxy functionalized ionic liquids as promising electrolytes for supercapacitor study of α -Fe₂O₃ thin films, *Journal of Materials Science: Materials in Electronics* **28** (2017) 11738-11748. https://doi.org/10.1007/S10854-017-6978-3
- [44] K. Y. Yasoda, S. Kumar, M. S. Kumar, K. Ghosh, S. K. Batabyal, Fabrication of MnS/GO/PANI nanocomposites on a highly conducting graphite electrode for supercapacitor application, *Materials Today Chemistry* **19** (2021) 100394. https://doi.org/10.1016/J.MTCHEM.2020.100394
- [45] E. Karaca, D. Gökcen, N. Ö. Pekmez, K. Pekmez, Galvanostatic synthesis of nanostructured Ag-Ag₂O dispersed PPy composite on graphite electrode for supercapacitor applications. *International Journal of Energy Research* **44** (2020) 158-170. https://doi.org/10.1002/ER.4881
- [46] Y. Albarqouni, G. A. M. Ali, S. P. Lee, A. R. Mohd-Hairul, H. Algarni, K. F. Chong, Dual-functional single stranded deoxyribonucleic acid for graphene oxide reduction and charge storage enhancement, *Electrochimica Acta* **399** (2021) 139366. https://doi.org/10.1016/J.ELECTACTA.2021.139366
- [47] V. Prabu, K. Geetha, R. Sekar, M. Ulaganathan, Binder-Free Electro-Deposited MnO₂@3D Carbon Felt Network: A Positive Electrode for 2V Aqueous Supercapacitor, *Energy Technology* **11** (2023) 2201345. https://doi.org/10.1002/ENTE.202201345
- [48] S. Azizi, M. B. Askari, S. M. Rozati, M. Masoumnezhad, Nickel ferrite coated on carbon felt for asymmetric supercapacitor, *Chemical Physics Impact* 8 (2024) 100543. https://doi.org/10.1016/J.CHPHI.2024.100543

© 2024 by the authors; licensee IAPC, Zagreb, Croatia. This article is an open-access article distributed under the terms and conditions of the Creative Commons Attribution license (https://creativecommons.org/licenses/by/4.0/)





Open Access:: ISSN 1847-9286 www.jESE-online.org

Original scientific paper

Optimal design of LiMn₂O₄ for high-rate applications by means of citric acid aided route and microwave heating

Yurii V. Shmatok^{1,⊠}, Hanna V. Potapenko^{1,2} and Sviatoslav A. Kirillov¹

¹Joint Department of Electrochemical Energy Systems of the National Academy of Science of Ukraine, 38A Vernadsky Ave., 03680 Kyiv, Ukraine

²Faculty of Materials Metallurgy and Chemistry, Jiangxi University of Science and Technology, Ganzhou 341000, China

Corresponding author: [™] <u>yu.shmatok@gmail.com</u>

Received: January 24, 2024; Accepted: June 11, 2024; Published: June 13, 2024

Abstract

Due to the shortening of the duration of the process and the possibility of obtaining crystals of smaller and uniform size, microwave heating is considered an effective and promising tool for the synthesis of $LiMn_2O_4$, a valuable cathode material for lithium-ion batteries. However, the electrochemical characteristics of $LiMn_2O_4$ obtained with its help are almost completely absent and do not allow for drawing a sound conclusion regarding the advantages and drawbacks of microwave processing. Here, we describe the microwave-assisted citric acid aided synthesis, characterization and electrochemical performance of $LiMn_2O_4$. The disclosure of detailed working protocols enabling one to manufacture samples tolerant to extremely high currents is the main novelty of this paper. Specifically, our material sustains current loads up to 40 C (5920 mA g^{-1}) and completely recovers after cycling in harsh conditions.

Keywords

Microwave processing; batteries; lithium manganese spinel; high-rate properties

Introduction

Thirty years after successful commercialization, lithium-ion batteries continue to conquer the world, making them increasingly independent of wired power supplies. Lithium manganese spinel LiMn₂O₄ belongs to a privileged group of successfully commercialized cathode materials [1]. Unlike ubiquitous LiCoO₂, lithium manganese spinel is cheap and non-toxic, so its application fields are being expanded steadily and have already captured the automotive industry [2].

The synthesis method plays a key role in obtaining high-performance spinels. Analysis reveals, however, that standard solid state and precipitation routes cannot provide proper electrochemical parameters [3]. The theoretical specific capacity of LiMn₂O₄ ($Q_{sp,theor.}$ = 148 mAh g⁻¹) is seldom attained, and the ability to sustain high current loads shows up in hard-to-reach nanostructured samples.

An idea of improving the quality of electrode materials by passing from micro- to nanosized level, first articulated by Aricò *et al.* [4], relies on the possibility of reducing the transport path of lithium ions and electrons within the electrode volume upon the subdivision of material particles, thereby augmenting their high-rate properties. This idea was involved in a huge variety of works carried out by means of sol-gel methods [5,6], spray pyrolysis [7], hydrothermal technology [8], as well as approaches inherent to nanochemistry, like self-assembly [9], template synthesis [10], *etc.* [11,12]. Most of these approaches can hardly be implemented in the near future due to their intricate nature. On the other hand, there are several easily scalable methods that look prospectively for significant enhancement of the properties of electrode materials. These are a citric acid-aided route and microwave heating, briefly discussed in what follows and constitute the subject of this work.

Oxy- and amino acid-aided routes are widely used for the synthesis of electrode materials [3,11] and have already been implemented on a small to medium-sized level [13,14]. The essence of the citric acid aided route lies in the pyrolysis of acidic metal citrates, which is strongly exothermal, involves the loss of a great amount of gaseous reaction products, and leads to oxides or their mixtures in the nanosized form. Much work has been done to optimize the synthetic conditions to obtain materials with the smallest particle size. It has been shown, in particular, that in the course of the synthesis, acidic metal citrates are forming, an optimal metal-to-acid ratio is 1:2, and additives, like ethylene glycol, are unnecessary [15,16]. This modified citric acid aided route has been employed for obtaining and detailed characterization of several electrode materials of exceptional high-rate performance [17-23].

Using microwave (MW) radiation in the synthesis of electrode materials has advantages from several viewpoints [24,25]. Due to the interactions of microwaves with particles, the heat is generated directly in the volume of a material and spreads rapidly and uniformly. First of all, this significantly reduces the duration of synthesis. Second, decreasing heat exposure time results in obtaining more finely dispersed and less agglomerated materials. This makes microwave heating an effective tool for controlling the particles' morphology. The possible use of MW heating in the manufacturing of electrode materials is favored by the widespread use of microwave ovens in industrial heating and drying applications like pharmaceutical production, food processing, crop and timber drying, etc.

As follows from literature sources dealing with LiMn₂O₄, the use of MW radiation is indeed an effective and promising method. Carrying out MW heating at various stages of solid state, sol-gel (combustion) and hydrothermal syntheses [26-43] reduces the duration of the process and promotes the formation of crystals of smaller and more uniform size. However, data on the electrochemical characteristics of such materials are either completely absent [27,28,31,35,36,42] or limited by a conclusion regarding fast capacity fade during relatively short cycling and discharge with currents up to 10 C [26,29,30,32-34,37-41,43]. The same is true for LiMn₂O₄ obtained by means of a citric acid aided route and MW heating [44,45]. Only very recently, LiMn₂O₄ synthesized in this manner has been subjected to detailed electrochemical tests [46]. It appears, however, that in spite of quite similar particle size, its high-rate properties are much worse than those of a material made with the help of conventional thermal treatment [17,20]. One may speculate that the synthetic protocol employed in [45] is far from optimal. For comparison, the electrochemical properties of LiMn₂O₄ spinels obtained by various synthesis methods in combination with MW heating are summarized in Table 1.

Synthesis method	Discharge capa	city, mAh g ⁻¹ (<i>C</i> -rate)	_ Capacity retention, % /	Ref.	
Synthesis method	C_{min}	$C_{\sf max}$	C-rate/ cycle	nei.	
MW solid state	120 (0.2 C)	-	72 / 1 C / 300	[26]	
MW solid state	102	-	~80 / 100	[30]	
MW solid state	112 (0.25 C)	95 (1 C)	82 / 1 C / 50	[37]	
MW solid state	142.5 (0.1 C)	~90 (10 C)	-	[38]	
MW solid state	121 (1 C)	57 (13.5 C)	95 / 1 C / 20	[47,48]	
MW combustion	112-133 (C/3)	117 (1 C)	90 / C/3 / 30	[32,33]	
MW combustion	114 (1 C)	-	75 / 1 C /100	[40]	
MW sol-gel	116 (0.3 C)	-	98 / 0.3 C / 30	[45]	
MW combustion	120 (1 C)	~60 (10 C)	~30 / 1 C / 1000	[46]	
MW rheological phase	127 (1/6 C)	117 (2/3 C)	~84 / C/3 / 40	[34]	
MW co-precipitation	132 (0.2 C)	92 (10 C)	75 / 0.5 C / 100	[39]	
MW hydrothermal	89 (0.14 C)	59 (1.4 C)	85 / 0.14 C / 25	[41]	
MW hydrothermal	132 (0.1 C)	34 (10 C)	73 / 0.1 C / 50	[43]	

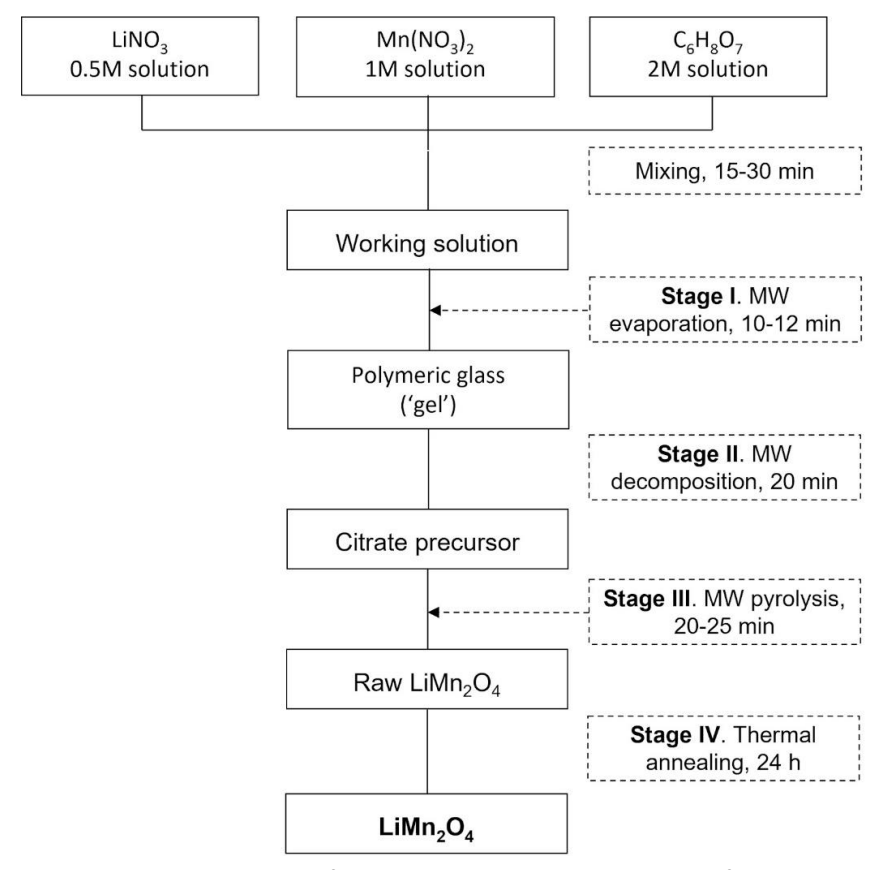
Table 1. Electrochemical properties of LiMn₂O₄ spinels obtained by various MW-assisted synthesis methods

In previous papers of our lab, conventional and MW-assisted solid-state routes of the synthesis of LiMn₂O₄ from various raw materials have been compared [47,48]. It has been found that the samples synthesized from carbonates behave better than those obtained from acetates, and microwave-heated specimens overwhelm those prepared by a conventional method. Specifically, they have $Q_{sp.}$ close to 120 mAh g⁻¹ and deliver ~50 % of their initial capacity being loaded with the current of 1500 to 2000 mA g⁻¹ (10-13.5 C). Here, we continue this work and present a description of the synthesis, characterization and electrochemical performance of LiMn₂O₄ obtained by means of microwave-assisted citric acid aided route. The combination of this synthesis technique with MW heating makes it possible to significantly reduce the particle size compared to the previously used MW-assisted solid-state method, which positively affects the kinetic characteristics of LiMn₂O₄. The disclosure of detailed working protocols enabling one to manufacture samples faster, sustaining the currents that exceed 5900 mA g⁻¹ (~40 C) is the main novelty of this paper.

Experimental

Reagents and MW synthesis

Solutions of lithium nitrate, manganese nitrate and citric acid were prepared from analytical grade LiOH, HNO₃, Mn(NO₃)₂·6H₂O, and C₆H₈O₇·H₂O (Makrokhim, Ukraine). To ensure twofold excess of the acid over the sum of metals, 60 ml of 0.5 M LiNO₃, 60 ml of 1 M Mn(NO₃)₂ and 90 ml of 2 M C₆H₈O₇ solutions were mixed and subjected to stirring on a magnetic stirrer for 15 to 30 min. The total volume of the working solution for a batch subjected to MW irradiation was 30 ml. MW synthesis was performed in household Saturn ST-MW7154 (Czech Republic) and LG MS-1949W (Korea) MW ovens with radiation frequency of 2.45 GHz and maximal power of 700 W. The MW radiation power was set in the range from 120 to 700 W, depending on the stage of synthesis, which is described in more detail below. Temperature measurement was carried out by means of a UT303A contactless infrared pyrometer after temporarily switching the furnace off. The final annealing was performed in a muffle furnace in the air for 24 h at 700 °C with heating and cooling rates of 5 and 2 °C min⁻¹, respectively. All operations were executed in alumina or thermal glass beakers. A flowchart of the synthesis is presented in Scheme 1.



Scheme 1. Flowchart of citric acid aided MW synthesis of LiMn₂O₄

Characterization

X-ray diffraction (XRD) measurements were made on a LOMO DRON-4-07 X-ray diffractometer (Russia) with Cu- K_{α} (λ = 0.15418 nm) radiation. Crystallite size was calculated using the Scherrer equation. Scanning electron micrographs (SEM) were taken on a JEOL JSM 6700F microscope (Japan). Surface area and porosity were measured on a Micromeritics ASAP 2000 device (USA).

Electrochemical tests

Electrochemical testing was carried out on a homemade automatic workstation in 2016 coin cells with lithium anode. The slurry containing 80.6 % of LiMn₂O₄, 11.4 % of a conducting additive (5 % SFG-6 and 6.4 % Super P, both Timcal) and 8 % of a binder (PVDF, Kureha) was cast on an aluminum foil by a doctor blade with a gap of 125 μ m. A Celgard 2500 separator (Switzerland) of 25 μ m thickness was employed. The mass load of LiMn₂O₄ was in the range of 4.4-5.2 mg cm⁻². Before cell assembling, electrodes were dried at 120 °C for 15 h in a vacuum. 1M solution of LiPF₆ in a mixture of ethylene carbonate and dimethyl carbonate (1:1 by mass, Aldrich, USA) served as electrolyte. Galvanostatic measurements were performed within the 3.4-4.5 V potential range employing a constant current constant voltage (CCCV) charge mode. Current densities were measured in C-rate values based on the theoretical specific capacity of LiMn₂O₄ (1 C = 148 mA g⁻¹). Cyclic voltammetric (CV) curves were registered within the same voltage limits at 0.1 mV s⁻¹ sweep rate.

Results and discussion

MW synthesis

The known scheme of a citric acid aided route consists of the following stages [11,15,16]. Evaporating solutions containing a metal nitrate and citric acid, one obtains glassy hydrous acidic

citrates, including nitric acid. Decomposing these glasses leads to precursors of hydrous acidic citrates in the form of sponge-like cakes. Pyrolysis of the precursors and (optionally) further annealing of pyrolysis products gives target oxides. All these stages are well distinguishable in MW synthesis.

The removal of water (stage I) and the formation of a citrate precursor (stage II) can be performed continuously. Stage I has been carried out at a radiation power of 260 W. The process lasts for 10 to 12 min; the viscosity of the solution grows, and emission centers of a brown gas (NO_2) appear on the surface, signifying that the displacement of nitric acid by citric acid begins and the formation of a citrate precursor starts. To decrease gas evolution rate, the radiation power must be reduced to 120 W for 5 min. For complete removal of nitrous oxides, further heating at 460 W for 5 min and at 600 W for 10 min. is required. At these conditions, the main part of gaseous products is removed and the citrate precursor is obtained in the form of the so-called sponge-like cake.

The pyrolysis of citrate precursors (stage III) is known to be a stepwise process involving (i) endothermic dehydration of a hydrous salt and decomposition of citrate anion to the anions of (ii) aconitic and (iii) citraconic acid and then to (iv) citraconic anhydride, whose breakdown (v) occurs exothermically. Performing stage III requires a radiation power of 700 W. At the initial stage, heating occurs quickly, and dehydration ends in 2 to 2.5 min at ~150 to 200 °C. In cases where a reaction product rises, it has to be deflated by punching down with a spatula. Further heating is slow and 15 to 20 min elapse until exothermic reaction begins. Its onset is marked by releasing an acrid smoke, changing the color of the reaction product to black. Then it becomes red hot (Figure 1) and sometimes an open flame appears. At this moment, the product has either been removed from the oven or subjected to MW post-heating at 420 W for 2 or 4 min. In the former case, the mean temperature equals 450 to 520 °C (at the peak moment of combustion, the temperature exceeds 600 °C) and visually, burning is self-propagating. Such a wide range of temperatures is associated with a change in the amount of heat released during the gradual propagation of combustion. In the latter cases, the mean temperature is the same, and the maximal temperature exceeds 650 °C. In this case, the higher temperature is associated with the simultaneous combustion of the precursor and the heating under the MW radiation of the oxide phase formed. Hereinafter, the samples are marked MW-0 (without MW post-heating), MW-2 (MW post-heating at 420 W for 2 min) and MW-4 (MW post-heating at 420 W for 4 min).



Figure 1. Burning of a citrate precursor

All these operations last for maximally 1 h in total and occur at least twice as shorter as at common heating. The synthesis was completed by prolonged annealing (stage IV) in a muffle furnace at the temperature of 700 °C, as indicated in the Experimental section.

Characterization

To understand how thermal treatment influences the parameters of materials, we have compared diffractograms of pyrolyzed products at different stages. As follows from Figure 2a, LiMn₂O₄ is directly forming from acidic citrates of manganese and lithium at Stage III just after burning and before MW post-heating at 420 W, this is evidenced by the presence of reflections from its (111), (311), (222), (400), (331), (511), (440) i (531) crystallographic planes. During this time, however, a great number of Mn₃O₄ admixtures are accumulated. Continuing MW treatment (post-heating) at Stage III and performing annealing at 700 °C for 24 h (stage IV), one obtains single-phase LiMn₂O₄ with no admixtures (Figure 2b-d).

Lattice parameters (a) and volumes (V), as well as crystallite sizes (d_{400}) determined using the reflection from the (400) plane for MW-0, MW-2 and MW-4 samples, are collected in Table 2. It is seen that all samples are commensurable by lattice parameters, volumes, and crystallite sizes, so the variation of residence time upon MW treatment does not influence these values. On the other hand, comparing a, V and d_{400} for our samples and materials synthesized by means of MW-assisted solid state reaction [47,48], one reassures that the latter leads to more dense specimens.

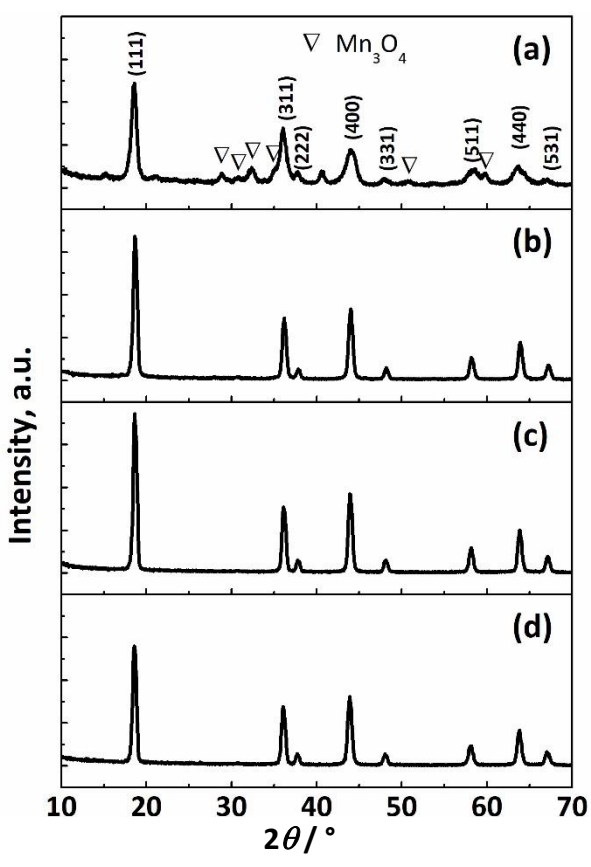


Figure 2. XRD patterns of LiMn₂O₄ just after burning and before MW post-heating at 420 W (a), and after MW post-heating at 420 W and annealing at 700 °C for 24 h (b) MW-0, (c) MW-2, (d) MW-4. Peak indexing corresponds to JCPDS 35-782 (LiMn₂O₄) and 24-0734 (Mn₃O₄)

SEM data for our samples are presented in Figure 3. Here, one can follow the influence of both MW-post-heating (stage III) and annealing (stage IV) on the sample morphology. LiMn₂O₄ taken just after burning has a particle size of less than 50 nm (Figure 3a). Further annealing at 700 °C for 24 h

causes expected particle enlargement to 50-60 nm size (Figure 3b). Interestingly, the samples were subjected to the MW post-heating for 2 and 4 min, and annealing increased their size to 100-120 nm (Figure 3c, d). For the same samples, the particles are more perfect (the edges of the faces of the crystals characteristic of the $LiMn_2O_4$ octahedral shape are clearer), which is evidence of the higher crystallinity of these samples. This observation confirms that crystal growth, sintering and recrystallization are much faster upon MW treatment. In our case, the particle size doubles upon MW heating at 420 W for 4 min. Given this, more prolonged MW post-heating was not performed to avoid further growth of particle size.

Porosimetric studies signify that the samples obtained are non-porous. This is common for spinels [16,17]. It appears that the MW-post-heating significantly decreases both specific surface area ($S_{sp.}$) and pore volume (V_{pore}) (Table 2). Such observation is consistent with SEM data and probably results from compaction upon sintering.

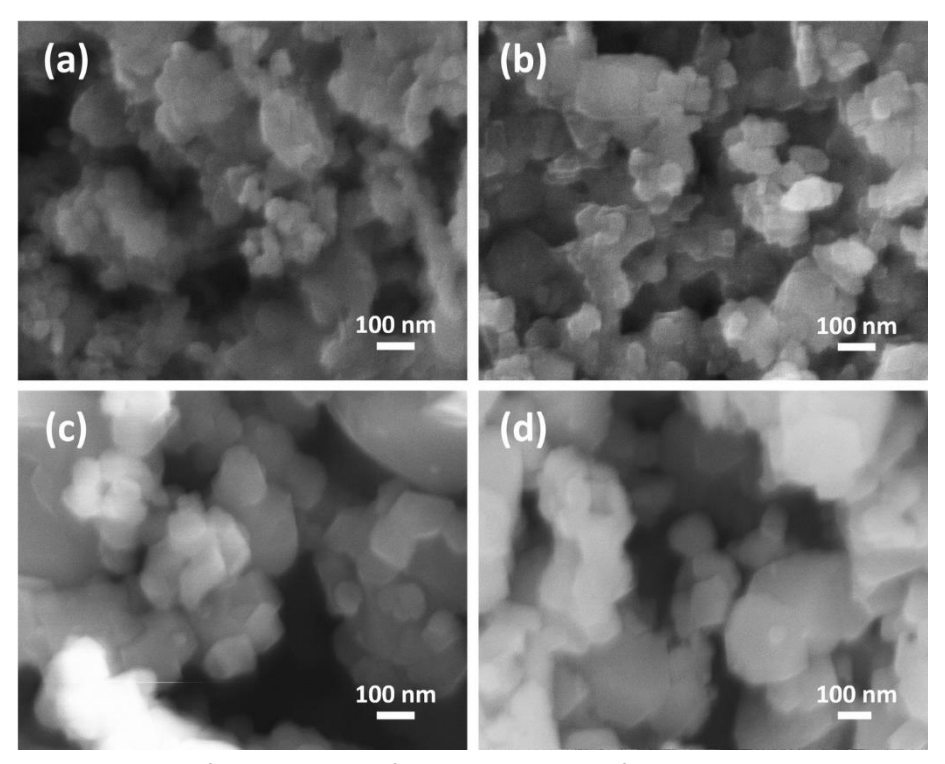


Figure 3. SEM micrographs of LiMn₂O₄ just after burning and before MW post-heating at 420 W(a), and after MW post-heating at 420 W and annealing at 700 °C for 24 h (b) MW-0, (c) MW-2, (d) MW-4

•	Sample	<i>a</i> / nm	V/nm³	d ₄₀₀ / nm	Particle size, nm	$S_{sp} / m^2 g^{-1}$	V _{pore} / cm ³ g ⁻¹
	MW-0	0.8195	0.550	17	50	13.3	0.147
	MW-2	0.8204	0.552	18	100	5.4	0.048
	MW-4	0.8212	0.554	18	120	5.4	0.047

Table 2. Parameters of various LiMn₂O₄ samples

Electrochemical tests

Figure 4a-c shows the first three charge/discharge cycles for MW-0, MW-2 and MW-4 samples. All these curves have a typical form demonstrating two plateaus corresponding to equilibria between $LiMn_2O_4$ and an intermediate $Li_{0.5}Mn_2O_4$ and between the latter and MnO_2 . In all cases, a solid electrolyte interface forms at the first charge, causing a great excess of charge capacity over discharge capacity: Coulombic efficiencies measured as $CE = Q_{sp, discharge}/Q_{sp, charge}$ ratio do not exceed 86 %. Upon 2^{nd} and 3^{rd} cycles, these become close to 100 %. The specific capacities of MW-0, MW-2 and MW-4

samples on the 3rd cycle appear equal to 85, 97 and 90 mAh g⁻¹. In general, the specific capacity of spinels is often significantly lower than the theoretical value, which is a typical phenomenon for this electrode material [3]. For example, in conventional citrate syntheses of LiMn₂O₄, the best Q_{SD} obtained is 110 mAh g-1 [20]. In our case, a significant part of lithium ions (about a third of the theoretical content) is unavailable for certain reasons and does not participate in the electrochemical process at all. However, it should be noted that during the combined CCCV charge mode, the share of the capacity obtained in the constant voltage mode is small compared to the capacity in the constant current mode, which indicates a sufficiently high mobility of the lithium ions available for the electrochemical process. The same conclusion follows from the shape of cyclic voltammetry (CV) curves (Figure 4d). The CV curves of MW-2 and MW-4 samples have two distinct peaks corresponding to the intercalation/deintercalation of lithium ions in the spinel structure. These samples are close to each other and are characterized by higher peak intensities than the MW-0 sample. In the latter case, the peaks are practically not split and shifted to higher potentials during charge and to lower potentials during discharge due to polarization. According to the data presented in Table 3, the difference between the corresponding CV peaks ΔE_1 and ΔE_2 in the case of MW-2 and MW-4 samples is actually half as much as compared to MW-0 sample. CV data registered for MW-2 and MW-4 samples suggest their lower current resistance and better kinetics of charge/discharge processes.

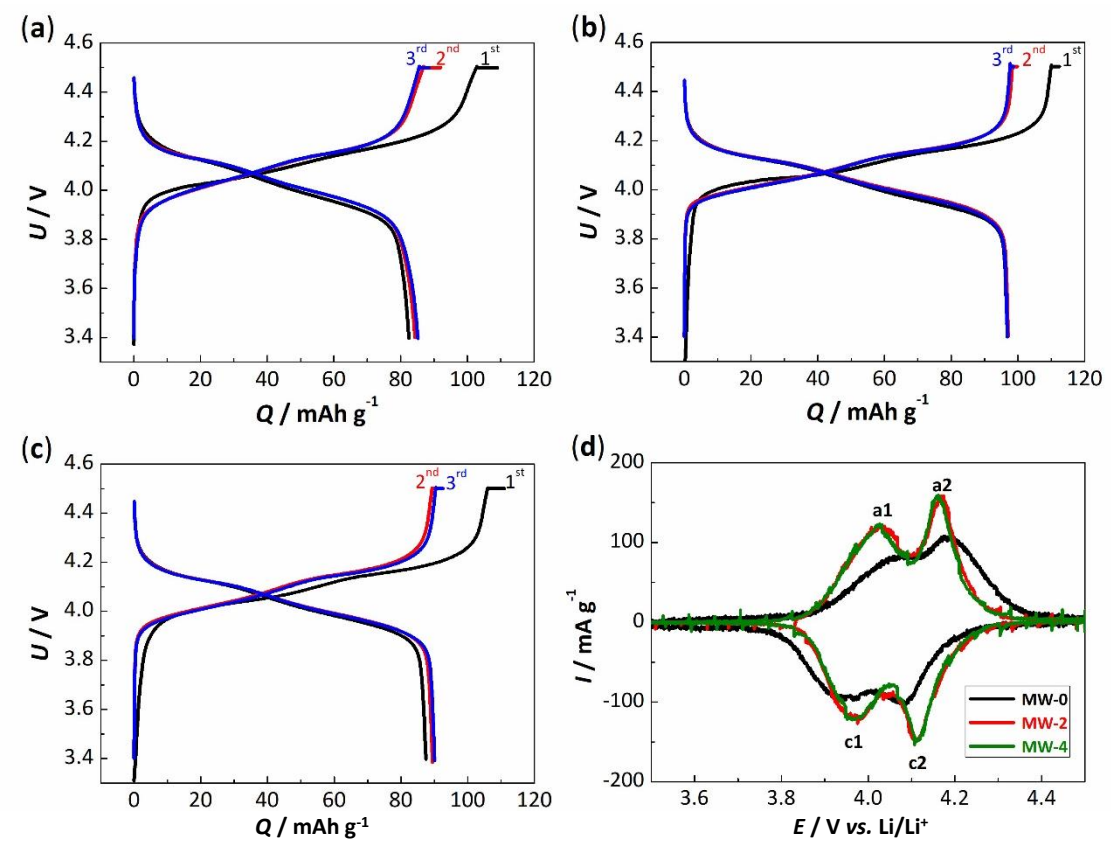


Figure 4. Charge/discharge curves for (a) MW-0, (b) MW-2 and (c) MW-4 samples at cycling current 0.5 C and tapered current on charging 0.1 C, (d) CV curves at potential sweep rate 0.1 mV s⁻¹

Table 3. Peak parameters of CV curves for various LiMn₂O₄ samples

Sample	E_{a1} / V	E_{a2} / V	<i>E</i> _{c1} / V	E_{c2} / V	ΔE_1 / mV	ΔE_2 / mV
MW-0	4.076	4.186	3.955	4.085	121	101
MW-2	4.029	4.170	3.966	4.110	63	60
MW-4	4.023	4.160	3.969	4.115	54	45

Figure 5 shows the results of cycling of LiMn₂O₄ samples at the current density of 1 C for 100 cycles. As can be seen, the stability of the specific capacity during cycling increases with an increase in the duration of the MW post-heating. The initial discharge capacity at 1 C is almost identical to that obtained at the current density of 0.5 C and is 85, 96, and 90 mAh g⁻¹ for samples MW-0, MW-2, and MW-4, respectively. The values of the specific capacity obtained after 100 cycles for samples MW-0, MW-2 and MW-4 are 73, 94, and 90 mAh g⁻¹, respectively, which corresponds to capacity retention (CR) of 86, 97, and 100 %. Thus, sample MW-4 demonstrates excellent cycling stability despite a slightly lower specific capacity than sample MW-2.

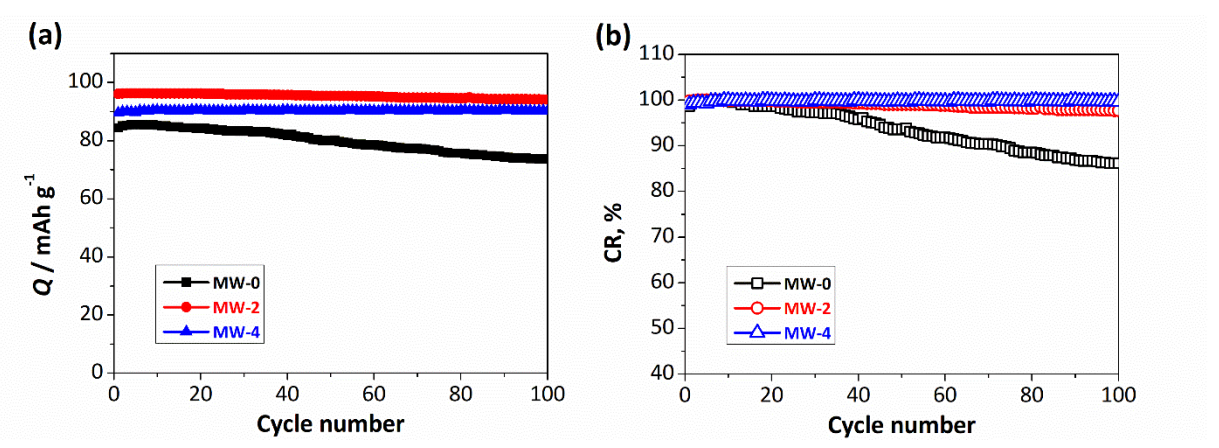


Figure 5. Cycling performances of LiMn₂O₄ samples at the current density of 1 C: dependence of discharge capacity on cycle number (a), and capacity retention curves (b)

High-rate testing results are presented in Figure 6. It turns out that the ability to sustain high-rate current loads is better for the samples subjected to longer MW post-heating. The MW-0 material, which has not been MW post-heated, quickly loses its capacity upon a 6 C current load and, at a 12 C rate, delivers 25 mAh g $^{-1}$ (Figure 6a). The MW-2 sample MW post-heated for 2 min is more stable and delivers the same capacity at \sim 25 C rate. The best results are demonstrated by the MW-4 sample sustaining current loads up to 40 C (5920 mA g $^{-1}$) and returning 20 mAh g $^{-1}$ at this current rate. Furthermore, after cycling at such harsh conditions (up to 80 C, *i.e.*, 11840 mA g $^{-1}$ for MW-2) and returning to discharge by low currents, all samples completely retain their initial capacity (see control cycles by 1 C current in Figure 6a-c). This suggests that the obtained samples do not actually degrade in the range of 50-100 cycles.

In Figure 6d, we compare the high-rate abilities of all three synthesized samples, plotting capacity retention determined as $CR / \% = Q_{sp.}(C)/Q_{sp. max.} vs.$ C-rates. This plot shows that the capacity retention significantly grows with increasing the MW post-heating time. For spinels post-heated for 0, 2 and 4 min, half of the initial capacity is delivered upon current load of 9, 19.5 and 26.5 C. This is significantly higher than for the best samples obtained by means of MW solid-state [47,48] and MW co-precipitation [39] routes, as well as for the spinels synthesized by conventional solid-state [49] and co-precipitation [50] techniques in recent five years. At the same time, it should be noted that the nominal specific capacity obtained at low discharge rates is higher when using both MW and traditional solid-state and co-precipitation synthesis techniques. If the LiMn₂O₄ obtained by the citric acid aided route with MW heating and the conventional time-consuming citric acid aided route are compared [17,20], in both cases, the closeness of the specific capacities, as well as the maximum discharge rates (up to 40 C). Taking this into account, the obvious advantage of MW heating is its short duration, which allows it to significantly intensify the entire synthesis process without losing the functional properties of the material.

Interestingly, the results of existing high-rate tests of LiMn₂O₄ synthesized in a similar way (microwave-assisted citric acid aided route) [46] are quite close to our data obtained without post-heating and are significantly inferior to those attained for MW-2 and MW-4 samples, see Figure 5d. This clearly shows that MW post-heating is advantageous for improving the electrochemical performance of lithium-manganese spinels, *i.e.*, apparently, small action greatly affects the properties of a material.

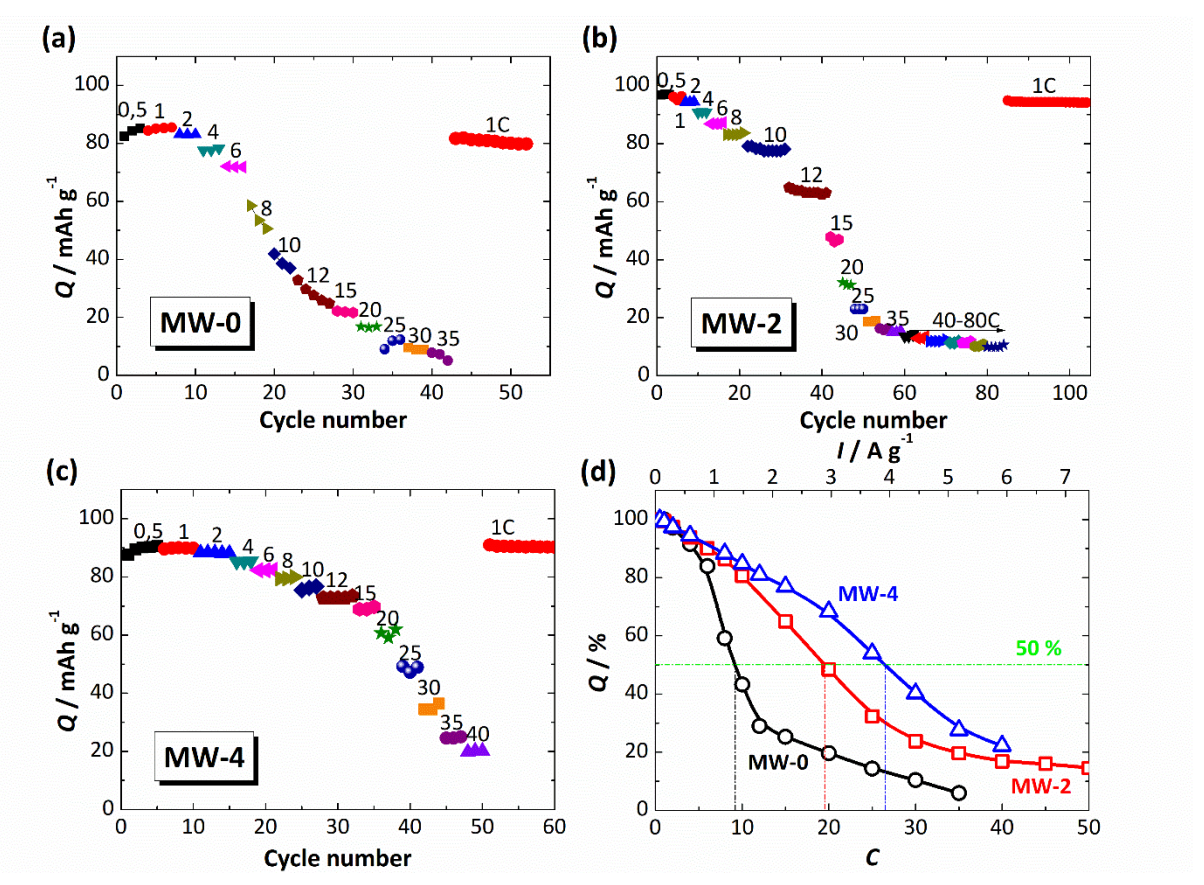


Figure 6. Dependences of specific capacity at various current loads on cycle number for MW-0 (a), MW-2 (b) and MW-4 (c) samples, and of capacity retention on current rate (d). Charge current 1 C with tapered current 0.1 C. Figures at points in (a-c) panels denote current C-rates

Conclusions

In this paper, we have presented an in-depth description of the synthesis, characterization and electrochemical performance of $LiMn_2O_4$ obtained by means of the microwave-assisted citric acid aided route. Detailed working protocols are disclosed, enabling one to reproduce this work completely and to manufacture spinels that sustain current loads at least two times as high as common heating methods. Like in the case of conventional citrate synthesis, the best-synthesized samples sustain current loads up to 40 C (5920 mA g⁻¹) and completely recover after cycling at harsh conditions. Compared with samples obtained by microwave-assisted solid-state routes, our materials are much superior in high-rate properties. All microwave-assisted operations last for maximally 1 h in total and occur at least twice as shorter than at common heating. It is found that microwave post-heating of the reaction mixture after its exothermal decomposition is crucial for obtaining a high-rate cathode material.

References

- [1] M. M. Thackeray, E. Lee, B. Shi, J.R. Croy, Review-from LiMn₂O₄ to partially-disordered Li₂MnNiO₄: the evolution of lithiated-spinel cathodes for Li-ion batteries, *Journal of The Electrochemical Society* **169** (2022) 020535. https://doi.org/10.1149/1945-7111/ac50dd.
- [2] G. E. Blomgren, The development and future of lithium ion batteries, *Journal of The Electrochemical Society* **164** (2017) A5019-A5025. https://doi.org/10.1149/2.0251701jes
- [3] A. V. Potapenko, S. A. Kirillov, Lithium manganese spinel materials for high-rate electrochemical applications, *Journal of Energy Chemistry* **23** (2014) 543-558. https://doi.org/10.1016/S2095-4956(14)60184-4
- [4] A. S. Aricò, P. Bruce, B. Scrosati, J. M. Tarascon, W. Schalkwijk, Nanostructured materials for advanced energy conversion and storage devices, *Nature Materials* **4** (2005) 366-377. https://doi.org/10.1038/nmat1368
- [5] Z. Zhang, B. McNall, A. B. Kanagaraj, J. R. Park, J. E. Ryu, D. Choi, Electrochemical characterization of LiMn₂O₄ nanowires fabricated by sol-gel for lithium-ion rechargeable batteries, *Materials Letters* **273** (2020) 127923. https://doi.org/10.1016/j.matlet.2020.127923
- [6] A. M. Hashem, A. E. Abdel-Ghany, H. M. Abuzeid, R. S. El-Tawil, S. Indris, H. Ehrenberg, A. Mauger, C. M Julien, EDTA as chelating agent for sol-gel synthesis of spinel LiMn₂O₄ cathode material for lithium batteries, *Journal of Alloys and Compounds* **737** (2018) 758-766. https://doi.org/10.1016/j.jallcom.2017.12.153
- [7] R. Kun, P. Schlee, E. Pal, M. Busse, T. Gesing, Role of the precursor chemistry on the phase composition and electrochemical performance of thin-film LiMn₂O₄ Li-ion battery cathodes prepared by spray pyrolysis. *Journal of Alloys and Compounds* **726** (2017) 664-674. https://doi.org/10.1016/j.jallcom.2017.08.039
- [8] H. Gao, Q. Yan, P. Xu, H. Liu, M. Li, P. Liu, J. Luo, Z. Chen, Efficient direct recycling of degraded LiMn₂O₄ cathodes by one-step hydrothermal relithiation. *ACS Applied Materials & Interfaces* **12** (2020) 51546-51554. https://doi.org/10.1021/acsami.0c15704
- [9] W. B. Hua, S. N. Wang, X. D. Guo, S. L. Chou, K. Yin, B. H. Zhong, S. X. Dou, Vacuum induced self-assembling nanoporous LiMn₂O₄ for lithium ion batteries with superior high rate capability, *Electrochimica Acta* **186** (2015) 253-261. https://doi.org/10.1016/j.electacta.2015.10.093.
- [10] S. Chen, Z. Chen, C. Cao, Mesoporous spinel LiMn₂O₄ cathode material by a soft-templating route, *Electrochimica Acta* **199** (2016) 51-58. https://doi.org/10.1016/j.electacta.2016.03.135.
- [11] S. A. Kirillov, Electrode materials and electrolytes for high-rate electrochemical energy systems: a review, *Theoretical and Experimental Chemistry* **55** (2019) 73-95. https://doi.org/10.1007/s11237-019-09598-2.
- [12] A. H. Marincaş, F. Goga, S. A. Dorneanu, P. Ilea, Review on synthesis methods to obtain LiMn₂O₄-based cathode materials for Li-ion batteries, *Journal of Solid State Electrochemistry* **24** (2020) 473-497. https://doi.org/10.1007/s10008-019-04467-3
- [13] C. Bluthardt, C. Fink, K. Flick, A. Hagemeyer, M. Schlichter, A. Volpe Jr, Aqueous synthesis of high surface area metal oxides, *Catalysis Today* 137 (2008) 132-143. https://doi.org/10.1016/j.cattod.2008.04.045
- [14] C. Fink, A. Hagemeyer, Z. Hogan, A. Volpe Jr., J. Yoder, High surface area cerium oxide, *Current Catalysis* **5** (2016) 182-202. https://doi.org/10.2174/2211544705666160509161559
- [15] I. A. Farbun, I. V. Romanova, S. A. Kirillov. Optimal design of powdered nanosized oxides of high surface area and porosity using a citric acid aided route, with special reference to ZnO, *Journal of Sol-Gel Science and Technology* 68 (2013) 411-422. https://doi.org/10.1007/s10971-013-3024-7
- [16] I. V. Romanova, S. A. Kirillov, Preparation of Cu, Ni and Co oxides by a citric acid-aided route, Journal of Thermal Analysis and Calorimetry 132 (2018) 503-512. https://doi.org/10.1007/s10973-017-6880-5

- [17] A. V. Potapenko, S. I. Chernukhin, S. A. Kirillov, A new method of pretreatment of lithium manganese spinels and high-rate electrochemical performance of Li[Li_{0.033}Mn_{1.967}]O₄. *Materials for Renewable and Sustainable Energy* **3** (2014) 40. https://doi.org/10.1007/s40243-014-0040-7
- [18] A. V. Potapenko, S. I. Chernukhin, I. V. Romanova, K. Sh. Rabadanov, M. M. Gafurov, S. A. Kirillov, Citric acid aided synthesis, characterization, and high-rate electrochemical performance of LiNi_{0.5}Mn_{1.5}O₄, *Electrochimica Acta* **134** (2014) 442-449. https://doi.org/10.1016/j.electacta.2014.04.083
- [19] V. V. Kosilov, A. V. Potapenko, S. A. Kirillov, Effect of overdischarge (overlithiation) on electrochemical properties of LiMn₂O₄ samples of different origin, *Journal of Solid State Electrochemistry* **21** (2017) 3269-3279. https://doi.org/10.1007/s10008-017-3671-7
- [20] A. V. Potapenko, S. A. Kirillov, Enhancing high-rate electrochemical properties of LiMn₂O₄ in a LiMn₂O₄/LiNi_{0.5}Mn_{1.5}O₄ core/shell composite, *Electrochimica Acta* **258** (2017) 9-16. https://doi.org/10.1016/j.electacta.2017.10.108
- [21] S. A. Kirillov, I. V. Romanova, T. V. Lisnycha, A. V. Potapenko, High-rate electrochemical performance of Li₄Ti₅O₁₂ obtained from TiCl₄ by means of a citric acid aided route, *Electrochimica Acta* **286** (2018) 163-171. https://doi.org/10.1016/j.electacta.2018.08.034
- [22] A. V. Potapenko, M. Wu, S. A. Kirillov, Remarkable electrochemical performance of 0.5Li₂ MnO₃·0.5LiNi_{0.5}Mn_{0.3}Co_{0.2}O₂ synthesized by means of a citric acid-aided route, *Journal of Solid State Electrochemistry* **23** (2019) 3383-3389. https://doi.org/10.1007/s10008-019-04442-y
- [23] S. A. Kirillov, A. V. Potapenko, A. V. Potapenko, Effect of overdischarge (overlithiation) on electrochemical properties of LiNi_{0.5}Mn_{1.5}O₄ samples of different origin, *Journal of Solid State Electrochemistry* **24** (2020) 1113-1121. https://doi.org/10.1007/s10008-020-04601-6.
- [24] S. Balaji, D. Mutharasu, N. S. Subramanian, K. Ramanathan, A review on microwave synthesis of electrode materials for lithium-ion batteries, *Ionics* **15** (2009) 765-777. https://doi.org/10.1007/s11581-009-0350-4.
- [25] F. K. Butt, A. S. Bandarenka, Microwave-assisted synthesis of functional electrode materials for energy applications, *Journal of Solid State Electrochemistry* **20** (2016) 2915-2928. https://doi.org/10.1007/s10008-016-3315-3
- [26] H. Yan, X. Huang, L. Chen, Microwave synthesis of LiMn₂O₄ cathode material, *Journal of Power Sources* **81-82** (1999) 647-650. https://doi.org/10.1016/S0378-7753(99)00112-3
- [27] P. S. Whitfield, I. J. Davidson, Microwave synthesis of $Li_{1.025}Mn_{1.975}O_4$ and $Li_{1+x}Mn_{2-x}O_{4-y}F_y$ (x=0.05, 0.15; y=0.05, 0.1), Journal of The Electrochemical Society **147** (2000) 4476-4484. https://doi.org/10.1149/1.1394089
- [28] M. H. Bhat, B. P. Chakravarthy, P. A. Ramakrishnan, A. Levasseur, Microwave synthesis of electrode materials for lithium batteries, *Bulletin of Materials Science* **23** (2000) 461-466. https://doi.org/10.1007/BF02903884
- [29] H. Hao, H.-X. Liu, S.-X. Ouyang, Microwave synthesis of cathode material Li_xMn₂O₄ for lithium-ion battery, *Journal of Wuhan University of Technology-Material Science* **17** (2002) 36-38. https://doi.org/10.1007/BF02838413
- [30] M. Nakayama, K. Watanabe, H. Ikuta, Y. Uchimoto, M. Wakihara, Grain size control of LiMn₂O₄ cathode material using microwave synthesis method, *Solid State Ionics* **164** (2003) 35-42. https://doi.org/10.1016/j.ssi.2003.08.048
- [31] S. Kobayashi, T. Usui, H. Ikuta, Y. Uchimoto, M. Wakihara, Preparation of cathode active materials for lithium ion secondary batteries utilizing microwave irradiation: Part II. Electronic structure of lithium manganese oxide, *Journal of Materials Research* **19** (2004) 2421-2427. https://doi.org/10.1557/JMR.2004.0313



- [32] Y.-P. Fu, C.-H. Lin, Y.-H. Su, J.-H. Jean, S.-H. Wu, Electrochemical properties of LiMn₂O₄ synthesized by the microwave-induced combustion method, *Ceramics International* **30** (2004) 1953-1959. https://doi.org/10.1016/j.ceramint.2003.12.183
- [33] Y.-P. Fu, Y.-H. Su, C.-H. Lin, S.-H. Wu, Comparison of the microwave-induced combustion and solid-state reaction for the synthesis of LiMn₂O₄ powder and their electrochemical properties, *Ceramics International* **35** (2009) 3463-3468. https://doi.org/10.1016/j.ceramint.2009.06.027
- [34] B.-L. He, W.-J. Zhou, S.-J. Bao, Y.-Y. Liang, H.-L. Li, Preparation and electrochemical properties of LiMn₂O₄ by the microwave-assisted rheological phase method, *Electrochimica Acta* **52** (2007) 3286-3293. https://doi.org/10.1016/j.electacta.2006.10.002
- [35] S. Balaji, S. Shanmugan, D. Mutharasu, K. Ramanathan, Structural, morphological and electrochemical characterization of electron beam deposited $Li_{1+x}Mn_2O_4$ (x = 0, 0.05) thin films, *Materials Science-Poland* **28** (2010) 583-593.
- [36] D. Huo, Nanostructured morphology of spinel LiMn₂O₄ oxide under microwave heating, Advanced Materials Research 936 (2014) 452-458. https://doi.org/10.4028/www.scientific.net/AMR.936.452
- [37] J. P. Silva, S. R. Biaggio, N. Bocchi, R. C. Rocha-Filho, Practical microwave-assisted solid-state synthesis of the spinel LiMn₂O₄, *Solid State Ionics* **268** (2014) 42-47. https://doi.org/10.1016/j.ssi.2014.09.025
- [38] H. Zhang, Y. Xu, D. Liu, X. Zhang, C. Zhao, Structure and performance of dual-doped LiMn₂O₄ cathode materials prepared via microwave synthesis method, *Electrochimica Acta* **125** (2014) 225-231. https://doi.org/10.1016/j.electacta.2014.01.102
- [39] X. Liu, P. Liu, H. Wang, Preparation of spinel LiMn₂O₄ with porous microscopic morphology by simple coprecipitation-microwave synthesis method, *Ionics* **25** (2019) 5213-5220. https://doi.org/10.1007/s11581-019-03072-8
- [40] L. Tian, C. Su, Y. Wang, B. Wen, W. Bai, J. Guo, Electrochemical properties of spinel LiMn₂O₄ cathode material prepared by a microwave-induced solution flameless combustion method, *Vacuum* **164** (2019) 153-157. https://doi.org/10.1016/j.vacuum.2019.03.011
- [41] P. Ragupathya, H. N. Vasana, N. Munichandraiah, Microwave driven hydrothermal synthesis of LiMn₂O₄ nanoparticles as cathode material for Li-ion batteries, *Materials Chemistry and Physics* **124** (2010) 870-875. https://doi.org/10.1016/j.matchemphys.2010.08.014
- [42] M. Michalska, L. Lipińska, R. Diduszko, M. Mazurkiewicz, A. Małolepszy, L. Stobinski, K.J. Kurzydłowski, Chemical syntheses of nanocrystalline lithium manganese oxide spinel, *Physica Status Solidi C* **8** (2011) 2538-2541. https://doi.org/10.1002/pssc.201001195
- [43] B. N. Rao, P. Muralidharan, P. R. Kumar, M. Venkateswarlu, N. Satyanarayana, Fast and facile synthesis of LiMn₂O₄ nanorods for Li ion battery by microwave assisted hydrothermal and solid state reaction methods, *International Journal of Electrochemical Science* **9** (2014) 1207-1220.
- [44] H. Liu, C. Hu, X. Zhu, H. Hao, J. Luo, J. Zhou, S. Ouyang, Solid chemical reaction in microwave and millimeter-wave fields for the syntheses of LiMn₂O₄ compound, *Materials Chemistry and Physics* **88** (2004) 290-294. https://doi.org/10.1016/j.matchemphys.2004.06.037
- [45] S.-J. Bao, Y.-Y. Liang, H.-L. Li, Synthesis and electrochemical properties of LiMn₂O₄ by microwave-assisted sol-gel method, *Materials Letters* **59** (2005) 3761-3765. https://doi.org/10.1016/j.matlet.2005.07.012
- [46] R. Chen, B. Wen, C. Su, W. Bai, J. Guo, Significant improvement of LiMn₂O₄ cathode capacity by introducing trace Ni during rapid microwave-induced solution combustion, *Electrochemistry* **88** (2020) 532-539. https://doi.org/10.5796/electrochemistry.20-00083
- [47] N. I. Globa, Yu. V. Shmatok, V. D. Prisyazhnyi, Structural and electrochemical characteristics of Li_xMn₂O₄ spinel synthesized using a microwave-assisted method, *Surface Engineering and Applied Electrochemistry* **49** (2013) 488-492. https://doi.org/10.3103/S1068375513060094

- [48] N. I. Globa, Y. V. Shmatok, V. D. Prisyazhnyi, Comparison of the characteristics of Li_xMn₂O₄ synthesized by microwave and solid-state methods, *ECS Transactions* **48** (2014) 123-127. https://doi.org/10.1149/04801.0123ecst
- [49] J. Cao, S. Guo, R. Yan, C. Zhang, J. Guo, P. Zheng, Carbon-coated single-crystalline LiMn₂O₄ nanowires synthesized by high-temperature solid-state reaction with high capacity for Li-ion battery, *Journal of Alloys and Compounds* **741** (2018) 1-6. https://doi.org/10.1016/j.jallcom.2018.01.107
- [50] W. Zhang, Z. Zhao, Y. Lei, J. Xing, X. Cao, A facile and eco-friendly approach to synthesis of spinel LiMn₂O₄ with high electrochemical performance, *International Journal of Electrochemical Science* **15** (2020) 6188-6197. https://doi.org/10.20964/2020.07.77

©2024 by the authors; licensee IAPC, Zagreb, Croatia. This article is an open-access article distributed under the terms and conditions of the Creative Commons Attribution license (https://creativecommons.org/licenses/by/4.0/)



Open Access : : ISSN 1847-9286

www.jESE-online.org

Original scientific paper

Characteristics of graphite obtained by recycling lithium - iron phosphate batteries

Ivan Shcherbatiuk¹, Hanna Potapenko^{1,2}, Danylo Panchenko¹, Volodymyr Khomenko^{3,4}, Dmytro Patlun⁴, Borys Haliuk³, Roman Derkach², Oleksandr Potapenko^{1,3} and Viacheslav Barsukov^{3,⊠}

¹Joint Department of Electrochemical Energy Systems of National Academy of Science of Ukraine, Vernadsky ave., 38-A, Kyiv, 03142, Ukraine

²Faculty of Materials Metallurgy and Chemistry, Jiangxi University of Science and Technology, Ganzhou, 341000, China

³Institute for Sorption and Problems of Endoecology of National Academy of Science of Ukraine, 13, Generala Naumova str., Kyiv 03164 Ukraine

⁴Kyiv National University of Technologies and Design, Mala Shyianovska (Nemyrovycha-Danchenka) Street, 2, Kyiv 01011, Ukraine

Corresponding author: [™]<u>q.vasyliev@kpi.ua</u>; Tel.: +38-096-924-9888; Fax: +38-044-204-9773

Received: January 27, 2024; Accepted: March 27, 2024; Published: April 27, 2024

Abstract

Based on both the economic and environmental points of view, processing used lithiumion batteries (LIBs) is of great importance. The valuable components contained in LIB (cathode, anode and current collectors) generate high interest in solving the problem of resource deficiency and reducing environmental destruction due to overexploitation. The starting anode material extracted from a used lithium iron phosphate battery is a mixture of graphite, acetylene carbon black, and polymer binder. Reusing this material in lithium batteries without additional cleaning is impractical owing to poor electrochemical characteristics and the presence of impurities. To achieve effective regeneration, the recycled anode material is first treated in a nitric acid solution to remove copper foil and lithium ions with electrolyte interaction products formed during battery operation. The next step is heat treatment of the material, which allows the removal of acetylene soot and polymer glue binder. The tests showed sufficiently high values of the specific capacity of recycled graphite (\sim 330 mA h g $^{-1}$ at 0.1 C), which are comparable to commercial materials and meet the requirements of reuse.

Keywords

Lithium-ion batteries; recycling; graphite anode; electrochemical parameters; impedance

Introduction

In the context of global population growth to seven billion people, it is projected that electricity production will need to be doubled by the middle of the 21st century to ensure a stable standard of living [1-3]. The problem of increasing the volume of electricity is complex, given that most of the energy is currently generated from non-renewable sources. This causes significant carbon dioxide emissions. Therefore, it is important to focus on the development of renewable energy sources such as wind, solar, tidal and geothermal energy. This involves innovation in the areas of electricity generation and storage, where batteries are becoming a key element in an alternative energy strategy.

Since Sony's first commercial introduction of lithium-ion batteries (LIBs) in 1990, they have been widely adopted. LIBs have a successful combination of energy density, durability, and convenience, making them a popular choice for a wide range of devices and applications.

The global demand for LIB is predicted to approach 3600 GWh by 2030 (Figure 1) [4]. The global production capacity market shares of <1 % today for Europe and USA could increase greatly in the future. By 2030, both regions could reach 5-6 % global shares. In total, the forecasts for the development of production capacities for graphite as an anode material amount to about 4 million tons by 2027/2028. However, the most startling feature in global battery cell manufacturing is the dominance of Asian companies and the localization of production in China because more than half of the declared production capacities are located in Asia. However, by 2030, around one-quarter of cell production could be sited in Europe and around one-fifth in the USA. In a similar manner, half of the production capacities are made by Chinese companies. Moreover, the announcements of Korean companies are the same as the sum of all potential European battery cell fabricators [5-7].

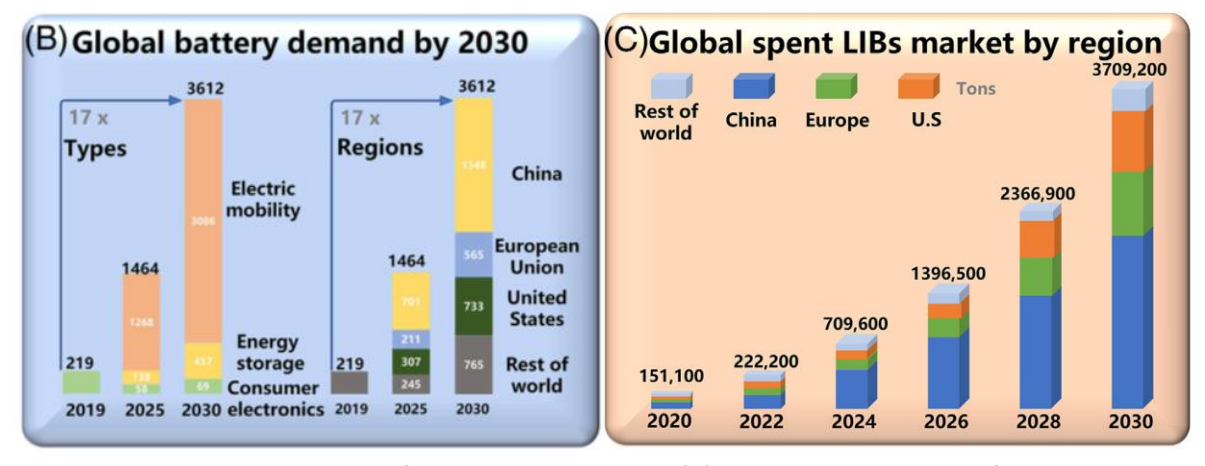


Figure 1. Projected global demand for batteries until 2030 (B) and the global market for spent lithium-ion batteries (C). (Reprint from [4] The Creative Commons Attribution License from Wiley)

From both economic and environmental points of view, the processing of used LIBs is of great importance. The valuable components contained in LIB (cathode, anode and current collectors) can make a significant contribution to solving the problem of resource scarcity [8,9] and reducing environmental destruction due to overexploitation.

Graphite is used as the primary anode material in most commercial LIBs. Other anode materials, such as silicon, tin, amorphous carbon, and lithium titanite-based anode, account for only about 9 % [10]. The advantages of a graphite anode include high cycling stability, capacity, and low price [11].

Due to the increase in the production of electric vehicles, there may be a shortage of materials for making batteries over the next few years. Reusing materials from used LIBs can reduce possible material shortages.

However, despite significant progress in LIBs recycling, the use of graphite from used batteries lags behind the recycling and use of cathode materials [12]. The economic feasibility of processing a graphite anode is also confirmed by the fact that various contaminants present in natural grades of graphite prevent its direct use as a LIB anode. As a rule, the production of battery graphite includes several stages, including mining, beneficiation, purification and processing [13]. All these stages lead to significant environmental pollution and pose a risk to human health. A significant, albeit less well-known, aspect is that 1 kg of graphite is needed to produce 1 kWh of commercial LIB capacity [14]. Given that the graphite content in LIB ranges from 12 to 21 percent by weight (depending on the type of battery), graphite production from spent LIB can be considered as an alternative method for obtaining graphite for LIBs [12,15].

In this study, we present a way to recycle graphite anode, together with some physicochemical and electrochemical parameters of the reduced graphite obtained during the processing of a lithium iron phosphate battery.

Experimental

The source of spent graphite in our studies was the anode of lithium iron phosphate battery HWE200A, LF54174200 3.2 V 200 Ah (China) [16]. The reasons for the failure of this battery were an internal short circuit due to thermal runaway, as evidenced by the lack of voltage between the battery terminals, and partially fused and burned electrodes.

According to *Zhang et al.* [17], spent graphite containing various impurities has a lower initial discharge capacity of 298.7 mA·h/g compared to the capacity of 354.2 mA·h/g for the original battery graphite. Note that the theoretical capacity of high-purity graphite (99.99 %) is 372 mA·h/g.

To restore the original properties of spent graphite, it is very important to remove residual impurities from it. For this purpose, we used diluted solutions of nitrate acid. As shown by Barsukov *et al.* [18], the treatment of natural flake graphite in nitric acid solutions makes it possible to remove almost all metal impurities with the exception of silicon and aluminum compounds. The latter are extracted either by sintering with alkali [18] or HF [19] or by high-temperature treatment at 3000 °C. The advantage of spent graphite material is that silicon and aluminum compounds have already been extracted earlier, at the stage of purification of natural graphite to the level of 99.95 % C. Therefore, the treatment of spent graphite in nitric acid may be quite sufficient to remove any metal impurities.

The battery was mechanically disassembled to separate the cathode, anode, and separator. The anode, a graphite-based electrode mass deposited on both sides of copper foil, was cut into small pieces and placed in a 20 % nitric acid solution. The ratio of the solid to liquid phase was 1:12. After the copper was completely dissolved, the solution turned blue, indicating the formation of copper (II) nitrate. The treatment of the graphite anode in nitric acid made it possible not only to separate the carbon material of the anode from the copper foil but also to get rid of the solid electrolyte film (SEI) on its surface. A mixture of graphite, acetylene soot and polymer binder glue remained as an insoluble precipitate. In order to grind and more completely extract the impurities present in the graphite anode, the resulting suspension was subjected to ultrasonic treatment on the disperser XM-650DT (China) for 20 minutes. After separating the sediment, the latter was repeatedly washed with distilled water to a pH 7. In order to remove the polymer binder and amorphous carbon impurities from the graphite anode, the resulting sample was annealed for 2 h at 700 °C. The heating and cooling rate of the furnace was 5° min⁻¹. After cooling, the resulting material was crushed and sifted through a sieve with a mesh size of 40 μm.

The method for determining the ash content of graphite was based on the process of calcination of certain quantities of graphite and weight analysis of the ash residue. To do this, 2 grams of

graphite were placed in a crucible and heat treated in a muffle furnace for eight hours at 1050 °C. After calcination, the crucibles were removed from the muffle, cooled for 10 minutes on a metal plate, and then placed in a desiccator without a desiccant for further cooling. At the final stage, the ash residue was weighed on analytical balances. According to the analysis of a series of three crucibles, the ash content of regenerated graphite from LIB did not exceed 0.02 %.

It should be noted that in addition to copper nitrate, the solution contains a certain amount of lithium nitrate, which was formed as a result of the dissolution of the solid-electrolyte film from the surface of the graphite anode. The results of atomic emission flame spectrometry of the solution (Shimadzu AA-6300, Japan) for the residual lithium content show a value of 430 ± 5 mg/l. To do this, an excessive amount of sodium hydroxide is added to the solution in order to obtain an insoluble precipitate of copper (II) hydroxide. After separating the latter, sodium carbonate was added to the resulting solution and evaporated. Due to the weak solubility of lithium carbonate in water, it precipitates during evaporation. This method is the main method for obtaining lithium carbonate in the processing of cathode materials [20].

The scheme of graphite anode processing is shown in Figure 2.

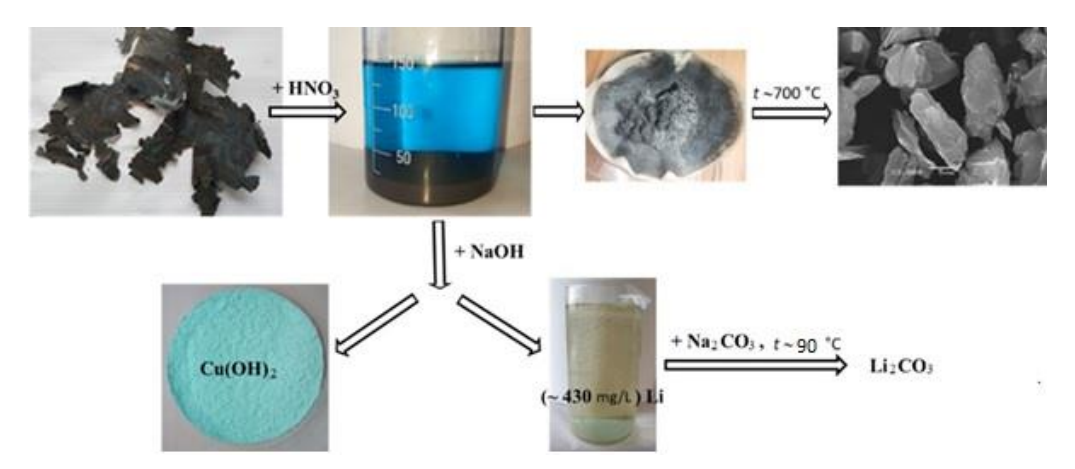


Figure 2. The scheme of graphite anode processing

The phase composition, morphology, and particle size of reduced graphite were analyzed by X-ray diffraction (Dron-4-07, LOMO, Russia, Co- K_{α} radiation) and scanning electron microscopy (JSM-6700f, JEOL, Japan) methods.

Electrochemical tests were done using a half-cell with a working graphite electrode and lithium as the reference and counter electrodes. Working electrodes consist of 94 wt.% of the graphite, 1 wt.% of the conductive additive (soot) and 5 wt.% of the water-soluble binder (NV-1T, "Casnovo" corporation, China).

The suspension of the composite electrode was prepared by mixing the starting materials on an IKA RW 20 mixer for 50 minutes. The resulting suspension was applied to copper foil by a doctor blade method with the 80 μ m thickness. The porosity of the electrode was determined by the ratio of the crystallographic density of graphite (~2.16 g/cm³) to the measured density of the electrode material.

The parameters of the obtained electrodes, after drying and pressing, are shown in Table 1.

 Sample
 Electrode mass, g
 Mass of graphite, g
 Electrode thickness, μm
 Porosity, %

 1
 0.006
 0.0048
 30±5
 54

 2
 0.007
 0.0063
 40±5
 56

Table 1. Parameters of graphite electrodes

CR2032-type coin cells were assembled using the dried anode and Celgard 2500 as a separator in a glove box. The electrolyte used in this study was 1M LiPF $_6$ in a mixture of ethylene carbonate and dimethyl carbonate, both at a volume ratio of 1:1. A lithium disk of 16 mm in diameter served as both the reference and counter electrode in the cell assembly. Galvanostatic studies of these cells were conducted using the Neware BTS 4000 battery analyzer (China). Additionally, electrochemical impedance spectroscopy (EIS) was performed with an Autolab PGSTAT 302 (Switzerland). The impedance spectra obtained were subsequently analyzed using Nova 2.1 software. EIS measurement were taken between 1 MHz to 0.01 Hz with a voltage amplitude of 5 mV after full lithiation of the graphite electrode (0.01 V vs. Li/Li⁺ electrode).

Results and discussion

As known, graphite has a layered, planar structure. In each layer, the carbon atoms are arranged in a honeycomb lattice with a bond length of 0.142 nm, and the distance between planes is 0.335 nm [21].

Figure 3 shows the X-ray diffraction pattern of purified graphite prepared according to the scheme proposed above, which has well structural and phase purity. The XRD of graphite possesses three signature peaks at 26.3° (002), 44.2° (100) and 54.5° (004). The peak at $2\theta = 26.3$ ° indicates well-organized structure of graphite with an interlayer spacing of 0.338 nm. This layer spacing is in agreement with the spacing in graphite. The broad peak at $2\theta = 44.2$ ° is attributed to the presence of some defects [22].

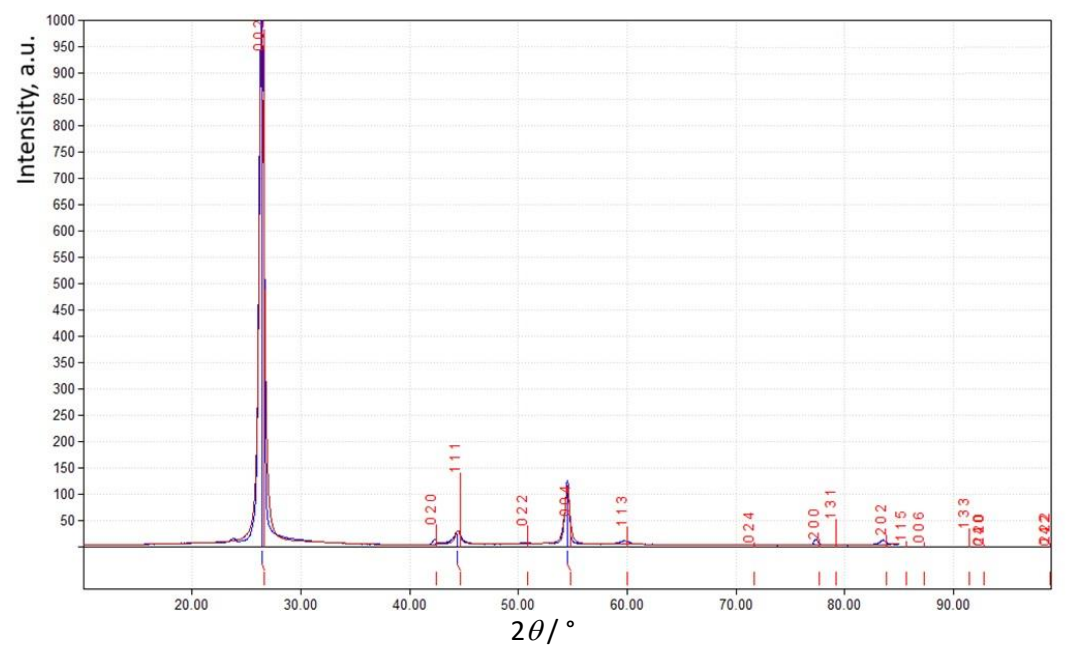


Figure 3. XRD pattern of purified graphite

Figure 4 represents the SEM image of purified graphite. As can be observed, well-defined sheets of graphite 1-3 μ m in diameter are presented.

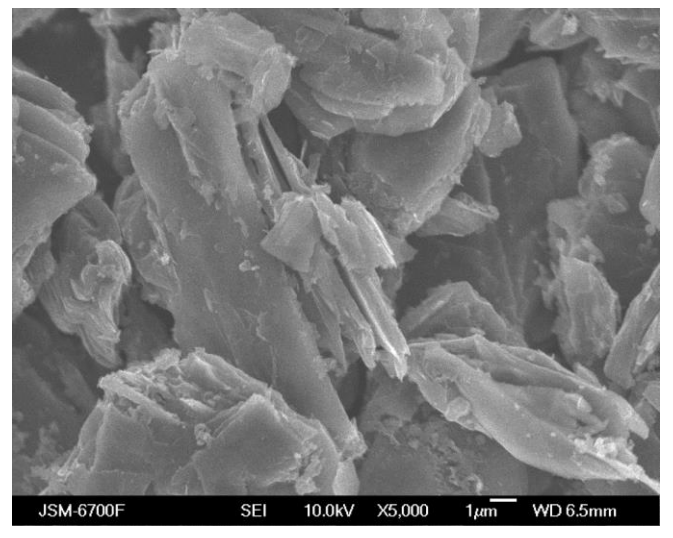


Figure 4. SEM image of purified graphite

On the galvanostatic curve of the 1^{st} charge/discharge cycle of a graphite electrode (Figure 5), it can be noted that there is an irreversible capacity of about 40 mA·h/g, which can be attributed to the formation of SEI on its surface. In addition, there are three small plateaus at potentials below 0.2 V relative to Li⁺/Li during the cathode sweep. These plateaus are caused by the insertion of lithium ions into the layered graphite structure and transformations between different stages of intercalation compounds from the LiC₃₆ stage to the LiC₆ stage, respectively [23,24].

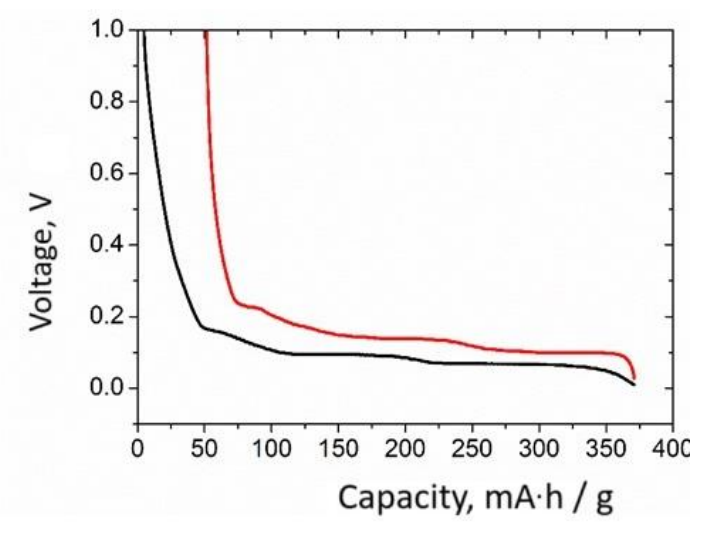


Figure 5. Changing the profile of the charge/discharge curve of the 1^{st} cycle of the graphite electrode (sample 1): black – charge, red – discharge. Current rate is 0.05C (I = 0.089 mA)

During the anodic sweep, three plateaus are also observed, which relate to the deintercalation of lithium ions from the graphite electrode. An increase in the intercalation/deintercalation current rate of lithium ions leads to a slight decrease in the specific capacitance of the electrode (Figure 6) at current values not exceeding 0.2 C (1-3 cycle - current rate was 0.05C; 4-9 cycles - 0.1C; 10-19 cycles - 0.2C) and increase coulombic efficiency during cycling. A further increase in the discharge current rate to values of 0.5C leads to a more significant decrease in the specific capacity of the graphite electrode. This can be observed in Figure 6 (cycles: 20-29) due to limitations in the intercalation of lithium ions between the graphite layers. Thus, when using the constant current-constant voltage (CCCV) mode or reducing the intercalation current of lithium ions to 0.1 C, higher currents can be realized during subsequent de-insertion (Figure 7).

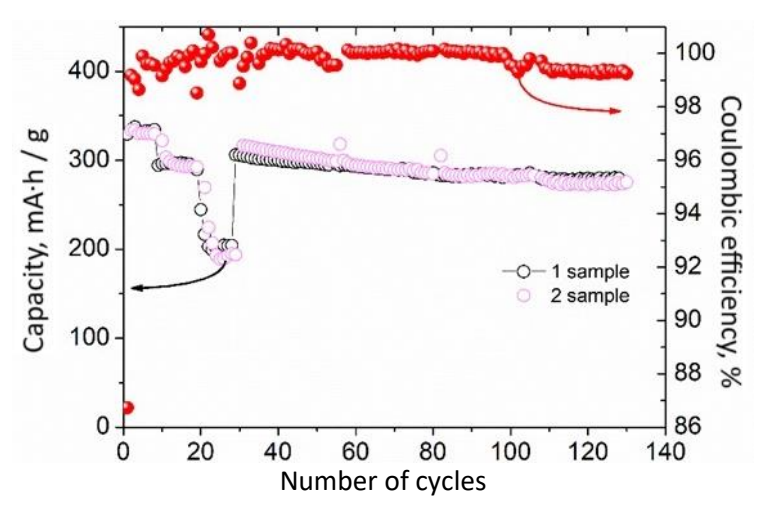


Figure 6. Change in specific capacity and Coulomb efficiency of the graphite electrode during cycling. Current rate: I = 0.05 C (cycles 1-3); I = 0.1 C (cycles 4-9); I = 0.2 C (cycles 10-19); I = 0.5 C (cycles 20-29); I = 0.2 C (cycles 30-130)

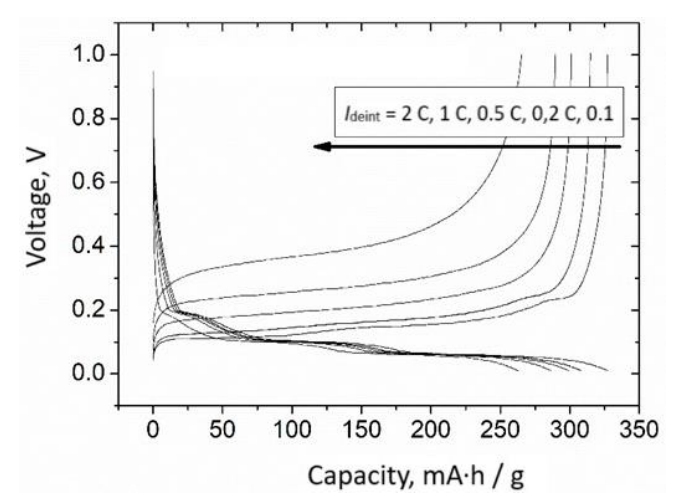


Figure 7. Galvanostatic cycling curves of the graphite electrode depending on the current rate in the range: $I_{\text{int.}} = 0.1 \text{ C (const.)}$; $I_{\text{deint.}} = 0.1 - 2.0 \text{ C}$

Upon cycling of the graphite anode, an increase in coulombic efficiency is observed during the initial 20 cycles, after which it stabilizes, reaching approximately 99.2±0.2 %. This effect can be attributed to the reduced contribution of irreversible capacitance, which is associated with the formation and compaction of the solid electrolyte interface (SEI) on the surfaces of both the working and counter electrodes. However, increasing the current rate to 0.5 C during cycles 20 to 30 results in a marked decrease in specific capacitance, dropping to about 200 mA·h/g. Subsequently, lowering the intercalation/deintercalation current rate to 0.2C helps to restore the capacity values to around 300 mA·h/g. Despite this recovery, a slight decline in capacity is observed with further cycling, extending from cycles 30 to 130. The gradual decrease in the capacity of the graphite electrode over these cycles is illustrated in Figure 8.

Here, it is worth noting that in the process of cycling, there is a decrease in the average voltage at the insertion of lithium ions into graphite on each of the "shelves" at cathodic polarization and an increase in the average voltage at de-insertion of lithium ions – at anodic polarization, which indicates an increase in the internal resistance of the cell. First of all, the increase in internal resistance should be attributed to the formation of a dense SEI on the lithium electrode. This assumption is also evidenced by impedance hodographs (Figure 9) obtained on the 30th and 130th cycles at the potential of 0.01 V.

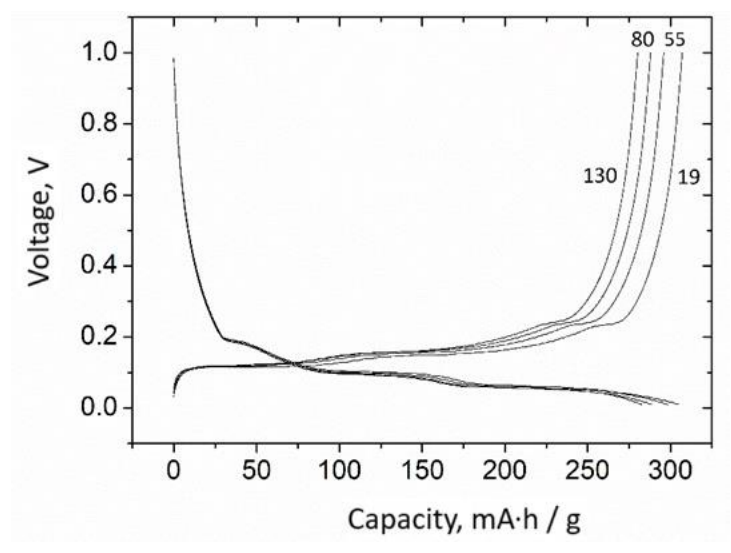


Figure 8. Changing the profile of the charge/discharge curves during the cycling of the graphite electrode.

Current rate is 0.2 C. Numbers indicate cycle numbers

To describe the processes occurring during the silencing of the electrode, several equivalent circuits have been proposed. For instance, *Wang et al.*[25] interpret changes in the appearance of impedance hodographs in terms of five possible processes. In another study [26], simpler schemes are proposed to describe the resistance of the electrochemical system to the alternating current flowing through it.

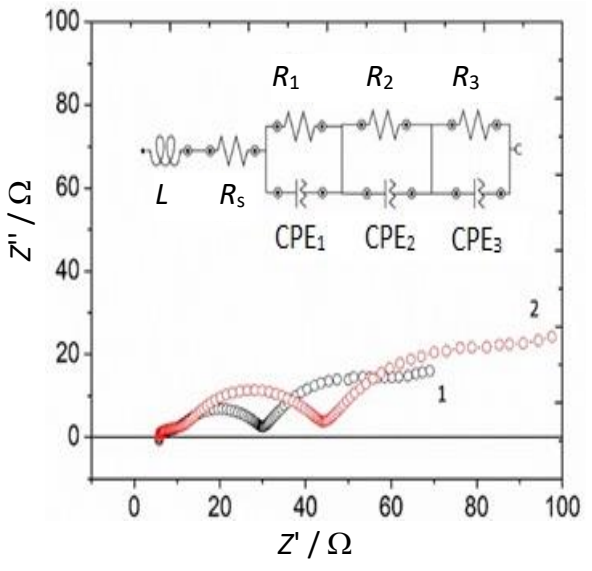


Figure 9. Nyquist diagram and equivalent electrical circuit of a graphite electrode (sample 1) $1 - 30^{th}$ cycle; $2 - 130^{th}$ cycle

The equivalent electrical circuit from Figure 9 describes the processes in Table 2.

Table 2. The process explains the equivalent electrical circuit

No	Process	Frequency area
1	Inductive wiring of metal contacts (L ₀)	High
2	Resistance of electrolytes in the pores of the separator (Celgard 2500) (R _S)	(10 to 0.1 MHz)
3	Charge transfer through the SEI on a graphite electrode	Middle (100 to 0.01 kHz)
4	Charge transfer through the SEI/metallic lithium	Low
5	Diffusion of lithium ions compatible with adsorption into the structure of the material	(1.00 to 0.01 Hz)

However, it is important to note that since the impedance hodographs of the elements are obtained after full lithiation of the graphite electrode, the classical Warburg impedance, typically represented as an inclined line at a 45° angle, transforms into a semicircle. This semicircular shape is characteristic of porous and rough surfaces. Consequently, to accurately describe the equivalent circuit in this scenario, a parallel connection composed of a resistance (R_3) and a distributed capacitance (CPE₃) was utilized in place of the Warburg diffusion impedance. The values for the elements obtained using this revised equivalent circuit model are presented in Table 3.

Table 3. Values of some electrical equivalent circuit parameters

Sample	Number of cycles	<i>L</i> ₀ / H	$R_{ extsf{S}}$ / Ω	R_1/Ω	R_2/Ω	R_3 / Ω
1	30	270·10 ⁻⁹	5.85	6.06	20.6	45.6
2	130			9.24	33.9	75.4

The values of inductance (L_0) and electrolyte resistance in the separator pores (R_s) practically do not change during cycling. The resistance to charge transfer through SEI on the graphite electrode (R_1) increases by ~30 % over 95 cycles from 6.06 to 9.24 Ω . However, the greatest contribution to the increase in charge transfer resistance through SEI falls on the lithium counter electrode (R_2), which increases by 13 Ω .

Conclusions

In conclusion, the anode material retrieved from a malfunctioning lithium iron phosphate battery, primarily composed of graphite, acetylene black, and a polymer-based adhesive, presents a significant recycling potential. The direct reutilization of this material in lithium-ion batteries without prior purification is not feasible due to its diminished electrochemical properties, largely attributable to the presence of impurities. To address this, a two-stage regeneration process is employed. Initially, the anode material undergoes treatment in a nitric acid solution, effectively removing the copper foil and extracting lithium ions, as well as other electrolyte interaction byproducts accumulated during the battery's operational life. This is followed by a thermal treatment, which is essential for eliminating the acetylene soot and decomposing the polymer binder. The efficacy of this regeneration process is underscored by the experimental results, wherein the specific capacity of the recycled graphite is recorded at approximately 330 mA·h/g at 0.1 C discharge rate. These values are not only on par with commercially available graphite but also meet the requisite standards for reuse in LIBs, thereby underscoring the viability of this recycling approach.

Acknowledgements: The work was carried out with the support of the National Research Foundation of Ukraine within the framework of the project "Development of new types of high-capacity solid-state lithium batteries to ensure the energy security of Ukraine" (ID 2022.01/0154).

Conflict of interest: The authors declare no conflict of interest.

References

- [1] M. Li, M. Li, J. Lu, Z. Chen, K. Amine, 30 Years of lithium-ion batteries, *Advanced Materials* **30** (2018) 1800561. https://doi.org/10.1002/adma.201800561
- [2] J. Xie, Y. Lu, A retrospective on lithium-ion batteries, *Natural Communication* **11** (2020) 2499. https://doi.org/10.1038/s41467-020-16259-9

- [3] X. Feng, R. Dong, T. Wang, Q. Zhang, Ab-initio simulations accelerate the development of high-performance lithium sulfur batteries, *Material Lab* 1 (2022) 220031. https://doi.org/10.54227/mlab.20220031
- [4] Y. Qiao, H. Zhao, Y. Shen, L. Li, Z. Rao, G. Shao, Y. Lei, Recycling of graphite anode from spent lithium-ion batteries: Advances and perspectives, *EcoMat* **5** (2023) e12321. https://doi.org/10.1002/eom2.12321
- [5] T. Hettesheimer, C. Neef, S. Link, T. Schmaltz, F. Schuckert, A. Stephan, M. Stephan, T. Wicke, Lithium-Ion Battery Roadmap – Industrialization Perspectives Toward 2030, Fraunhofer Institute for Systems and Innovation Research ISI, Karlsruhe, Germany, 2023. https://doi.org/10.24406/publica-2153
- [6] Fraunhofer ISI Meta-Market-Monitoring, https://metamarketmonitoring.de/ (Accessed on December 25, 2023).
- [7] Battery Materials Review the 2024. Yearbook the state of play in battery materials, https://www.batterymaterialsreview.com/ (Accessed on December 25, 2023)
- [8] X. T. Wang, Z. Y. Gu, E. H. Ang, X. X. Zhao, X. L. Wu, Y. Liu, Prospects for managing end-of-life lithium-ion batteries: present and future, *Interdisciplinary Materials* 1 (2022) 417-433. https://doi.org/10.1002/idm2.12041
- [9] S. Natarajan, M. L. Divya, V. Aravindan, Should we recycle the graphite from spent lithium-ion batteries? The untold story of graphite with the importance of recycling, *Journal of Energy Chemistry* **71** (2022) 351-369. https://doi.org/10.1016/j.jechem.2022.04.012
- [10] X. Zeng, M. Li, D. A. El Hady, W. Alshitari, A. S. Al-Bogami, J. Lu, K. Amine, Commercialization of lithium battery technologies for electric vehicles, *Advanced Energy Materials* 9 (2019) 1900161. https://doi.org/10.1002/aenm.201900161
- [11] B. Scrosati, J. Garche, Lithium batteries: status, prospects and future, *Journal of Power Sources* **195** (2010) 2419-2430. https://doi.org/10.1016/j.jpowsour.2009.11.048
- [12] B. Moradi, G. G. Botte, Recycling of graphite anodes for the next generation of lithium ion batteries, *Journal of Applied Electrochemistry* **46** (2016) 123-148. https://doi.org/10.1007/s10800-015-0914-0
- [13] T. C. Wanger, The lithium future-resources, recycling, and the environment, *Conservation Letters* **4** (2011) 202-206. https://doi.org/10.1111/j.1755-263X.2011.00166.x
- [14] S. Natarajan, V. Aravindan, An urgent call to spent LIB recycling: whys and wherefores for graphite recovery, *Advanced Energy Materials* 10 (2020) 2002238. https://doi.org/10.1002/aenm.202002238
- [15] P. Perumal, B. Raj, M. Mohapatra, S. Basu, Sustainable approach for reclamation of graphite from spent lithium-ion batteries, *Journal of Physics: Energy* **4** (2022) 045003. https://doi.org/10.1088/2515-7655/ac8a17
- [16] 3.2 V 200 A·h Prismatic Deep Cycle LiFePO₄ Rechargeable Solar Batteries, https://howellenergy.en.made-in-china.com/product/vOjnfzCVIDkq/China-3-2V-200ah-Prismatic-Deep-Cycle-LiFePO4-Rechargeable-Solar-Batteries.html (Accessed on December 15, 2023)
- [17] J. Zhang, X. Li, D. Song, Y. Miao, J. Song, L. Zhang, Effective regeneration of anode material recycled from scrapped Li-ion batteries, *Journal of Power Sources* **390** (2018) 38-44. https://doi.org/10.1016/j.jpowsour.2018.04.039
- [18] V. Barsukov, V. Lysin, V. Khomenko, K. Lykhnitskii, Yu. Skrypnyk, *Method for chemical purification of graphite*, Ukrainian patent for a utility model No. 56888. Jan. 25 (2011)
- [19] V. Barsukov, V. Lysin, V. Khomenko, K. Lykhnitskii, Yu. Skrypnyk, *Method for chemical purification of graphite*, Ukrainian patent for a utility model No. 98691. June 11 (2012)



- [20] N. Fatima, N. Solangi, F. Safdar, J. Kumar, A short overview of recycling and treatment of spent LiFePO₄ battery, *North American Academic Research* 5 (2022) 76-87. https://doi.org/10.5281/zenodo.6970023
- [21] Y. Sheng, X. Tang, E. Peng, J. Xue, Graphene Oxide Based Fluorescent Nanocomposites for Cellular Imaging, *Journal of Material Chemistry B* 1 (2013) 512-521. https://doi.org/10.1039/c2tb00123c
- [22] Y. Wu, B. Wang, Y. Ma, Y. Huang, N. Li, F. Zhang, Y. Chen, Efficient and Large-Scale Synthesis of Few-Layered Graphene Using an Arc-Discharge Method and Conductivity Studies of the Resulting Films, *Nano Research* **3** (2010) 661-669. https://doi.org/10.1007/s12274-010-0027-3
- [23] Z. X. Shu, R. S. McMillan, J. J. Murray, Electrochemical Intercalation of Lithium into Graphite, Journal of The Electrochemical Society 140 (1993) 922-927. https://doi.org/10.1149/1.2056228
- [24] V. A. Sethuraman, L. J. Hardwick, V. Srinivasan R. Kostecki, Surface Structural Disordering in Graphite upon Lithium Intercalation/Deintercalation, *Journal of Power Sources* **195** (2010) 3655-3660. https://doi.org/10.1016/j.jpowsour.2009.12.034
- [25] C. Wang, A. J. Appleby, F. E. Little, Electrochemical impedance study of initial lithium ion intercalation into graphite powders, *Electrochimica Acta* 46 (2001) 1793-1813. https://doi.org/10.1016/S0013-4686(00)00782-9
- [26] R. Yazami, Y. F. Reynier, Mechanism of self-discharge in graphite—lithium anode, Electrochimica Acta 47 (2002) 1217-1223. https://doi.org/10.1016/S0013-4686(01)00827-1



Open Access:: ISSN 1847-9286 www.jESE-online.org

Original scientific paper

Strategy on enhancing ionic conductivity of biocompatible hydroxypropyl methyl cellulose/polyethylene glycol polymer blend electrolyte with TiO₂ nanofillers and LiNO₃ ionic salt

Mohan Srinivas and Rajashekhar F. Bhajantri[⊠]

Department of Physics, Karnatak University, Dharwad 580003, Karnataka, India

Corresponding author: □rfbhajantri@kud.ac.in; Phone: +91-836-2215316(O); Mobile: +91 9448623319

Received: April 20, 2024; Accepted: June 9, 2024; Published: June 26, 2024

Abstract

A biocompatible and biodegradable polymer in the fabrication of solid polymer electrolytes for high energy density rechargeable batteries is gaining interest owing to their safety, compatibility and flexibility. In this study, a polymer electrolyte based on hydroxypropyl methylcellulose (HPMC)/polyethylene glycol (PEG) biopolymers, incorporating TiO₂ nanofillers and LiNO $_3$ as a lithium source, was fabricated using the solution casting method. Mixed-phase TiO₂ nanofillers were synthesized via hydrolysis of titanium tetraisopropoxide. The crystal structure, phase morphology, and electrochemical impedance spectra of the films and nanofillers were investigated. X-ray diffraction analysis confirmed the amorphous nature of the polymer electrolyte and crystalline nature of nanofiller. In addition, it was noted that the amorphous phase of the polymer blend remained unaltered despite the incorporation of TiO₂ and LiNO₃. Thermogravimetric analysis and differential thermal analysis confirmed that the pure blend exhibited a melting point of around 60°C and complete degradation of around 340 °C, while the blend electrolyte with additives demonstrated thermal stability with a broad melting point. The blend containing 5 wt.% TiO₂ fillers and 10 wt.% LiNO₃ionic salt exhibited the highest ionic conductivity of 0.213 mS cm⁻¹ at room temperature. The polymer blend electrolyte displayed a narrow electrochemical stability window of 2.85 V, with the highest cationic transfer number of 0.323. The temperature-dependent ionic conductivity of the prepared polymer blend electrolyte followed Arrhenius behaviour, with an activation energy of 0.1 eV. The study examined and reported the effect of aging on the interfacial resistance of polymer blend electrolyte. The mechanical properties of the optimized HPMC/PEG/TiO₂/LiNO₃ polymer blend electrolyte were investigated and reported. Thus, this research elucidated the role of nanofillers and ionic salt in enhancing the performance of biocompatible polymer electrolytes.

Keywords

Mixed polymer; polymer composite; Arrhenius behaviour; cationic transference number; electrochemical stability

Introduction

The world's growing population and economic demands have led to a significant rise in global energy consumption. To meet the current energy needs of the world, it is imperative to engage in the mass production of energy [1]. However, relying solely on non-renewable sources like nuclear power plants, coal, and fossil fuels, as well as renewable resources like solar, wind, and hydroelectric power, is insufficient to fulfil the energy requirements of today. Moreover, the extraction of energy from non-renewable sources has contributed to the alarming global threats of global warming and pollution [2]. The effective resolution for these concerns lies in efficiently harnessing energy from sustainable and eco-friendly sources. The primary obstacle in maximizing energy extraction from environmentally friendly sources is the storage of the harnessed energy [3]. From the perspective of energy storage, new-generation energy storage devices with maximum energy density are investigated.

New generation supercapacitors and batteries with higher power and energy density gained much interest. In case of rechargeable batteries, the overall performance is not solely dependent on electrodes but also on the electrolytes within the cell. These electrolytes play a crucial role in achieving higher battery energy density [4]. The electrolytes can be in the form of liquid, gel, or solid, with liquid electrolytes offering certain advantages such as good wettability with electrodes, ionic conductivity, and reduced dendrite formation [5]. However, they are more susceptible to vulnerabilities and suffer significant drawbacks due to safety concerns, environmental issues, and limited energy density than solid electrolytes [6]. On the other hand, gel electrolytes composed of liquid components and polymer matrix have emerged as a promising alternative to liquid electrolytes, offering good heat resistance, higher ionic conductivity, and a stable electrodeelectrolyte interface. The gel polymer electrolytes also offer electrode protection and control of the thermal runaway [7]. Nonetheless, the mechanical integrity of the cell remains a major drawback for gel electrolytes. Additionally, the presence of liquid fails to suppress dendrite formation [8]. In order to attain favourable mechanical cell integrity and interfacial properties, the solid polymer composite appears to be a viable option. Typically, solid polymer electrolytes (SPE) composed of polymer chains exhibit flexibility and integrity, providing a range of adjustable parameters alongside excellent thermal stability and ionic conductivity [9].

The low-flammable solid polymer electrolyte has major restrictions based on the nanocomposite and the host polymer matrix. Brittle ceramic electrolytes exhibit lower ionic conductivity at room temperature, whereas sulphide electrolytes exhibit poor stability but higher conductivity. The polymer electrolyte made of host polymer matrix usually includes polyvinylidene fluoride (PVDF), polyethylene oxide (PEO), polyvinyl alcohol (PVA) and several polymer blends like PEO-methylcellulose (MC), PVDFhexafluoropropylene (HFP), etc. [10]. Among numerous polymer blends like PEO-carboxyl methyl cellulose (CMC), PVA-sodium alginate (SA) and PEO-polyvinyl pyrrolidone (PVP) [11], the blending of crystalline polymer with amorphous one gains tremendous interest. PEO and PVDF-co-hexafluoropropylene (HFP) polymer matrix with active nanofillers have been widely studied as electrolytes. The enhanced ionic conductivity observed in PVDF-HFP is attributed to the reduction in crystallinity of PVDF with the addition of amorphous HFP, while the blending of PEO with methylcellulose(MC)/ /polyvinyl chloride (PVC) yields better ionic conductivity and good mechanical properties [12,13]. The dielectric oxide ceramics embedded in polymers make solid electrolytes appear as potential candidates due to their affordability and demonstrated ability to offer increased power density, flexibility, and improved ionic conductivity. Furthermore, including active oxide fillers in the polymer composite improves ionic conductivity and increases the ion transference number and wider electrochemical stability window [14]. The ionic conductivity, along with the electrochemical window and thermal stability, can further be increased by the addition of ionic liquids along with oxide fillers, which have to be optimized. The increase in ionic conductivity can be attributed to the dissociation of ions resulting from Lewis acid-base interactions between the anions of ionic species and the surface groups of polymer chains containing nanofillers [15]. Most widely studied passive inorganic oxide fillers include TiO₂, ZnO, MgO, Al₂O₃, CeO₂, BaTiO₃ and SiO₂, while the active fillers based on Li includeLi₇La₃Zr₂O₁₂ (LLZO), Li_{6.4}La₃Zr_{1.4}Ta_{0.6}O₁₂ (LLZTO) and Li_{0.29}La_{0.57}TiO₃ (LLTO) [9,15]. For active fillers, higher interfacial resistance, poor compatibility with electrodes, and comparatively higher dendrite formation limit their commercialization [16]. Additionally, these passive fillers reduce the crystallization of the polymer matrix, simultaneously enhancing the channels for ion migration [9].

A water-soluble semi-synthetic hydroxypropyl methylcellulose (HPMC) is a nonionic cellulose amorphous polymer with a molecular formula ($C_{56}H_{108}O_{30}$), derived from polysaccharide units of plant cells through etherification of cellulose in which the hydroxyl groups are replaced by hydroxy propyl and methyl groups [17]. The presence of functional groups made HPMC thermo-sensitive with water retention capabilities. Biodegradable and biocompatible HPMC found applications in moderate coatings, tablet binders, drug delivery, adhesives, agriculture and cosmetics [18]. A synthetic non-immunogenic polyether (PEO), which is based on molecular weight and called also polyethylene glycol (PEG), is a semi-crystalline polymer. Moreover, PEG is a linear water-soluble polymer with molecular formula $HO(CH_2CH_2O)_nH$, and it is widely used in many biomedical, pharmaceutical, and industrial applications. PEG is also broadly used in tissue engineering and drug delivery systems due to its biocompatibility. PEG offers good film flexibility, tensile strength and barrier properties in addition to phase partitioning [19].

An extensive study has already been conducted on inorganic passive TiO₂ fillers in polymer matrix due to their good thermal stability and chemical inertness properties [15,20]. The nano TiO₂ has gained tremendous interest due to its non-toxicity, chemical inertness and optical energy band gap [21]. Also, TiO₂ has excellent mechanical, thermal and chemical properties and favours the formation of minute crystallites, thus reducing the crystallization of polymer, consequently providing new pathways for the migration of ions and charge carriers through the polymer ceramic interface [22]. Further, few surveys have reported that just the shapes of nanomaterial in the polymer blend/host polymer matrix enhance ionic conductivity. The nanomaterial with rod/wire structure exhibits excellent electrochemical properties over the spherical-shaped nanomaterial [23]. Moreover, some studies have also reported that modification of the surface of TiO₂ rods, or oxygen-induced structural modification, exhibits a good interfacial interface and enhanced ionic conductivity [16]. The defect-induced 1D nano TiO₂ micro rods developed by Luo et al. reported that the addition of TiO₂ micro rods into the PEO matrix not only reduces the crystalline phase but also improves the interfacial region with electrodes [16]. Li et al. reported that TiO₂ forming large surface area nanowires and length-diameter ratio doped with Ti³⁺ ions in PEO polymer exhibit enhanced Li-ion conductivity of the order 10 mS cm⁻¹ [23]. Furthermore, an excellent electrochemical stability window of 5.5 V at 60 °C, and a higher Li transport number of 0.36 was achieved. The addition of TiO₂ into PVDF-co-HFP reduces the porousness of the electrolyte while enhancing the ionic conductivity and interfacial stability, as reported by Ramaiah et al. [24].

Rechargeable Li-ion batteries have gained the interest of worldwide researchers due to the standard lithium reduction potential of -3.04 V (vs. SHE) and outstanding reversible electrochemical efficiency with theoretical specific capacity of 3860 mAh g⁻¹, long life, and easy intercalation of smaller Li ions compared to other ions [25]. As Li-ion source is not abundant, its reactivity with the environment and high risk of short circuits due to dendrite formation encourages researchers to find a new

alternative with the same efficiency and performance [10]. In this perspective, sodium and magnesium ion batteries emerge as possible alternatives to Li-ion batteries. Nevertheless, the movement of Na and Mg ions is slow due to their sluggish behaviour and larger ionic size. Additionally, the energy density of these batteries is comparatively lower than that of Li-ion batteries [26].

Herein, we report the synthesis of nano TiO₂ particles *via* hydrolysis of titanium tetra-isopropoxide. To the best of our knowledge, the biocompatible hybrid nano ceramic polymer composite made of polymer blend HPMC/PEG with the addition of LiNO₃ salt and TiO₂ filler has not been previously reported. The effect of TiO₂ and LiNO₃ applied as filler and ionic salt on structural, electrical and mechanical properties of HPMC/PEG/TiO₂/LiNO₃ polymer blend electrolyte has been systematically investigated. The ionic conductivity, the interaction of the polymer with filler, cationic transfer number, electrochemical stability window, and mechanical tensile strength of the optimized HPMC/PEG/TiO₂/LiNO₃ polymer blend electrolyte have been evaluated and reported.

Experimental

Chemicals

Titanium tetra-isopropoxide(Assay 98 %, Spectrochem, India), nitric acid (HNO₃, AR, SD-Fine Chem, India), hydroxypropyl methylcellulose (HPMC, methoxy content:28 to 30 %, hydroxy content: 7 to 12 %, SD-dine chem, India), polyethylene glycol 6000 (PEG, 98 %, Spectrochem, India), lithium nitrate (AR grade, 98 %, Loba Chemie Pvt. Ltd, India) were used in the present study without any further purification. Distilled water is used as a solvent throughout the experiment.

Synthesis of TiO₂

TiO₂ nanoparticles were synthesized by controlled hydrolysis of titanium tetraisopropoxide (TTIP). A 50 ml of TTIP was taken in a dry beaker, and another 50 ml of double distilled water was slowly added dropwise to the TTIP solution under continuous stirring. pH was adjusted using 1:1 HNO₃, which was added slowly while continuously monitoring the pH. Upon adding distilled water, the white precipitate of titanium hydroxide was formed and vacuum filtered using Whatman filter paper, which was washed several times with distilled water [27]. The filtrate was dried at 100 °C for 15 hours in a hot air oven. The obtained powder was finely grounded using an agate mortar and placed in a muffle furnace at 300 °C for 3 hours in the air to remove any residual content [27]. The calcined TiO₂ powder was characterized and used as a nano-filler in polymer electrolytes.

Fabrication of HPMC/PEG/TiO₂/LiNO₃ polymer blend electrolytes

The circular polymer film of 100 mm diameter was prepared by the standard solution casting technique. Initially, the blends of HPMC(100-x)/PEG(x), (x = 25 to 60 wt.%)were prepared by dissolving stoichiometric weights of HPMC and PEG 6000 polymers in distilled water. The colloidal solution was then stirred for around 400 rpm at room temperature for 16 hours to obtain a homogeneous mixture. The HPMC/PEG mixed solution was then sonicated at 15 kHz for 10 min to get the uniform electrolyte slurry. Finally, the slurry was cast onto plastic Petri dishes and dried in a hot air oven for 24 hours at 50 °C. The polymer films of around 50-100 μ m thickness were obtained for different compositions of HPMC/PEG. Further, the films were stored in a zip lock cover under a vacuum and subjected to electrochemical studies.

Nano TiO_2 particles were introduced into the polymer blend by taking HPMC/PEG/(y) TiO_2 (y =1, 2, 5, 10 wt.%), stirred at 500 rpm for 18 h, and solution casted as mentioned above. After optimizing HPMC/PEG/ TiO_2 films, a white colour, HPMC/PEG/ TiO_2 /LiNO₃ (polymer composite) films of

thickness 120-175 μ m were made by the addition of LiNO₃salt up to 15 wt.%, keeping 5 wt.% of titanium oxide constants. The schematic representation of a polymer composite containing TiO₂ and LiNO₃ and the interaction of polymer chains with nanofillers and Li ions is shown in Figure 1.

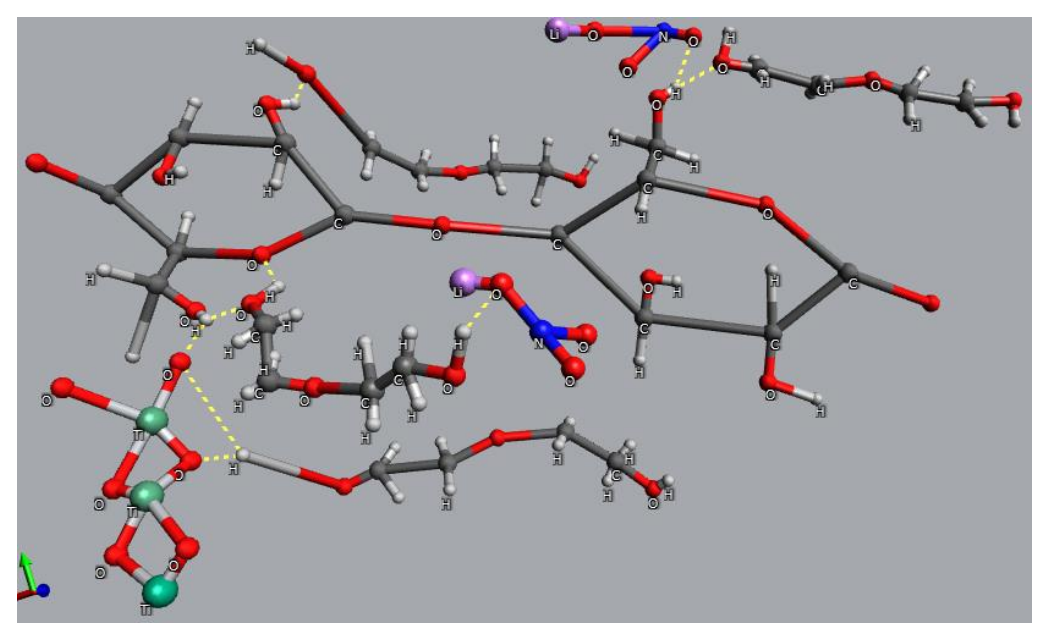


Figure 1. Schematic representation of polymer composite containing TiO₂ and LiNO₃ with hydrogen bonding

Characterization techniques

The phase and structural properties of nano TiO2and polymer blend electrolyte were investigated by Powder X-ray diffraction technique using Rigaku SmartLabSE(Japan) X-ray diffractometer with Cu- $K\alpha$ radiation, in the range 2θ from 15 to 75°, with a step size of 0.01°. The presence of functional groups, interaction of filler with polymer chains and characteristic bands corresponding to the polymer backbone were confirmed by Fourier transform infrared spectroscopy (Thermo Scientific Nicolet 6700 FT-IR Spectrometer) sweeps in the range 4000 to 400 cm⁻¹. The stability, phase transition, and decomposition of polymer blend electrolytes as a function of temperature were studied by TGA/DTA (Thermal Analysis System, Hitachi High-Tech Science Corporation, Japan). The impedance response of the polymer blend electrolytes was assessed by a Hioki IM3570 Impedance analyser, sweeping the measurement between 4 MHz to 4 Hz with a perturbation potential of 10 mV. The polymer blend electrolyte with a diameter of 1.45 cm was sandwiched between two stainless steel blocking electrodes. The temperature-dependent conductivity measurements were carried out from room temperature to 40 °C using DPI 1100 dry temperature calibrator and Hioki Impedance analyser. The linear sweep voltammetry (LSV) (between 0 and 5 V at a scan rate 10 mV s⁻¹) and chronoamperometry (polarization potential of 10 mV for 25 minutes) tests were carried out on polymer blend electrolytes by sandwiching the film in Swagelok stainless steel electrodes and recorded by OrigaFlex (OGF+500) instrument at room temperature. The mechanical properties of polymer blend electrolytes were evaluated according to ASTM - D882 standard test by Universal Testing Machine (DAK system Inc, 7200-1KN) with a speed of 1 mm min⁻¹.

Results and discussion

Powder X-ray diffraction

The X-ray diffraction (XRD) patterns of nano TiO_2 and polymer blend electrolytes are illustrated in Figure 2. The slightly broadened XRD peaks of TiO_2 nanoparticles confirm the presence of a mixed

anatase-brookite phase. Multiple sharp diffraction peaks are observed at 2θ values of 25.35, 37.95 and 48.15°, corresponding to the (101), (103), and (200) planes of the anatase phase, respectively. These peaks closely match the JCPDS file no -00-001-0562, confirming the tetragonal phase of the TiO_2 particles within the I41/amd space group. Notably, characteristic peaks at 31.1 and 54.61° correspond to the orthorhombic brookite phase of TiO_2 , attributed to the (211) and (131) planes, respectively, which is consistent with JCPDS file no- 00-002-0514. The absence of other characteristic peaks within 2θ range of 20 to 60° confirms the purity of the TiO_2 nanoparticles. These observations align with those reported by Mahata *et al.* [28]. However, the most intense peak of the brookite phase, around 54.61° is lower compared to their study and the most intense peak was observed at 27.68°.

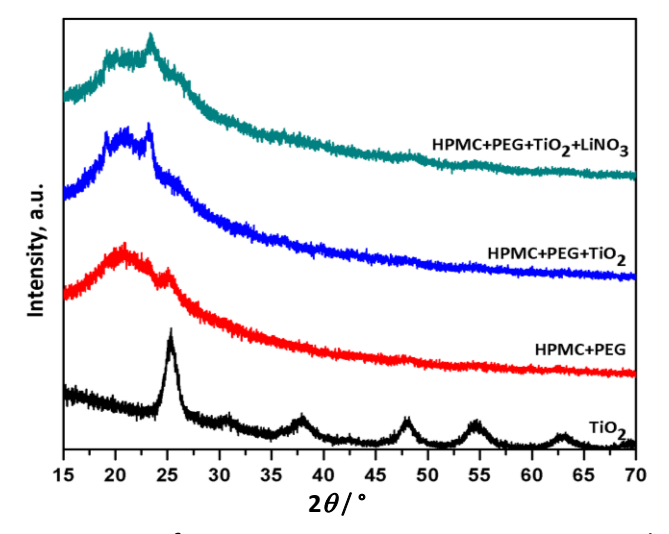


Figure 2. X-ray diffraction patterns of TiO₂, HPMC+PEG, HPMC+PEG+TiO₂ and HPMC+PEG+TiO₂+LiNO₃ polymer blends

In the mixed phases of TiO₂, the weight fraction of the brookite phase is calculated using Eq.(1) by considering the integrated intensities of both anatase and brookite phases [29]:

$$W_{\rm B} = \frac{K_{\rm B}I_{\rm B}}{K_{\rm A}I_{\rm A} + K_{\rm B}I_{\rm B}} \tag{1}$$

where I_A and I_B are the integrated intensities of the anatase and brookite phases, respectively. The correction coefficients K_A and K_B are as mentioned elsewhere [29]. The total weight fraction of the brookite phase in the mixed phase was found to be 41.6 %. Additionally, the crystallite size of TiO₂ is determined from the obtained diffraction peaks using Debye Scherrer's equation (Eq.(2)), by considering the most intense peaks of the anatase and brookite phases separately, as mentioned elsewhere [30].

$$D = \frac{k\lambda}{\beta\cos\theta} \tag{2}$$

In Eq. (2), D, λ and β stand for crystallite size, the wavelength of Cu- $K\alpha$ radiation (0.15406 nm) and full width at half maximum of the peak, respectively.

The tetragonal phase of anatase TiO_2 has an average crystallite size of 4.94 nm with edge lengths of 0.378 and 0.956 nm, attributed a, b and c axes, respectively. Whereas the orthorhombic structure of the brookite phase has a crystallite size of 5.15 nm with edge lengths 0. 908, 0.553 and 0.518 nm along a, b and c axes, respectively. The characteristic c broad hump observed in XRD pattern around 20° for bare polymer blend electrolyte and polymer electrolyte containing ionic salt and nanofillers

points toward the amorphous nature of polymer electrolyte. Further, it is noteworthy that the amorphous nature of the polymer blend electrolyte is retained with the addition of TiO_2 (5 wt.%) nanofiller and $LiNO_3$ (10 wt.%) ionic salt. This confirms that added TiO_2 fillers facilitate ionic conduction paths rather than inducing crystallization in the HPMC/PEG polymer electrolyte. Moreover, a minor peak shift is observed upon the addition of nanofillers, possibly due to induced strain in the polymer blend electrolyte.

FTIR analysis

The FTIR spectra analysis enables the determination of vibrational energies associated with distinct functional groups in polymer chains and the interactions between nanofillers and polymer matrix. In this study, the FTIR spectra of the HPMC/PEG polymer blend loaded with TiO₂ and LiNO₃, as shown in Figure 3, were examined.

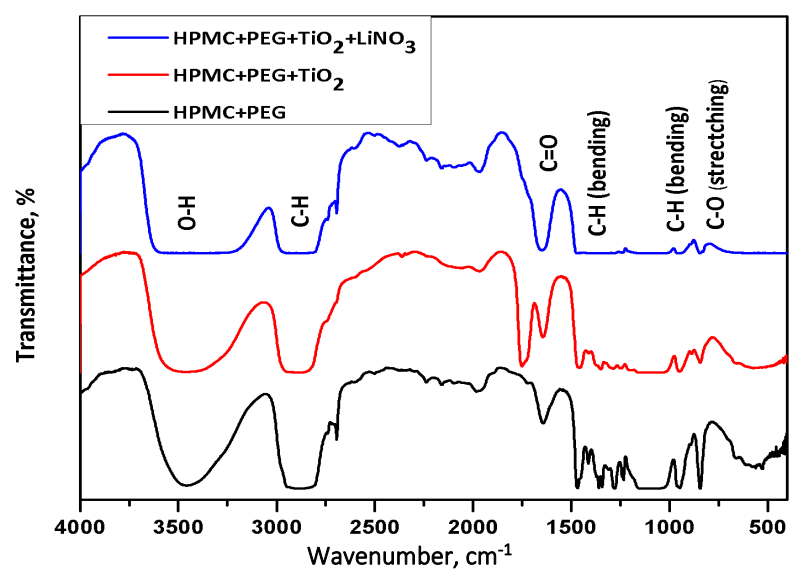


Figure 3. FTIR spectra of HPMC+PEG, HPMC+PEG+TiO₂ and HPMC+PEG+TiO₂+LiNO₃ polymer blends

The symmetric stretching vibrations of the O-H molecule, found in both HPMC and PEG, were observed within the range of 3400 to 3600 cm⁻¹. Additionally, symmetric stretching vibrations of -CH groups in the polymer chain backbone were detected around 2880 to 2930 cm⁻¹. The band around 1450 cm⁻¹ was attributed to the C-H group bending vibrations of both HPMC and PEG polymers [31]. Furthermore, stretching vibrations of C-O and C-O-C groups were identified at 1280 and 947 cm⁻¹, respectively, in HPMC polymer chains [32]. The band around 1650 cm⁻¹, indicative of carbonyl groups, was also identified by Bianchi *et al.* [33]. The presence of carbonyl groups could be attributed to the synthesis of HPMC polymer *via* esterification. Moreover, a small, negligible band at 1750 cm⁻¹ in pure HPMC/PEG blends became prominent upon the addition of TiO₂, corresponding to the C=O stretching vibration due to carbonyl groups in HPMC [34]. The characteristic band corresponding to the Ti-O-Ti bending mode was observed at 569.99 cm⁻¹ [35]. The introduction of nanofillers and salt into the pure HPMC/PEGpolymer blend led to noticeable shifts in these bands due to various kinds of interaction with the polymer chain. A successful fabrication of the complex HPMC/PEG/TiO₂/LiNO₃ polymer blend electrolyte was confirmed through the shifting and disappearance of several vibrational characteristic peaks, as summarized in Table 1.

3406

1461.81

1284, 945

Polymer blend electrolyte characteristics bands, cm⁻¹ Samples O-H C-H C=O C-H C-O-C Ti-O-Ti Stretching bending stretching stretching stretching bending **HPMC+PEG** 3456.11 2896.50 1646.58 1467.58 1280, 947 HPMC+PEG+TiO₂ 3459.03 2881.38 1646.33 1455.33 1286, 947 569.99

1650.56

2923.35

Table 1. FTIR characteristic bands of polymer blend electrolytes

TGA/DTA analysis

HPMC+PEG+TiO₂+LiNO₃

The thermal transitions of the polymer electrolyte were analysed through differential thermal analysis (DTA). Figure 4a illustrates DTA thermograms of pure HPMC/PEG and HPMC/PEG/TiO₂/ LiNO₃ polymer blend electrolytes. The thermogram reveals that the pure HPMC/PEG polymer blend undergoes melting with an endothermic peak at approximately 60 °C. Further temperature elevation induces phase separation and subsequent polymer backbone breakage, leading to the evaporation of polymer contents. The most prominent exothermic peak around 340 °C indicates rapid vaporization of fragmented polymer molecules. The incorporation of TiO₂ and LiNO₃ into the polymer blend alters its properties, as evidenced by a broader melting peak, possibly due to the partial bonding of TiO₂ with the polymer chains. Additionally, the broader exothermic peak around 340 °C for polymer blend electrolyte containing filler and salt suggests slower thermal degradation of the polymer chain backbone. Thermo-gravimetric analysis (TGA) of the prepared HPMC/PEG and HPMC/PEG/TiO₂/LiNO₃ electrolytes was conducted within the temperature range from room temperature to 500 °C to evaluate thermal stability. The resulting TGA curve in Figure 4b indicates that the polymer blend electrolyte undergoes irreversible decomposition from 3.59 to 0.012 mg. Initial weight loss in the range of 25 to 250 °C may be attributed to the water content vaporization and polymer matrix melting. However, rapid weight loss occurs in the temperature range of 320 to 380 °C, indicating thermal stability up to 250 °C, beyond which the polymer backbone breaks down into volatile compounds.

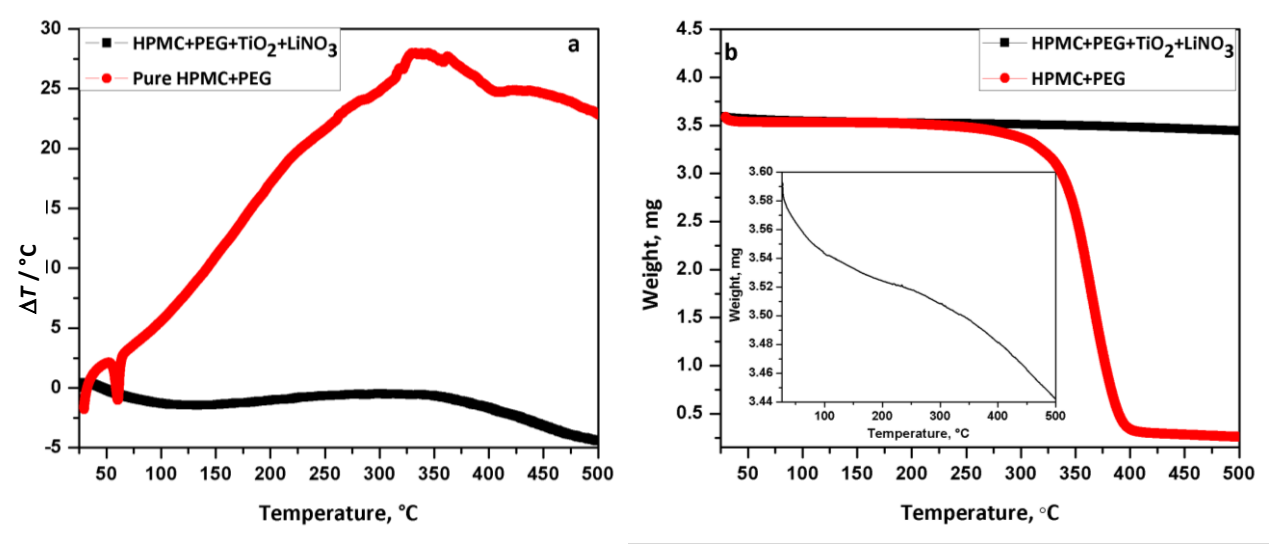


Figure 4. (a) DTA and (b) TGA curvesof HPMC/PEG and HPMC/PEG/TiO₂/LiNO₃ polymer blend electrolytes

Above 350 °C, almost 95 % weight loss is observed as broken polymer chains and molecules completely evaporate. With the addition of TiO_2 and $LiNO_3$, the polymer becomes highly thermally stable with a weight loss of approximately 15 % at 500 °C. Furthermore, the observed initial weight loss of the composite in the range of 50 to 200 °C may be attributed to solvent and volatile molecule melting and evaporation. A slight weight loss observed in the temperature range of 200 to 280 °C

may result from strong bonds between the polymer electrolyte and nanofillers, enhancing thermal stability. Continued temperature increase leads to thermal degradation of the polymer content, consistent with existing literature [22]. However, the obtained results confirm the pronounced effect of TiO₂ and LiNO₃ on the thermal stability of the polymer blend electrolyte.

Impedance spectra analysis

In energy storage systems, ionic conductivity plays a pivotal role in determining their efficiency. Polymer electrolytes of higher ionic conductivity are likely to achieve optimal efficiency. An investigation of the effect of varying concentrations of TiO_2 in flexible polymer electrolyte films on the ionic conductivity was conducted through impedance spectroscopy analysis.

The Nyquist plots in Figure 5a correspond to the optimization of weight percentages of HPMC and PEG in the HPMC/PEG polymer blend electrolyte. For all polymer blends, semicircle responses at higher to mid-frequency ranges and some spikes at the lowest frequencies suggest a dominance of the bulk polymer blend electrolyte impedance over interfacial electrolyte/electrode response.

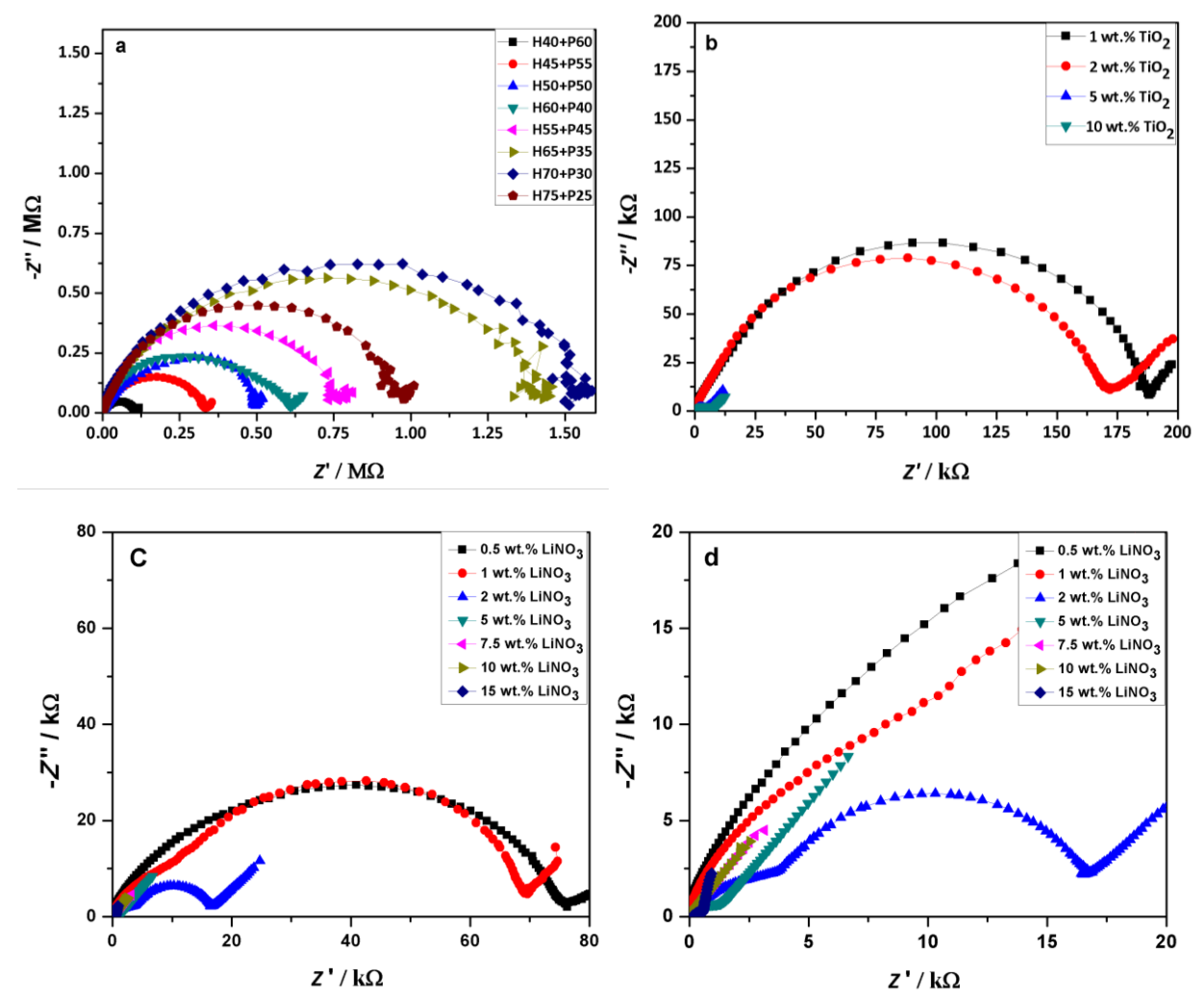


Figure 5. Nyquist plots of (a) HPMC/PEG, (b) HPMC/PEG/TiO₂, (c) HPMC/PEG/TiO₂/LiNO₃, (d) enlarged view of HPMC/PEG/TiO₂/LiNO₃ at higher frequencies

Semicircle diameters are determined by the bulk ionic resistance (R_b) values, which are relatively high, from about 1.5 M Ω for the HPMC(70)/PEG (30) polymer blend electrolyte. The notable reduction in semicircle diameters down to about 0.125 M Ω was observed with increasing PEG concentration within the HPMC polymer matrix up to 60 wt.%. This reduction may be due to improved chain mobility

at optimized weight percentages, where PEG acts as a plasticizer [36]. Additionally, blending polymers induced controlled phase separation, creating additional grain boundaries conducive to ion mobility within the host polymer matrix [37]. It was observed that the HPMC(40)/PEG(60) showed the lowest R_b value. At the same time, it has lower mechanical strength and is highly brittle, with noticeable phase separation. In contrast, the HPMC(45)/PEG(55) blend exhibited better mechanical strength and flexibility. Therefore, HPMC(45)/PEG(55) was chosen as the optimized pure polymer blend electrolyte. Additionally, TiO₂ was added as a nanofiller to the HPMC(45)/PEG(55) blend.

The Nyquist plots for HPMC(45)/PEG(55-y)/TiO₂(y),(y = 1, 2, 5 and 10 wt.%) polymer blend electrolytes at room temperature are shown in Figure 5b. These impedance plots exhibit depressed semicircles due to the bulk ionic resistance of polymer electrolytes, followed by Warburg impedance, seen as a -45° slope line in the lower frequency region. The appearance of Warburg impedance indicates the presence of ionic diffusion in the electrolyte toward blocking electrodes [38]. The decreasing trend of R_b with the addition of TiO₂ fillers from about 0.2 M Ω at 1 wt.% TiO₂, to less than 10 k Ω at 5 wt.% TiO₂ (Figure 5b) is attributed to improved chain mobility. However, further increase in TiO₂ above 5 wt.% exhibited a contrary effect on R_b . Additionally, the presence of a slope line in the low-frequency range of the Nyquist plot indicates ion diffusion through grain boundaries formed by the composite [38]. Hence 5 wt.% TiO₂ loaded HPMC/PEG was chosen as an optimized polymer blend electrolyte.

Finally, lithium nitrate (LiNO₃) ionic salt was incorporated into the optimized HPMC/PEG/ /TiO₂ polymer blend electrolyte in varying weight percentages, ranging from 0.5 to 15 wt.%, as illustrated in Figures 5c and 5d and outlined in Table 2. Observations revealed that at 0.5 and 1 wt.% of LiNO₃, R_b value remained high, at about 77.4 and 67.6 k Ω , respectively. At 2 wt.% of LiNO₃, R_b values decreased, while impedance spectra comprised two semicircles (Figure 5c). The diameter of the first semicircle can be ascribed to R_b while the other, to a contribution of impedance attributed to the electrode-electrolyte interface, where some interfacial charge transfer resistance is followed by Warburg diffusion impedance. As LiNO₃ concentration further increased up to 10 wt.%, both R_b and charge transfer resistances decreased, leading to a noticeable reduction in the diameters of both semicircles (Figure 5d). This reduction, resulting from the increased number of ionic charges generated by added LiNO₃ ionic salt, indicates a dominance of ionic diffusion and implies that most ions are effective charge carriers [39]. Upon further increasing of LiNO₃ concentration above 10 wt.%, a semicircle re-appeared in the mid-frequency region, possibly due to alterations in the polymer electrolyte owing to ionic agglomeration, ionic collision and hence the formation of double layer capacitance, which results in the increase of charge transfer resistance [40].

Optimization of polymer blend composite electrolyte through ionic conductivity evaluation

The ionic conductivity (σ) of the polymer blend electrolytes was calculated using Eq. (3)

$$\sigma = \frac{d}{R_{\rm b}A} \tag{3}$$

where d and A represent the thickness and area of the polymer electrolyte, respectively. The bulk resistance R_b values were measured from Nyquist plots as intercepts on the Z'-axis.

For the HPMC/PEG/TiO₂ polymer electrolyte of thickness in the range of 60-85 μ m, an increase of TiO₂ concentration up to 5 wt.% resulted in an enhancement of the ionic conductivity of films that was found to increase from 0.0283 μ S cm⁻¹ (at 1 wt.% TiO₂) to 1.02 μ S cm⁻¹ (at 5 wt.% of TiO₂). This increase can be attributed to the formation of more mobile chains within the polymer electrolyte. Additionally, the Lewis acid-base inherent characteristics exhibited by TiO₂ and polymer chains could increase the amorphous phase of polymer blend electrolyte, providing a potential tunnel for ion migration [12].

Further increase of TiO_2 content reduces ionic conductivity to 0.624 μ S cm⁻¹. The reduction of ionic conductivity is possibly due to aggregation of nanofillers impeding ionic conductivity by blocking interfacial pathways along with reduced salt disassociation and chain mobility [22]. Hence, 5 wt.%TiO₂ would be the optimal concentration in HPMC/PEG/TiO₂ polymer blend electrolyte that shows better performance. Following the optimization of the TiO_2 , we incorporated the ionic salt LiNO₃ by adjusting the weight percentages of PEG and HPMC, as outlined in Table 2.

Sample	Р	olymer blend co	n / O	- /C a1		
code	HPMC	PEG	TiO ₂	LiNO ₃	$R_{ m b}$ / Ω	σ / μS cm ⁻¹
HPTL 1	45	49.5	5	0.5	77400	0.921
HPTL 2	45	49.0	5	1	67600	1.65
HPTL 3	45	48.0	5	2	8360	5.25
HPTL 4	42.5	47.5	5	5	455	12.5
HPTL 5	42.5	45.0	5	7.5	69.02	80.5
HPTL 6	42.5	42.5	5	10	38.2	213
HPTL 7	40.0	40.0	5	15	611	6.47

Table 2. Optimization of HPMC/PEG/TiO₂/LiNO₃ polymer blend electrolyte

As the concentration of LiNO3 increased from 0.5 to 10 wt.%, the ionic conductivity of the electrolyte films (with thicknesses ranging from 120 to 150 µm) improved significantly, ranging from 0.921 µS cm⁻¹ to 0.213 mS cm⁻¹. This observation suggests that the addition of Li salts increases the concentration of ions serving as charge carriers within the polymer matrix, thereby enhancing ionic conductivity. Meanwhile, TiO2 facilitates ion migration by reducing the crystallinity of the polymer [41]. Furthermore, the polymer blend electrolyte acts as a solid solvent containing hydroxyl (-OH) groups, where oxygen is partially negative, and hydrogen is partially positive. The partially positive hydrogen ions interact and form hydrogen bonds with the negatively charged NO₃ ions of LiNO₃, promoting the dissociation of LiNO₃ salt and facilitating the release of more Li⁺ ions. Nevertheless, the electrostatic attraction between Li⁺ and NO₃⁻ ions may be diminished as a result of hydrogen bond formation. Additionally, the surface charge of TiO₂ competes with Li ions in forming complexes with polymer chains, thereby altering the structure and promoting the creation of more ionic conduction pathways [42]. This behaviour was also observed by Sasikumar et al. [22] in their study. It is worth mentioning that the polymer composite with 15 wt.% of LiNO3 exhibits high hygroscopicity and adhesive surface in nature, while the ionic conductivity of the film reduces to 6.47 μS cm⁻¹ (Table 2). Table 3 summarizes optimization results based on ionic conductivity obtained for HPMC/PEG, HPMC/PEG/TiO₂ and HPMC/PEG/TiO₂/LiNO₃ polymer blend electrolytes.

Table 3. Estimated bulk resistance and ionic conductivity for optimized wt.% of polymer blend electrolytes

Sample	Optimized polymer blend electrolyte content, wt.% Bulk resistance, Ω $\sigma/\mu S$ cm					σ / uS cm ⁻¹
Sample	НРМС	PEG	TiO ₂	LiNO₃	Bulk resistance, \$2	υ ο / μο τιτι
HPMC/PEG	45	55	0	0	2.87×10^{5}	0.02
HPMC/PEG/TiO ₂	45	50	5	0	3.99×10^{3}	1.02
HPMC/PEG/TiO ₂ /LiNO ₃	42.5	42.5	5	10	38.2	213

Jonscher's power law

The relationship between AC conductivity and the types of involved charge carriers, including electrons, ions and defects, can be related by Jonscher power law given by Eq. (4)

$$\sigma_{AC} = \sigma_{DC} + A\omega^2 \tag{4}$$

where ω is the hopping frequency, A is the pre-exponential factor, and s denotes the interaction of charge carriers during the hopping process. Also, both AC and DC conductivities are related by the type of charge carriers involved in conduction. Eq. (4) was used to fit the alternating current conductivity (σ_{ac} / S cm⁻¹) as a function of the logarithm of frequency (log ω), as demonstrated for the optimized HPMC/PEG, HPMC/PEG/TiO₂, and HPMC/PEG/TiO₂/LiNO₃ polymer blend electrolytes in Figure 6(a-c). Table 4 summarizes the estimated parameter values from the Jonscher power law fitting.

In the case of the pure HPMC/PEG blend (Figure 6a, Table 4), the AC conductivity remains relatively constant in the lower and mid-frequency range but exhibits an increase at higher frequencies.

 Sample code
 σ_{DC} / μS cm⁻¹
 A
 s

 (HPMC+PEG)
 0.016
 1.99 × 10⁻¹⁰
 0.58

 (HPMC+PEG+TiO₂)
 0.08
 9.93×10⁻⁹
 0.36

 (HPMC+PEG+TiO₂+LiNO₃)
 1.38
 3.85×10⁻⁸
 0.84

Table 4. Estimated parameter values from Jonscher power law fitting (for optimized conditions)

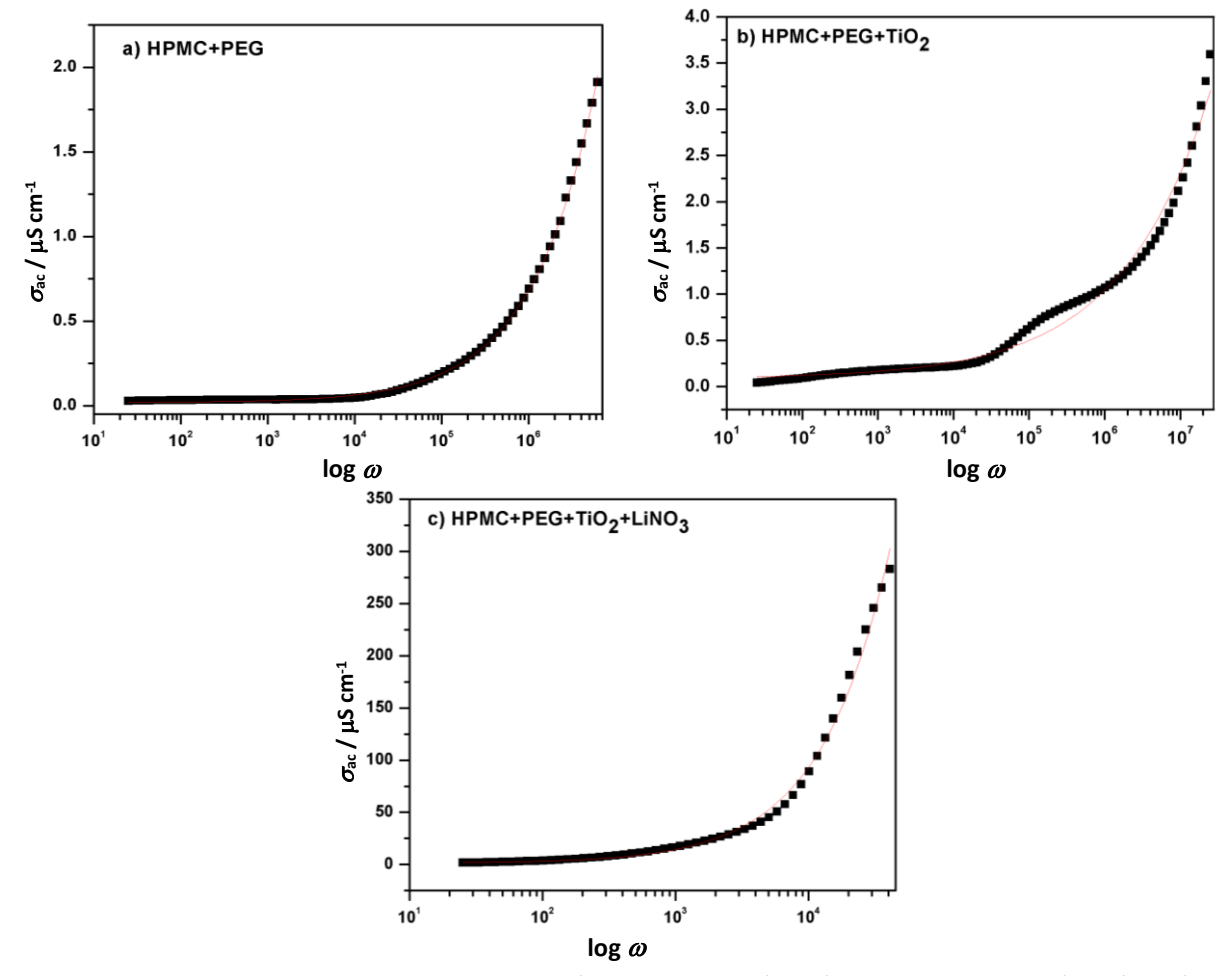


Figure 6. Jonscher power law fitting for (a) HPMC/PEG, (b) HPMC/PEG/TiO₂, and (c) HPMC/PEG/TiO₂/LiNO₃ polymer blend electrolytes

The increased conductivity at higher frequencies is due to two main factors: firstly, to the protonation and deprotonation of polar functional groups (such as -OH and -O- groups) along with enhanced segmental motion, and secondly, the hopping of ions between sites, a phenomenon observed in the Grotthuss mechanism [43]. However, the pre-factor *A*, which corresponds to the frequency-dependent conductivity, is found to be 1.99×10⁻¹⁰, two orders of magnitude lower than

DC conductivity. This suggests that the DC conductivity predominates. The parameter *s* is 0.58, which is less than 1, indicating multiple ion relaxation processes [38].

Upon introduction of TiO_2 into the polymer electrolyte (Figure 6b, Table 4), the pre-factor A increases by an order of magnitude while the value of s decreases. This indicates either a slightly slower backward motion of the charge carriers with respect to frequency or a change in the site relaxation time. Nevertheless, the DC conductivity increases, but the order of magnitude of DC conductivity remains the same [38]. With the addition of $LiNO_3$ (Figure 6c, Table 4), the AC conductivity starts to increase in the mid-frequency range. The DC conductivity experiences a substantial enhancement, reaching $1.38 \, \mu S \, cm^{-1}$, representing a two-order-of-magnitude increase. The pre-factor A also increased to 3.85×10^{-8} , suggesting the frequency-dependent relationship of conductivity. Additionally, the parameter s attains a value of 0.844, approaching unity, which signifies a pronounced dependence of AC conductivity on frequency. At higher frequencies, the increase in conductivity corresponds to enhanced mobility of Li ions within the polymer matrix. Furthermore, the Jonscher power law fitting confirms that the increased conductivity is indeed a consequence of a greater number of ions present [38].

Effect of aging on the optimized HPMC/PEG/TiO₂/LiNO₃ polymer blend electrolyte

Impedance analysis was conducted to observe the behaviour of the optimized HPMC/PEG//TiO $_2$ /LiNO $_3$ polymer blend electrolyte over time (1 to 6 days) (Figure 7). The results suggested that the resistance of the optimized polymer blend electrolyte containing 10 wt.% of LiNO $_3$ salt was mainly determined by the interfacial resistance. Figure 7 illustrates that the polymer blend electrolyte experienced notable changes in resistance with aging. Initially, on day 1, the interfacial resistance at the low-frequency intercept in Figure 7 was 84.8 Ω . By day 3, this resistance decreased to 38.2 Ω and then increased significantly to 82.0 Ω by day 5, after which it stabilized. These results suggest that the polymer electrolytes could exhibit improved interfacial stability after an optimal storage period, thereby enhancing performance. The reduction in resistance may be attributed to moisture absorption, possibly facilitated by the ability of nano TiO $_2$ to effectively retain the solvent through capillary action, allowing the polymer chain to undergo a relaxation process and creating more flexible pathways for ions [42].

Saikumar et~al.~ [22] reported that TiO₂-doped HSPE polymer composite film undergoes a significant variation in interfacial resistance, which rises from 154 to 758 Ω and reduces and stabilizes at 490 Ω after 10 days and claims that TiO₂-HSPE has better interfacial stability. A study by Zhai et~al.~ [42] on polymer composite made of TiO₂ and PVDF-HFP in addition to the ionic liquid reported that interfacial resistance of the sample NCPE-0 increased from 250 to 850 Ω after 12 days and reached a steady value of 900 Ω , whereas their sample NCPE-2 reaches a steady value of 400 Ω after 8 days.

The temperature-dependent Nyquist plots of optimized HPMC/PEG/TiO₂/LiNO₃ polymer blend electrolyte as a function of temperature are shown in Figure 8. The temperature-dependent ionic conductivity studies were carried out on the optimized polymer blend electrolyte on day 7 (after stabilization).

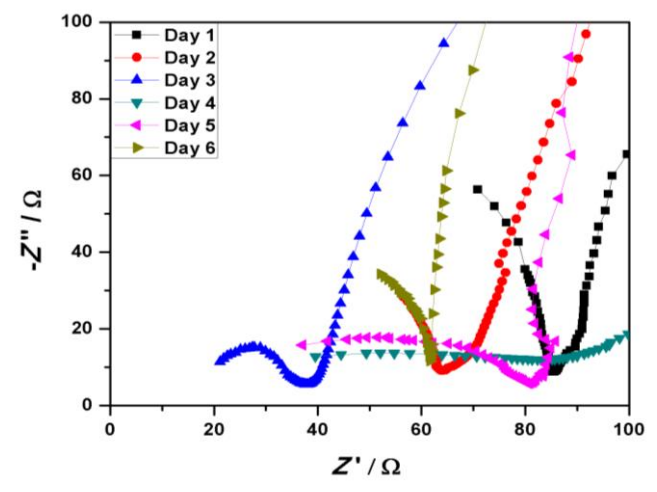


Figure 7. Nyquist plots of optimized HPMC+PEG+TiO₂+LiNO₃ polymer blend electrolyte aged up to 6 days

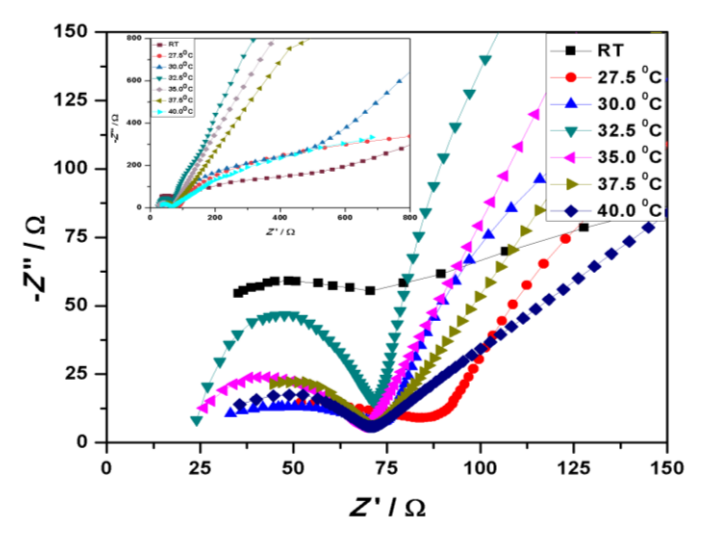


Figure 8. Temperature-dependent Nyquist plots of optimized HPMC/PEG/TiO₂/LiNO₃ polymer blend electrolyte

The ionic conductivity increases from 0.099 to 0.119 mS cm⁻¹ as temperature rises from room temperature (26 °C) to 40 °C. The Nyquist plots at room temperature, 27.5 and 30 °C have two semicircles. The mid-frequency semicircle indicated charge transfer resistance likely due to ionic agglomeration, while the high-frequency semicircle corresponds to the bulk of the solid electrolyte (on day 7) [6]. Interestingly, above 35 °C, the slope line corresponding to ionic diffusion dominates, while the interfacial resistance of the polymer electrolyte is also reduced. This confirmed that distributed nano TiO_2 in the polymer matrix will enhance the conductivity by creating voids and defects in the polymer matrix, thus preventing the crystallization of the polymer matrix. In addition, the polymer blend undergoes a thermal expansion above 30 °C, improving the motion of polymer chains and favouring the mobility of ionic charge carriers [42]. However, no significant improvement in ionic conductivity was observed above 37.5 °C.

The Arrhenius equation (5) corresponds to the temperature-dependent hopping mechanism of ions in polymer blend electrolytes. The Arrhenius plot of $\ln \sigma vs$. 1000 T^1 for optimized polymer blend electrolytes follows a linear relationship as depicted in Figure 9, confirming the Arrhenius behaviour. The plot reveals that optimized quantities show stronger temperature dependence.

$$\sigma = \sigma_0 e^{\frac{-E_a}{kT}} \tag{5}$$

In Eq. (5), σ_0 is the pre-exponential factor, E_a is the activation energy, k is the Boltzmann constant and T is the absolute temperature. By linear fitting the above equation, the estimated value of activation energy E_a is 0.1 eV. Quite close comparable values were reported by Trevisanello $et\ al$. [40] for Li|PEO, LLZO|PEO and lithium aluminium titanium phosphate (LATP)|PEO electrolytes. The work of Wang $et\ al$. [44] on pure lithium aluminium germanium phosphate (LAGP) and PEO/LAGP/LiTFSI composite materials reported an activation energy of 0.32 and 0.99 eV, respectively. Additionally, they reported that ice-templated LAGP/PEO attains 1.11 mS cm⁻¹ at 60 °C and corresponding activation energy of 0.45 eV. Similarly, Ahmed $et\ al$. [45] reported that 70 % of LiSn₂(PO₄)₃ (LSP powder) in PEO/LiClO₄ composite has an activation energy of 0.34 eV in the temperature range 27 to 60 °C which is impressively less than pure LSP powder whereas the conductivity is maximum of 0.118 mS cm⁻¹ at 60 °C. Zhai $et\ al$. [42] reported that activation energy in PVDF-HFP polymer composite containing TiO₂ and ionic liquid decreases with an increase in TiO₂ concentration. Mei $et\ al$. [46] reported the activation energy as high as 1.67 to 1.77 eV for LLZTO added PEO-based polymer composite material. They also noted that the crystalline phase of the polymer electrolyte necessitates higher activation energy due to the increased energy required for ion migration compared to the amorphous phase.

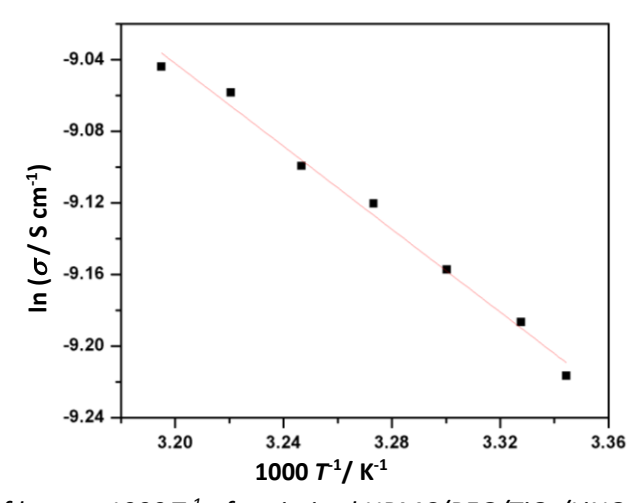


Figure 9. Arrhenius plot of In σ vs. 1000 T⁻¹ of optimized HPMC/PEG/TiO₂/LiNO₃ polymer blend electrolyte

The total conductivity of the composite is influenced by both cation and anion movement, as well as electronic conduction. The transference number of cations within an electrolyte significantly impacts recyclability and overall battery performance. Cation transport can be estimated using the Bruce-Vincent equation (6):

$$t_{+} = \frac{I_{SS} \left(\Delta V - I_{0} R_{0} \right)}{I_{0} \left(\Delta V - I_{SS} R_{SS} \right)} \tag{6}$$

where *I*₀, *I*_{SS}, *R*₀ and *R*_{SS} represent the initial current, steady-state saturation current, and interfacial resistance before and after polarization, respectively. The initial and steady-state currents were determined using potentiostatic polarization, where current is measured over time at the constant potential of 10 mV, with the polymer electrolyte sandwiched between two non-blocking stainless steel electrodes. The potentiostatic polarization curve at 10 mV DC bias for 1500 seconds and Nyquist plots before and after polarization are depicted in Figure 10a and b, respectively.

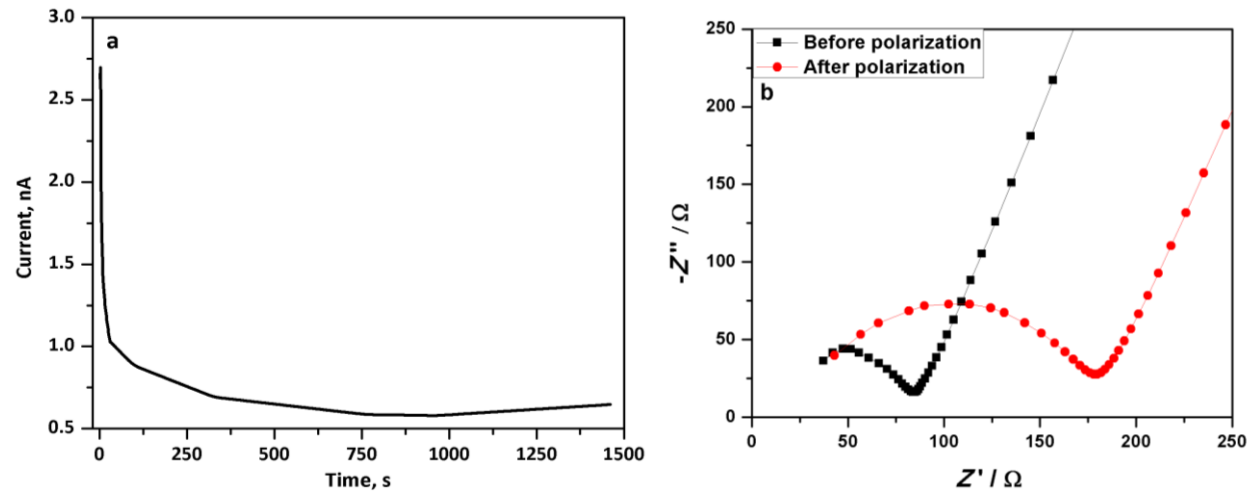


Figure 10.(a) Chronoamperometry response of optimized HPMC/PEG/TiO₂/LiNO₃ polymer blend composite electrolyte at 10mV bias, (b) Nyquist plots before and after polarization

Initially, the polarization current of 2.61 nA decreases over time, reaching a steady value of 0.58 nA after 650 s. The initial maximum current indicates the movement of all ionic species within the host polymer matrix, suggesting the contribution of both Li cations and nitrate anions as charge carriers, resulting in higher currents. The current exponentially decreases with time, reaching a steady state where only cationic species are involved in conductivity. The Nyquist plot after potentiostatic polarization shows higher interfacial resistance, indicating the formation of an anionic layer at the interface that may impede cation movement. Calculations reveal that the highest transference number for the optimized polymer blend composition is 0.323, a considerable value for battery fabrication, closely resembling polymer electrolytes with liquid plasticizers [47]. Previous study by Deivanayagam $et\ al.$ [47] reported a transference number (t_+) value of 0.23 for highly cyclable polymer electrolytes for Mg batteries. Hu $et\ al.$ [48] reported Li-ion transference numbers of 0.51 and 0.3 for Li/Al-SE/Li and Li/SE/Li cells, respectively, with enhanced ionic conductivity and dendrite suppression through the incorporation of alumina.

A new strategy for Li-based batteries with increased energy density, a wide electrochemical window, and excellent ionic conductivity has gained tremendous interest. To ensure the safety and cycling performance of batteries, an electrolyte with higher electrochemical and thermal stability is preferred. To assess the electrochemical potential window of the polymer electrolyte, linear sweep voltammetry (LSV) was conducted by sandwiching the polymer electrolyte between stainless-steel electrodes, with a scan rate of $1.0 \, \text{mV} \, \text{s}^{-1}$ at room temperature across the range of 0 to 5V as depicted in Figure 11.

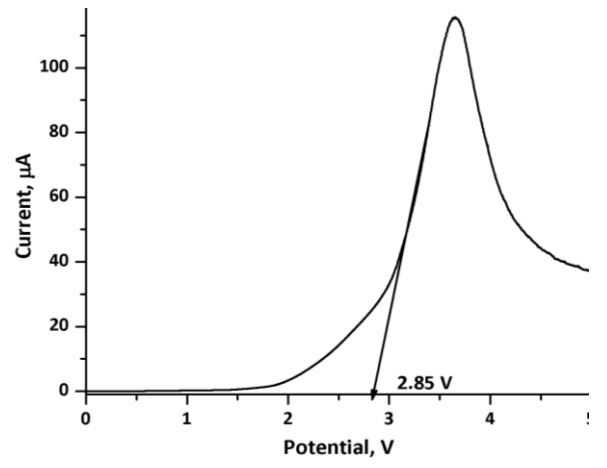


Figure 11. Linear sweep voltammogram of optimized HPMC/PEG/TiO₂/LiNO₃ polymer blend electrolyte

The observed increase in anodic current with potential corresponds to the degradation and decomposition of the polymer matrix and, hence, the contribution from anions present in the matrix [22,49]. However, an anodic peak is observed at 3.5 V, indicating an oxidation reaction of the polymer. The results show that the optimized polymer electrolyte has a relatively narrow chemical stability window of 2.85 V, determined by the intercept of the rapid current change curve on the voltage axis at zero current. These findings highlight the safe use of optimized polymer electrolytes in batteries with low-voltage cathode materials, ideally operating below 2.8 V.

Mechanical properties of optimized polymer blend electrolytes

Ensuring the safety and reliability of polymer electrolytes is crucial in Li-ion batteries. The strong mechanical integrity of solid-state electrolytes in batteries directly correlates with safety and reliability. The mechanical reliability is based on tensile strength, owing to the subsidiary properties in comparison with Ionic conductivity and growth of Li dendrite through polymer films. While the ionic conductivity of polymer films improves with enhanced flexibility, introducing organic plasticizers can compromise the mechanical integrity of these films. Consequently, achieving a balance between flexibility and mechanical strength becomes imperative to suppress dendrite growth effectively. Strategies such as incorporating nanofillers and reinforcement agents improve mechanical strength and suppress dendrite proliferation. A polymer electrolyte with good flexibility and mechanical strength is desired for the practical implementation in batteries [50].

The mechanical properties were evaluated using stress vs. strain curve for HPMC/PEG, HMC//PEG/TiO₂andHPMC/PEG/TiO₂/LiNO₃ polymer blend electrolytes, as demonstrated in Figure 12. Evaluated mechanical properties of optimized HPMC/PEG, HPMC/PEG/TiO₂ and HPMC/PEG/TiO₂//LiNO₃ polymer blend electrolytes are summarized in Table 5.

Sample	Tensile strength, MPa	Elongation at break, %	
HPMC/PEG	0.470	0.493	
HPMC/PEG/TiO ₂	2.838	1.866	
HPMC/PEG/TiO ₂ /LiNO ₃	5.700	6.021	

Table 5. Mechanical properties of optimized polymer blend electrolytes

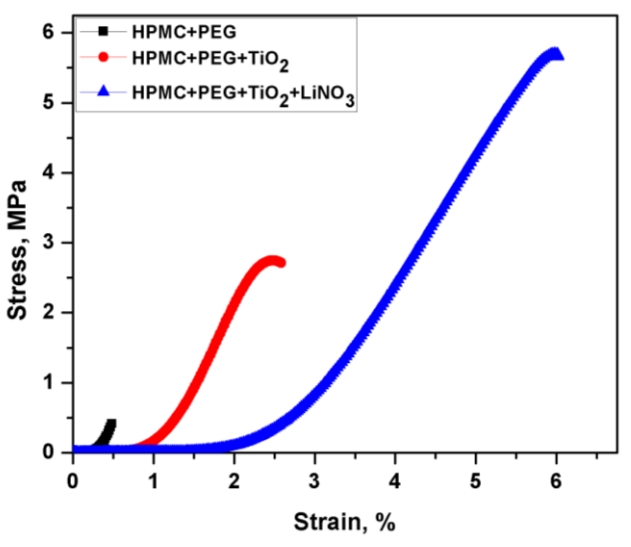


Figure 12. Tensile strength of optimized HPMC/PEG, HPMC/PEG/TiO₂ and HPMC/PEG/TiO₂/LiNO₃polymer blend electrolytes

Pure polymer blend HPMC/PEG exhibits a tensile strength of 0.470 MPa, whereas the introduction of 5 wt.% TiO₂ yields a notable increase to 2.83 MPa. Further tensile strength increased to 5.7 MPa by incorporating 10 wt.% LiNO₃. This improvement in tensile strength can be attributed to the interaction between nanofillers and polymer chains, imparting a reinforcing effect. The enhanced mechanical strength of polymer electrolytes is due to the uniform dispersion of nanofillers and the strong adhesion effect between nanofiller and polymer matrix. However, the introduction of inorganic filler into the polymer matrix may reduce flexibility due to the creation of defects and voids. Sasikumar *et al.* [22] reported the maximum mechanical strength of 9.3 MPa for 10 wt.% of TiO₂-NCF polymer electrolyte with ionic conductivity in the range of mS cm⁻¹. Song *et al.* [51] studied a gel polymer electrolyte for Li-ion batteries and reported a maximum mechanical strength of 4.07 MPa with good ionic conductivity of 6.22 mS cm⁻¹. It can be stated at the end that the optimized HPMC/PEG/TiO₂//LiNO₃ polymer electrolyte contains 5 wt.% TiO₂ with 10 wt.% LiNO₃ exhibits both good ionic conductivity and mechanical strength, making it a promising material for battery fabrication.

Conclusion

A flexible HPMC/PEG/TiO₂/LiNO₃ polymer blend electrolytes were fabricated by the solution casting method. XRD analysis confirmed that the addition of nano TiO₂ has no effect on the amorphous nature of the polymer film. FTIR analysis confirms the functional groups and their interactions within the polymer electrolyte. The observed shifts in the FTIR spectra bands are due to the interactions between TiO₂, the polymer chains, and LiNO₃. The thermal stability and phase transition of the flexible polymer blend electrolyte were evaluated by TGA/DTA analysis and found that enhanced thermal stability around 340 °C and a broader melting point. Nyquist plots indicated that the optimized HPMC/PEG/TiO₂/LiNO₃ (5 wt.% TiO₂ and 10 wt.% LiNO₃) polymer blend electrolyte exhibited a maximum ionic conductivity of 0.213 mS cm⁻¹ at room temperature. This enhanced conductivity suggests that the nanofillers facilitate additional pathways for ion migration. The temperaturedependent ionic conductivity followed linear Arrhenius behaviour, with a fitted activation energy of 0.1 eV. Jonscher power law fitting showed that the pure HPMC/PEG blend primarily contributed to DC conductivity, while the HPMC/PEG/TiO₂/LiNO₃ polymer blend electrolyte had a higher contribution from the frequency-dependent parameter A and s of the Arrhenius equation. The optimized polymer blend electrolyte, placed between stainless steel electrodes and polarized at 10 mV for 25 minutes, achieved a maximum Li ion transference number of 0.323. Linear sweep voltammetry, conducted at a scan rate of 1.0 mV s⁻¹ up to 5 V, revealed an electrochemical stability window of 2.85 V, with an oxidation peak at 3.5 V. The tensile strength of the polymer blend electrolytes improved with the addition of the nanofiller due to its reinforcing effect, reaching 5.70 MPa for the optimized polymer blend. Future research work will be focused on optimizing the composition through software-assisted experimental designs, incorporating ionic liquid, co-fillers, and introducing microporous structural defects.

Authorship contribution statement: Mohan S: Conceptualization, Methodology, Investigation, Data acquisition and analysis, visualization, original draft writing and editing. Rajashekar F Bhajantri: Conceptualization, Project administration, Supervision, Funding acquisition, formal analysis, review and editing.

Declaration of competing interests: Authors declare no competing financial or personal relationships that could influence the work reported in this project.

Submission declaration: The authors declare that the manuscript is our original work and all the authors contributed significantly. Further, this work is not previously published and not under consideration elsewhere.

Funding agency: Science and Engineering Research Board (SERB), Department of Science and Technology (DST), Ministry of Science and Technology, Government of India (File No. EEQ/2022/001028).

Acknowledgements: The authors acknowledge the Science and Engineering Research Board, Department of Science and Technology, Government of India, New Delhi for the Research Project (EEQ/2022/001028). Also, the authors are thankful to SAIF, Karnatak University Dharwad for XRD& FTIR Facilities. Authors acknowledges support from Dr. Saraswati Masti and her students, Department of Chemistry, Karnataka Science College, Dharwad for providing Universal Testing Machine facility.

References

- [1] T. Juqu, S. C. Willenberg, K. Pokpas, N. Ross, Advances in paper-based battery research for biodegradable energy storage, *Advanced Sensor and Energy Materials* **1** (2022) 100037. https://doi.org/10.1016/j.asems.2022.100037
- [2] L. Yang, X. Kong, F. Li, H. Hao, Z. Cheng, H. Liu, J.-F. Li, S. Zhang, Perovskite lead-free dielectrics for energy storage applications, *Progress in Materials Science* **102** (2019) 72-108. https://doi.org/10.1016/j.pmatsci.2018.12.005
- [3] E. E. R. Gómez, J. H. M. Hernandez, Obtaining Electrospun Membranes of Chitosan/PVA and TiO₂ as a Solid Polymer Electrolyte with Potential Application in Ion Exchange Membranes, *Membranes* **13** (2023) 862. https://doi.org/10.3390/membranes13110862
- [4] R. Borah, F. R. Hughson, J. Johnston, T. Nann, On battery materials and methods, *Materials Today Advances* **6** (2020) 100046. https://doi.org/10.1016/j.mtadv.2019.100046
- [5] N. Takami, M. Sekino, T. Ohsaki, M. Kanda, M. Yamamoto, New thin lithium-ion batteries using a liquid electrolyte with thermal stability, *Journal of Power Sources* **97-98** (2001) 677-680. https://doi.org/10.1016/S0378-7753(01)00699-1
- [6] J. Chattopadhyay, T. S. Pathak, D. M. F. Santos, Applications of Polymer Electrolytes in Lithium-Ion Batteries, *Polymers* **15** (2023) 3907. https://doi.org/10.3390/polym15193907
- [7] W. Ren, C. Ding, X. Fu, Y. Huang, Advanced gel polymer electrolytes for safe and durable lithium metal batteries: Challenges, strategies, and perspectives, *Energy Storage Materials* **34** (2021) 515-535. https://doi.org/10.1016/j.ensm.2020.10.018
- [8] J. Castillo, A. Santiago, X. Judez, I. Garbayo, J.A. Coca Clemente, M.C. Morant-Miñana, A. Villaverde, J. A. González-Marcos, H. Zhang, M. Armand, C. Li, Safe, Flexible, and High-Performing Gel-Polymer Electrolyte for Rechargeable Lithium Metal Batteries, *Chemistry of Materials* 33 (2021) 8812-8821. https://doi.org/10.1021/acs.chemmater.1c02952
- [9] S. Das, A. Ghosh, Symmetric electric double-layer capacitor containing imidazolium ionic liquid-based solid polymer electrolyte: Effect of TiO₂ and ZnO nanoparticles on electrochemical behavior, *Journal of Applied Polymer Science* **137** (2020) 48757. https://doi.org/10.1002/app.48757
- [10] X. Pan, P. Yang, Y. Guo, K. Zhao, B. Xi, F. Lin, S. Xiong, Electrochemical and Nanomechanical Properties of TiO₂ Ceramic Filler Li-Ion Composite Gel Polymer Electrolytes for Li Metal Batteries, *Advanced Materials Interfaces* **8** (2021) 2100669. https://doi.org/10.1002/admi.202100669
- [11] A. A. Al-Muntaser, R. A. Pashameah, A. E. Tarabiah, E. Alzahrani, S. A. AlSubhi, A. Saeed, A. M. Al-Harthi, R. Alwafi, M. A. Morsi, Structural, morphological, optical, electrical and dielectric features based on nanoceramic Li₄Ti₅O₁₂ filler reinforced PEO/PVP blend for optoelectronic and energy storage devices, *Ceramics International* **49** (2023) 18322-18333. https://doi.org/10.1016/j.ceramint.2023.02.204
- [12] J. Sugumaran, A. L. Ahmada, N. D. Zaulkiflee, Improvement of ionic conductivity of titanium dioxide incorporated PVDF-HFP/cellulose acetate electrolyte membrane, *IOP Conference Series: Materials Science and Engineering* **736** (2020) 052025. https://doi.org/10.1088/1757-899X/736/5/052025

- [13] H. T. Ahmed, O.G. Abdullah, Preparation and Composition Optimization of PEO:MC Polymer Blend Films to Enhance Electrical Conductivity, *Polymers* **11** (2019) 853. https://doi.org/10.3390/polym11050853
- [14] S. A. Rasaki, C. Liu, C. Lao, Z. Chen, A review of current performance of rare earth metal-doped barium zirconate perovskite: The promising electrode and electrolyte material for the protonic ceramic fuel cells, *Progress in Solid State Chemistry* **63** (2021) 100325. https://doi.org/10.1016/j.progsolidstchem.2021.100325
- [15] A. Jagadeesan, M. Sasikumar, R. Hari Krishna, N. Raja, D. Gopalakrishna, S. Vijayashree, P. Sivakumar, High electrochemical performance of nano TiO₂ ceramic filler incorporated PVC-PEMA composite gel polymer electrolyte for Li-ion battery applications, *Materials Research Express* **6** (2019) 105524. https://doi.org/10.1088/2053-1591/ab3cb8
- [16] B. Luo, W. Wang, Q. Wang, W. Ji, G. Yu, Z. Liu, Z. Zhao, X. Wang, S. Wang, J. Zhang, Facilitating ionic conductivity and interfacial stability via oxygen vacancies-enriched TiO₂ microrods for composite polymer electrolytes, Chemical Engineering Journal 460 (2023) 141329. https://doi.org/10.1016/j.cej.2023.141329
- [17] K. Deshmukh, M. Basheer Ahamed, R. R. Deshmukh, S. K. Khadheer Pasha, P. R. Bhagat, K. Chidambaram, *Biopolymer Composites With High Dielectric Performance: Interface Engineering*, in: *Biopolymer Composites Electronics*, Elsevier, 2017, pp. 27-128. https://doi.org/10.1016/B978-0-12-809261-3.00003-6
- [18] L. Ma, T. Shi, Z. Zhang, X. Liu, H. Wang, Wettability of HPMC/PEG/CS Thermosensitive Porous Hydrogels, *Gels* **9** (2023) 667. https://doi.org/10.3390/gels9080667
- [19] P. Zarrintaj, M. R. Saeb, S. H. Jafari, M. Mozafari, *Application of compatibilized polymer blends in biomedical fields*, in: Compatilization of Polymer Blends, Elsevier, 2020, pp. 511-537. https://doi.org/10.1016/B978-0-12-816006-0.00018-9
- [20] A. A. Al-Muntaser, R. A. Pashameah, A. Saeed, R. Alwafi, E. Alzahrani, S. A. AlSubhi, A. Y. Yassin, Boosting the optical, structural, electrical, and dielectric properties of polystyrene using a hybrid GNP/Cu nanofiller: novel nanocomposites for energy storage applications, *Journal of Materials Science: Materials in Electronics* **34** (2023) 678. https://doi.org/10.1007/s10854-023-10104-7
- [21] L. Zhang, J. Lian, L. Wu, Z. Duan, J. Jiang, L. Zhao, Synthesis of a Thin-Layer MnO 2 Nanosheet-Coated Fe 3 O 4 Nanocomposite as a Magnetically Separable Photocatalyst, *Langmuir* **30** (2014) 7006-7013. https://doi.org/10.1021/la500726v
- [22] M. Sasikumar, R. H. Krishna, M. Raja, H. A. Therese, N. T. M. Balakrishnan, P. Raghavan, P. Sivakumar, Titanium dioxide nano-ceramic filler in solid polymer electrolytes: Strategy towards suppressed dendrite formation and enhanced electrochemical performance for safe lithium ion batteries, *Journal of Alloys and Compounds* 882 (2021) 160709. https://doi.org/10.1016/j.jallcom.2021.160709
- [23] C. Li, Y. Huang, C. Chen, X. Feng, Z. Zhang, High-performance polymer electrolyte membrane modified with isocyanate-grafted Ti³+ doped TiO₂ nanowires for lithium batteries, *Applied Surface Science* **563** (2021) 150248. https://doi.org/10.1016/j.apsusc.2021.150248
- [24] N. Ramaiah, V. Raja, C. Ramu, Preparation and characterisation of electrolyte filled solid poly (viny-lidene difluoride-co-hexafluoropropylene) polymer TiO₂ membranes for battery application, *Materials Research Innovations* **26** (2022) 214-221. https://doi.org/10.1080/14328917.2021.1942406
- [25] J. C. Barbosa, R. Gonçalves, C. M. Costa, S. Lanceros-Méndez, Toward Sustainable Solid Polymer Electrolytes for Lithium-Ion Batteries, *ACS Omega* **7** (2022) 14457-14464. https://doi.org/10.1021/acsomega.2c01926
- [26] N. Farah, H. M. Ng, A. Numan, C.-W. Liew, N. A. A. Latip, K. Ramesh, S. Ramesh, Solid polymer electrolytes based on poly(vinyl alcohol) incorporated with sodium salt and ionic liquid for electrical double layer capacitor, *Materials Science and Engineering: B* **251** (2019) 114468. https://doi.org/10.1016/j.mseb.2019.114468



- [27] M. Grześkowiak, R. J. Wróbel, J. Grzechulska, J. Przepiórski, Preparation and characterization of titania powders obtained via hydrolysis of titanium tetraisopropoxide, *Materials Science-Poland* **32** (2014) 71-79. https://doi.org/10.2478/s13536-013-0163-z
- [28] S. Mahata, S.S. Mahato, M. M. Nandi, B. Mondal, Synthesis of TiO₂ nanoparticles by hydrolysis and peptization of titanium isopropoxide solution, AIP Conference Proceedings **1461(1)** (2012) 225-228. https://doi.org/10.1063/1.4736892
- [29] L. Cano-Casanova, A. Amorós-Pérez, M. Ouzzine, M.A. Lillo-Ródenas, M.C. Román-Martínez, One step hydrothermal synthesis of TiO2 with variable HCl concentration: Detailed characterization and photocatalytic activity in propene oxidation, *Applied Catalysis B:*Environmental 220 (2018) 645-653. https://doi.org/10.1016/j.apcatb.2017.08.060
- [30] S. Saravanan, M. Balamurugan, T. Soga, Synthesis of Titanium Dioxide Nanoparticles with Desired Ratio of Anatase and Rutile Phases and the Effect of High Temperature Annealing, *Transactions of the Materials Research Society of Japan* **43** (2018) 255-261. https://doi.org/10.14723/tmrsj.43.255
- [31] D. Kida, O. Gładysz, M. Szulc, J. Zborowski, A. Junka, M. Janeczek, A. Lipińska, A. Skalec, B. Karolewicz, Development and Evaluation of a Polyvinylalcohol -Cellulose Derivative-Based Film with Povidone-Iodine Predicted for Wound Treatment, *Polymers* **12** (2020) 1271. https://doi.org/10.3390/polym12061271
- [32] M. Sahu, V. R. M. Reddy, B. Kim, B. Patro, C. Park, W. K. Kim, P. Sharma, Fabrication of Cu₂ZnSnS₄ Light Absorber Using a Cost-Effective Mechanochemical Method for Photovoltaic Applications, *Materials* **15** (2022) 1708. https://doi.org/10.3390/ma15051708
- [33] S. E. Bianchi, V.W. Angeli, K. C. B. de Souza, D. dos S. Miron, G. de A. Carvalho, V. dos Santos, R.N. Brandalise, Evaluation of the solubility of the HPMC: PVA blends in biological fluids in vitro, *Materials Research* **14** (2011) 166-171. https://doi.org/10.1590/S1516-14392011005000033
- [34] Ri. Prasanna, Ku. Sankari, Design, evaluation and in vitro in vivo correlation of glibenclamide buccoadhesive films, *International Journal of Pharmaceutical Investigation* **2** (2012) 26. https://doi.org/10.4103/2230-973X.96923
- [35] S. Abbad, K. Guergouri, S. Gazaout, S. Djebabra, A. Zertal, R. Barille, M. Zaabat, Effect of silver doping on the photocatalytic activity of TiO₂ nanopowders synthesized by the sol-gel route, *Journal of Environmental Chemical Engineering* **8** (2020) 103718. https://doi.org/10.1016/j.jece.2020.103718
- [36] H. T. Ahmed, V. J. Jalal, D. A. Tahir, A. H. Mohamad, O. G. Abdullah, Effect of PEG as a plasticizer on the electrical and optical properties of polymer blend electrolyte MC-CH-LiBF₄ based films, *Results in Physics* **15** (2019) 102735. https://doi.org/10.1016/j.rinp.2019.102735
- [37] Harshlata, K. Mishra, D.K. Rai, Effect of polymer blending on the electrochemical properties of porous PVDF/PMMA membrane immobilized with organic solvent based liquid electrolyte, *International Journal of Materials Research* **114** (2023) 662-670. https://doi.org/10.1515/ijmr-2021-8758
- [38] A.K. Chauhan, D. Kumar, K. Mishra, A. Singh, Performance enhancement of Na⁺ ion conducting porous gel polymer electrolyte using NaAlO₂ active filler, *Materials Today Communications* **26** (2021) 101713. https://doi.org/10.1016/j.mtcomm.2020.101713
- [39] S. B. Aziz, E. M. A. Dannoun, M. H. Hamsan, H.O. Ghareeb, M. M. Nofal, W. O. Karim, A. S. F. M. Asnawi, J. M. Hadi, M. F. Z. A. Kadir, A Polymer Blend Electrolyte Based on CS with Enhanced Ion Transport and Electrochemical Properties for Electrical Double Layer Capacitor Applications, *Polymers* **13** (2021) 930. https://doi.org/10.3390/polym13060930
- [40] E. Trevisanello, T. Ates, S. Passerini, F.H. Richter, J. Janek, Influence of the Polymer Structure and its Crystallization on the Interface Resistance in Polymer-LATP and Polymer-LLZO Hybrid Electrolytes, *Journal of The Electrochemical Society* **169** (2022) 110547. https://doi.org/10.1149/1945-7111/aca125

- [41] M. Ravi, K. Kiran Kumar, V. Madhu Mohan, V.V.R. Narasimha Rao, Effect of nano TiO₂ filler on the structural and electrical properties of PVP based polymer electrolyte films, *Polymer Testing* **33** (2014) 152-160. https://doi.org/10.1016/j.polymertesting.2013.12.002
- [42] W. Zhai, Y. Zhang, L. Wang, F. Cai, X. Liu, Y. Shi, H. Yang, Study of nano-TiO₂ composite polymer electrolyte incorporating ionic liquid PP12O1TFSI for lithium battery, *Solid State Ionics* **286** (2016) 111-116. https://doi.org/10.1016/j.ssi.2016.01.019
- [43] J. Yang, X. J. Meng, M. R. Shen, L. Fang, J. L. Wang, T. Lin, J. L. Sun, J. H. Chu, Hopping conduction and low-frequency dielectric relaxation in 5 mol% Mn doped (Pb,Sr)TiO₃ films, *Journal of Applied Physics* **104** (2008) 104113. https://doi.org/10.1063/1.3021447
- [44] X. Wang, H. Zhai, B. Qie, Q. Cheng, A. Li, J. Borovilas, B. Xu, C. Shi, T. Jin, X. Liao, Y. Li, X. He, S. Du, Y. Fu, M. Dontigny, K. Zaghib, Y. Yang, Rechargeable solid-state lithium metal batteries with vertically aligned ceramic nanoparticle/polymer composite electrolyte, *Nano Energy* **60** (2019) 205-212. https://doi.org/10.1016/j.nanoen.2019.03.051
- [45] S. A. Ahmed, T. Pareek, S. Dwivedi, M. Badole, S. Kumar, LiSn₂(PO₄)₃-based polymer-in-ceramic composite electrolyte with high ionic conductivity for all-solid-state lithium batteries, *Journal of Solid State Electrochemistry* **24** (2020) 2407-2417. https://doi.org/10.1007/s10008-020-04783-z
- [46] X. Mei, Y. Wu, Y. Gao, Y. Zhu, S.-H. Bo, Y. Guo, A quantitative correlation between macromolecular crystallinity and ionic conductivity in polymer-ceramic composite solid electrolytes, *Materials Today Communications* **24** (2020) 101004. https://doi.org/10.1016/j.mtcomm.2020.101004
- [47] R. Deivanayagam, M. Cheng, M. Wang, V. Vasudevan, T. Foroozan, N. V. Medhekar, R. Shahbazian-Yassar, Composite Polymer Electrolyte for Highly Cyclable Room-Temperature Solid-State Magnesium Batteries, *ACS Applied Energy Materials* **2** (2019) 7980-7990. https://doi.org/10.1021/acsaem.9b01455
- [48] X. Hu, M. Jing, H. Yang, Q. Liu, F. Chen, W. Yuan, L. Kang, D. Li, X. Shen, Enhanced ionic conductivity and lithium dendrite suppression of polymer solid electrolytes by alumina nanorods and interfacial graphite modification, *Journal of Colloid and Interface Science* **590** (2021) 50-59. https://doi.org/10.1016/j.jcis.2021.01.018
- [49] T. Pareek, S. Dwivedi, S.A. Ahmad, M. Badole, S. Kumar, Effect of NASICON-type LiSnZr(PO4)₃ ceramic filler on the ionic conductivity and electrochemical behavior of PVDF based composite electrolyte, *Journal of Alloys and Compounds* **824** (2020) 153991. https://doi.org/10.1016/j.jallcom.2020.153991
- [50] B. Liu, Y. Huang, H. Cao, L. Zhao, Y. Huang, A. Song, Y. Lin, X. Li, M. Wang, A novel porous gel polymer electrolyte based on poly(acrylonitrile-polyhedral oligomeric silsesquioxane) with high performances for lithium-ion batteries, *Journal of Membrane Science* **545** (2018) 140-149. https://doi.org/10.1016/j.memsci.2017.09.077
- [51] A. Song, Y. Huang, X. Zhong, H. Cao, B. Liu, Y. Lin, M. Wang, X. Li, Novel lignocellulose based gel polymer electrolyte with higher comprehensive performances for rechargeable lithium-sulfur battery, *Journal of Membrane Science* **556** (2018) 203-213. https://doi.org/10.1016/j.memsci.2018.04.003

© 2024 by the authors; licensee IAPC, Zagreb, Croatia. This article is an open-access article distributed under the terms and conditions of the Creative Commons Attribution license (https://creativecommons.org/licenses/by/4.0/)

